Feedback in Galaxy Clusters and Brightest Cluster Galaxy Star Formation

by

Kevin Fogarty

A dissertation submitted to The Johns Hopkins University in conformity with the requirements for the degree of Doctor of Philosophy.

Baltimore, Maryland

August, 2017

Abstract

My main thesis work is to understand the relationship between star formation in the brightest cluster galaxy (BCG) and the thermodynamical state of the intracluster medium (ICM) of cool core galaxy clusters. Detailed photometry of BCGs in galaxy clusters observed in the Cluster Lensing and Supernova survey with Hubble (CLASH) reveal ultraviolet and Hα emitting knot and filamentary structures extending several tens of kpc. I initially focus on these structures, which harbor starbursts forming stars at rates between < 1 $M_\odot$ yr^{-1} and $\sim$ 250 $M_\odot$ yr^{-1}. I perform ultraviolet through far-infrared Spectral Energy Distribution (SED) fitting on combined Hubble, Spitzer, and Herschel photometry of CLASH BCGs, and measure star formation rates (SFRs), dust contents, and constrain the duration of starburst activity. Using X-ray data from Chandra, I find a tight relationship between CLASH BCG SFRs and the cooling-to-freefall time ratio in the ICM. I propose treating the cooling-to-freefall time ratio as a proxy for the mass condensation efficiency of the ICM in the core of cool-core clusters, an interpretation which is motivated by recent theoretical work de-

scribing feedback regulated condensation and precipitation of the ICM in cool core clusters. I follow up this work by performing similar SED fitting on a larger sample of clusters observed in the Cosmic Evolution Survey (COSMOS). I examine the evolution of star formation in BCGs and discuss the impact of cluster environment on BCG specific SFRs.

Besides this work, I have developed the polynomial apodized vortex coronagraph (PAVC). I describe the performance of this theoretical coronagraph design, which restores ideal starlight suppression to the vortex coronagraph in the presence of centrally obstructed telescope pupils. The PAVC offers substantial gains in throughput relative to other designs that optimize vortex coronagraphs for obstructed pupils, and can be combined with active correction techniques to account for pupils with both central obstructions and obstructions due to support structures, segment gaps, or defects.

Primary Reader and Advisor: Marc Postman

Secondary Reader: Tobias Marriage

Acknowledgments

During my five years at JHU, I have had the opportunity to study and contribute to a large breadth of astronomical research. Despite never formally making rotations, I have been able to study aspects of astronomy ranging from exoplanets to clusters of galaxies. Over the course of the past five years, I've worked with that data from more observatories than I can keep track of, wrote and re-wrote proposals until they were finally accepted, and designed coronagraphs. During it all, I've traveled to more places in the past five years than I have in the previous twenty-two, met new people, and got married to the wonderful Alice Li! To everyone who has made all of this possible, thank you!

- Thank you to my advisor, Marc Postman, for encouraging me to develop my ideas and write about them well, and for supporting my somewhat split-personality research. While working with you, I learned much about BCGs and galaxy clusters, but more importantly, I learned how to write a good paper and a good proposal. You taught me to be rigorous, pushed me to follow through, and always provided support. One of the most impor-

tant lessons learned developing ALMA project over three observing cycles is to play the long game, and that persistence pays.

- To my co-advisor, Toby Marriage, for always being available to discuss clusters, ACT, ALMA, and much more.

- To Laurent Pueyo for inspiring me to work on the vortex coronagraph. Thanks to you and to Johan Mazoyer and Mamadou NDiaye for an amazing collaboration, and for all the great results that are coming out of it! I am looking forward to working with all of you next year!

- To my co-authors Megan Donahue, John Moustakas, Kevin Cooke, Rebecca Larson, and Thomas Connor, for their invaluable contributions to the work presented here. To Mark Voit, Anton Koekemoer, and, Michael McDonald for their useful suggestions and thoughtful discussions. To the many members of CLASH who collaborated with Marc and me on ALMA proposals.

- To Ron Allen and Anand Sivaramakrishnan for teaching the course where I learned optics. Your class was hugely influential on my understanding of instruments and observations, and was one of the most influential factors in my graduate education in shaping my approach to astronomy.

- To Christine Jones, who guided me through my senior thesis in college and set me on course to pursuing the degree Im now finishing.

ACKNOWLEDGMENTS

- To my family and friends, who supported me through this endeavor, and especially Alice. Thank you for putting up with my late nights and early mornings! I am so lucky to have met you, and I could not have done this without you.

Contents

Abstract **ii**

Acknowledgments **iv**

List of Tables **xiii**

List of Figures **xiv**

1 Introduction **1**

1.1 Galaxy Cluster Environment 3

1.2 ICM Radiation 6

1.3 Cool Core Clusters 10

1.4 Cluster-Scale Feedback 13

1.5 BCG Star Formation 19

1.5.1 BCG Star Formation History and Evolution 20

1.5.2 Star Formation at Low to Moderate Redshifts 21

1.6 Measuring Stellar Populations with SED Fitting 23

1.7 Outline of the Dissertation 27

2 Star Formation Activity in CLASH Brightest Cluster Galaxies 31

2.1 Introduction 32

2.2 Observations 36

2.2.1 CLASH HST Observations 36

2.2.2 Chandra X-ray Observations 38

2.2.3 Spectra 38

2.3 Analysis 40

2.3.1 Mean UV Luminosities 40

2.3.2 Hα+[N II] Maps 43

2.3.3 Other Emission Lines 45

2.3.4 Reddening Correction 46

2.3.5 Broadband Aperture Photometry 53

2.3.6 Stellar Population Properties 55

2.4 Results 56

2.4.1 Broadband Luminosities and Star Formation Rates 56

2.4.2 SOAR Spectra Results 60

2.4.3 Correlation with ICM X-Ray Properties 67

2.4.3.1 Core Entropies 67

2.4.3.2 Core $\dot{M}_g$ Estimates 69

2.4.4 Model Fitting to RXJ1532.9+3021 74

2.5 Discussion 78
2.5.1 BCG-ICM Interactions 80
2.6 Conclusion 85
2.7 Appendix 88
2.7.1 SED Fitting Consistency Checks 90

3 The Relationship Between Brightest Cluster Galaxy Star Formation and the Intracluster Medium in CLASH 93

3.1 Introduction 94
3.2 Observations 100
3.2.1 HST: UV through near IR photometry 100
3.2.2 Spitzer: mid-IR photometry 101
3.2.3 Herschel: far-IR photometry 102
3.2.4 Chandra: X-ray Observations 102
3.3 Methods 104
3.3.1 BCG Photometry 104
3.3.1.1 Photometric Errors 108
3.3.2 SED Fitting 110
3.3.3 Cooling and Freefall Time Profiles 115
3.4 Results 120
3.4.1 The Starburst - ICM Connection 124
3.4.2 Star Formation and Dust Parameters 131

3.4.3 Testing Impact of AGN Emission on SED Results on MACS1931.8-2653 . . . 136
3.5 Discussion . . . 138
3.5.1 t_{cool}/t_{ff} As A Proxy For Thermal Instability and ICM Condensation . . . 138
3.5.1.1 The Role of t_{ff} in the SFR-t_{cool}/t_{ff} relationship . . 141
3.5.2 BCG Activity and Low Cooling Time Gas . . . 144
3.5.3 Characteristics of Large Starbursts in BCGs . . . 150
3.6 Conclusions . . . 151
3.7 Appendix . . . 154

4 3.4μm M/L Ratio and Stellar Mass Evolution of BCGs in COSMOS from $z < 1.0$ 169

4.1 Introduction . . . 170
4.2 Sample Selection . . . 173
4.3 Archival Data . . . 174
4.3.1 GALEX Observations . . . 176
4.3.2 Canada–France–Hawaii Telescope (CFHT) . . . 176
4.3.3 Subaru . . . 177
4.3.4 Vista . . . 177
4.3.5 Spitzer Observations . . . 178
4.3.6 Herschel Observations . . . 178

4.4 Methods 179
4.4.1 SED Construction 179
4.4.2 SED Fitting 180
4.5 Results 184
4.5.1 BCG Redshift Evolution 184
4.6 Discussion 190
4.6.1 Comparison Between Literature and Our Work 190
4.6.1.1 Differences in Behavior Between Literature Samples 192
4.6.2 Evolution of $M/L_{3.4\mu m}$ With Redshift 197
4.7 Conclusions 199
4.8 Appendix 201

5 Concluding Remarks **206**

A Polynomial Apodizers for Centrally Obscured Vortex Coronagraphs 209

A.1 Introduction 210
A.2 The Analytical Vortex Operator and Optimal Mask Algorithm . . 215
A.2.1 The Vector Vortex 215
A.2.2 Apodized Vortex Formalism 218
A.2.3 Optimal Mask Algorithm 223
A.3 The Apodizing Filter PAVC 230

A.3.1 Figure of Merit Selection 230

A.3.2 Total Energy Throughput Performance 231

A.3.3 Off-Axis Source Performance 235

A.4 The Shaped Mirror PAVC 239

A.4.1 Mirror Apodizations for the PAVC 241

A.4.2 Mirror Apodized PAVC Performance 245

A.5 Application To Future Telescopes 248

A.6 Conclusion 255

A.7 Vortex Operator for Analytical Pupil Shapes 258

Vita **287**

A.8 Refereed Articles 287

A.9 Proceedings 289

List of Tables

2.1 SOAR Observations of Brightest Cluster Galaxies 40
2.2 UV and Hα Filters for BCG Luminosities 54
2.3 BCG Star Formation Rates 59
2.4 t_{cool}/t_{ff} Threshold Radii 71
2.5 SED Fitting Parameter Choices 89

3.1 *Herschel* Observations 103
3.2 SED Fitting Parameters 116
3.3 BCG Stellar and Dust Parameters 125
3.4 Best Fit χ^2 Values 125
3.5 BCG Stellar and Dust Parameters assuming a Chabrier IMF and Calzetti attenuation law 157
3.6 BCG Stellar and Dust Parameters assuming a modified Calzetti attenuation law 158
3.7 BCG Stellar and Dust Parameters assuming Witt clumpy SMC-like dust in a shell geometry 159

4.1 SED Fitting Parameters 182
4.2 Redshift Binned SFR and sSFR 185
4.3 BCG Best-Fit Parameters 202

A.1 Summary of Important Variables for Deriving the Apodized Vortex Formalism 217
A.2 Definitions of Throughput 228

List of Figures

1.1 Example ICM Morphology 5
1.2 Example RGS Spectrum 14
1.3 Correspondence Between CLASH BCG UV Morphology and Simulated Molecular Gas Distributions 18
1.4 Multicolor Image of the Phoenix BCG 22
1.5 CLASH Photometric Bands 24

2.1 BCG Color Composite Images 37
2.2 Old Stellar SED 42
2.3 BCG UV, Hα, and $E(B-V)$ Triptychs 47
2.3 *Continued* 48
2.3 *Continued* 49
2.4 Reddening Correction Procedure 50
2.5 RXJ1532.9+3021 Hα Map 56
2.6 CLASH L_{UV} vs $L_{H\alpha+[NII]}$ 57
2.7 CLASH UV SFR vs. Area 60
2.8 CLASH L_{UV} vs $L_{[OII]}$ 61
2.9 CLASH L_{UV} vs $L_{H\beta}$ 62
2.10 CLASH BPT and Blue Line Diagrams 64
2.11 SFR vs. Core Entropy 68
2.12 SFR-$\dot{M}_g$ Correlation 70
2.13 SFR vs $\dot{M}_g$ 73
2.14 RXJ1532.9+3021 SED Posterior Distribution 75
2.15 RXJ1532.9+3021 SED Fit Maps 76
2.16 RXJ1532.9+3021 Cavities 83
2.17 SED Fit Parameter Correlation 90

3.1 Photometric Apertures for SED Fitting 107
3.2 SFH Example 113
3.3 Synthetic Spectrum Example 114

3.4 SFR vs. t_{cool}/t_{ff} . . . 126
3.5 Estimate of the Probability of Measuring a Given Intrinsic Scatter when Comparing SFR and t_{cool}/t_{ff} . . . 129
3.6 Starburst Duration vs. t_{cool} . . . 132
3.7 SFR vs. Starburst Duration . . . 134
3.8 SFR vs. Dust Mass . . . 135
3.9 SFR vs. t_{cool} . . . 143
3.10 SFR-t_{cool}/t_{ff} vs. t_{cool}/t_{ff} Measurement Radius . . . 145
3.11 Best Fit Residuals for SFR-t_{cool} and SFR-t_{cool}/t_{ff} Relationships . 146
3.12 Marginal Posterior Probability Distributions . . . 160
3.12 *Continued* . . . 161
3.12 *Continued* . . . 162
3.13 Marginal Burst Duration vs. FBURST Posterior Distribution . . . 163
3.14 Marginal Burst Duration Posteriors . . . 164
3.15 Posterior Probability Distribution of all Parameters for the Abell 383 BCG . . . 165
3.16 CLASH Best Fit SEDs . . . 166
3.16 *Continued* . . . 167
3.16 *Continued* . . . 168

4.1 COSMOS BCG SFR vs. Redshift . . . 186
4.2 COSMOS BCG sSFR vs. Redshift . . . 187
4.3 COSMOS BCG Mass vs. Redshift . . . 187
4.4 Evolution of the Mass-to-Light Ratio . . . 188
4.5 sSFR vs. BCG Stellar Mass . . . 192
4.6 sSFR vs. Cluster M_{500} . . . 197
4.7 COSMOS Best Fit SEDs . . . 203
4.7 *Continued* . . . 204
4.7 *Continued* . . . 205

A.1 Layout of the PAVC . . . 220
A.2 Vortex Operator Acting on Polynomials . . . 224
A.3 Example Optimal Pupil Mask Profiles . . . 232
A.4 Throughput vs. Secondary Mirror Radius . . . 236
A.5 Inner Lyot Stop Radius vs. Secondary Mirror Radius . . . 237
A.6 PAVC Charge 2-6 Off-Axis Throughput Curves . . . 240
A.7 Layout of the Shaped-Mirror PAVC . . . 241
A.8 Inner Lyot Stop Radius vs. Secondary Mirror Radius . . . 244
A.9 Mirror Shapes for Charge 4 PAVC . . . 246
A.10 Mirror Shapes for Charge 6 PAVC . . . 247
A.11 Off-Axis Throughput for Charge 4 and 6 PAVC with Shaped Mirrors 249
A.12 PAVC+ACAD-OSM Instrument Design . . . 253

A.13 PAVC+ACAD-OSM Off-Axis Throughput 254

Chapter 1

Introduction

The most massive galaxies in the universe occupy gas and dark matter rich environments that drive their evolution and in rare cases can give rise to highly energetic feedback phenomena. Recent active galactic nucleus (AGN)-regulated feedback models propose that the evolution of cluster environments and of massive brightest cluster galaxies (BCGs) can be regulated by the activity of a single central black hole under conditions that allow clusters to form cool-cores. AGN feedback, once it starts, is potentially cyclic or could be perennially active (Mittal et al., 2015). The imprints feedback leaves in cluster cores and BCGs, in the form of excavated cavities in the intracluster medium (ICM), large reservoirs of molecular gas, and nebulous starbursts tens of kpc across, provide a wide array of avenues for constraining cluster-scale feedback and its role in BCG evolution.

Understanding the nature of feedback in cluster cores is necessary for understanding the physics of galaxy clusters. The energy output by AGN observed in BCGs of cool-core clusters is sufficient to offset the $\sim 100-1000\,\mathrm{M}_{\odot}\,\mathrm{yr}^{-1}$ cooling flows predicted to occur in the ICM of cool-core clusters (Fabian, 2012). The fact that these cooling flows, and correspondingly large BCG starbursts, are not observed is often called the "cooling flow problem" (Peterson et al., 2003). By offsetting cooling, feedback processes in BCGs can provide the solution to this problem by restoring a global equilibrium between heating and cooling in the ICM.

I will present insights gained into cluster-scale feedback by studying the star formation activity of BCGs in cool-core clusters. Star formation is an unusual property in BCGs, which are predominantly elliptical galaxies with early-type stellar populations (Zwicky, 1938; Morgan & Lesh, 1965; Von Der Linden et al., 2007a; Blanton & Moustakas, 2009). By examining relationships between BCG star formation and the detailed properties of the ICM measured using X-ray data, in this thesis I will provide observational constraints for the evolution of both feedback and BCGs.

1.1 Galaxy Cluster Environment

Galaxy clusters are the extremely high-mass end of the dark matter halo mass distribution, and are among the most massive gravitationally bound objects that have been observed (Abell, 1958; Peebles, 1980; Bahcall, 1999). Clusters are composed of a dark matter halo which contains a hot tenuous plasma atmopshere called the intracluster medium (ICM), and galaxies. The mass budget of the most massive clusters is dominated by the dark matter– a typical massive galaxy cluster may be $\sim$83-89$\%$ dark matter, $\sim$10-15$\%$ ICM, and $\sim$1-2$\%$ member galaxies by mass (Lin et al., 2003; Sanderson et al., 2003; Vikhlinin et al., 2006). The proportion of mass in the ICM decreases and in stellar mass in galaxies increases as the mass of the cluster halo decreases, and in the galaxy group regime, mass is split approximately evenly between stellar mass and the intra-group medium (Gonzalez et al., 2013).

The masses of galaxy clusters are typically measured within radii containing matter with a mean density exceeding some factor of the critical density, δ_{crit}, of the cosmos at the redshift of the cluster. R_{200}, the radius within which the mean density of the cluster is 200 times δ_{crit}, is close to the virial radius of a dynamically relaxed cluster[1] , so the corresponding mass M_{200} is used to es-

[1]A galaxy cluster is dynamically relaxed when enough time has passed for the motions of material that have become bound to the system to randomize through gravitational interactions and, in the case of the ICM, thermal interactions (Spitzer, 1962; Binney & Tremaine, 2008). Observationally, the relaxation state of a cluster is estimated by examining morphological indicators such as ellipticity, symmetry, or the presence of substructures (Jones & Forman, 1999).

timate the total mass of the cluster. M_{500} is also often quoted as the total mass of the cluster, especially in papers involving X-ray observations of the ICM, since the ICM is oftentimes too faint to observe at R_{200}. Clusters can have a mass $M_{200} \gtrsim 10^{15} M_{\odot}$; the largest know galaxy cluster, ACT-CL J0102-4915 ("El Gordo"), has a mass $M_{200} = (3.13 \pm 0.56) \times 10^{15} M_{\odot}$ (Jee et al., 2014).

The dark matter halos of galaxy clusters tend to obey a Navarro-Frenck-White, or NFW, density profile (Navarro et al., 1997). The NFW profile follows the form

$$\rho\left(r\right) = \frac{\rho_0}{1 + \left(\frac{r}{r_s}\right)^2}, \tag{1.1}$$

where r_s is the NFW profile scale radius and ρ_0 is the central density. The centers of galaxy clusters can deviate from this form. In particular, the matter density profile in the central 10-20 kpc of the cluster can be influenced by the mass contribution of the BCG, which can be relatively well approximated by either a singular isothermal sphere (Burke et al., 2015) or a Hernquist (1990) profile.

The overall morphology of a galaxy cluster may be directly observed via X-ray emission from the ICM, and may be traced by the distribution of cluster galaxies. Morphologies range from highly circular to "trainwrecks" (see Figure 1.1). More complex ICM morphologies are indicative of recent cluster mergers, and are often accompanied by observable shocks in the ICM and radio relics

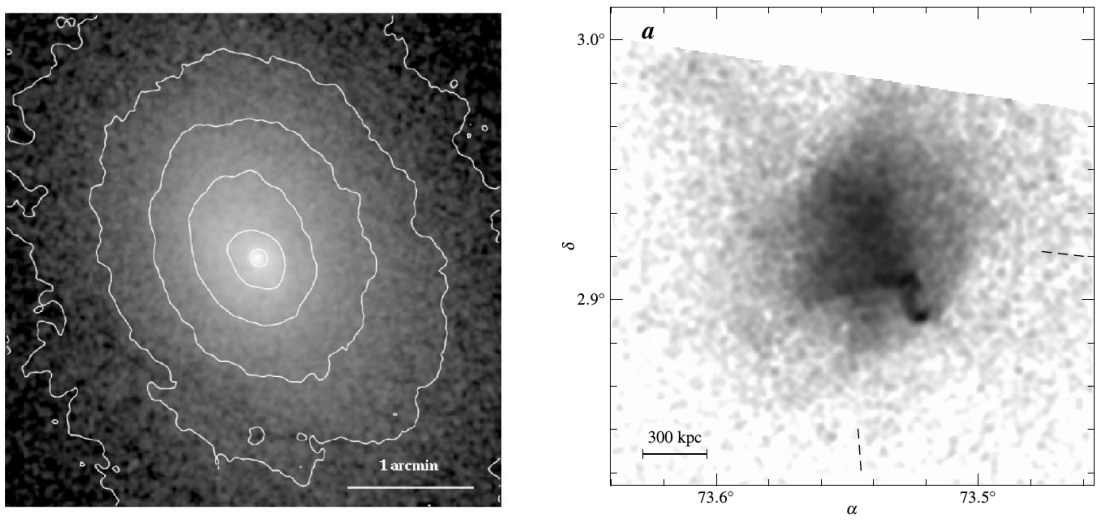

Figure 1.1 *Left:* The 0.3-8.0 keV *Chandra* X-ray image of Abell 2029 (Figure 1 in Lewis et al. (2002)). Abell 2029 is a dynamically relaxed cluster featuing a morphologically elliptical ICM. *Right:* The 0.5-2.0 keV *Chandra* X-rag image of Abell 520 is shown (Figure 1 in Markevitch et al. (2005)). Abell 520 is an example of a merger between two clusters.

and halos as dormant electron populations in the merging cluster halos are re-energized by shocks (van Weeren et al., 2017). On the other hand, in clusters that have not recently experienced mergers, the dynamic motions of the ICM will equilibrate to form a regular elliptical distribution (Jones & Forman, 1992; Buote & Tsai, 1996; Nurgaliev et al., 2013). BCGs in relaxed clusters usually are found at or near the bottom of the gravitational potential well of the cluster, and reside in close proximity to the ICM X-ray brightness peak, although some can be offset by as much a 1 Mpc (Bildfell et al., 2008; Lauer et al., 2014).

It is in the dynamically relaxed clusters that large BCG starbursts can occur and cool-cores can form. In these clusters, cooling due to X-ray radiation

from the ICM produces cool cores in the centers of clusters that are several keV cooler and several orders of magnitude denser than the surrounding ICM. These cool cores have also been predicted to form cooling flows, giving rise to the cooling flow problem and creating the environment for observed BCG feedback phenomena.

1.2 ICM Radiation

The ICM in a galaxy cluster radiates primarily through a process of thermal Bremsstrahlung emission. The ICM is a tenuous plasma with a typical particle density in the range of $10^{-4} - 10^{-2}$ cm^{-3}; when free electrons in this plasma interact with ions they accelerate, emitting an X-ray to make up the energy difference (Fabian, 1994). For massive galaxy clusters, which have $\sim 10^{14}$ M$_{\odot}$ of ICM plasma with a temperature of ~ 5 keV, this process produces X-ray luminosities on the order of $10^{44} - 10^{45}$ ergs s^{-1}.

Following the discussion in Rybicki & Lightman (1986), the Bremsstrahlung power emitted per unit frequency by an electron passing an approximately stationary ion is proportional to the change in the electron's velocity produced by this interaction. This is true for frequencies ν where $1/\nu$ is small relative to the time the electron spends interacting with the ion; when ν is large the power emitted is ~ 0. We can approximate the change in velocity, Δv, as the change

in velocity normal to the trajectory of the electron, as long as $\|\Delta v\| \ll \|v\|$. For an impact parameter b, and an ion of charge Ze, where e is the charge of an electron, the acceleration of an electron located at ion-centric coordinates (r, θ) is

$$\begin{aligned} a &= \frac{F_\perp}{m_e} \\ &= \frac{1}{m_e}\frac{Ze^2 \sin\theta}{r^2} \\ &= \frac{Ze^2}{m_e}\frac{1}{b^2 + v^2t^2}\frac{b}{\left(b^2 + v^2t^2\right)^{1/2}}, \end{aligned} \tag{1.2}$$

where the time, t, is defined such that $t = 0$ when $r = b$ and where m_e is the mass of the electron. Integrating the acceleration over time results in the expression given in Rybicki & Lightman (1986):

$$\Delta v = \frac{2Ze^2}{m_e b v}. \tag{1.3}$$

Therefore, the emission from an individual electron colliding with an individual ion at speed v is proportional to v^{-1}.

For a thermal plasma, the velocity of electrons follows a Maxwellian distri-

bution. The power per electron/ion interaction is therefore

$$\begin{aligned}\frac{dP}{d\nu} &\propto \int_{(2h\nu/m_e)^(1/2)}^{\infty} v^{-1} e^{-\frac{m_e v^2}{k_B T}} d^3\vec{v} \\ &\propto \int_{(2h\nu/m_e)^(1/2)}^{\infty} v e^{-\frac{m_e v^2}{k_B T}} dv \\ &\propto T^{-1/2} e^{-h\nu/k_B T},\end{aligned} \tag{1.4}$$

where k_B is the Boltzmann coefficient and T is the temperature of the plasma (Rybicki & Lightman, 1986). The volume emissivity is the power per electron/ion interaction multiplied by the density of electrons, n_e, and density of ions, n_i. Therefore,

$$\epsilon_\nu \propto n_e n_i T^{-1/2} e^{-h\nu/k_B T}, \tag{1.5}$$

and the frequency-integrated emission is

$$\epsilon \propto n_e n_i T^{1/2}. \tag{1.6}$$

The ICM emits via other processes, including electron capture and two photon collisional excitation. Line emission produced by excitation and recombination also produce features in the ICM spectrum (Peterson & Fabian, 2006). These features are important for measuring the properties of the ICM; in particular the Fe K-complex is used to constrain metallicity, while several other lines (notably the Fe L-complex and OVIII) are used to measure the rate of

low-temperature plasma cooling (Peterson et al., 2001; Peterson & Fabian, 2006). Since all of these processes involve interactions between ion/electron pairs, they are $\propto n_e n_i$.

Since the ICM is constantly radiating away energy in collisional and recombination processes where electrons are losing momentum, it will gradually cool in the absence of energy injected into the plasma. From the features of ICM radiation described above, it is possible to define both a cooling function, $\Lambda\left(T, Z_{\odot}\right)$, and a cooling time, t_{cool}. $\Lambda\left(T, Z_{\odot}\right)$ is the bolometric power per pairwise interaction per unit volume, taking into account all of the continuum and line emission processes that occur in the plasma (Kaastra et al., 2008). Since ICM emission in a massive cluster is mostly due to Bremsstrahlung,

$$\Lambda\left(T, Z_{\odot}\right) \sim T^{1/2}. \tag{1.7}$$

Precise values of $\Lambda\left(T, Z_{\odot}\right)$ that take into account the metallicity of the plasma are computed numerically in tables such as those found in Sutherland & Dopita (1993).

The cooling time of the ICM, t_{cool}, is defined as the thermal energy of the ICM divided by the radiatively emitted power. t_{cool} is an estimate of the total time it will take for the ICM to cool, assuming no heat source exists and that the ICM is an optically thin plasma. Since the enthalpy of a ideal diffuse gas

is $\frac{5}{2}nk_BT$, where n is the density of the gas, the cooling time is

$$t_{cool} = \frac{\frac{5}{2}nk_BT}{n_e n_H \Lambda\left(T, Z_\odot\right)}, \tag{1.8}$$

where n_H is the hydrogen density (Peterson & Fabian, 2006). $n \sim n_e$ for a mostly hydrogen plasma, and as discussed above, $\Lambda \sim T^{1/2}$, so the approximate behavior of t_{cool} in the ICM is

$$t_{cool} \sim \frac{T^{1/2}}{n_e}. \tag{1.9}$$

The ICM cools more quickly as it gets denser and colder. Cooling is also mildly enhanced by increased metallicity, so the cooling time is driven down as the metallicity of the ICM increases (Sutherland & Dopita, 1993).

1.3 Cool Core Clusters

The tendency of the denser, colder ICM to cool more rapidly leads to formation of cool cores in dynamically relaxed clusters. The first evidence for the existence of cool core clusters was observed in the 1970s with the *Copernicus* X-ray Observatory (Fabian et al., 1974; Fabian, 1994). Observers identified clusters with core densities sufficient for the ICM to radiatively cool to below the range of temperatures where it emits in the X-rays ($\gtrsim 10^7$ K) in less than a Hubble time. Later, observations with *Chandra* and *XMM-Newton* confirmed

the existence of high-density, low-temperature cores with low cooling times (Peterson & Fabian, 2006).

The discovery of clusters with highly dense ICM cores with cooling times less than a Hubble time led to the prediction of cooling flows in these clusters. These cooling flows were predicted to deposit $\sim 100 - 1000$ $M_\odot$ yr^{-1} of cold gas in the centers of galaxy clusters, and fuel comparably intense starbursts in BCGs. However, cooling flows have gone unobserved at the levels implied by the temperatures and densities observed in ICM cores, and except in a handful of cases BCG star formation rates (SFRs) fall below the predicted cooling rate by at least an order of magnitude as well (Peterson & Fabian, 2006).

If the ICM of a dynamically relaxed galaxy cluster starts out in hydrostatic equilibrium, then locally the thermal pressure supporting a layer of gas balances the pressure due to gravity. The ICM 'atmosphere' in this case will be stratified, such that it becomes progressively denser and hotter at smaller radii (Sarazin, 1988). Since the gas in this atmosphere radiatively cools through Bremmstrahlung, it cools more rapidly the closer one gets to the center of the cluster. As the material in this idealized ICM cools, it loses pressure support and flows inwards towards the cluster center, until it eventually condenses out of the ICM.

In clusters with cool cores, the cooling time profile increases with radius (at least, outside the central few kpc), and only the central few hundred kpc is pre-

dicted to cool in less than a Hubble time, t_{Hubble} (Cavagnolo et al., 2009). Since the cores of galaxy clusters with $t_{cool} < t_{Hubble}$ are surrounded by envelopes of gas with $t_{cool} > t_{Hubble}$, the ICM in a cool-core can be replenished as it cools. In most cool-core clusters, the radius of the core (defined to be the radius within which the cooling time of the ICM is $< t_{Hubble}$) is about $0.1-0.15R_{500}$ (this radius is $\sim 100-200$ kpc for $M_{500} \sim 10^{15}$ clusters) (*e.g.* Vikhlinin et al. (2006)*, see also Chapters 2 and 3*). Therefore, most of the ICM in a cool core cluster is not in the core, and in a hydrostatic environment will take longer than the present age of the Universe to cool. This allows for cooling flows in galaxy clusters to be steady state (Sarazin, 1988).

The cooling flow spectrum can be calculated by estimating the contribution of gas at various temperatures in the flow to the overall spectrum as the gas cools from $\sim 10^7 - 10^8$ K to $\sim 10^4$ K. X-ray spectra from the *XMM-Newton* Reflection Grating Spectrograph (RGS) provide direct evidence for limited or non-existent cooling flows in galaxy clusters (see Figure 1.2). In the early 2000s, astronomers observed several prominent examples of clusters with large inferred cooling rates with RGS, but found upper limits on the isobaric cooling flow that were a small fraction of the inferred rate (Peterson et al., 2001). The observations revealed that ICM in cool cores appears to behave like a cooling flow only until the gas reaches $\sim 2-3$ keV ($\sim 2.3-3.5\times10^7$ K) (Molendi et al., 2016). This discrepancy demonstrated the existence of the cooling flow problem

in cluster cores.

Nonetheless, there is still substantial evidence that cold gas is produced out of the ICM in cool core clusters. In addition to starbursts, active BCGs have been observed with molecular gas reservoirs of up to several 10^{10} $M_\odot$ (O'Dea et al., 2008; McNamara et al., 2014). Cooling line emission in the UV is also observed in some cool core clusters, with notable examples including Abell 1795 and the Phoenix cluster (O'Dea et al., 2004; McDonald & Veilleux, 2009; McDonald et al., 2015). Therefore, while cooling flows appear to be ruled out in cool-core clusters, the ICM does appear to cool into multiphase gas which can fuel feedback and star formation in BCGs. This implies a feedback mechanism which quenches most cooling, most of the time, and understanding how and over what timescales feedback operates in cool-core cluster is a topic of current investigation.

1.4 Cluster-Scale Feedback

The cooling flow problem has given rise to a search for mechanisms that can suppress cooling flows. Feedback from AGN is currently the most plausible possibility; AGN mechanical mode feedback can inject enough energy into the ICM to offset cooling, and evidence for this form of feedback is observed in most cool-core clusters. Mechanical mode feedback is detected emanating from the

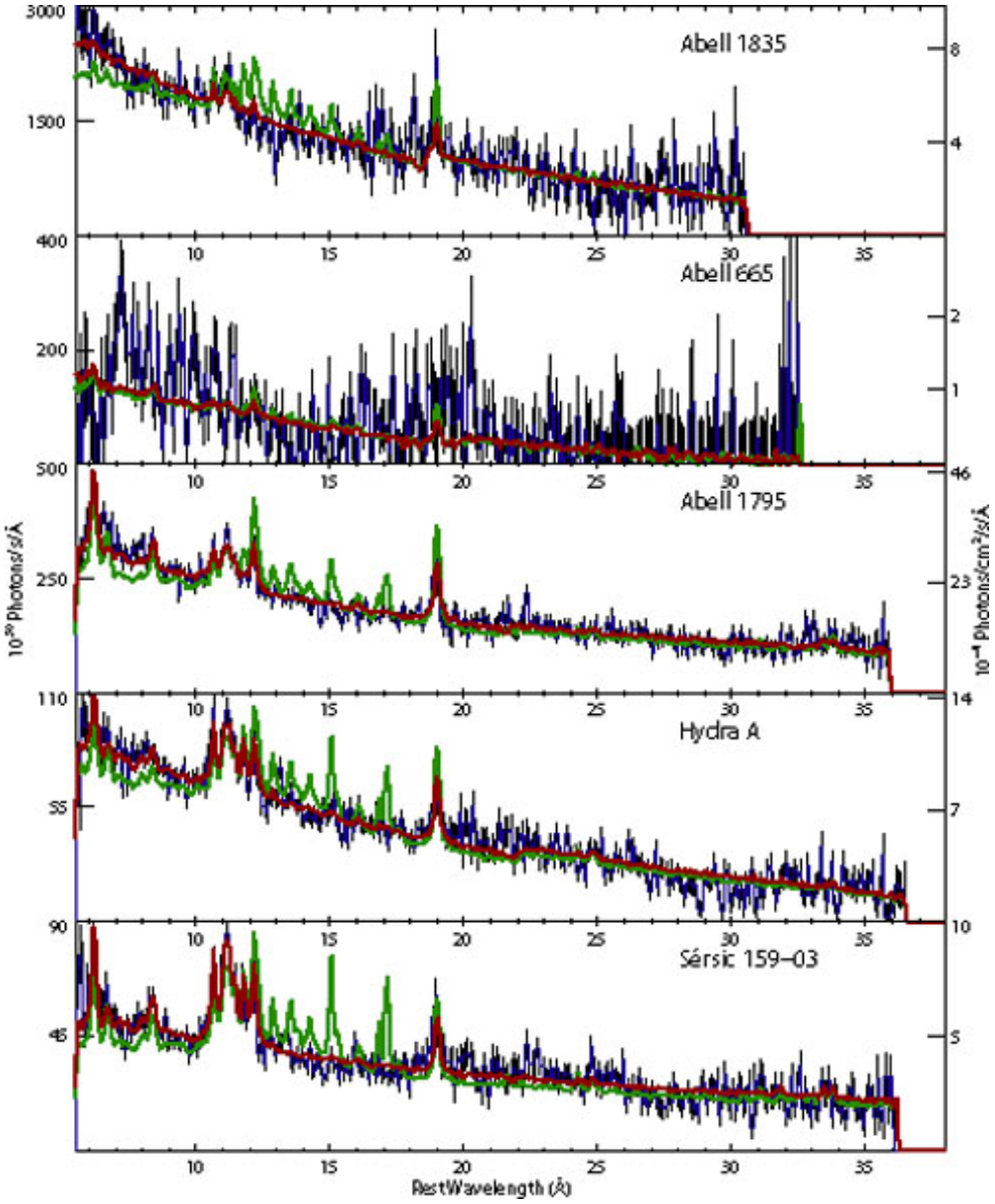

Figure 1.2 The RGS spectra of the central 5x20 arcminutes of five massive galaxy clusters, adapted from Figure 10 in Peterson & Fabian (2006). RGS data is shown in blue. The clusters shown, Abell 1835, Abell 665, Abell 1795, Hydra A, and Sérsic 159-03 are predicted to harbor cooling flows. Green lines are the best-fit isobaric cooling flow models, while red lines are the best-fit models allowing the cooling flow to cut off below a best-fit minimum temperature. Green model spectra predict what would be observed from a cooling flow where the ICM cools out of the plasma phase, while for red model spectra the flow is arrested at $\sim 2-3$ keV.

BCGs of cool-core clusters as radio plumes that can rise some 10s of kpc from the position of the BCG optical brightness peak. These jets excavate cavities in the ICM, such as the pair of cavities depicted in Figure 16 in Chapter 2 (Hlavacek-Larrondo et al., 2013b).

AGN feedback fueled by accreting material that cooled out of the ICM will tend to balance ICM cooling– too little reheating of the ICM will result in the central engine of the AGN being provided more 'fuel' to power feedback, while too much reheating of the ICM will deprive the engine of fuel. By calculating the infall velocity of molecular clouds using CO J(2-1) emission observed with ALMA, Tremblay et al. (2016) recently provided a direct observation of cold material infalling towards the AGN in the Abell 2597 BCG.

The mechanism governing the interaction between AGN feedback and the ICM may involve a combination of several processes. Feedback is observed occurring in cluster cores which feature low cooling time ICM, BCG starbursts, and multiphase material (Voit et al., 2015). Alternating cycles of cooling flows and feedback-induced quenching could explain these results if cooled material inefficiently forms stars while slowly precipitating onto the BCG AGN over Gyr timescales (Molendi et al., 2016). However, this scenario implies there should exist examples of cooling flows in systems which have yet to see AGN activity. More commonly considered explanations involve AGN jets interacting with the ICM to trigger rapid condensation of thermally unstable material while

heating the ambient gas. These models can explain much of the observed phenomena in cool cores, and have seen considerable development in recent years (Voit et al., 2017).

Feedback driven condensation and precipitation of the ICM provides an overall balance between cooling and heating in cool-core clusters, while locally thermally unstable volumes of gas cool to create the multiphase material that fuels BCG starbursts and further AGN output. The work done on ICM plasma by AGN jets can render volumes of gas thermodynamically unstable. These volumes will cool more quickly than they can descend the cluster gravitational potential well to an altitude where they are in local hydrostatic equilibrium, and so they rapidly condense into cold, multiphase gas with both atomic and molecular components (Meece et al., 2016). In simulated studies, the onset of local thermodynamical instability occurs when the cooling time to freefall time ratio (t_{cool}/t_{ff}) [2] is about 10 (Voit et al., 2017). ICM plasma with $t_{cool}/t_{ff} \lesssim 10$ can cool rapidly enough to condense before descending down the the gravitational potential to an altitude where the entropy contrast with the ambient medium is too small for the gas to condense.

Furthermore, simulations of cool core clusters with AGN mechanical-mode feedback which produce condensation and precipitation reproduce the UV and

[2] $t_{ff}\,(r) \equiv \sqrt{(\frac{2r^3}{GM(r)}}$, where G is the gravitational constant and $M\,(r)$ is the mass enclosed in a radius r. t_{ff} measures the time needed for ICM gas to flow into the cluster center under the influence of gravity.

line-emission nebulae observed in starbursting BCGs (Donahue et al., 2015; Tremblay et al., 2015; Li et al., 2015; Gaspari et al., 2017). The correspondence between simulated and real-world morphologies is illustrated in Figure 1.3.

A similar, but contrasting view of condensation and precipitation holds that the threshold for instability in ICM plasma with a low cooling time is not set by the freefall time but by the drag forces acting on the gas (McNamara et al., 2016). Condensation is dominated by uplift, wherein rising jet-inflated cavities displace ICM in their wake. When the infall timescale set the gravitational potential and drag on the displaced ICM from the surrounding gas prevent the gas from returning to hydrostatic equilibrium in less than a cooling time, it will condense.

This uplift-dominated condensation model may explain why the $t_{cool}/t_{ff} = 10$ threshold does not neatly separate cluster cores with multiphase gas from cluster cores without (Hogan et al., 2017). Specifically, Hogan et al. (2017) argues that t_{cool}/t_{ff} does not provide more predictive power than t_{cool} alone for separating cluster cores with multiphase gas from cluster cores without. Furthermore, recent ALMA observations provide dramatic illustrations of molecular gas entraining jet-excavated cavities (McNamara et al., 2014; Russell et al., 2014). While uplifted gas condensing is a feature of condensation models generally, the McNamara et al. (2016) model suggests that uplift is required for condensation to proceed.

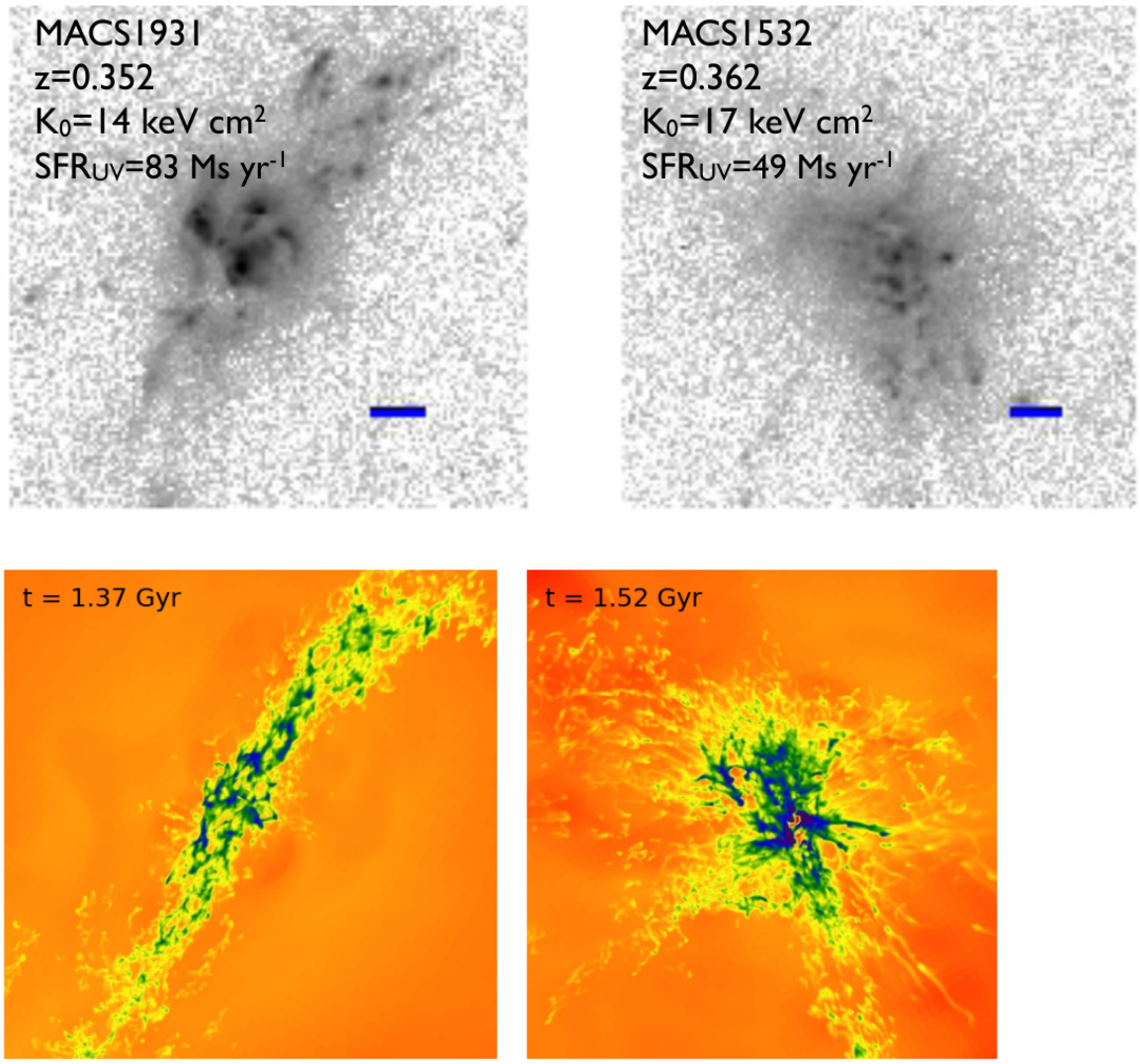

Figure 1.3 *Top:* UV photometry of the BCGs in CLASH clusters MACSJ1931.8-2653 and RXJ1532.9+3021. The blue bar in each images depicts a 1" scale. The reported SFRs are estimated from UV continuum fluxes without correcting for dust. *Bottom:* Snapshots of the cold gas distribution from the simulated cool core cluster in Li & Bryan (2014) that have morphologies similar to the extended UV emission in the BCGs above. The timestamp in the upper left of each snapshot corresponds to the time since the simulation was "turned on." Figure adapted from Donahue et al. (2015).

1.5 BCG Star Formation

BCGs differ substantially from both field galaxies and other cluster galaxies in ways that are heavily influenced by the cluster environment. BCGs exhibit merger-driven mass growth at far greater rates than those found in field galaxies owing to their positions in galaxy-rich cluster environments (Von Der Linden et al., 2007a). As a result, these galaxies can be many times more massive than other galaxies in the cluster environment, and extensive merger histories can result in BCGs having flatter central surface brightness profiles than other cluster ellipticals (Lauer et al., 2007; Bernardi et al., 2007; Lauer et al., 2014). Nonetheless, this merger history produces very little star formation, since both the BCG and the satellite galaxies that merge with it are ram-pressure stripped by moving through the ICM (Ruszkowski & Springel, 2009). The star formation that does occur in BCGs is typically either a product of initial proto-BCG and proto-cluster formation or mergers at high-redshift, or due to ICM cooling and feedback in low- to intermediate- redshift clusters (Webb et al., 2015b; McDonald et al., 2016).

1.5.1 BCG Star Formation History and Evolution

Recently, observations of proto-clusters have revealed clues about the initial stages of BCG formation. Images obtained with the *Hubble Space Telescope* (*HST*) show galaxies in the centers of forming clusters which are the site of sprawling bursts of star formation ignited when infalling progenitor galaxies merge or initial cooling flows spark massive starbursts (Webb et al., 2015a). This initial mass growth is believed to peak before a redshift of $z = 1$, after which *in situ* star formation quickly becomes a negligible component driving BCG mass growth (Webb et al., 2015b).

While initial predictions indicated that BCGs formed most of their stellar mass during this initial period of robust star formation, recent semi-analytical models predict that BCGs double or triple in stellar mass between $z = 1.0$ and the present day (De Lucia & Blaizot, 2007). This mass growth is believed to be merger driven (Ruszkowski & Springel, 2009; Liu et al., 2009). Satellite galaxies falling into the potential well of the dark matter halo are essentially swallowed up by the BCG. In simulations, by late times this often takes the form of gas-poor satellites accreting onto a main progenitor without fueling star formation, although above $z \sim 0.6$, galaxy mergers in young clusters may drive elevated rates of star formation (McDonald et al., 2016).

1.5.2 Star Formation at Low to Moderate Redshifts

BCG star formation is unusual in the sense that the old stellar populations and overall elliptical morphologies of BCGs suggests that star formation is not fueled by a molecular gas-rich ISM. Indeed, the majority (between $\sim 70 - 80\%$ depending on sample selection) of BCGs are quiescent red galaxies (Crawford et al., 1999; Edwards et al., 2007). Nonetheless, starbursts in low- to moderate-redshift BCGs span several orders of magnitude. The SFR in the most extreme recorded BCG starburst, found in the Phoenix Cluster, is $\sim 500 - 2000$ $M_\odot$ yr^{-1} (Mittal et al., 2017).

Spatially resolved observations of 'active' BCGs at $z \lesssim 0.6$ demonstrate that the majority of optical line and UV emission in these galaxies is situated in extended knot-and-filament structures (for example, Figure 1.4). Star forming nebulae in BCGs can extend tens of kpc from the BCG center. Therefore, while some of the emission is due to AGN activity, the majority is most likely due to recent star formation (Conselice et al., 2001; O'Dea et al., 2004; McDonald & Veilleux, 2009; McDonald et al., 2014a; Tremblay et al., 2012, 2015). A handful of BCGs harbor type II quasars, with sizable optical fluxes, while most active BCGs do not have bright AGN (Kirk et al., 2015).

Multiple lines of evidence suggest that BCG star formation is fueled by ra-

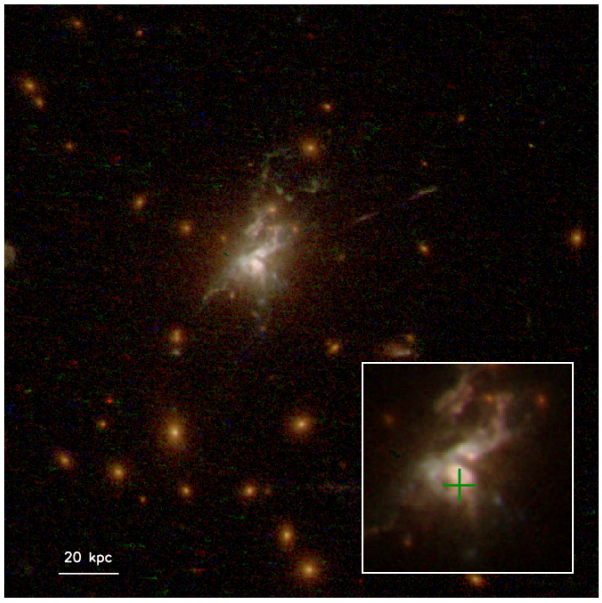

Figure 1.4 A combined color image of the Phoenix Cluster BCG, observed with *HST*. Taken from Figure 2 in McDonald et al. (2013). Blue knots and filaments are regions of enhanced star formation, and extend tens of kpc from the center of the BCG. The inset in the lower right details the complex structure of the starburst in the center of the BCG, along with the position of an X-ray point source (green cross).

diatively cooled ICM gas. BCGs found at the bottom of the gravitational potential well of clusters with cool ICM cores exhibit star formation with an incidence of $\gtrsim 70\%$ or more (Donahue et al., 2010). Furthermore, the entropy of the ICM in a clusters core is a reliable indicator of whether the BCG will exhibit star formation or not; clusters with core entropies ≤ 30 keV cm^2 host active BCGs, while clusters with higher core entropies overwhelmingly do not (Hoffer et al., 2012).

1.6 Measuring Stellar Populations with SED Fitting

I examine star formation in BCGs using multi-wavelength near-UV through far-IR photometric datasets, along with optical spectra. The main thrust of this thesis, in particular Chapter 3, uses multi-observatory data from the Cluster Lensing and Supernova survey with Hubble (CLASH) (Postman et al., 2012) to constrain stellar population parameters in star-forming BCGs. CLASH is a survey of 25 massive galaxy clusters taken with *HST*, of which 20 were selected on the basis of X-ray mass and morphology. The central regions of these clusters were observed with 16 bands of photometry covering $\sim$2000-17000 Å for 15-20 orbits per band (see Figure 1.5) (Postman et al., 2012). These data can be supplemented with archival observations from *Spitzer* and *Herschel* to create spectral energy distributions (SEDs) spanning the near-UV to the far-IR.

Much of the analysis performed in this thesis relies on using the deep and highly detailed datasets available for CLASH to construct SEDs of star forming regions in BCGs and fit these SEDs to model spectra. In order to perform SED fitting, I used the tool `iSEDFIT` throughout, and made several modifications to `iSEDFIT` in order to maximize its utility for fitting the NUV-FIR SEDs of BCGs. `iSEDFIT` is a Bayesian Monte Carlo fitting routine designed to fit large numbers of SEDs to a given set of models in order to both constrain stellar

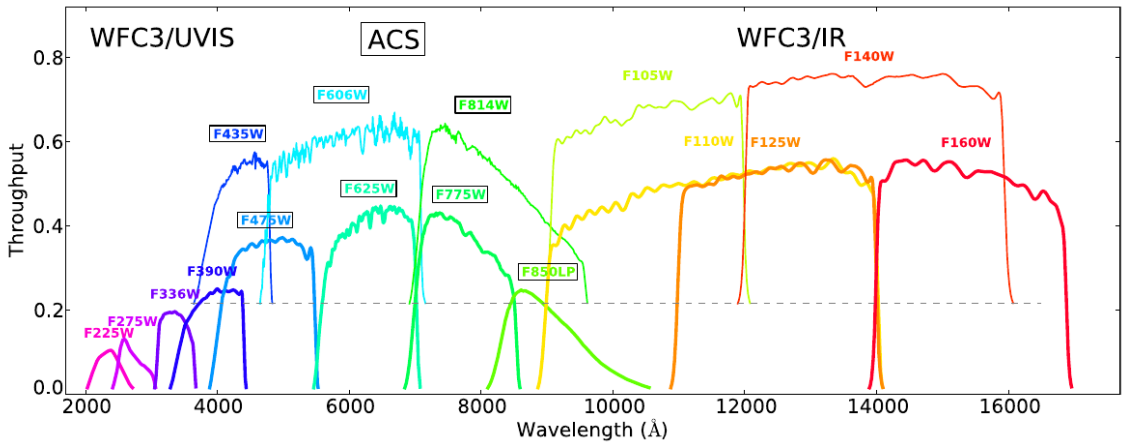

Figure 1.5 The throughput curves of the *HST* filterset used by CLASH. Taken from Figure 10 in Postman et al. (2012).

population parameters and photometric redshifts (Moustakas et al., 2013).

Monte Carlo SED fitting finds best-fit values and credible intervals for the parameters of a model believed to describe an SED by sampling the posterior probability distribution of those parameters. First, a grid of parameter values is created by drawing parameter values from their prior probability distributions, p_{prior}. Model photometry is calculated for each point on the grid based on these values, and the likelihood of each model is calculated by

$$\ln \mathcal{L} \propto \chi^2 = \sum_{i=1}^{N} \frac{(F_i - \mathcal{A}M_i)^2}{\sigma_i^2}, \tag{1.10}$$

where F_i and σ_i are the SED fluxes and uncertainties, M_i are the model fluxes. $\mathcal{A}$ is a scaling factor that scales the model photometry, which is normalized to 1 $M_\odot$ of stars + gas, to the observed SED photometry. The minimum χ^2 and best-

fit $\mathcal{A}$ are found by solving for $\partial\chi^2/\partial\mathcal{A} = 0$. Sampling the model grid at random with probabilities set by $\mathcal{L}$ produces a histogram with functional form $p_{prior} \times \mathcal{L}$, which is the posterior probability distribution of the models (Moustakas et al., 2013).

SED models of stellar and dust emission consist of an initial mass function (IMF), a stellar population synthesis-derived simple stellar population (SSP) model, a star formation history (SFH), a dust attenuation model, and a dust emission model. These components are outlined briefly here, since they are discussed in more detail in Chapter 2, Section 3 and Chapter 3, Section 3. The IMF describes the mass distribution of recently formed stars. Salpeter (1955), Chabrier (2003), and Kroupa (2001), provide functional forms of the IMF which differ on the low mass end of the stellar mass distribution, thus the underlying IMF of stars in moderate redshift BCGs is difficult to distinguish with photometric data. Given an IMF and metallicity, stellar evolution tracks provided by a stellar population synthesis model determines how an SSP evolves by time t, and this evolved stellar population can be used to determine the stellar spectrum at time t. The SPS model used throughout this thesis is the Bruzual & Charlot (2003) model. The SSP stellar spectrum serves as a convolution kernel, which, when convolved with the SFH, produces the emission spectrum of the model stellar population (Moustakas et al., 2013).

The final steps of generating a model SED are to account for dust absorption

and emission in the model spectrum, and to convolve the model spectrum with the filter response functions of the SED to generate synthetic photometry. The stellar spectrum is multiplied by dust attenuation factor $10^{-0.4A(\lambda)}$, where $A(\lambda)$ is the wavelength-dependent attenuation curve obtained either empirically or by radiative transfer modeling. A model dust emission spectrum is added to the absorbed stellar emission spectrum. The model dust emission is normalized to have the same total energy as the energy absorbed by the dust. The dust emission model used in Chapters 3 and 4 is the Draine & Li (2007) model, while in Chapter 2 dust emission is not included in the fits. Finally, the model spectrum is convolved with the filter response functions of the data.

SED fitting can provide several advantages when it comes to constraining the stellar populations of highly extended BCGs observed by programs such as CLASH. SED fitting can take advantage of the many bands of photometry these surveys provide to simultaneously fit data covering a wavelength range of several orders of magnitude. While in Chapter 2, SFRs of CLASH BCGs are measured several ways, using separate photometric and spectral indicators (broadband UV, Hα, Hβ, O II), in Chapters 3 and 4 SED fitting measures several stellar parameters using all of the available photometric data in CLASH. Furthermore, measuring the SED of an extended galaxy can do a better job than its spectrum at capturing the flux from the entire galaxy. While estimates of total galaxy magnitude obtained with Kron or Petrosian magni-

tude (or other model magnitudes) may still underestimate galaxy magnitudes, longslit or fiber-fed spectra (such as SDSS) will only capture the core regions of galaxies. Furthermore, with datasets such as CLASH, where starforming regions are highly resolved, SEDs of specific features may be constructed by extracting photometry from apertures drawn around those features.

Finally, SEDs can be used to spatially resolve stellar parameters. While IFU spectrometers are currently online that can spatially resolve spectra, SED mapping has the potential to provide greater levels of spatial detail. This can be useful when, for example, one wants to examine the stellar populations in individual star forming knots or filaments. In Chapter 2, Section 4, the results of fitting the spatially resolved SED of RXJ1532.9+3021 are presented. The CLASH *HST* data used allows the SFR and age of individual features in the starburst to be resolved down to ~ 350 pc scales.

1.7 Outline of the Dissertation

This dissertation is divided into three chapters and includes one appendix. Chapters 2 and 3 examine the star forming properties of BCGs in clusters observed in the CLASH program and compares these properties to the thermodynamical state of the ICM in the clusters' cores. Chapter 4 expands on the SED fitting technique developed in Chapter 3 to examine the evolution of star

formation in a larger sample of clusters observed as part of the Cosmic Evolution Survey (COSMOS) (Scoville et al., 2007). The appendix discusses an high-contrast imaging instrumentation project I have had the opportunity to develop that improves on the vector vortex coronagraph. I do not include this work with the main body of the thesis since it is not directly relevant to studying BCG star formation; however, I intend to develop this instrument further and use the coronagraphs to construct the optical and near-IR picture of precipitation and accretion fueling AGN feedback.

- **Chapter 2: Star Formation Activity in CLASH Brightest Cluster Galaxies** (published in the Astrophysical Journal). The star formation and dust attenuation properties of the CLASH cluster BCGs are measured using photometric and spectroscopic indicators. I constrain the contribution star formation makes to line emission in these BCGs. I then demonstrate that BCG star formation is related to the thermodynamically inferred cooling rate, and use spatially resolved SED mapping to show that the ages of filamentary structures in the BCG of RXJ1532.9+3021 are correlated with X-ray cavities in the cluster.

- **Chapter 3: The Relationship Between Brightest Cluster Galaxy Star Formation and the Intracluster Medium in CLASH** (accepted for publication in the Astrophysical Journal). I construct UV through far-IR SEDs and use these to measure SFRs, dust masses, and starburst ages

in 11 CLASH BCGs showing signs of star formation activity. I present relationships between these quantities and cooling times and cooling-to-freefall time ratios in the ICM. I present a tight correlation between SFR and t_{cool}/t_{ff} and discuss the implications of this result.

- **Chapter 4: 3.4 M/L Ratio and Stellar Mass Evolution of BCGs in COSMOS from $z < 1.0$** (in preparation for Submission to the Astrophysical Journal). We fit SEDs of the 40 most massive BCGs in X-ray selected clusters observed by COSMOS. We find evidence for minimal evolution of specific SFRs and SFRs, and find that overall COSMOS BCGs are more quiescent than would be predicted from the star forming main sequence, and discuss possible environmental effects. The work presented in this chapter is nearing completion, but is still an ongoing effort, and will be published in a different form than is presented here.

- **Appendix: Polynomial Apodizers for Centrally Obscured Vortex Coronagraphs** (accepted for publication in the Astronomical Journal). I present the polynomial apodized vortex coronagraph (PAVC) and discuss its possible use for observing terrestrial exoplanets. The PAVC theoretically completely suppresses on-axis starlight with telescopes that have large secondar mirror central obscurations while providing $\sim 70\%$ total energy throughput and small inner working angles relative to similar de-

signs for centrally obscured telescopes. The PAVC solves the problem of designing a coronagraph that can be used on telescopes with large secondary mirrors, and has potential applications to future extremely large ground- and space-based observatories.

Chapter 2

Star Formation Activity in CLASH Brightest Cluster Galaxies

Abstract

The CLASH X-ray selected sample of 20 galaxy clusters contains ten brightest cluster galaxies (BCGs) that exhibit significant ($>5\,\sigma$) extinction-corrected star formation rates (SFRs). The star formation activity is inferred from photometric estimates of UV and Hα+[N II] emission in knots and filaments detected in CLASH HST ACS and WFC3 observations. These measurements are supplemented with [O II], [O III], and Hβ fluxes measured from spectra obtained with the 4.1 meter SOAR telescope. We find that the reddening-corrected UV-derived SFRs in these BCGs are broadly consistent with Hα-derived SFRs and span two orders of magnitude, including five BCGs exhibiting SFRs $>$10 $M_\odot$ yr^{-1} and an additional two with a SFR $>$ 100 $M_\odot$ yr^{-1}. We confirm that photoionization from ongoing star formation powers the line emission nebulae in these BCGs, although in many BCGs there is also evidence of a LINER-like contribution to the line emission.

Coupling these data with Chandra X-ray measurements, we infer that

the star formation occurs exclusively in low-entropy cluster cores and exhibits a correlation with properties related to the cooling. We also perform an in-depth study of the starburst history of the BCG in the cluster RXJ1532.9+3021, and compare starburst ages to the ages of X-ray cavities produced by AGN activity. We create 2D maps of the BCG stellar properties on scales down to $\sim$350 pc. These maps reveal evidence for an ongoing burst occurring in elongated filaments, generally on relatively long ($\sim$ 0.5-1.0 Gyr) timescales, although some filaments are consistent with much younger ($\lesssim$ 100 Myr) burst timescales. The longer timescales for star formation far exceed the expected timescale for any AGN-induced activity, while the younger filaments may be correlated with recent activity from the AGN. The relationship between BCG SFRs and the surrounding ICM gas properties provide new support for the process of feedback-regulated cooling in galaxy clusters and is consistent with recent theoretical predictions.

2.1 Introduction

Brightest cluster galaxies (BCGs) in cool core galaxy clusters exhibit nebular emission features that are thought to be related to the intracluster medium (ICM) in the centers of these objects (e.g. Heckman et al., 1989; Fabian, 1994; Crawford et al., 1999). Observations of substantial continuum UV and FIR fluxes have been recorded in many of these nominally early-type galaxies as well (Hicks et al., 2010; Rawle et al., 2012). Resolved images of low-redshift ($z\lesssim0.1$) BCGs suggest that while some of this activity is triggered by active galactic nuclei (AGN), most of the emission appears to be powered by recent star formation, located in knots and filaments (Conselice et al., 2001; O'Dea et al., 2004; McDonald & Veilleux, 2009; McDonald et al., 2014a; Tremblay

et al., 2012). Similar structures have also been observed in the Phoenix cluster ($z = 0.596$), which hosts a massive starbursting BCG producing new stars at a rate of nearly 1000 $M_\odot$ yr^{-1} (McDonald et al., 2012, 2013).

The most plausible candidate for the source of the gas being converted into stars in these galaxies is radiatively cooled ICM plasma (Fabian, 1994). In a cool core cluster, the cooling time below a critical radius is less than the Hubble time at the redshift of the cluster, and plasma initially at this radius ought to have cooled. The ICM that manages to cool descends into the gravitational well in order to maintain pressure equilibrium, ultimately condensing into star forming gas inside the virial radius of the BCG (Fabian, 1994). However, the cooling inferred from a simple cooling flow model is far more rapid than the star formation rates in these systems (e.g. Heckman et al., 1989; McNamara & O'Connell, 1989).

Activity in BCGs in the form of AGN outbursts is an important component of feedback mechanisms proposed to reconcile the tension between the predicted and observed ICM cooling in cool core clusters (McNamara & Nulsen, 2007; Voit et al., 2015). Specifically, the hot, X-ray emitting ICM of a relaxed galaxy cluster is predicted to radiatively cool more rapidly than is typically observed, and this manifests in star formation rates (SFRs) in BCGs which are roughly an order of magnitude lower than what would be predicted if all the available gas did indeed condense into cold gas (O'Dea et al., 2008). However, in the

presence of a feedback mechanism, such as energy injection from an AGN, the ICM is partially reheated and prevented from cooling catastrophically. Instead, residual cooling or cooling during an off-mode in the feedback duty cycle can account for the extended star forming structures observed. Studying the residual cooling using observations of BCGs spanning a wide range of activity will allow us to learn about different phases of cooling and feedback, and help us to determine whether a single feedback mechanism accounts for the variety of BCG features we observe.

The high-resolution, multi-band HST observations available from the Cluster Lensing And Supernova survey with Hubble (Postman et al. (2012); hereafter referred to as CLASH) are ideal for examining the star forming structures in BCGs. In Donahue et al. (2015), we examined UV photometry for the entire CLASH sample of 25 galaxy clusters, and found evidence for significant, extended emission attributable to recent star formation in 10 of them. Two BCGs in this sample, RXJ1532.9+3021 and MACS1931.8-2653, stand out due to their strikingly large and luminous UV filaments.

In the present study, we examine BCGs in the subset of CLASH clusters that were X-ray selected. This subsample includes 20 of the 25 CLASH clusters and includes all of the star-forming BCGs as identified by UV features. Using the CLASH HST photometry, along with spectra from the Southern Astrophysical Research (SOAR) telescope and archival *Chandra* data, we investigate the

nature of star formation in these BCGs, and provide new constraints on the source of the star formation activity in the structures we observe.

This paper consists of two parts. First we derive SFRs for all BCGs using HST photometry and characterize the source of nebular line-emission in UV-bright BCGs using a combination of the HST photometry and SOAR-Goodman spectra. Second, we analyse the connection between the star formation and the properties of the ICM. This second part includes a detailed star formation history (SFH) analysis of the BCG in RXJ1532.9+3021 derived from SED fitting of the CLASH photometry to create maps of stellar population parameters. RXJ1532.9+3021 was chosen for more detailed study because of the spectacular nature of its UV and Hα structure (see Figure 2.1).

We report on the incidence and distribution of reddening-corrected SFRs in our sample, and demonstrate that structures qualitatively comparable with those in the massive outburst in the Phoenix cluster are the sites of BCG activity in these 'intermediate' starbursts as well. Structures observed in CLASH clusters also bear similarities to BCGs analysed in Tremblay et al. (2015). These SFRs are compared with *Chandra* derived ICM core entropies and predicted cooling rates in the low-entropy core ICM in order to test the hypothesis that star formation is being fed by ICM cooling.

For RXJ1532.9+3021 we are able to compare the properties of BCG filaments with the properties of X-ray cavities in the ICM, which we use to assess

recent AGN jet-mode activity. We compare our results to previous analysis of the morphology of the cluster ICM (Hlavacek-Larrondo et al., 2013b). The maps produced for this BCG allow us to examine the star formation history in individual knots and filaments, down to ~ 350 pc scales. These data allow us to investigate the source of the gas that condenses into the star forming regions and, for the case of RXJ1532.9+3021, to examine this condensation in significant detail.

Our paper is organized as follows. We describe the observational data in Section 2. In Section 3, we present the analysis of these data. Results are presented in Section 4, and the astrophysical implications are discussed in Section 5. We summarize our main conclusions in Section 6. We adopt the following cosmological parameters throughout this work: $H_o = 70.0$ km s^{-1} Mpc^{-1}, $\Omega_m = 0.30$, and $\Omega_\Lambda = 0.70$. We assume a Salpeter (1955) IMF throughout.

2.2 Observations

2.2.1 CLASH HST Observations

The CLASH program is detailed in Postman et al. (2012). The 20 X-ray selected clusters were each observed for 15-20 orbits (for a total of at least 20 orbits including archival data) divided among 16 bands of photometry spanning

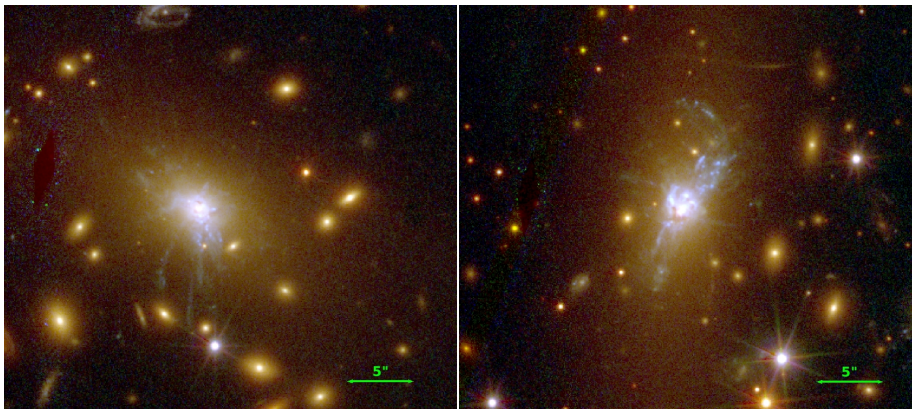

Figure 2.1 Color composite images of the most active star-forming BCGs of RXJ1532.9+3021 (z=0.363) on the left and MACS1931.8-2653 (z=0.352) on the right. The RGB color composites are made using WFC3-IR filters F105W+F110W+F125W+F140W+F160W in red, the ACS filters F606W + F625W + F775W + F814W + F850LP in green, and the ACS filters F435W + F475W in blue.

an observer-frame wavelength range of ∼2000-17000 Å. We use multi-band mosaics drizzled to a common $0''.065$ pixel scale (Koekemoer et al., 2011). All flux measurements are corrected for foreground reddening using the (Schlegel et al., 1998) dust maps. A single reddening correction due to dust in the Milky Way was calculated for each BCG in each filter. Additionally, we perform a background subtraction using a combination of iterative 3-sigma clipping on large scales along with a local median flux measurement in an annulus around each BCG in the UV.

Early CLASH WFC3/UVIS observations are affected by non-uniform flat-fielding on scales of hundreds to thousands of pixels. We accounted for this in observations of BCGs with faint or possibly no significant detection of UV by extracting photometry from multiple identical apertures in WFC3/UVIS im-

ages placed on empty patches of sky, and adding the scatter in these apertures to our error budget. For all CLASH observations, we apply a 3% floor to the total photometric uncertainty to account for all sources of systematic error and absolute flux calibration uncertainty.

2.2.2 Chandra X-ray Observations

All the clusters in the CLASH X-ray sample have archival *Chandra* data. For this work, we use the ICM parameters published in the Archive of Chandra Cluster Entropy Profile Tables (ACCEPT) (Cavagnolo et al., 2009). Gas density and temperature profiles were measured in ACCEPT, and the core entropies and cooling times used in the present study are calculated using these profiles. Gas density profiles were measured in concentric annuli 5" wide. Temperature profiles, which were used in combination with the gas density profiles to derive both cooling time and entropy profiles, were measured in concentric annuli containing at least 2500 counts per bin.

2.2.3 Spectra

Optical spectra of the BCGs were obtained for 15 of the 20 CLASH X-ray selected clusters. Objects were observed with the Goodman High Throughput Spectrograph on the SOAR 4.1 meter telescope using either the KOSI 600

grating or the SYZY 400 grating. The KOSI grating's dispersion is approximately 0.65 Å pix^{-1}, while the SYZY grating's is approximately 1.0 Å pix^{-1}. Their spectral ranges are roughly 2670 Å and 4000 Å, respectively (see Table 1). Central wavelengths were selected to best include the [O II] doublet ([O II] $\lambda, \lambda 3726, 29$), the [O III] doublet (O III] $\lambda, \lambda 4959, 5007$), and H$\beta$ at their redshifted positions. Position angles were chosen to sample observed filamentary structures or other objects of interest. For all observations, the 1.68″ long slit was used.

Observations were reduced following Werner et al. (2014). Bias correction and trimming were performed with the `IRAF`[1] task `CCDPROC`. Quartz lamp frames, taken before and after observation images, were used to flat-field the images. Wavelength calibration was performed with FeAr arc lamp exposures, with distortion along the spatial direction corrected for by tracing the position of standard stars. Sensitivity functions were produced from same-night observations of standard stars with the 10.0″ long slit that, along with an extinction correction based on `IRAF`'s extinction file `ctioextinct.dat` and a correction for airmass, were used to flux calibrate observations. After background subtraction to minimize the contribution of night sky lines, observations were then median combined using `IMCOMBINE`.

[1]IRAF is distributed by the National Optical Astronomy Observatory, which is operated by the Association of Universities for Research in Astronomy (AURA) under a cooperative agreement with the National Science Foundation.

Table 2.1
SOAR Observations of Brightest Cluster Galaxies

Cluster	Obs Date (YYYY-MM-DD)	Exposure Times (s)	Grating (l/mm)	Range Å	PA[a] (°)	Airmass	Standard Star
Abell 209	2012-09-24	1×1200, 1×1800	400	4514-7555	135	1.2	LTT7379
Abell 383	2012-10-09	2×1200, 1×600	400	4126-7568	0	1.3	LTT1020
MACS0329.7−0211	2012-11-09	3×1200	400	4612-7555	125	1.1	LTT7379
MACS0429.6−0253	2012-11-19	2×1200, 1×900	400	4566-7556	167	1.3	LTT1020
MACS1115.9+0219	2013-05-11	4×900	400	4401-8462	130	1.2	LTT4364
MACS1206−0847	2013-05-11	4×900	400	4398-8457	100	1.1	LTT4364
MACS1311.0−0310	2013-05-11	1×1500, 1×900	400	4412-8470	40	1.5	LTT4364
MACS1423.8+2404	2015-02-26	3×1200	600	5049-7724	0	1.8	LTT4364
MACS1720.3+3536	2015-06-13	3×1200	600	4570-7235	160	2.2	LTT6248
MACS1931.8−2653	2012-04-17	1×1800	600	4271-6938	252	1.0	LTT7379
MS2137−2353	2015-06-13	4×1200	600	4570-7235	145	1.1	LTT6248
RXJ1347.5−1145	2012-07-15	1×1200, 1×900	600	4556-7223	125	1.6	LTT9491
RXJ1532.9+3021	2012-04-17	2×1200	600	4811-7471	187	2.1	LTT3864
RXJ2129.7+0005	2012-07-15	4×1200	600	4560-7228	201	1.2	LTT3864
RXJ2248.7−4431	2013-09-08	4×1200	600	4299-6969	352	1.1	LTT1020

[a] Position Angle measured east of north.

2.3 Analysis

2.3.1 Mean UV Luminosities

We calculate the UV luminosity of CLASH BCGs in order to estimate SFRs using the Kennicutt (1998) relation. To do this, we extract the flux from those CLASH filters whose pivot wavelengths fall in the range $1500 - 2800$Å in the cluster rest frame, corresponding to the wavelength range used by Kennicutt (1998) to calibrate the L_{UV}-SFR relation. Since the continuum L_{UV} due to young stars is flat for a Salpeter (1955) IMF and continuous star formation, we use fluxes extracted from the relevant UV filters to calculate the average

luminosity $\langle L_{\nu,UV} \rangle$. This quantity is one of two SFR proxies we are able to calculate from the HST photometry alone, the other being $L_{H\alpha+[NII]}$, which we discuss in Section 3.2.

For the majority of the BCGs, we extract fluxes from a subset of the CLASH WFC3/UVIS filters, F225W, F275W, F336W, and F390W. For the highest redshift clusters ($z > 0.542$), we use ACS filters F435W and sometimes F475W as well. Filter selections are shown in Table 2.2.

Since we are interested in the UV flux from young stars, we must remove the contribution from the UV-upturn in the quiescent stellar population in the BCGs. The UV-upturn has been well-studied and is due to post AGB stars and extreme blue horizontal branch stars (e.g Brown, 2004; Yi, 2008; Ferguson & Davidsen, 1993; Yi et al., 1998). This component of the UV flux mimics low-level star formation and would, if left uncorrected, bias our SFR estimates in UV-faint BCGs.

A template SED of the UV-upturn population is derived by averaging the normalized ACS-WFC3IR rest-frame photometry of 5 satellite galaxies in each of 20 CLASH clusters (for a total of 100 satellite galaxies). We do not include WFC3/UVIS in the satellite galaxy photometry to avoid complications in estimating the sensitivity to weak UV sources, and instead opt to use the GALEX-2MASS J colors in Hicks et al. (2010) to extend the range of our data below 2000 Å_{rest}. These data are fit to a fifth order spline, and the uncertainty in the

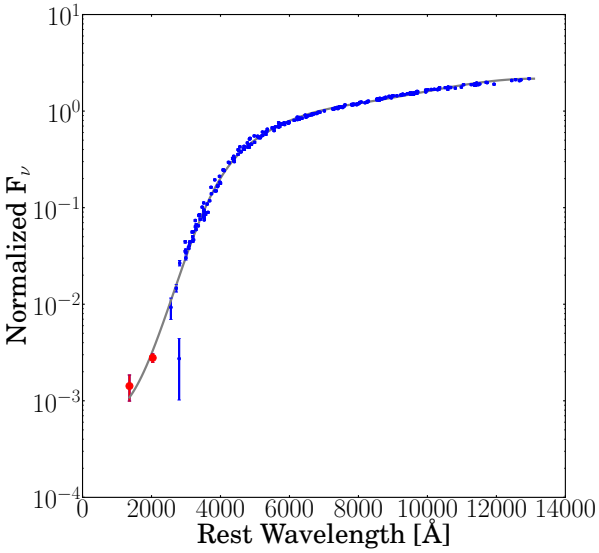

Figure 2.2 Rest frame SED for quiescent starlight in BCGs. The blue points are ACS/WFC3IR photometry taken from 100 satellite galaxies, and represent the averages of 5 galaxies per CLASH cluster in each of 20 clusters. The red points are derived using the GALEX-2MASS J color calibration from Hicks et al. 2010 for a sample of quiescent BCGs at an average redshift of 0.115. The FUV/NUV rest wavelengths depicted in this figure are for Abell 209 ($z = 0.209$), after accounting for the average redshift of the Hicks et al. color calibration. The grey line represents the spline fit to the data. Fluxes are reported in normalized units of F_ν.

fit is estimated using a Monte Carlo distribution of spline fits.

We estimate the UV contribution from old stars by subtracting out a model of the underlying early-type galaxy. A 2D non-parametric model of each BCG was fit to the F160W image, which is dominated by the BCG's old stellar population. The model is scaled according to the template SED shown in Figure 2.2 and subtracted from the UV images. The residual UV flux measured after the subtraction is our UV-upturn-corrected estimate due to ongoing star formation activity.

2.3.2 Hα+[N II] Maps

The CLASH data allow us to estimate $H\alpha$ emission in the BCGs using a broadband subtraction technique in cases where the emission is strong relative to the stellar continuum. For each BCG, a 'line' and 'continuum' filter is chosen based on the cluster redshift (see Table 2.2). One or more satellite early-type galaxies are chosen based on having an IR$-$optical color similar to the BCG, and the mean ratio of the satellite galaxy fluxes between the line and continuum filters is used to scale the continuum filter to the line filter. We subtract the scaled continuum filter image from the line filter image, leaving a residual flux that is primarily due to Hα+[N II] emission. The Hα nebulae of clusters with significant UV emission are shown in Figure 2.3.

This method for estimating $H\alpha$+[N II] is reliable only for line emission with a large equivalent width (EW). $H\alpha$+[N II] EWs may be approximated by

$$EW = \int \frac{f_\lambda - f_{\rm cont}}{f_{\rm cont}} d\lambda \approx {\rm B}_{\rm line} \frac{f_{\rm line} - f_{\rm cont}}{f_{\rm cont}}, \tag{2.1}$$

where $f_{\rm line}$ and $f_{\rm cont}$ are the fluxes through the line and continuum filters, and ${\rm B}_{\rm line}$ is the photometric bandwidth of the line filter. If we assume a 3% uncertainty for the surface photometry in both the 'line' and 'continuum' filters, we can reliably recover features with $H\alpha$+[N II] EWs that are $0.044\times{\rm B}_{\rm line}$. Because the BCGs are very bright in both the 'line' and 'continuum' filters, so

the dominant source of uncertainty on our photometry will be the absolute flux calibration. For BCGs where we adopt ACS filters (either F775W or F850LP) as the line filters, we can recover $H\alpha$+[N II] features with EWs $\gtrsim$ 20 Å in the observer frame. For BCGs where we adopt WFC3IR filters (either F105W or F125W), we can recover features with EWs $\gtrsim$ 40 Å in the observer frame.

2.3.3 Other Emission Lines

Longslit spectra provide coverage of the [O II], [O III] $\lambda, \lambda 4959, 5007$, and H$\beta$ emission lines. We measure line luminosities by fitting a Gaussian line profile and a continuum to reduced, 1-D longslit spectra using the IRAF task **splot**. Continuum levels in **splot** are identified by averaging regions of continuum emission adjacent to emission lines, and continuum-subtracted Gaussian line profiles are fit using the default iterative Levenberg-Marquardt algorithm. An [O II] luminosity could not be calculated for Abell 383, owing to contamination of the spectrum at $\sim$ 4424 Å. [O III] λ 5007 is unavailable for RXJ1347.5-1145 since the available spectrum does include this line.

[O II] luminosities are an independent check on the SFR derived from our UV and Hα luminosities. While [O II] luminosities are usually considered to be a less reliable estimator of SFRs due to their dependence on ionization and metallicity, they can provide extra constraining power when used in conjunction with other SFR estimators (Charlot & Longhetti, 2001; Rosa-González et al., 2002; Kewley et al., 2004; Moustakas et al., 2006). We can use Hβ luminosities in a similar fashion. Assuming case B recombination, we can derive an SFR from Hβ, using the relation Hα/Hβ = 2.85 (Veilleux, 2002).

[O III] λ 5007 is useful for constructing diagnostic diagrams to separate regions heated by normal stars versus other sources of ionization like AGN and shocks. The classic diagram for distinguishing star forming regions from AGNs

is the BPT diagram (Baldwin et al., 1981; Kewley et al., 2001; Kauffmann et al., 2003b). We construct a modified version of the BPT diagram based on a combination of spectral and broadband data. We use an additional diagnostic, when possible, that is nearly insensitive to extinction, and only uses our spectroscopic data. The so-called 'blue-line' diagram barely depends on the accuracy of the reddening correction because it is derived solely from equivalent width values. In this work, we use the 'blue-line' diagram derived from the [O II], [O III], and Hβ lines (Lamareille, 2010; Lamareille et al., 2004). Specifically, this diagram compares the ratios of equivalent widths [O III] λ 5007/Hβ to [O II]/Hβ and we can measure these ratios directly from the SOAR spectra.

2.3.4 Reddening Correction

HST and SOAR observations (when stated explicitly) are corrected for intrinsic dust reddening in a manner similar to McDonald et al. (2013). Assuming continuous star formation, the young-stellar continuum $L_\nu(\nu)$ in the rest wavelengths $1500-2800$Å is flat, and we can thus construct reddening maps for the CLASH BCGs by assuming the gradual slope in flux we observe between pairs of UV images is due to mild dust extinction. In most cases we select the F275W and F336W filter to calculate the reddening. Filter selections for individual BCGs are given in Table 2.2. Even though this procedure assumes continuous star formation, the effect of SFH is relatively small– a starburst

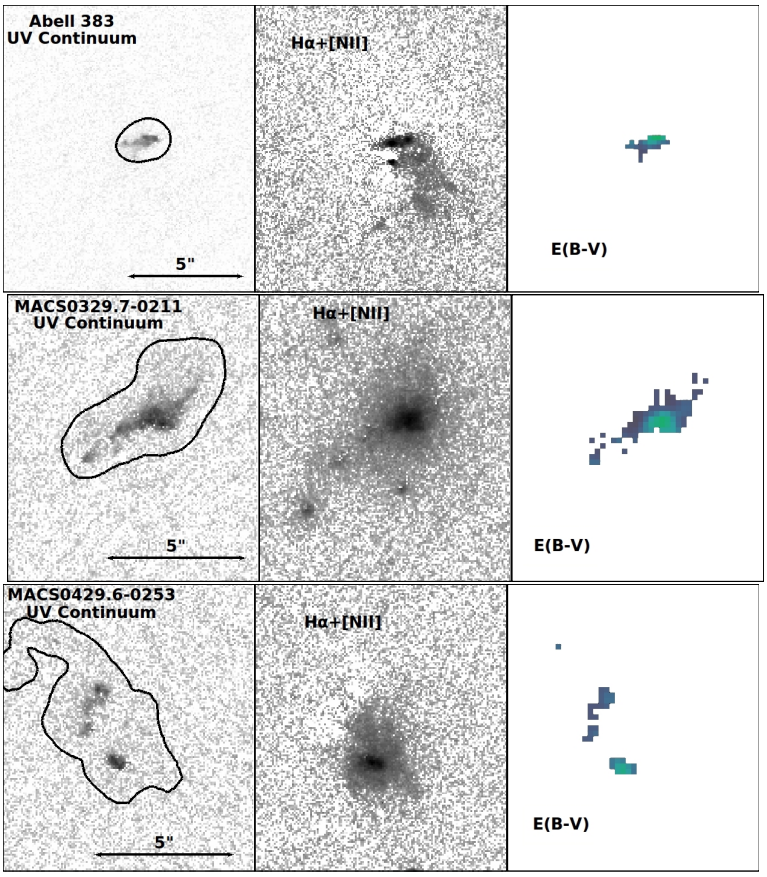

Figure 2.3 The reddening corrected UV luminosity map for CLASH BCGs are shown in the left panel. The region used to extract L_{UV} for each BCG is outlined in black. Likewise, the Hα images are shown in the center panel. The estimated Calzetti reddening map is in the rightmost panel, in units of $E(B-V)$. The uniform color code in the $E(B-V)$ ranges from 0.0 (black) to 0.8 (red), with typical values between 0.1 and 0.5. White regions in the $E(B-V)$ maps have insufficient UV flux to perform the reddening estimate. Galaxies shown are the BCGs of Abell 383, MACS0329, MACS0429, MACS1115, MACS1423, MACS1720, MACS1931, MS2137, RXJ1347, RXJ1532, and RXJ2129, in that order.

with a finite burst duration above 10 Myr will have a slope that differs from a model with continuous star formation by $\lesssim 5\%$.

We construct spatially resolved reddening estimates by covering the UV emission features in each BCG with grid squares 0.195" on a side, correspond-

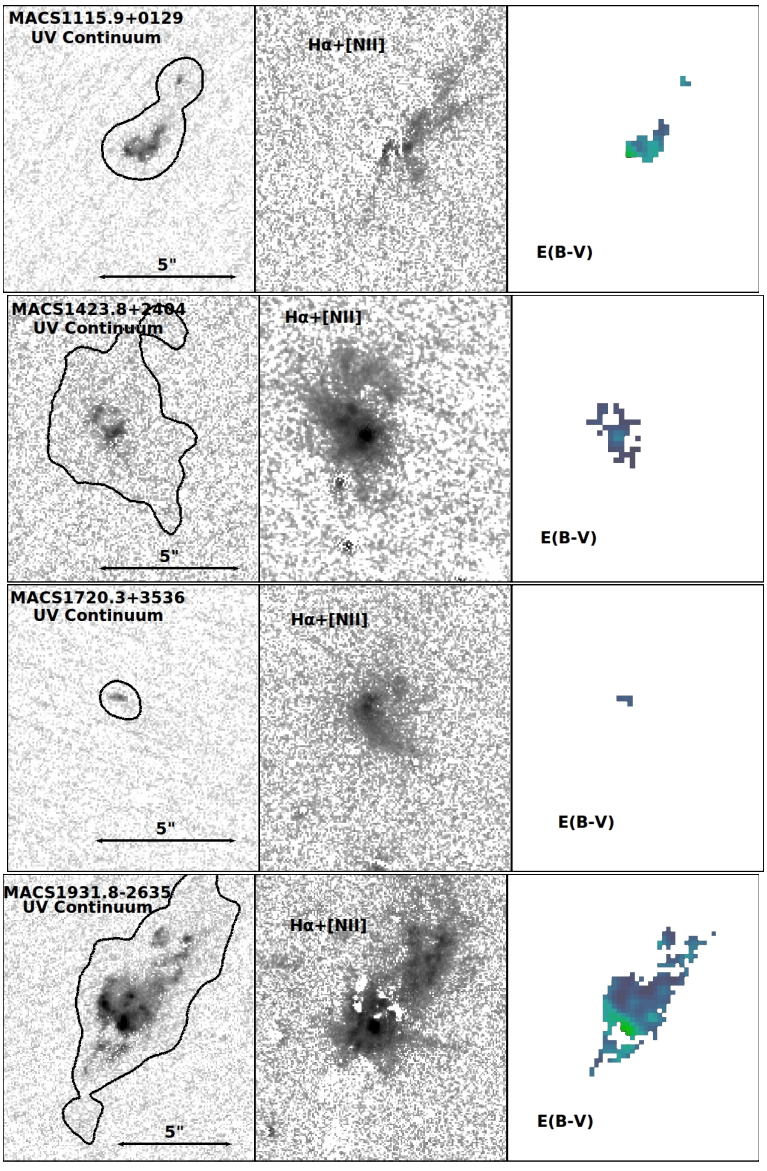

Figure 2.3 *Continued*

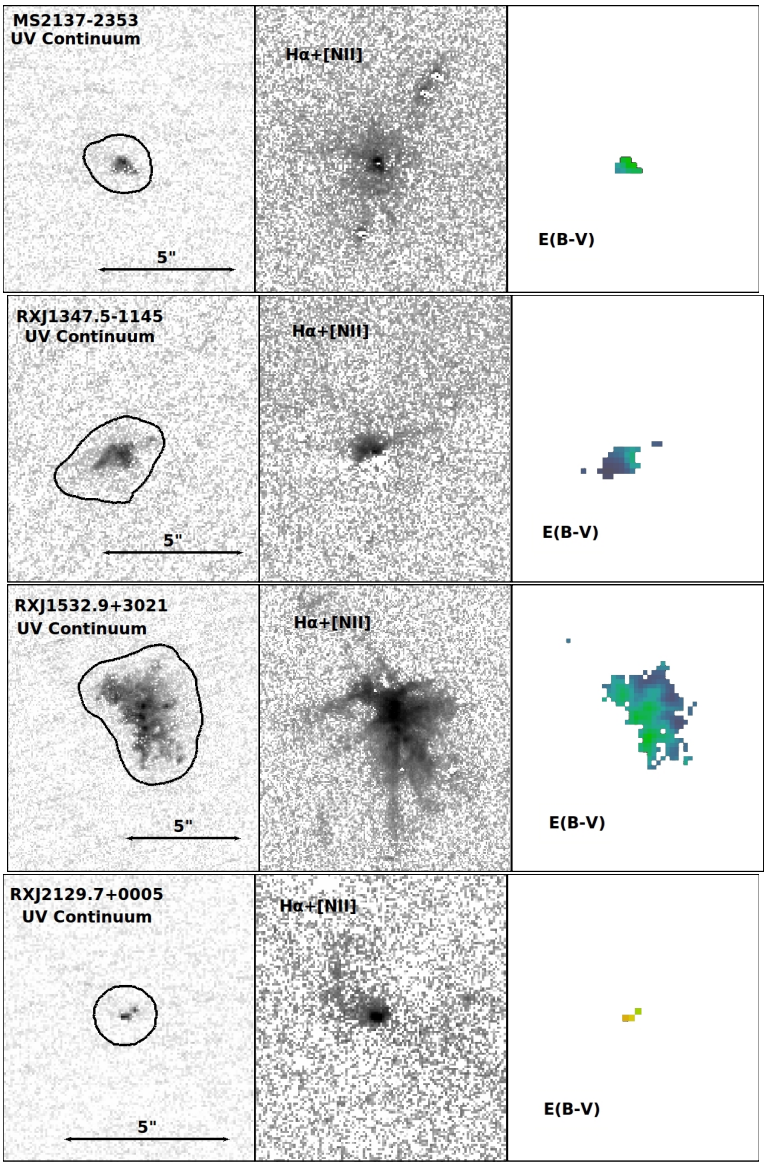

Figure 2.3 *Continued*

ing to 3×3 pixels in the drizzled images. Grid squares of this size are a compromise between sensitivity and spatial resolution, and make our corrections directly comparable to the reddening correction employed in McDonald et al. (2013). Squares which do not have a minimum of 5σ of UV flux in the two filters used to calculate $E(B-V)$ are rejected, leaving behind a grid covering just the significant UV emission, like the example given in Figure 2.4.

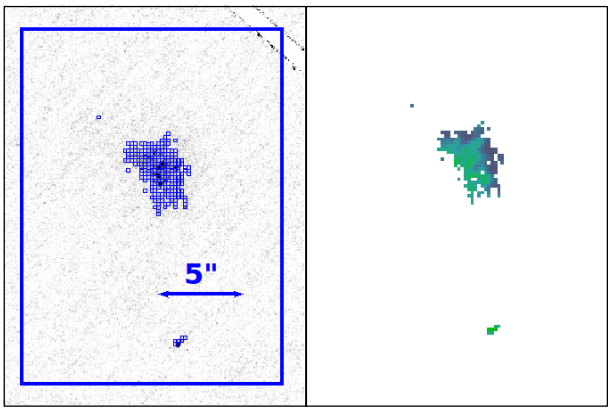

Figure 2.4 Illustration of the method for extracting reddening information from UV filters, for RXJ1532.9+3021. The final reddening map is shown in the right. The layout of grid squares used to calculated E(B-V) is shown overlaid on the F275W filter on the left.

We calculate two reddening maps for each BCG, one using a Calzetti et al. (2000) extinction curve, and one using the Milky Way dust curve parameterized in O'Donnell (1994). When using the Milky Way dust model, we avoid the effect of the 2175 Å bump by both subtracting the best-fit model of the bump in Fitzpatrick & Massa (1986) and by choosing UV filters that minimize coverage of the bump. In each grid square, $E(B-V)$ is calculated by solving for the dust extinction necessary to flatten the slope between the UV-upturn-corrected

fluxes in the two filters. The resulting reddening maps are Gaussian smoothed with a 0.195" kernel, in order to blur out the effects of binning.

Out of the 20 clusters examined from the CLASH sample, 11 have sufficient UV flux to estimate intrinsic reddening over at least part of the BCG. Images of the estimated intrinsic reddening maps are shown in the rightmost panel for each of these clusters in Figure 2.3. We find that, with few exceptions, $E(B-V) \lesssim 0.5$, which is consistent with the dust content typical of cluster BCGs (Crawford et al., 1999; McDonald et al., 2011).

Non-resolved dust extinctions for UV-faint BCGs and faint regions in UV-bright BCGs are calculated using F140W-IRAC colors assuming an underlying early-type stellar population. These bands are suitable for estimating extinction in these galaxies and regions since the F140W band is slightly extinguished at the rest wavelengths of CLASH BCGs while the IRAC bands are essentially reddening free. Furthermore, the F140W-IRAC color at these redshifts is insensitive to the SFH, so the assumed underlying population does not affect the resulting dust estimate. Spitzer/IRAC 3.6μm and 4.5μm fluxes are available for all CLASH clusters except Abell 1423. We use fluxes measured in 3.0" diameter apertures and apply the aperture corrections used in Sanders et al. (2007), selecting either the 3.6 μm and 4.5 μm band for each BCG separately in order avoid the polycyclic aromatic hydrocarbon feature at 3.3 μm rest-frame.

Detections of H_2 vibrational modes are also prevalent in the IR between 5-25μm in starforming BCGs (Donahue et al., 2011). We note that the presence of these lines in IRAC filters may affect our estimate of the dust reddening; however, we are mostly relying on this estimate of the reddening in BCGs with little evidence of ongoing star formation where we would not expect there to be wide vibrational H_2 lines.

We use the spatially resolved extinctions to correct observed fluxes in UV-bright structures and the non-resolved extinctions to correct fluxes outside these structures and in UV-faint BCGs. To correct line luminosities, we adopt the relation $E(B-V)_* = 0.44E(B-V)_{\rm gas}$ reported in Calzetti et al. (2000). While this is the empirically observed relation between the extinction of nebular and stellar emission in starburst galaxies, our choice of extinction model will introduce a systematic uncertainty, since starburst BCGs may differ from the starburst galaxies used to calibrate this relationship.

The reddening correction multiplies our values for L_{UV} in UV luminous BCGs by a factor of $\sim 2-5$, which is consistent with what Donahue et al. (2015) expected, given the typical dust content of an active cool core BCG. For example, Donahue et al. (2015) reports an unobscured SFR for RXJ1532 of ~ 40 $M_\odot$ yr^{-1}, which is less than the Herschel-estimated value of ~ 100 $M_\odot$ yr^{-1}. The reddening corrected UV SFR for RXJ1532 we find is 97 ± 4 $M_\odot$ yr^{-1} (only accounting for statistical uncertainty). For this BCG, the reddening corrected UV

SFR yields a rate comparable to the IR estimate.

2.3.5 Broadband Aperture Photometry

To extract photometry for estimating the mean UV luminosities $\langle L_{\nu,UV} \rangle$ in UV-bright BCGs, we chose regions that contain all of the substantial UV flux with the aid of the ds9[2] contour tool (see Figure 2.3). These regions trace surface brightness contours of 7.14×10^{24} erg s^{-1} Hz^{-1} pix^{-2}, corresponding to a star formation rate surface density of 10^{-3} M$_\odot$ yr^{-1} pix^{-2}. For the ten UV-faint BCGs (those lacking sufficient UV flux to make a spatially resolved estimate of reddening), we measured fluxes inside circular apertures that were as large as possible but still excluded satellite galaxies. We opted for this strategy for measuring photometry because it makes it straightforward to capture the flux in the highly irregular morphologies present in the CLASH BCGs. We calculated Hα+[N II] luminosities using the same apertures selected for significant UV flux.

Line luminosities measured in our spectra were measured in rectangular apertures that, while similar in area in most cases to the apertures we used to measure broadband luminosities, nonetheless do not cover the same regions of the BCGs that were included in our calculations of L_{UV} and $L_{H\alpha+[NII]}$. Therefore, when comparing line luminosities obtained from SOAR spectroscopy with

[2]http://ds9.si.edu

Table 2.2
UV and Hα Filters for BCG Luminosities

Cluster	z[a]	UV filters	E(B-V) filters	Hα 'continuum'	Hα 'line'
Abell 209	0.209	F225W, F275W F336W	—	F850LP	F775W
Abell 383	0.187	F225W, F275W	F225w, F275w	F850LP	F775W
Abell 611	0.288	F225W, F275W F336W	—	F775W	F850LP
Abell 1423	0.213	F225W, F275W F336W	—	F850LP	F775W
Abell 2261	0.224	F225W, F275W F336W	—	F625W	F775W
MACS0329.7−0211	0.450	F225W, F275W F336W, F390W	F275W, F390W	F775W	F850LP
MACS0429.6−0253	0.399	F225W, F275W F336W	F275W, F336W	F775W	F850LP
MACS0744.9+3927	0.686	F275W, F336W F390W, F435W	—	F140W	F105W
MACS1115.9+0129	0.352	F225W, F275W F336W	F275W, F336W	F775W	F850LP
MACS1206.2−0847	0.440	F225W, F275W F336W, F390W	F275W, F390W	F775W	F850LP
MACS1423.8+2404	0.545	F225W, F275W F336W, F390W F435W	F275W, F390W	F125W	F105W
MACS1720.3+3536	0.391	F225W, F275W F336W	—	F775W	F850LP
MACS1931.8−2635	0.352	F225W, F275W F336W	F275W, F336W	F775W	F850LP
MS2137−2353	0.313	F225W, F275W F336W	F275W, F336W	F775W	F850LP
RXJ1347.5−1145	0.451	F225W, F275W F336W, F390W	F275W, F390W	F775W	F850LP
RXJ1532.9+3021	0.363[b]	F225W, F275W F336W	F275W, F336W	F775W	F850LP
RXJ2129.7+0005	0.235	F225W, F275W F336W	F275W, F336W	F850LP	F775W
RXJ2248.7−4431	0.348	F225W, F275W F336W	—	F775W	F850LP
CLJ1226.9+3332	0.890	F336W, F390W F435W, F475W	—	F105W	F125W
MACS1311-0310	0.499	F225W, F275W F336W, F390W	—	F125W	F105W

[a] Redshifts are the same as those quoted in Postman et al. (2012), unless otherwise stated.
[b] (Crawford et al., 1999)

broadband luminosities, it was necessary to measure the broadband luminosities in the apertures corresponding to the position and shape of the slit. Since our reduced spectra are 1-D, we used the mean value of $E(B-V)$ in each rectangular aperture to estimate the extinction correction for both the spectral line luminosities and the UV and Hα+[N II] luminosities we compare them to.

2.3.6 Stellar Population Properties

We use `iSEDfit` to calculate the probability distributions for model approximations of the SED in RXJ1532.9+3021, either in single apertures or in individual pixels to create stellar parameter maps. See Moustakas et al. (2013) for details on `iSEDfit`. SEDs are composed of fluxes extracted from identical apertures (or individual pixels), in each of the 16 bands of CLASH HST photometry. We do not correct for fluxes for intrinsic reddening, since `iSEDfit` allows for local extinction to be treated as a fit parameter.

When creating parameter maps using SEDs fit on individual pixels, we PSF-match each image to the F160W PSF and extract SED for each pixel using the PSF-matched photometry. For approximately normally distributed parameters, we assigned the mean values for the posterior probability density functions (PDF) for model SED parameters for each pixel SED to the locations of pixels in order to create maps of the BCG. The model predicted rest-frame flux for Hα+[N II] provides a sanity check on the physical parameter maps for the

16 band SED, since we can compare its morphology to the $L_{H\alpha+[NII]}$ map described in Section 3.2. The two images are shown in Figure 2.5 with matching coordinates, where it can be seen that the filamentary features in the $L_{H\alpha+[NII]}$ map correspond to the features derived from the SED. The two images depict the same pair of Hα 'bulges' in the center of the BCG as well.

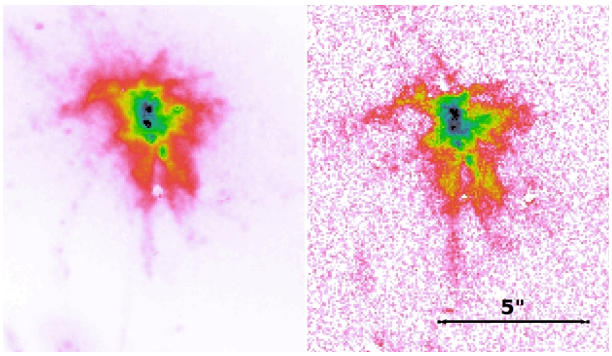

Figure 2.5 *Left:* Map of the Hα+[N II] luminosity constructed using `iSEDfit`. *Right:* Hα+[N II] luminosity map estimated by scaling F850LP and F775W images. We juxtapose the two to demonstrate the morphological similarity between them. The structures in our starburst maps in Figure 2.15 appear to be dominated by the filamentary structure in the Hα+[N II] image.

2.4 Results

2.4.1 Broadband Luminosities and Star Formation Rates

Mean UV and Hα+[N II] luminosities are given in Table 2.3. We present the reddening corrected $\langle L_{UV} \rangle$ both for a Calzetti reddening law and for Milky

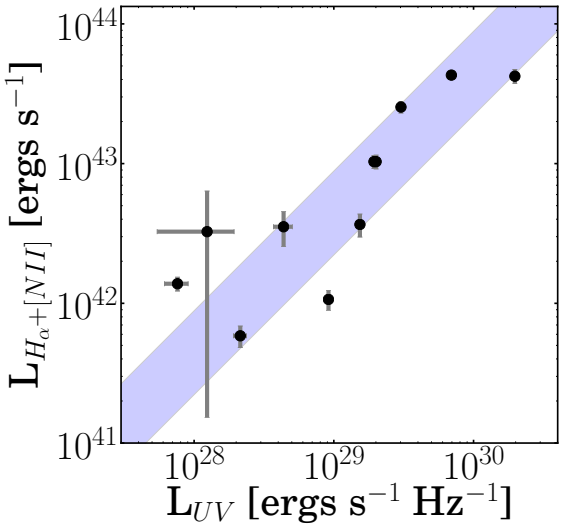

Figure 2.6 L_{UV} and $L_{H\alpha+[NII]}$ are plotted for the regions tracing UV emission. The luminosities are corrected for dust obeying a Calzetti reddening curve. The light blue band shows the region corresponding to where the two luminosities predict the same SFR according to the Kennicutt SFR calibrations, to within the 0.3 dex scatter in the Kennicutt UV calibration. Absent error bars are too small to see as plotted.

Way-type dust. Luminosities are converted to SFRs using the Kennicutt SFR calibrations. There are several sources of potential scatter in this estimate, including contamination of the UV luminosity by AGN activity, and variations in the IMF and SFH of the stellar population (Kennicutt (1998) assumes a continuous SFH and a Salpeter (1955) IMF). For the L_{UV} based SFR estimates, we have not attempted to correct for these effects. However, the UV features we observe are not likely to be due to AGN activity, which is ruled out by the complicated UV morphology reported in Donahue et al. (2015).

In order to estimate Hα based SFRs using Kennicutt (1998), we need to esti-

mate the ratio [N II]/Hα. The line ratio of [N II] to Hα can vary between BCGs, and within filamentary structures in BCGs, so whatever choice we adopt will add scatter to our estimate of the Hα based SFR (McDonald & Veilleux, 2009; McDonald et al., 2014a; Crawford et al., 1999). This ratio is typically 0.5 for optical galaxies (Kennicutt, 1992; Kewley et al., 2001, 2004). However, the ratio [N II]/Hα is often larger than 0.5 in BCGs (Heckman et al., 1989; Crawford et al., 1999). For Hα luminous BCGs in the X-ray selected sample of clusters in Crawford et al. (1999), the typical [N II] $\lambda6584$/Hα is 1.1 ± 0.4. We adopt this value in order to calculate SFRs using $L_{H\alpha+[NII]}$, bearing in mind that this is a rough approximation with considerable scatter. Nonetheless, we believe that variation in [N II]/Hα is a secondary consideration for the purposes of estimating SFRs, given the scatters in the Kennicutt (1998) calibrations between $L_{H\alpha}$ and SFR and between L_{UV} and SFR.

The correlation between UV and Hα+[N II] luminosities is shown in Figure 2.6. The two luminosities are broadly consistent with the ratio expected from Kennicutt (1998), in that the SFR estimates derived from the UV and Hα+[N II] luminosities are consistent with each other. This result is differs from the findings of McDonald et al. (2010, 2011), since they find on average the UV/Hα ratio is slightly lower than that predicted from the Kennicutt relationships. This is most likely because they do not correct for extinction due to dust in the BCG. Indeed, they propose adding a correction of $E\left(B-V\right)=0.2$ to

Table 2.3
BCG Star Formation Rates

Cluster	L_{UV} (Cal)[a] 10^{27} ergs s^{-1} Hz^{-1}	L_{UV} (MW)[b]	$L_{H\alpha+[NII]}$ (Cal)[a] 10^{41} ergs s^{-1}	UV SFR[a] $M_\odot$ yr^{-1}	Hα SFR[a]	Area[c] kpc^2
Abell 209	0.1 ± 0.3	0.1 ± 0.3	–	0.01 ± 0.04	–	–
Abell 383	21.4 ± 2.3	37.2 ± 3.3	5.9 ± 1.0	3.0 ± 0.3	1.9 ± 0.6	14.26 ± 0.02
Abell 611	< 0.3[d]	< 0.3	–	< 0.04	–	–
Abell 1423	0.5 ± 0.2	0.6 ± 0.3	–	0.07 ± 0.03	–	–
Abell 2261	0.2 ± 0.2	0.2 ± 0.2	–	0.02 ± 0.02	–	–
MACS0329.7−0211	302.3 ± 12.1	349.9 ± 12.6	254.0 ± 24.1	42 ± 2	80 ± 21	173.9 ± 0.2
MACS0429.6−0253	200.1 ± 11.2	234.2 ± 10.6	103.3 ± 11.8	28 ± 2	33 ± 9	72.2 ± 0.2
MACS0744.9+3927	4.2 ± 0.6	4.6 ± 0.7	–	0.6 ± 0.1	–	–
MACS1115.9+0129	91.6 ± 6.5	92.8 ± 5.5	10.7 ± 1.7	13 ± 1	3.4 ± 1.0	52.32 ± 0.05
MACS1206.2−0847	20.8 ± 4.4	25.4 ± 3.9	–	2.9 ± 0.6	–	–
MACS1423.8+2404	193.7 ± 8.2	212.4 ± 8.3	103.3 ± 11.1	27 ± 1	33 ± 9	121.2 ± 0.2
MACS1720.3+3536	7.6 ± 1.5	22.5 ± 5.7	13.8 ± 1.6	1.1 ± 0.2	4.4 ± 1.2	10.08 ± 0.02
MACS1931.8−2635	1975 ± 135	1756 ± 79	422.1 ± 49.5	280 ± 20	130 ± 40	331.5 ± 0.5
MS2137-2353	43.7 ± 6.7	22.4 ± 2.2	35.3 ± 9.9	6.1 ± 0.9	11 ± 4	15.41 ± 0.07
RXJ1347.5−1145	153.7 ± 9.0	175.4 ± 8.6	36.7 ± 6.9	22 ± 1	12 ± 4	71.3 ± 0.2
RXJ1532.9+3021	694.0 ± 25.0	765.6 ± 24.5	429.9 ± 29.1	97 ± 4	140 ± 40	308.1 ± 0.2
RXJ2129.7+0005	12.4 ± 6.9	9.3 ± 3.0	32.5 ± 31.1	1.7 ± 1.0	17.2 ± 16.4	10 ± 10
RXJ2248.7−4431	0.8 ± 0.4	0.9 ± 0.4	–	0.1 ± 0.1	–	–
CLJ1226.9+3332	6.2 ± 0.4	6.5 ± 0.5	–	0.9 ± 0.1	–	–
MACS1311.0−0310	3.9 ± 2.9	4.0 ± 3.0	–	0.5 ± 0.4	–	–

[a] Calzetti model dust was used to calculate the reddening correction.
[b] Milky Way model dust was used to calculate the reddening correction.
[c] Areas of UV emitting regions as observed with the F336W filter. Uncertainties are calculated by using Monte Carlo draws to sample the distribution of the number of pixels containing positive flux in the regions shown in Figure 2.3.
[d] 3σ upper limits are shown.

their data, which would make their results consistent with continuous star formation, and this value is typical for the dust extinction we observe in CLASH BCGs.

UV SFRs are correlated with the areas of the star forming region in CLASH BCGs (Figure 2.7). CLASH BCGs have an average SFR surface density ($\langle\Sigma$SFR$\rangle$) of $\sim 0.3\,M_\odot$ yr^{-1} kpc^{-2}, with typical values ranging between $\sim 0.1 - 0.4\,M_\odot$ yr^{-1} kpc^{-2}. Areas of the UV flux emitting regions were measured using the F336W filter. In order to calculate the uncertainty, we sampled the distribution of fluxes in each pixel in the regions shown in Figure 2.3 using a Monte Carlo method, which we used to create a distribution of flux-emitting areas. The ex-

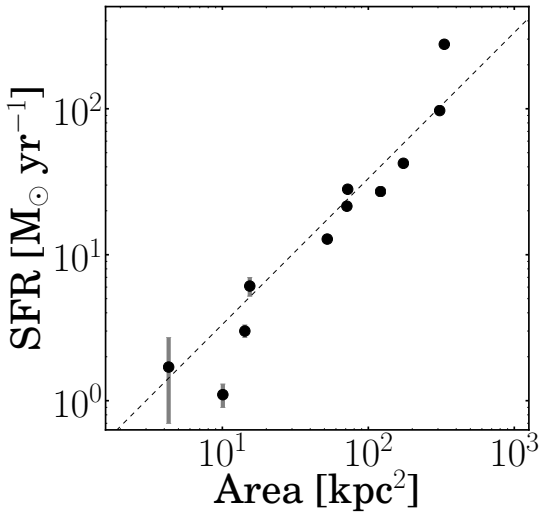

Figure 2.7 The UV derived SFR is shown as a function of the area of the UV flux emitting regions measured in the F336W filter. The dotted line represents an $\langle\Sigma\mathrm{SFR}\rangle$ of ~ 0.3 M$_\odot$ yr^{-1} kpc^{-2}. Absent error bars are too small to be seen as plotted.

ception to this is MACS1931.8−2635, which exhibits a $\langle\Sigma\mathrm{SFR}\rangle$ of 0.83 ± 0.06 M$_\odot$ yr^{-1} kpc^{-2}.

2.4.2 SOAR Spectra Results

The CLASH BCG UV and [O II] luminosities, displayed in Figure 2.8, scale with each other, but produce divergent SFR estimates. However, UV and Hβ luminosities (Figure 2.9) have a tight correspondence and produce consistent estimates of the SFR in CLASH BCGs. The agreement between UV and Hβ based SFRs is tighter than the agreement between UV and Hα+[N II] derived SFRs, which is to be expected considering the limited precision of SFRs esti-

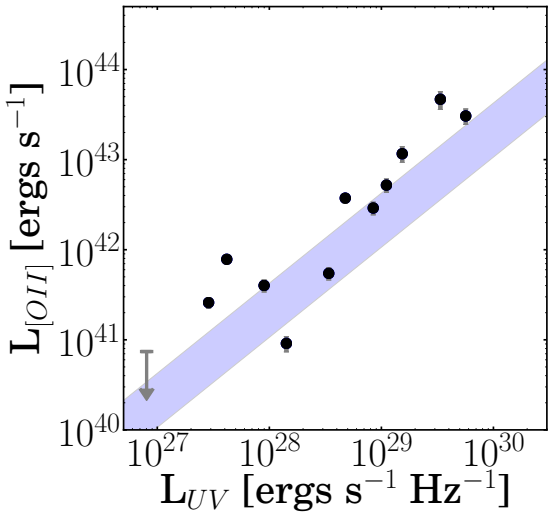

Figure 2.8 The distribution of BCG UV luminosities, L_{UV}, compared to [O II] luminosities, $L_{[OII]}$, for all BCGs with SOAR coverage of [O II]. UV luminosities were measured in rectangular apertures that correspond to the spectral slit placements. The light blue band corresponds to where these luminosities predict the same star formation rate to within 0.3 dex, as in Figure 2.6.

mated using broadband Hα+[N II].

The SFR-$L_{[OII]}$ relation we use is calculated in Kewley et al. (2004) by using a sample mean [O II]/Hα to convert from the Kennicutt (1998) SFR-$L_{H\alpha}$ relation to an SFR-$L_{[OII]}$ relation. However, the theoretical value of $L_{[OII]}$/SFR depends on the metallicity of the nebular region (peaking near $Z \sim 0.5$ $Z_{\odot}$) as well as ionization parameter (peaking near $q \sim 1 \times 10^7$ cm s^{-1}) (Kewley et al., 2004). CLASH BCG redenning corrected flux ratios [O III]/[O II] are typically ~ 0.1, implying an ionization parameter near $q \sim 1 \times 10^7$ cm s^{-1} for solar and sub-solar metallicities (Kewley & Dopita, 2002). The combination of these two parameter depedencies may explain the systematic tension between UV and

[O II] SFRs. Furthermore, the offset between UV and [O II] SFRs we observe in CLASH clusters is consistent with the observation in Kennicutt (1998) that $L_{[OII]}$/SFR is typically boosted in starbursts relative to galaxies undergoing continuous star formation by a factor of $\gtrsim 2$.

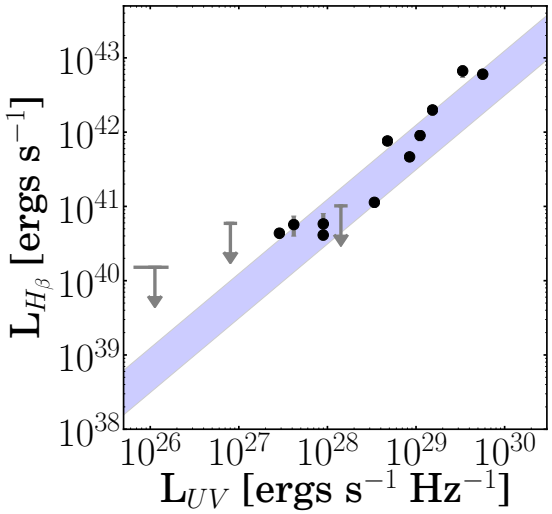

Figure 2.9 BCG UV and Hβ luminosities for all BCGs with SOAR coverage of Hβ. UV luminosities were measured in rectangular apertures that correspond to the spectral slit placements. In order to determine the region in the plot where the two luminosities predict consistent continuous SFRs, we scaled the Kennicutt law relating $L_{H\alpha}$ to the SFR by a factor of 2.85. The light blue band is analogous to the band depicted in Figures 2.6 and 2.8. Typical uncertainties on $L_{H\beta}$ are $\sim$10%, and typical uncertainties on L_{UV} are $\sim$ 5%.

SOAR spectra were also used to constrain the source of the photoionizing emission we observe. We place active CLASH BCGs on the blue-line diagnostic diagram for distinguishing starbursting galaxies from AGN, described in Lamareille et al. (2004) and Lamareille (2010), as well as on the BPT diagram, in Figure 2.10. We cannot directly separate Hα from [N II] in our broadband

Hα+[N II] fluxes, so when available, we use line fluxes from the SDSS Data Release 12[3] to determine the locations of CLASH BCGs on the BPT diagram (Alam et al., 2015). In order to place the remaining active BCGs on the BPT diagram, instead of comparing [O III]/Hβ to [N II]/Hα, we compare [O III]/Hβ to $X \equiv 0.75\left(\frac{H\alpha+[NII]}{2.85H\beta} - 1\right)$. Our expression for X assumes case B recombination. Regardless of the presence of AGN emission, case B recombination allows us to derive a reasonable estimate of the ratio of Hα to Hβ, since for systems with hydrogen densities in the range $10^3 - 10^6$ cm^{-3}, Hα/H$\beta \sim$ 2.7-3.2 (Netzer, 2013). Because AGN often produce harder photoionizing spectra than young stellar populations, our assumption will tend bias X slighter higher than [N II]/Hα in the presence of an AGN. However, such a bias will cause the estimated line ratios to appear more 'AGN-like,' so the resulting BPT diagram is a conservative estimate of the contribution of ongoing star formation to the line ratios we observe. The positions of BCGs on the BPT diagram determined using X depend on both the accuracy of our reddening corrections and broadband Hα+[N II] estimates. Therefore, their value is primarily as a consistency check of the blue-line diagram.

For the blue-line diagram, we use equivalent widths observed with SOAR for all CLASH BCGs except Abell 383 and MACS1423.8+2404. Since these BCGs have incomplete line flux data from the SOAR spectra (Abell 383 does

[3]http://dr12.sdss3.org/

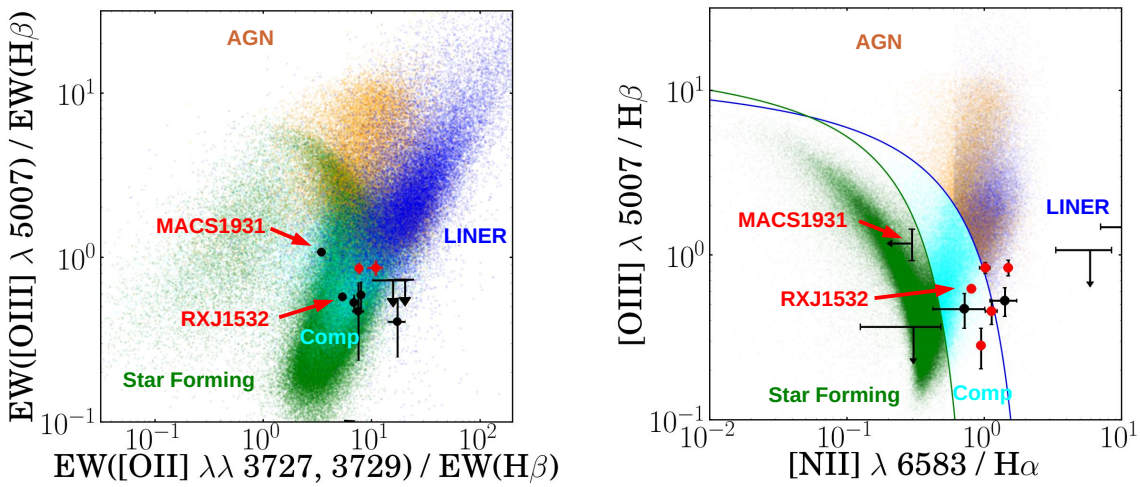

Figure 2.10 *Left:* The blue line diagnostic diagram for line-emitting CLASH BCGs. CLASH BCGs are overplotted on reference data from SDSS. Galaxies from galSpec are shown color-coded by BPT classification. Green galaxies are starforming galaxies, light blue galaxies are composites, blue galaxies are LINERs and orange galaxies are AGNs. The positions of MACS1931 and RXJ1532 are highlighted, since these two are the largest starbursts in the CLASH BCG sample. Black points are measured from SOAR data, while red point are measured from SDSS data. *Right:* The BPT diagram incorporating CLASH broadband line flux estimates. Red points are measured from SDSS data, while black points are estimated using a combination of SOAR fluxes and HST broadband Hα+[N II] flux estimates. For the black points, we defined a proxy for [N II]/Hα on the x-axis of the BPT diagram, X, to be $0.75\left(\frac{H\alpha+[NII]}{2.85H\beta}-1\right)$. Region labels match color coding and approximate locations of regions populated by different classifications of galaxy.

not have an [O II] measurement and MACS1423 has an upper limit for [O III] λ5007 estimated from an upper limit of [O III] λ4959) but were observed in Data Release 12, we use SDSS equivalent widths for these lines instead. In general, our SOAR spectra are better suited to observing extended nebular emission in CLASH BCGs because we were able to place the slit to maximize

coverage of the nebulae. We overplot our results on the SDSS galSpec[4] galaxy sample (Brinchmann et al., 2004; Kauffmann et al., 2003a; Tremonti et al., 2004). CLASH BCGs tend to lie in a particular region of this diagram, with low [O III]/Hβ and high [O II]/Hβ relative to the SDSS dataset. Our results imply that most of the BCGs line in the composite starforming-LINER region described in Lamareille (2010), with the exception of MACS1931.8-2653.

The BPT diagram shows the Kewley et al. (2001) line in blue and Kauffmann et al. (2003b) line in green. CLASH BCGs are distributed in the starforming and composite-starforming regions of the diagram. The CLASH BCGs cluster around log([O III]/Hβ) ~ -0.3, which puts them below the BPT discriminating boundary between starforming galaxies and AGN (Kauffmann et al., 2003b). The exception to this is MACS1931, which is consistent with emission powered predominantly by star formation. We observe an X-ray AGN in the *Chandra* image of MACS1931; however, given the extent of the UV emission region it makes sense to classify the BCG as starbursting. For the most part, the blue-line and BPT indicate consistent sources powering line emission in CLASH BCGs.

Based on these diagnostics, we conclude that the line emission in most of the BCGs is either predominantly due to ongoing star formation, or to a composite starforming-LINER-like source. In particular, the two most UV luminous

[4]http://www.sdss.org/dr12/spectro/galaxy_mpajhu/

BCG in our sample, MACS1931 and RXJ1532, are consistent with star formation being the main photoionization mechanism when taking into account both diagnostic diagrams. MACS1720, MS2137 and possibly Abell 383 may be LINERS, although much of their UV and Hα+[N II] flux is not in a nuclear emission region. Likewise, the majority of the composite galaxies fall into the composite starforming-LINER classification. This is consistent with previous results finding LINER-like emission in cool-core BCGs (Véron-Cetty & Véron, 2000; Edwards et al., 2007). However, while the emission line diagnostics in these BCGs are LINER-like, they cannot be LINERs since they cannot be powered by a central black hole (Heckman et al., 1989). Several hypotheses have been proposed for the source of this extended LINER-like emission. Stellar populations may be responsible for this emission, which could be due to photoionization from O-stars and young starbursts, shocks, and old stars (Shields, 1992; Olsson et al., 2010; Loubser & Soechting, 2013). Emission lines may also be due to nebular gas being heated by the surrounding medium (e.g. Donahue & Voit, 1991; Werner et al., 2013), turbulent mixing layers (Begelman & Fabian, 1990), or collisional heating (Sparks et al., 1989; Ferland et al., 2009).

2.4.3 Correlation with ICM X-Ray Properties

2.4.3.1 Core Entropies

SFRs derived from L_{UV} in our sample are correlated with the X-ray properties of the ICM. Figure 2.11 shows the relationship between CLASH BCG SFRs and ICM core entropies. The core entropy K_0 used in the present study is defined to be the innermost bin of the entropy profile in ACCEPT, and is a proxy for the existence of a cool core in a galaxy cluster (Hudson et al., 2010). Entropy as measured by X-rays is defined to be

$$K \equiv kT_x n_e^{-2/3}, \tag{2.2}$$

where T_x is the X-ray temperature in keV, n_e electron density in cm^{-3}, and k is the Boltzmann constant.

Low values of K_0 typically accompany activity in BCGs. BCG activity, such as elevated NUV flux relative to the predicted quiescent UV emission, is observed to occur only in clusters where K_0 is $\lesssim 30$ keV cm^2 (Cavagnolo et al., 2008; Hoffer et al., 2012). McDonald et al. (2010) reported on this phenomenon as well with resolved Hα emission maps in low-redshift BCGs. In Donahue et al. (2015), a similar entropy threshold was found for the UV-NIR color of CLASH BCGs, indicating the threshold does not change substantially out to z$\sim$0.5.

Here, we demonstrate that a tight correlation exists between reddening corrected SFRs and K_0. Specifically, all of the BCGs with an SFR > 10 $M_\odot$ yr^{-1} have a core entropy consistent with a value ≤ 30 keV cm^2 (see Figure 2.11). Meanwhile, BCGs that lack significant UV or Hα+[N II] luminosities occupy a range of core entropies that extends up to $\sim$ 200 keV cm^2. Considering the difference between the two observables, the tight correspondence between SFR and core entropy is compelling.

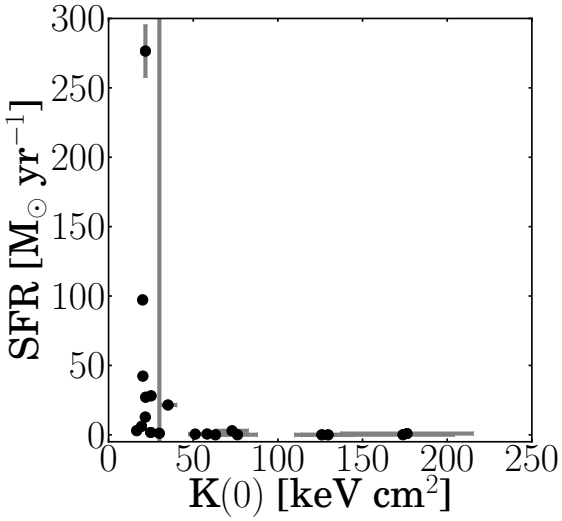

Figure 2.11 BCG SFRs compared to cluster core entropies. Core entropies below ~ 30 keV cm^2 are associated with the onset of UV emission in BCGs, and all of the CLASH BCGs with a UV SFR > 10 $M_\odot$ yr^{-1} reside clusters with a core entropy $\lesssim 30$ keV cm^2. The grey vertical line depicts this 30 keV cm^2 entropy threshold. Core entropies are taken from the ACCEPT cluster profile archive. For several points, errorbars for the SFR and K_0 are too small to be depicted on this plot.

2.4.3.2 Core $\dot{\mathrm{M}}_g$ Estimates

ICM cooling rates inferred by X-ray densities and temperatures bear little relation to the spectroscopic cooling rate in cool-core clusters (e.g Peterson et al., 2001). However, we may to be able to find a relationship between star formation and a simple proxy for cooling at radii where we hypothesize ICM cooling actually occurs. The quantity we examine, $\dot{\mathrm{M}}_g\left(r\right)$, is analogous to the predicted cooling rate as a function of radius, and is defined by

$$\begin{aligned}\dot{\mathrm{M}}_g\left(r\right) &\equiv \frac{4\pi\int_0^r \rho_g\left(\tilde{r}\right)\tilde{r}^2 d\tilde{r}}{t_{cool}\left(r\right)} \\ &= \frac{M_{enc}\left(r\right)}{t_{cool}\left(r\right)},\end{aligned} \tag{2.3}$$

where $\rho_g\left(r\right)$ is the azimuthally average X-ray gas density, and $t_{cool}\left(r\right)$ is the averaged X-ray cooling time at radius r. $M_{enc}\left(r\right)$ is the gas mass enclosed in the radius r. We use

$$t_{cool} = \frac{3}{2}\frac{nkT}{n_e n_H \Lambda\left(Z,T\right)}$$

to define the cooling time, and use the assumption in Cavagnolo et al. (2009) that $n \approx 2.3 n_H$. The cooling curve $\Lambda\left(Z,T\right)$ is estimated by interpolating the Sutherland & Dopita (1993) cooling function at solar metallicity.

We choose to measure $\dot{\mathrm{M}}_g\left(r\right)$ at $r = 35$ kpc ($\dot{\mathrm{M}}_{g,r35}$), and at the radius in each cluster where the ratio between the cooling time and free-fall time is $t_{cool}/t_{ff} = 20$ ($\dot{\mathrm{M}}_{g,t20}$). We calculate free-fall times by estimating cluster den-

sity profiles as the sum of NFW profiles derived from lensing in Merten et al. (2015a) and singular isothermal sphere profiles of BCG stellar density derived from stellar mass estimates in Burke et al. (2015). The impact of the stellar mass component on our overall result is not substantial; however, we include it for completeness.

$\dot{\mathrm{M}}_{g,r35}$ is useful to measure because 35 kpc is typical of the maximum radius we observe Hα+[N II] and UV structures in CLASH clusters, and because this radius maximizes the correlation between UV SFR and $\dot{\mathrm{M}}_g\,(r)$ (see Figure 2.12). This quantity can be calculated for all the CLASH clusters using ACCEPT data.

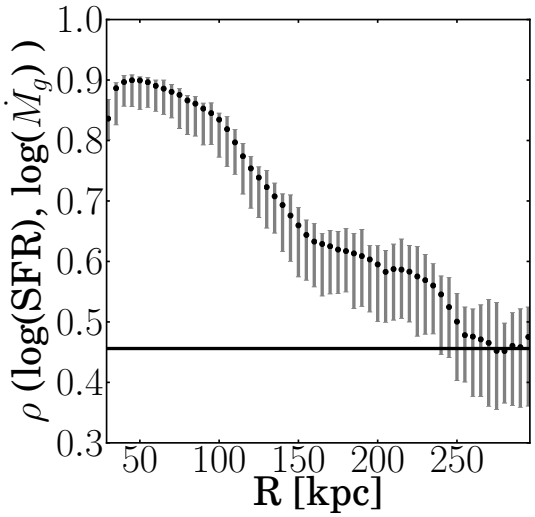

Figure 2.12 Pearson correlation coefficients are shown between log(SFR) and log($\dot{\mathrm{M}}_g$) as a function of radius R. Green line denote the minimum correlation to rule out the null hypothesis at P$<$0.05.

The choice of $\dot{\mathrm{M}}_{g,t20}$ reflects the finding that BCG activity occurs in clusters

with a minimum value in their t_{cool}/t_{ff} profile between 4 and 20 (Voit et al., 2015). Since BCG activity is associated with potentially cooling ICM gas where $t_{cool}/t_{ff} \leq 20$, $\dot{\mathrm{M}}_{g,t20}$ measures the predicted cooling rate in gas that we suspect is directly involved in cooling. Radii where $t_{cool}/t_{ff} = 20$ are listed for each cluster in Table 2.4. Clusters where $t_{cool}/t_{ff} > 20$ in the innermost bin of the cooling time profile calculated from ACCEPT data are not included.

Table 2.4
t_{cool}/t_{ff} Threshold Radii

Cluster	Radius [kpc]
Abell 383	50 ± 5
MACS0329.7−0211	79 ± 5
MACS0429.6−0253	83 ± 9
MACS0744.9+3927	50 ± 11
MACS1115.9+0129	108 ± 17
MACS1423.8+2404	83 ± 8
MACS1720.3+3536	68 ± 6
MACS1931.8−2635	105 ± 14
MS2137−2353	83 ± 6
RXJ1347.5−1145	69 ± 18
RXJ1532.9+3021	121 ± 12
RXJ2129.7+0005	59 ± 8
MACS1311.0−0310	83 ± 24

We show the relationship between the UV SFR and both $\dot{\mathrm{M}}_{g,r35}$ and $\dot{\mathrm{M}}_{g,t20}$ in Figure 2.13. The dashed lines denote, from right to left, where the BCG is forming stars at 100%, 10%, 1%, and 0.1% of the cooling rate implied by $\dot{\mathrm{M}}_{g}$. If we interpret the SFR as a proxy for the actual cooling rate in this system, and interpret $\dot{\mathrm{M}}_{g}$ as the 'potential' cooling rate in the absence of feedback, then the larger starbursts are cooling much more efficiently than smaller starbursts.

We fit trend lines to the data for both the SFR-$\dot{\mathrm{M}}_{g,r35}$ and SFR-$\dot{\mathrm{M}}_{g,t20}$ relations using orthogonal least squares regression. We find that the slope on the trends fit to the two datasets (0.35 ± 0.05 for SFR-$\dot{\mathrm{M}}_{g,r35}$ and 0.27 ± 0.06 SFR-$\dot{\mathrm{M}}_{g,t20}$) are nearly consistent, leading to the conclusion that the two definitions of $\dot{\mathrm{M}}_g$ measure a similar quantity.

Several limitations impacting our measurements may affect how tightly correlated SFR-$\dot{\mathrm{M}}_g$ (both $\dot{\mathrm{M}}_{g,r35}$ and $\dot{\mathrm{M}}_{g,t20}$) appear to be in our data. Gas density profiles in ACCEPT have a limited resolution (between $10-30$ kpc per bin depending on the CLASH cluster), so values for M_{enc} are typically calculated by interpolating on the central few bins of each profile. Temperature profiles are less well resolved than ρ_g profiles, which adds scatter to our estimate of $t_{cool}\,(r)$ profiles. Deeper X-ray observations will beat down the systematics in $\dot{\mathrm{M}}_g$, and a larger sample of cool core clusters will allow us to more precisely constrain the SFR-$\dot{\mathrm{M}}_g$ relationship and examine the effects of sample selection. With our current data, we establish that a relationship exists between these two quantities, and that this relationship implies that as the BCG SFR increases, there is a steady increase in the ratio of ongoing star formation relative to the predicted cooling time in the reservoir of hot gas.

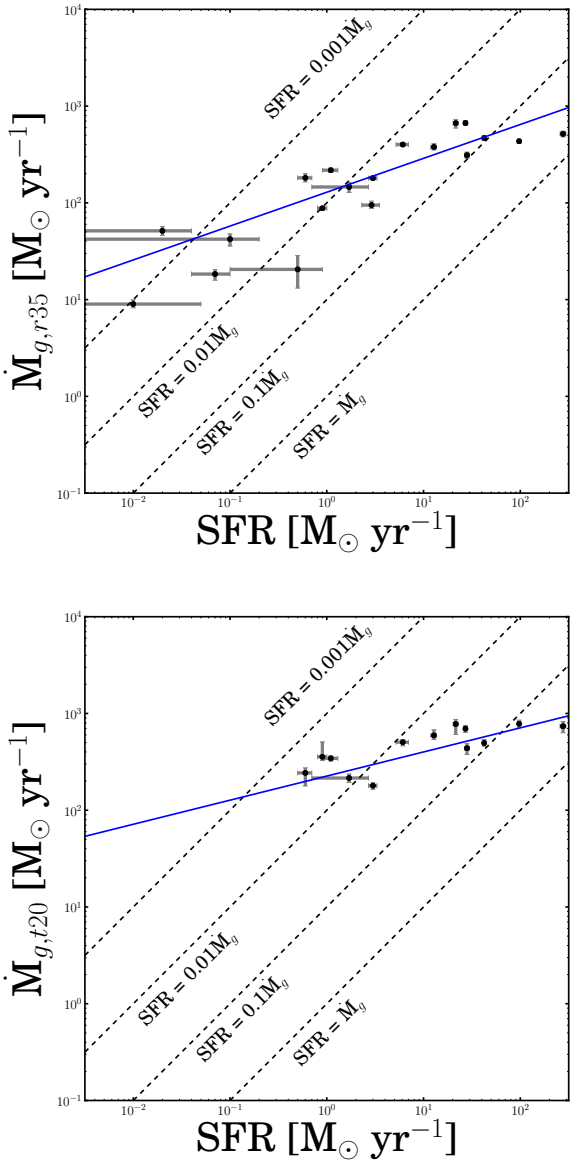

Figure 2.13 Relationship between SFR and $\dot{M}_g$ measured at 35 kpc (*top*) and radii where $t_{cool}/t_{ff} = 20$ (*bottom*). Solid lines fit the data. Dashed lines indicate (from furthest right) where SFR is 100% of $\dot{M}_g$, 10%, 1%, and 0.1%.

2.4.4 Model Fitting to RXJ1532.9+3021

We adopt RXJ1532.9+3021 as a case study and use its HST SED to delve into the SFH of the BCG in this galaxy cluster. RXJ1532 exhibits the second highest star formation in our sample and is replete with UV and Hα bright filaments and knots. This BCG makes a better case study than the strongest star forming galaxy in our sample, MACS1931.8-2635, because the latter exhibits a strong X-ray AGN which could complicate pixel-scale SED fitting. RXJ1532 also has detailed auxiliary data including an SDSS spectrum covering Hα and [N II] and a deep *Chandra* observation (Hlavacek-Larrondo et al., 2013b). RXJ1532 is therefore an excellent prototype for exploring the characteristics of the star forming regions in CLASH BCGs.

We both fit a single-aperture SED from the region used to calculate L_{UV} and constructed stellar parameter maps. The best-fit SFR in the single-aperture SED is 118^{+215}_{-42} $M_\odot$ yr^{-1}. The average extinction is E(B-V) $= 0.27 \pm 0.07$. Since the posterior probability distribution of the SFR is close to log-normal, the best-fit value we report is the mode of the distribution and the uncertainty we report is the 68.3% confidence interval. The best-fit starburst is relatively long-lived, with a burst duration logΔt_b [Gyr] = -0.16 ± 0.47, and massive, with a total burst mass log M_b [$M_\odot$] = 11.03 $\pm$ 0.36. The burst parameters in the fit have degeneracies (see Figure 2.14), although the peaks in the probability distribution suggest that we are constraining the parameters.

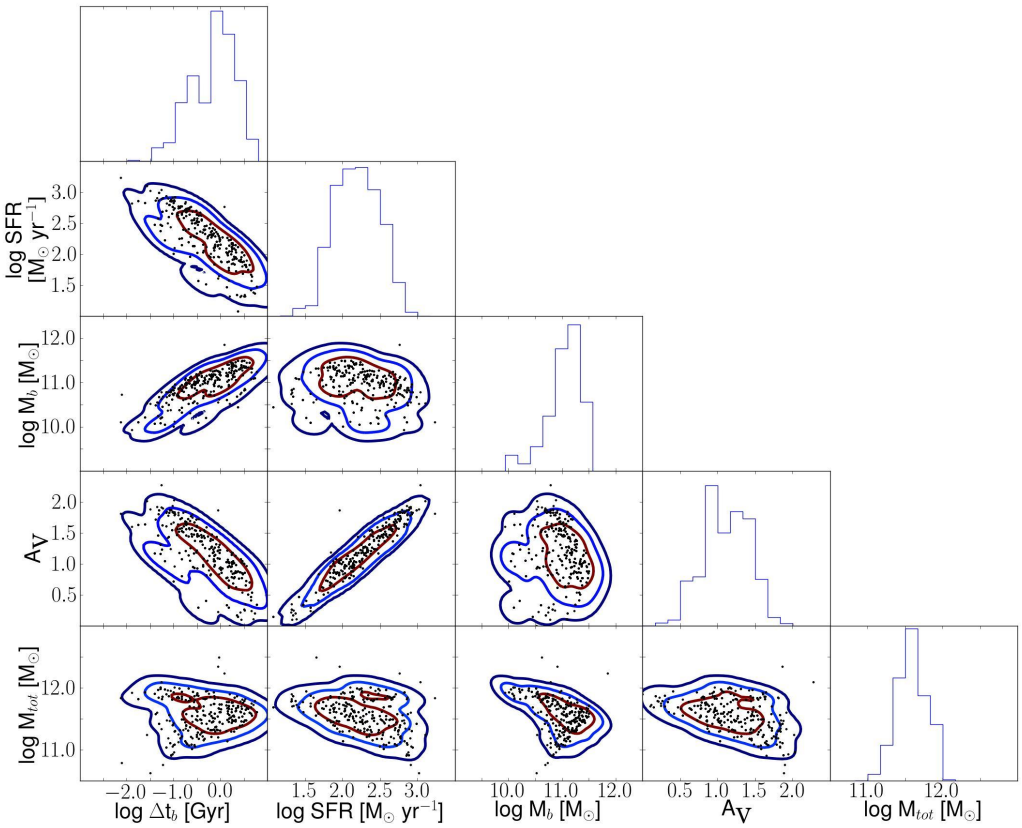

Figure 2.14 We show the two dimensional posterior probability distributions for Δ t$_b$×SFR, Δ t$_b$×Burst Mass, Δ t$_b$×Total Mass, SFR×Burst Mass, SFR×Total Mass, and Burst Mass×Total Mass. Black points denote the individual Monte Carlo draws used to construct the posterior probability distribution, and contours are the 68%-95%-99.7% contours calculated from the kernel density estimate smoothed distribution. The marginal distributions for individual parameters are shown by the histograms on the diagonal.

We show stellar parameter maps in Figure 2.15, including Δt_b, the SFR, and the spatial distribution of the total mass of the BCG. Star formation is concentrated in knots in the center of the BCG, along with a network of six bright filaments and several dimmer filaments. The SFR morphology is consis-

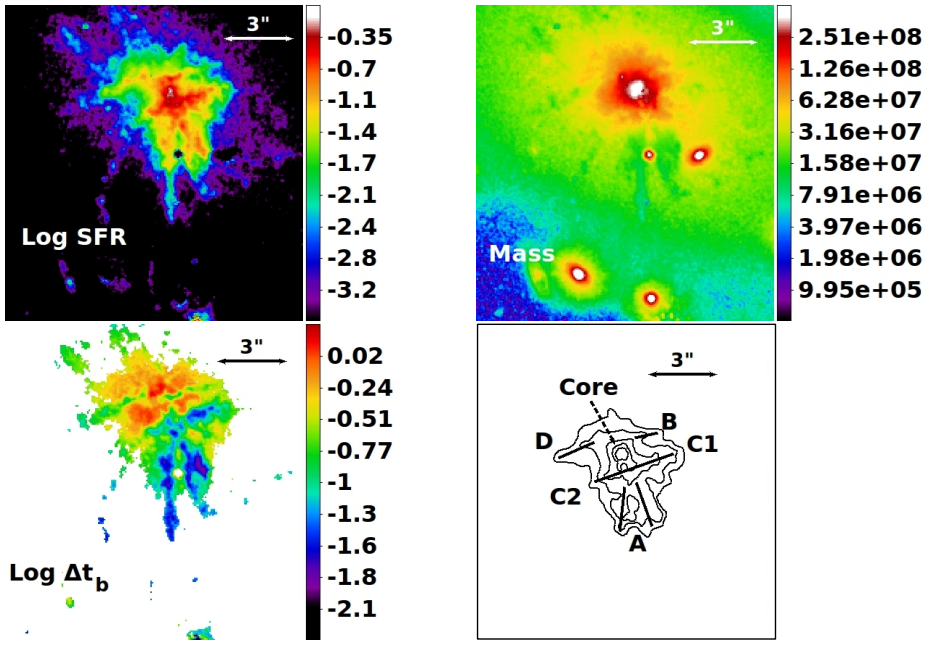

Figure 2.15 Two dimensional maps of SFR, log Δ t_b, and the total mass surface density for RXJ1532. The bottom right panel provides labels for the morphological features in the parameter maps. The SFR map is in units of log $M_\odot$ yr^{-1}, log Δ t_b in log Gyr, and the total mass in units of $M_\odot$ pix^{-2}. All values are expectation values. log Δ t_b is masked to only depict regions where the likelihood of a starburst is $\geq 1\sigma$. The pair of filaments to the south of the center of the BCG, and the filament along the NW/SE are noteworthy for being by $\gtrsim 1$ order of magnitude younger than the average age of the starburst in this system. Possible conical shaped underdensities are roughly along the positions of bright filaments. At the redshift of the cluster, z=0.363, the 3" reference scale in the figures corresponds to about 15.2 kpc.

tent with the Hα and UV morphology. The sum of the pixel SFR modes in the single-aperture SED region is 119 $M_\odot$ yr^{-1}, which matches the single-aperture value remarkably well.

Two filaments point south (A in Figure 2.15), two point northwest (B, C1), one points southeast (C2), and one extends northward before bending to the east (D). The filament pointing southeast and the brighter nothwest pointing

filament (C1 and C2) appear to lie along a single axis. The clumps in the core and the filaments in the north account for the bulk of the ongoing star formation. The starbursts in these structures are long-lived, on the order of $10^8 - 10^9$ yr, which is consistent with the results of the single aperture SED. The filaments to the south, and the two that lie along a single southeast-northwest axis passing through the center of the BCG, are more than an order of magnitude younger than the rest of the burst system.

The peak and western 'bulge' in the total mass corresponds to the central knot morphology in the BCG. Meanwhile, two roughly conical 'drop-offs' appear to the east and west, and both of them extend outward from the positions of star-forming filaments. Similar drop-offs are be visible at the positions of the young, southern filaments. These drop-offs may reflect real deficits in the stellar surface density of the BCG, but may also be a consequence of the dust geometry in this system. Since dusty filaments in the BCG screen the elliptical stellar populations behind them, it is possible that the drop-offs are regions where the mass estimate is biased low due to the positions of filaments along the line of sight.

In the Appendix to this chapter, we demonstrate that the `iSEDfit` derived values for SFR and $E(B-V)$ agree with the broadband values and show that the SED predicted Hα+[N II] line emission equivalent width matches the SDSS spectrum. We also discuss the importance of the Hα feature to characteriz-

ing the SFH using SED fitting. The particulars of the SFH model (a uniform starburst superimposed on an exponentially decaying SFH) and our choice of parameter space are documented in the Appendix as well.

2.5 Discussion

Half (10 out of 20) of the X-ray selected sample of CLASH clusters show evidence for significant ($> 5\ \sigma$) rates of reddening-corrected star formation using both UV and Hα indicators. CLASH BCGs occupy regions of line diagnostic diagrams that are typical of composite starforming-LINER galaxies, and in several cases line emission may be primarily powered by star formation. This rate of incidence is substantially higher than previous published rates of incidence of star formation or line emission in X-ray selected cluster BCGs, which are in general closer to 20-30$\%$ (e.g. Crawford et al., 1999; Edwards et al., 2007). However, the CLASH X-ray selected sample differs from these populations of galaxy clusters, since it is comprised of high gas temperature (kT$_x \geq$ 5 keV) clusters chosen according to a relaxation criterion based on X-ray morphology. The CLASH sample of BCGs has an incidence of line emission similar to the incidence of line emission in REXCESS cool core clusters (70$\%$) (Donahue et al., 2010). Our sample characteristics differ from REXCESS in that it is at higher redshift ($z = 0.2 - 0.7$ compared to $z = 0.06 - 0.18$) and contains comparatively

massive amounts star formation.

The trends between L_{UV} and $L_{H\alpha+[NII]}$ and between L_{UV} and $L_{H\beta}$ suggest applying the Kennicutt SFR calibrations produces consistent star formation rates. However, SFRs predicted using $L_{[OII]}$ are systematically elevated relative to UV based SFRs. These results may not be unusual for starburst galaxies, although they may also indicate that the [O II] emission line is being partially powered by an additional source heating the ionized gas.

The SFRs in several BCGs are very large. In particular, two galaxies exhibit SFRs $\gtrsim$ 100 $M_\odot$ yr^{-1}, and an additional five have SFRs $>$ 10 $M_\odot$ yr^{-1}. The strongest star formers (MACS1931, RXJ1532) are forming stars several times more slowly than the Phoenix cluster, which to date exhibits the largest known SFR of a BCG (McDonald et al., 2013, 2014b). However, MACS1931 is noteworthy because its UV SFR (280 $M_\odot$ yr^{-1}) is $\sim$ 40% of the cooling rate in the absence of heating ($\sim$700 $M_\odot$ yr^{-1}) measured in Ehlert et al. (2011). The Phoenix SFR is $\sim$30% of the cooling rate in the absence of heating measured in McDonald et al. (2014b), so it is plausible that MACS1931 and the Phoenix cluster harbor BCGs undergoing similar feedback events. The presence of an X-ray AGN in each BCG also suggests that the AGN is undergoing a similar evolutionary phase. Furthermore, MACS1931 is forming stars more densely than the rest of the CLASH sample, which suggests it is an outlier relative to other starforming BCGs.

2.5.1 BCG-ICM Interactions

Examination of core entropies implies that the extended star forming features in CLASH BCGs are likely due to an interaction between the BCG and the enveloping ICM. Reddening corrected SFRs obey the 30 keV cm^2 core entropy threshold reported in e.g. Hoffer et al. (2012) – all the strong star formers (SFR > 10 M$_\odot$ yr^{-1}) fall at or below the threshold. From these results we conclude that ongoing star formation in the BCGs is correlated with the thermodynamics of the surrounding ICM. It is plausible that a low ICM core entropy is necessary for the onset of star formation in these BCGs. However, it does not directly trigger star formation, as evidenced by the existence of low-SFR BCGs with core entropies below 30 keV cm^2.

We also analyze observables related to cooling in the low-entropy ICM surrounding BCGs, in order to better understand the interaction between the low-entropy ICM and BCG starbursts. We define two quantities, $\dot{\mathrm{M}}_{g,r35}$ and $\dot{\mathrm{M}}_{g,t20}$, which approximate the cooling rate of ICM gas in the vicinity of the BCG. For both definitions of the cooling rate, we observe a similar trend between SFR and $\dot{\mathrm{M}}_g$. The positive correlations between SFR and both $\dot{\mathrm{M}}_{g,r35}$ and $\dot{\mathrm{M}}_{g,t20}$ are reasonable since the low-entropy gas near the BCG is a prime candidate for the reservoir of gas that cools to become star forming molecular gas. Since the correlation between SFR and $\dot{\mathrm{M}}_g\,(r)$ drops as $\dot{\mathrm{M}}_g\,(r)$ is measured at larger radii, these findings are consistent with the tension between observed ICM cooling

rates those predicted by measuring ICM gas masses with t_{cool} less than a Hubble time.

According to the framework recently laid out in Voit et al. (2015) and Voit & Donahue (2015), the ICM cools by condensing into clouds when AGN jets destabilize ICM gas with t_{cool} below 5-20 times the free-fall time. Detailed simulations carried out in Li & Bryan (2014) and Li et al. (2015) examine AGN jet-triggered condensation of unstable ICM gas onto clumps of cold molecular gas at distances of tens of kpc from the cluster core and track how these clouds evolve, form stars, and precipitate onto the AGN. Simulated AGN jet-triggered precipitation and feedback results in a feedback duty cycle, wherein jet mechanical pressure condenses low-entropy gas while the AGN simultaneously heats the surrounding gas. Once the supply of cold gas precipitating onto the AGN can no longer be replenished by condensation, the AGN shuts off allowing a brief period of cooling directly onto the AGN and restarting the cycle (Li et al., 2015). These simulations reproduce the UV morphologies of cool-core BCGs in CLASH, shown in Donahue et al. (2015), and in lower-redshift BCGs studied in Tremblay et al. (2015).

Since jet-triggered precipitation ought to have a morphological relationship with the jet and a characteristic timescale set by the AGN duty cycle, we can look for evidence that may support or contradict this prediction by comparing the SED-derived stellar parameter maps in RXJ1532 to X-ray measurements

of recent AGN activity. In the single-aperture SED of RXJ1532, the starburst lifetime is log Δt_b [$M_\odot$] = 8.8 $\pm$ 0.5 $\log_{10}$yr, so the bulk of the starburst has a lifetime on the order of $\sim$1 Gyr. However, the southern filaments and the northwest-southeast filaments are $10^7 - 10^8$ yr old. The *Chandra* X-ray image reveals two well-defined cavities to the east and west of the BCG, and possible evidence of ghost cavities to the north and south (Hlavacek-Larrondo et al., 2013b). The cavity refill times, which are the largest estimates of the cavity ages provided by Hlavacek-Larrondo et al. (2013b), are 6.3$\pm$0.7 and 8.2$\pm$0.7 $\times$ 10^7 yr. The cavities appear to be young relative to the timescale of the starburst we recover in our analysis, but match the ages of the young filaments. Our results in RXJ1532 are consistent with an ongoing process of clumps and filaments precipitating out of the ICM when pushed out of equilibrium by jets. Application of the SED fitting techniques developed in this paper to other BCGs in the CLASH sample will determine if this narrative is consistent for all of the star forming BCGs.

The cavities in RXJ1532 also appear to be aligned with the northwest-southeast oriented young filament, and anti-aligned with the shape of the BCG filament network more generally. This morphological relationship is depicted in Figure 2.16. The young filament traces one of the bright Hα filaments as well. The most prominent X-ray cavity corresponds to the brighter (western) end of this filament, suggesting a system with the western edge inclined to-

wards us. Given the available data, we do not rule out a coincidence; however, the corresponding ages and morphologies suggest jet-triggered formation of the young filaments. We hypothesize that the northwest-southeast filament may have been the result of positive feedback triggered by compression from a jet inflating the X-ray cavities.

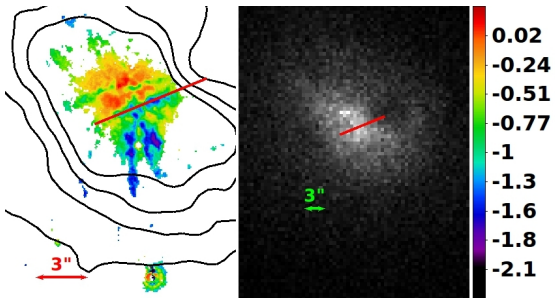

Figure 2.16 *Left:* The burst log lifetime map for the RXJ1532 BCG, which emphasizes the young filaments, is shown with contours of 0.5-7.0 keV counts from the *Chandra* observation of the cluster shown in black. The red line traces the position of the young filament extending along a northwest-southeast axis. *Right:* The 0.5-7.0 keV *Chandra* image of RXJ1532. The red line is identical to the line shown depicted in the left panel. The red line points directly into the prominent cavity in the northwest of the image, and appears to lie along the axis connecting the northwest cavity to the much fainter southeast cavity, which is evident in the unsharp-masked image presented in Hlavacek-Larrondo et al. (2013b).

The narrative we propose for RXJ1532 may be typical for other BCGs in cool core clusters. The SFH of RXJ1532 agrees with a study of line emitting BCGs in the SDSS survey produced by Liu et al. (2012b). While their interpretation of the burst history differs from ours (they assume a stellar population divided into three components– a recent starburst, young stars, and old stars), they find that the majority of the flux they observe in that sample of BCGs is due

to stars forming within $\sim$2.5 Gyr. Furthermore, estimates of molecular gas masses imply that BCG starbursts typically have fuel to last $\sim$1 Gyr (O'Dea et al., 2008). While the case of RXJ1532 may be extreme in terms of SFR, its burst history may be the norm for star forming BCGs. The sum of the results described here, taken in addition to the evidence provided by Donahue et al. (2015), shows agreement between the resolved star structures we observe in the CLASH BCGs and recent theoretical work on feedback in cool core clusters.

The idea of an AGN jet-driven mechanism for ICM condensation could also account for our finding that as the SFR increases in the BCG, the SFR accounts for a larger fraction of the total cooling implied by $\dot{\mathrm{M}}_g$. $\dot{\mathrm{M}}_{g,r35}$ and $\dot{\mathrm{M}}_{g,t20}$ can be interpreted as what the cooling rate of gas in these radii in the absence of re-heating. Based on this interpretation, we suspect that larger starbursts occur in BCGs where gas is cooling more efficiently. The correlation between cool core BCG SFRs and 'efficiency' can be explained neatly if cooling is localized around AGN jets and cavities. If larger SFRs occur in BCGs exhibiting AGN feedback in larger areas, a larger fraction of unstable ICM gas inside a given radius may be triggered into condensing by feedback. This scenario is consistent with our finding that SFR is correlated with the area of the star forming regions in BCGs. Future simulations can test whether a jet-driven cooling mechanism produces a density distribution of cold clouds that correspond to the range of $\langle\Sigma\mathrm{SFR}\rangle$ we observe.

Alternatively, in the feedback cycle modeled in Li et al. (2015), a large amount of gas is cooled quickly with the initial onset of jet feedback (on the order of 10s of Myr), and is slowly consumed by star formation (on the order of a Gyr). Larger SFRs tend to occur earlier in the feedback cycle, when proportionally more of the ICM is precipitating. If this concern dominates the SFR-$\dot{M}_g$ relationship, then we expect to see evidence that larger BCG starbursts are younger on average. In RXJ1532, we see evidence connecting the durations of star forming knots and filaments to the duration of AGN activity (as evidenced by estimates of the ages of X-ray cavities in this system), although a more detailed study of multiple systems will be necessary to establish whether or not there is a relationship between burst age, SFR, and low-entropy ICM gas.

2.6 Conclusion

We have conducted a detailed analysis of the star forming structure in the BCGs in the CLASH X-ray selected sample of galaxy clusters. Using the rich set of CLASH photometry, we estimated the dust reddening in BCGs with significant UV emission and calculated reddening corrected mean UV luminoisities and Hα+[N II] luminosities. We compared these measurements to observations of [O II] and Hβ taken using the Goodman spectrograph. Additionally, we compared the UV derived SFR to X-ray properties calculated using the AC-

CEPT catalog, including the core entropy, K_0, and predicted cooling rates for low entropy gas inside $r = 35$ kpc ($\dot{M}_{g,r35}$) and inside radii where $t_{cool}/t_{ff} = 20$ ($\dot{M}_{g,t20}$). We concluded our analysis by creating a resolved map of the starburst in RXJ1532.9+3021, for which we also have an SDSS spectrum and detailed X-ray data from Hlavacek-Larrondo et al. (2013b).

Using measurements of [O II], [O III], and Hβ lines in conjunction with broadband Hα+[N II] estimates, we constructed diagnostic diagrams for the CLASH BCGs in order to constrain the line-emission power source in these galaxies. Line emission in CLASH BCGs are powered by a combination of star formation and a LINER-like source (possibly the signature of hot, young stars or interaction between the ICM and nebular gas), while the biggest starburst (MACS1931) has a line emission spectrum dominated by ongoing star formation.

CLASH SFRs span a range of magnitudes up to $\gtrsim 100$ $M_\odot$ yr^{-1}, and significant, extended star formation occurs in 10 out of 20 BCGs in our sample. Based on comparisons with K_0 and $\dot{M}_g$, we establish a link between the star formation in the BCG and the state of the surrounding ICM. All of the star forming BCGs with an SFR > 10 $M_\odot$ yr^{-1} are consistent with a ~ 30 keV cm^2 entropy threshold, and a trend exists between SFR and $\dot{M}_g$. These findings imply SFR is fueled by a reservoir of low entropy gas.

SED analysis of RXJ1532.9+3021 reveals a long-lived starburst, with a log

lifetime of 8.8±0.5 $\log_{10}$yr, and a total star formation rate of 118^{+215}_{-42} $M_\odot$ yr^{-1}, which is consistent with our estimates from UV and Hα luminosities. The overall burst timescale is much longer than the AGN on-cycle as inferred by the ages of AGN cavities in the ICM of this cluster, although several of the individual filaments are consistent with the $\sim 60 - 80$ Myr cavity refill times. These results are consistent with recent jet-triggered filaments super-imposed on an older long-lived starburst, which may have been the result of jets from previous AGN on-cycles. The burst history in RXJ1532 is also consistent with another study of stellar populations by Liu et al. (2012b) conducted on SDSS BCGs, so we hypothesize that in upcoming work we will find similar evidence for sporadic starbursts corresponding to episodes of AGN activity.

The SFH of knots and filaments in RXJ1532 suggest a jet-induced precipitation scenario such as Li et al. (2015) is responsible for converting the ICM into cold, starforming gas. If true for all CLASH BCGs, this mechanism would explain the relationship between the thermodynamic state of the ICM surrounding CLASH BCGs and the SFRs in the BCGs. The increasing 'efficiency' of BCG SFRs relative to the cooling rates implied by $\dot{M}_g$ as a function of SFR is plausibly explained by this scenario, as well.

2.7 Appendix

This appendix includes the details of the parameter space chosen to fit the photometry of RXJ1532.9+3021 to a distribution of model SEDs. We describe the parameterization of the SFH, along with the parameter space we defined. Finally, we describe the consistency tests performed on fitting the CLASH SED.

For the 16 band SEDs we construct using all the available bands of CLASH photometry, we used the Salpeter (1955) IMF and Bruzual & Charlot (2003) SSP. The SFH we fit consists of a uniform starburst imposed on a background population with an exponentially decaying SFR, thus the SFH is modeled by

$$\psi_e(t) = \frac{M_{\text{early}}}{\tau} e^{-t/\tau} \tag{2.4}$$

$$\psi_b(t) = \begin{cases} F_b M_{\text{early}} \frac{1-e^{-(t_{\text{age}}-\Delta t_b)/\tau}}{\Delta t_b} & t_{\text{age}} - t \leq \Delta t_b \\ 0 & t_{\text{age}} - t > \Delta t_b \end{cases} \tag{2.5}$$

$$\psi_{net}(t) = \psi_e(t) + \psi_b(t), \tag{2.6}$$

which is a variant of the SFH described in Moustakas et al. (2013). ψ_e is the SFH for the background early-type population of stars, which is parameterized by the time constant τ. ψ_b is the burst SFH, and it is parameterized by the burst lifetime Δt_b and the fractional burst amplitude F_b. Our SFH consists of one burst for simplicity.

We allowed the age of the galaxy to vary between 6 and 9.5 Gyr, and we allowed τ to vary between $\frac{1}{5}$ and $\frac{1}{20}$ the age of the BCG, thereby ensuring that the background population corresponds to a quiescent, early-type galaxy. We allowed the metallicity of the stellar population to vary between 0.04 $Z_\odot$ and 1.6 $Z_\odot$, and the dust attenuation A_V to vary between 0 and 5 mag. In order to sample a wide range of possible burst histories, we sampled burst parameters logarithmically, selecting Δt_b in the range -3 $\leq \log\Delta t_b$ [Gyr] $\leq$ 0.8, and F_b in the range -2 $\leq \log F_b \leq$ 1.0. This parameter space is summarized in Table A1. We drew 10^4 models from this parameter space for each SED we fit to.

Table 2.5
SED Fitting Parameter Choices

Parameter	Range	Units
SSP	BC03[a]	
IMF	Salpeter[b]	
Model Draws	10^4	
t_{age}	[6, 9.5]	Gyr
τ	[0.05, 0.2]	t_{age}
Metallicity	[0.04, 1.6]	$Z_\odot$
A_V	[0.0, 5.0]	mag
log [O III]/Hβ	[-0.5, 0.5]	dex
log Δ t_b	[-3.0, 0.8]	log Gyr
log F_b	[-2.0, 1.0]	dex

[a] Bruzual & Charlot (2003)
[b] Salpeter (1955)

2.7.1 SED Fitting Consistency Checks

The equivalent width of [N II]+Hα, EW([N II]+Hα), is exquisitely sensitive to the SFH of a galaxy, since it is a measure of the ratio of an SFR indicator to the red continuum (Kennicutt, 1998; Leitherer, 2005). Since this value was measured directly by SDSS, and our model SEDs predict line strengths, we can compare the best fit EW([N II]+Hα) for the CLASH SED with the SDSS measured value. This in turn indicates how reliable our estimate of the burst duration is.

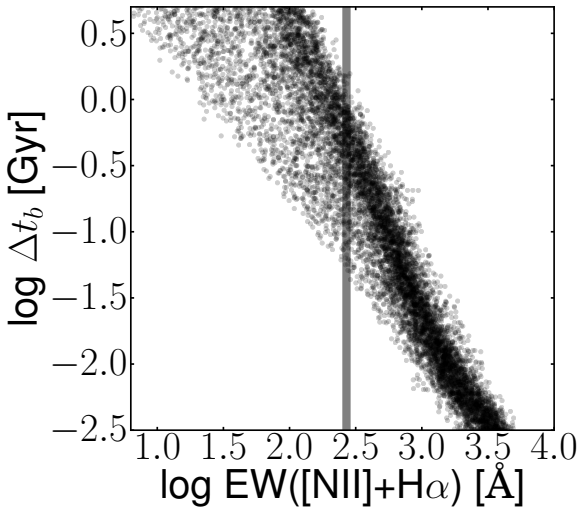

Figure 2.17 We plot the distribution in Δ t_b and EW([N II]+Hα) for all the models gridded in the parameter space summarized in Table A1. Each point corresponds to the values of these two parameters for each individual model, and the vertical line denotes 269.3 $Å_{rest}$, the SDSS measured EW. This plot reveals a densely populated trend tracing out a curve of decreasing burst lifetimes as a function of EW, with a wider, more sparsely populated envelope.

We perform this comparison by fitting the SED of fluxes extracted in a 3″

diameter aperture centered on the coordinates of the SDSS fiber used to take spectra of RXJ1532. Our predicted EW([N II]+Hα) = 269$\pm$120 Å$_{rest}$, which matches the SDSS measurement of 269.3$\pm$2.4 Å$_{rest}$. The probability distribution we recover also shows that the burst duration (Δt_b) is logΔt_b = 8.8 ± 0.5 [yr] and burst mass (M$_b$) is log M$_b$ = 10.83 $\pm$ 0.35 [M$_\odot$]. The overlap between the SDSS fiber and the observable UV structure in RXJ1532 is substantial, so it is not surprising that we recover the same burst history and burst mass for this SED as the SED fit in the Results.

As shown in Figure 2.17, Δt_b is highly dependent upon the equivalent width. The sensitivity of the equivalent width to the burst history makes it straightforward to constrain a relatively narrow range of burst durations for the model SED. The agreement between the spectral equivalent width and our SED fit value is important because it shows that the Hα+[N II] feature is detected strongly enough in the CLASH photometry that a meaningful constraint on the burst history can be made with it.

We used `iSEDfit` to fit only the three bands of WFC3/UVISIS photometry that were used to estimate L$_{UV}$, and show that the results agree with our broadband estimates. We fit photometry extracted from the region used to calculate L$_{UV}$ and assumed fit parameter constraints that are consisent with Kennicutt (1998). For this step, we assumed the metallicity in the stellar population is 1 Z$_\odot$, that the observed age of the BCG, $t_{\rm age}$, is at least 6 Gyr, and that

the decay timescale for the SFH, τ, is 100 Gyr in order to force a continuous SFR model. We also assume a Salpeter (1955) IMF, Bruzual & Charlot (2003) SSP, and a Calzetti et al. (2000) reddening law.

Using this method, we calculated an SFR of 99 ± 24 $M_\odot$ yr^{-1}, and an average reddening of E(B-V) $= 0.26 \pm 0.04$. As before, the SFR PDF is log-normal and we report the mode of the distribution. This result is consistent with the UV photometry results. The agreement implies that while taking a single-aperture SED fit washes out the correlation seen between the spatial distribution of the dust and the SFR, this effect is not a strong source of systematic variation in our fits.

Chapter 3

The Relationship Between Brightest Cluster Galaxy Star Formation and the Intracluster Medium in CLASH

Abstract

We study the nature of feedback mechanisms in the 11 CLASH brightest cluster galaxies (BCGs) that exhibit extended ultraviolet and nebular line emission features. We estimate star formation rates (SFRs), dust masses, and starburst durations using a Bayesian photometry-fitting technique that accounts for both stellar and dust emission from the UV through far IR. By comparing these quantities to intracluster medium (ICM) cooling times and free-fall times derived from X-ray observations and lensing estimates of the cluster mass distribution, we discover a tight relationship between the BCG SFR and the ICM cooling time to free-fall time ratio, t_{cool}/t_{ff}, with an upper limit on the intrinsic scatter of 0.15 dex. Furthermore, starburst durations may correlate with ICM cooling times at a radius of $0.025R_{500}$, and the two quantities converge upon reaching the Gyr regime. Our results provide a direct observational link between the thermodynamical state of the ICM and the intensity and duration of BCG

star formation activity, and appear consistent with a scenario where active galactic nuclei (AGN) induce condensation of thermally unstable ICM overdensities that fuel long-duration (> 1 Gyr) BCG starbursts. This scenario can explain (a) how gas with a low cooling time is depleted without causing a cooling flow and (b) the scaling relationship between SFR and t_{cool}/t_{ff}. We also find that the scaling relation between SFR and dust mass in BCGs with SFRs < 100 $M_{\odot}$ yr^{-1} is similar to star-forming field galaxies; BCGs with large (> 100 $M_{\odot}$ yr^{-1}) SFRs have dust masses comparable to extreme starbursts.

3.1 Introduction

The brightest cluster galaxy (BCG) in the center of the Perseus cluster, NGC1275, was long known to be an emission-line system with ionized hydrogen gas spanning ~ 100 kpc (Lynds, 1970). While BCGs are typically quiescent systems, the correlation of emission-line BCGs inside so-called "cooling flow" clusters was noted by the early studies of X-ray clusters and the optical spectra of their BCGs (e.g. Heckman, 1981; Cowie et al., 1983; Hu et al., 1985; Johnstone et al., 1987). Such clusters, more recently termed "cool core" clusters since their central gas X-ray temperatures are somewhat cooler than their outskirts, have highly peaked central X-ray surface brightness profiles arising from relatively high central gas densities. Initially, it was thought that since the cooling time for this gas (the ratio of the thermal energy content to the radiative loss rate) was short compared to the Hubble time, that such gas would cool, lose pressure, and gradually allow more gas to settle into the center of

such a cluster: a "cooling flow". The rates inferred were 100-1000 $M_\odot$ yr^{-1} in some cases (see, e.g. Fabian (1994) for a review). Subsequent high-resolution X-ray spectroscopy from XMM-Newton convincingly showed that this simple model was incorrect (e.g. Peterson et al., 2003; Peterson & Fabian, 2006). Nevertheless, observations of the BCGs in samples of X-ray luminous galaxy clusters have revealed that in up to 70% of cool-core clusters, the otherwise quiescent elliptical BCG shows signs of ultraviolet and nebular line emission. This emission, in some cases, is consistent with star formation rates (SFRs) on the order of 100 $M_\odot$ yr^{-1} (e.g. McNamara & O'Connell, 1989; Crawford et al., 1999; Edwards et al., 2007; Donahue et al., 2010). This activity is observed to be related to the presence of low entropy intracluster gas (the intracluster medium, or ICM) in the cluster core. Since low-entropy ICM gas has a short cooling time, this correlation suggests that the observed star formation is fueled by cold gas that has condensed from a hot gas reservoir, however at a far gentler rate than the simple cooling flow model predicted (Rafferty et al., 2006, 2008; Cavagnolo et al., 2008, 2009; McDonald et al., 2010; Hoffer et al., 2012). One viable source of heat replacing energy lost via radiative cooling is energy injected by active galactic nuclei (AGN) into the ICM. The mechanical work indicated by the size and ICM gas pressure surrounding X-ray cavities filled by radio-emitting plasma demonstrates that there is sufficient energy to counter radiative cooling (Rafferty et al., 2006; McNamara & Nulsen, 2007; Fabian,

2012; McNamara & Nulsen, 2012).

There is a growing body of evidence supporting AGN feedback-driven precipitation and condensation as being responsible for balancing heating and cooling in cool-core galaxy clusters. AGN jet feedback is thought to inject energy into the ICM, thus offsetting cooling while also triggering condensation of thermodynamically unstable volumes of ICM plasma, which then precipitate onto the BCG and fuel star formation and further AGN activity (Voit et al., 2015; Voit & Donahue, 2015; Li & Bryan, 2014; Li et al., 2015; Gaspari et al., 2012, 2013, 2015; Fogarty et al., 2015; Gaspari et al., 2016; Prasad et al., 2015; Yang & Reynolds, 2016; Meece et al., 2016). Recently, the precipitation aspect of this model was shown to be consistent with observations of molecular gas accretion onto the AGN in the Abell 2597 BCG (Tremblay et al., 2016). The morphologies of UV and nebular emission structures in observed BCGs in cool core clusters (e.g. Donahue et al., 2015; Tremblay et al., 2015) are reproduced in simulations of AGN feedback-regulated condensation and precipitation in low-entropy ICM gas (Li et al., 2015; Gaspari et al., 2017). Furthermore, submillimeter observations of cool core clusters reveal reservoirs of as much as $\sim 10^{11}$ $M_\odot$ of molecular gas (Edge et al., 2002; O'Dea et al., 2008; Russell et al., 2016). The picture that is emerging is one of a complex feedback-driven interaction between the BCG and ICM in the cluster core which produces substantial gas condensation but suppresses runaway ICM cooling.

The condensation model follows thermal instabilities that are both triggered and regulated by AGN feedback. In this model, the hot ICM gas is near hydrostatic equilibrium with the gravitational potential, and the gas entropy at large cluster-centric distances is governed by cosmological processes. At very small radii close to the central AGN, the gas can develop a nearly flat entropy profile that allows thermal instabilities to rapidly grow. However, Meece et al. (2016) showed that even a modest fraction of AGN feedback in the form of mechanical jets can transport energy beyond the region local to the AGN. Rather than resulting in unphysical catastrophic cooling, such systems can self-regulate. The resulting entropy profile within 5-10 kpc of the simulated AGN with jet feedback is somewhat shallower than in the outer parts of the cluster, but condensation of low-entropy inhomogeneities which have been uplifted to greater altitudes can produce multi-phase structure at radii larger than 10 kpc (Meece et al., 2016; Voit et al., 2017). Key to this model is the prediction that ICM plasma with a cooling-to-freefall time ratio (t_{cool}/t_{ff}) $\lesssim 10$ is sufficiently unstable that jets trigger condensation. Supporting this prediction are observations indicating that $t_{cool}/t_{ff} \leq 20$ in the center of a galaxy cluster is a good predictor of BCG activity (Voit & Donahue, 2015; Voit et al., 2017). In simulations, material will condense out of the ambient ICM when $t_{cool}/t_{ff} \lesssim 10$ locally (Li & Bryan, 2014; Li et al., 2015).

Alternatively, McNamara et al. (2016) posit that most cold molecular gas

condenses in the vicinity of BCGs when AGN jets uplift low entropy plasma from within the BCG to high enough radii for the plasma to condense. In this scenario, jet uplifting can cause core plasma to condense if drag prevents it from sinking back to its original altitude in a time shorter than the cooling time of the gas. Observations of massive (up to 10^{10} $M_{\odot}$) flows of molecular gas with velocities of several hundred km s^{-1} in cool core clusters such as Abell 1835 and Abell 1664 suggest that this mode of condensation and precipitation plays an important role in AGN-regulated feedback (McNamara et al., 2014; Russell et al., 2014). Both condensation due to uplifting and condensation in the ambient ICM in a cluster core are studied in models of cluster-scale feedback (Li et al., 2015; Gaspari et al., 2016; Voit et al., 2017).

Molendi et al. (2016) propose a possible scenario where star formation in BCGs lags behind cooling by up to a Gyr, owing to molecular gas in the environs of the BCG forming stars at only a few percent efficiency, as one possible explanation for the presence of star forming BCGs in the absence of cooling flows. This scenario can explain relationships between BCG SFRs and the thermodynamical state of the ICM, but would imply that the density and temperature of the hot ICM in the vicinity of the BCG is related to the amount of gas that had cooled in a previous cooling phase.

In this paper, we analyze the spectral energy distributions of the UV-luminous

BCGs in the full X-ray selected cluster sample from the CLASH[1] program. Our aim is to explore physical connections between BCG star formation activity and the properties of the surrounding ICM and constrain models for possible mechanisms of condensation in the ICM. We take full advantage of deep, multi-band imaging of the relatively uniform and massive sample of galaxy clusters observed by CLASH, and we are able to reveal relationships that may have previously been confounded by analyses of less deeply observed and/or less uniform samples. Specifically, by studying the BCGs of cool-core clusters in CLASH, we explore how cooling and thermal instability timescales (t_{cool} and t_{cool}/t_{ff}) in the ICM may relate to BCG star formation.

This chapter is structured as follows: in Section 3.2 we describe the observational data set used to construct the spectral energy distributions (SEDs) for the 11 active CLASH BCGs studied in this sample. In Section 3.3, we describe constructing and fitting UV-through-FIR SEDs, as well as the X-ray derived parameters we use to study the ICM. In Section 3.4 we present our results, which we discuss in Section 3.5. We summarize our conclusions in Section 3.6. Throughout our analysis we adopt a ΛCDM cosmology with $\Omega_m = 0.3$, $\Omega_\Lambda = 0.7$, H_0 = 70 km/s/Mpc, and $h = 0.7$.

[1]Cluster Lensing And Supernova survey with *Hubble*

3.2 Observations

The near UV through far IR SEDs in this paper are based on photometry from the CLASH *HST* data set in combination with mid- and far-IR data from *Spitzer* and *Herschel*. X-ray data used for measuring the temperature, density and metallicity profiles of the ICM were taken from the *Chandra* archive.

3.2.1 HST: UV through near IR photometry

A detailed summary of the science-level data products for CLASH may be found in Postman et al. (2012). For the 11 X-ray selected clusters with evidence of BCG star formation activity, we used the CLASH photometric data set covering 16 filters spanning from ∼2000-17000 Å in the observer frame. We used drizzled mosaics with a 65 milliarcsecond pixel scale, the same image data used in Fogarty et al. (2015). These data are publicly available via MAST HLSP [2]. Drizzled mosaics were constructed using the `MosaicDrizzle` pipeline (Koekemoer et al., 2011). In keeping with our previous work, we calculated a single Milky Way foreground reddening correction for each BCG in each filter using the Schlegel et al. (1998) dust maps. Our drizzled images are background corrected using an iterative 3-sigma clipping technique. Owing to additional uncertainty in the flat-fielding of WFC3/UVIS photometry over large

[2] https://archive.stsci.edu/prepds/clash/

spatial scales, discussed in Fogarty et al. (2015), the median flux measured in an annulus around each BCG was subtracted from each of the UV filters as well.

3.2.2 Spitzer: mid-IR photometry

Spitzer/IRAC 3.6 μm and 4.5 μm mosaicked observations and catalogs are available for all of the BCGs studied in this paper, and 5.7 μm and 7.9 μm observations are available for Abell 383, MACS1423.8+2404, and RXJ1347.5-1145. Fluxes for *Spitzer* IR sources in the CLASH fields were taken from the publicly available CLASH/*Spitzer* catalog [3]. We describe aperture selection and our method for correcting for crowded fields in the *Spitzer* photometry in Section 3.3.1.

Photometry for each channel was measured on mosaic images generated using the `MOPEX` software package. The default `MOPEX` settings for the catalog use the 3.6 μm channel, and use the fiducial image frame for this channel to generate the mosaics for longer wavelength IRAC channels for each CLASH cluster. The *Spitzer* mosaic images have a pixel scale of 0.6 arcseconds. Flux values were obtained with `Source Extractor` in double-image mode using `MOPEX` weights (Bertin & Arnouts, 1996). The `Source Extractor`-generated catalogs consist of aperture photometry for sources in fixed-diameter apertures

[3] http://irsa.ipac.caltech.edu/data/SPITZER/CLASH/

ranging from 2 to 40 pixels. Full details about the parameters used with `MOPEX` and `Source Extractor` to generate the CLASH catalog are given in the online documentation[4].

3.2.3 Herschel: far-IR photometry

We used archival data from *Herschel*/PACS (*100 μm, 160 μm*) and *Herschel*/SPIRE (250 μm, 350 μm, and 500 μm) to extend BCG photometry into the far-infrared. Table 3.1 details the observations used and their exposure times. We obtained level 2 archival data using the *Herschel* Science Archive reduction pipeline for SPIRE observations and the HSA MADMAP reduction pipeline for PACS observations. Observations were co-added and photometric parameters were measured using the `HIPE` software package. We describe *Herschel* aperture selection and background subtraction in Section 3.3.1.

3.2.4 Chandra: X-ray Observations

Chandra data exists for all CLASH clusters, with exposure times for individual observations ranging from 19.3 ks (for Abell 383) to 115.1 ks (for MACS1423.8+2404). These data were assembled in Donahue et al. (2014) to construct the parameter profiles that we use to analyze the thermodynamics of

[4]http://irsa.ipac.caltech.edu/data/SPITZER/CLASH/docs/README.CLASHSpitzer

Table 3.1 *Herschel* Observations

BCG	Instrument	Observation ID	Exposure Time (seconds)
Abell 383	PACS	1342189151	7704
		1342189152	7704
		1342189153	7185
		1342189154	7185
	SPIRE	1342189503	5803
		1342201147	3172
MACS0329.7−0211	PACS	1342249280	7704
		1342249281	7704
	SPIRE	1342214564	169
		1342239844	1411
MACS0429.6−0253	PACS	1342250641	7704
		1342250836	7704
	SPIRE	1342239932	169
		1342241124	1411
MACS1115.9+0219	PACS	1342247672	7704
		1342247691	7704
	SPIRE	1342223226	169
		1342256866	1411
MACS1423.8+2404	PACS	1342188215	9850
		1342188216	9850
	SPIRE	1342188159	6636
MACS1720.3+3536	PACS	1342243800	7704
		1342243801	7704
	SPIRE	1342229601	169
		1342239976	1411
MACS1931.8−2653	PACS	1342241619	7704
		1342241681	7704
	SPIRE	1342215993	169
		1342254639	1411
MS2137−2353	PACS	1342187803	9850
		1342187804	9850
	SPIRE	1342195938	5786
RXJ1347.5−1145	PACS	1342213836	9420
		1342213837	9420
	SPIRE	1342201256	859
		1342201257	859
		1342201258	859
		1342201259	859
		1342201260	859
		1342201261	859
		1342201262	859
		1342201263	859
		1342247859	1952
		1342247860	1952
		1342247861	1952
RXJ1532.9+3021	PACS	1342258435	7704
		1342258435	7704
	SPIRE	1342234776	169
		1342261681	1411
RXJ2129.7+0005	PACS	1342187256	9569
		1342187257	9569
		1342196791	7185
		1342196792	7185
	SPIRE	1342188167	6636
		1342209312	3172

the ICM in the environs of each BCG. We also examine the archival data for evidence of X-ray loud AGN, in order to determine whether it is important to consider AGN emission models in our SED fits. We found evidence for only one X-ray loud AGN, in the cluster MACS1931.8-2635. The AGN classification is based on the presence of a *Chandra* point source, with a spectrum showing evidence for hard X-ray (>5 keV) emission over that expected from hot gas with $kT \sim 5 - 7$ keV.

3.3 Methods

In Fogarty et al. (2015), we identified 11 BCGs in the CLASH X-ray selected sample with evidence of ongoing star formation. In each of these BCGs, we detected extended UV emission in WFC3/UVIS photometry and extended Hα + [N II] emission by differencing ACS images. The extended UV and line emission features were shown in Donahue et al. (2015) and Fogarty et al. (2015) to be the site of nebular emission and star formation. These 11 BCGs form the star-forming BCG sample we study in this paper.

3.3.1 BCG Photometry

We constructed multi-instrument UV-through-IR SEDs for the UV-bright filamentary features in each UV-luminous CLASH BCG. Since we are inter-

ested in measuring the star formation properties of the BCGs, for the *Hubble* UV through near-IR photometry we extracted flux from within the apertures described in Fogarty et al. (2015) (apertures for each BCG are shown in Figure 3 in that paper). These apertures were selected to encompass the region in each BCG exhibiting a UV luminosity of 7.14×10^{24} erg s^{-1} Hz^{-1} pix^{-2}, corresponding to a star formation surface density of $\Sigma_{\rm SFR} \geq 0.001$ M$_\odot$ yr^{-1} pix^{-2}, after accounting for dust reddening. Measuring fluxes in these apertures maximizes the contribution made by the recently formed stellar population to the SED, while it minimizes the contribution made by the passive stellar population in the bulk of the BCGs. Our procedure for measuring fluxes minimizes the risk of underestimating dust attenuation in the star forming regions of the BCGs since we are not averaging dust attenuation over the dusty star-forming and relatively dust-free quiescent parts of the galaxy. We do not match the *Hubble* point spread functions (PSF) since the photometric aperture sizes we use are much larger than the sizes of the PSFs for the *HST* passbands.

Estimating mid-IR fluxes using *Spitzer* was more complicated, since star-forming features are not well resolved spatially in *Spitzer* photometry. We measured IR fluxes from *Spitzer* in apertures in the CLASH/*Spitzer* catalogs that were selected to encompass the BCG while minimizing inclusion of satellite galaxies. Both the old stellar population and dust emission (primarily in the form of PAH features) contribute significantly to the flux in these filters.

Since the angular resolution of *Spitzer* (> 1.45 arcsec) is insufficient to resolve the star forming features we wish to study, we needed to subtract the contribution made by old stellar light from outside our *Hubble* apertures to the *Spitzer* IR fluxes. We accomplished this by first measuring the *HST*/WFC3 F160W flux in the region covered by the *Spitzer* apertures but not the *Hubble* apertures. We assumed this flux is due entirely to old stellar light, and estimated (IRAC-F160W) color by modeling old stellar populations experiencing dust attenuation ≤ 0.5 A_V using the Bayesian SED fitting algorithm `iSEDfit` (see Section 3.3.2 for details) for each BCG. We used these colors to scale the F160W fluxes corresponding to the old stellar population outside the *Hubble* apertures to *Spitzer* IRAC fluxes and subtracted these scaled fluxes from our *Spitzer* photometry. The resulting *Spitzer* IRAC photometry corresponds to the fluxes in the *Hubble* apertures. An example pair of *Spitzer* and *Hubble* apertures is shown in Figure 3.1.

We note that H_2 vibrational modes and other near-IR emission lines have been detected between 5-25μm in star-forming BCGs (Donahue et al., 2011). However, contamination from emission lines similar to those observed in Donahue et al. (2011) would only contribute a few percent to the mid-IR fluxes derived for the stellar and dust emission in star forming regions, while the uncertainties on these fluxes after subtracting the excess old stellar light component is $\gtrsim 20\%$. Therefore, we do not attempt to estimate the contribution of

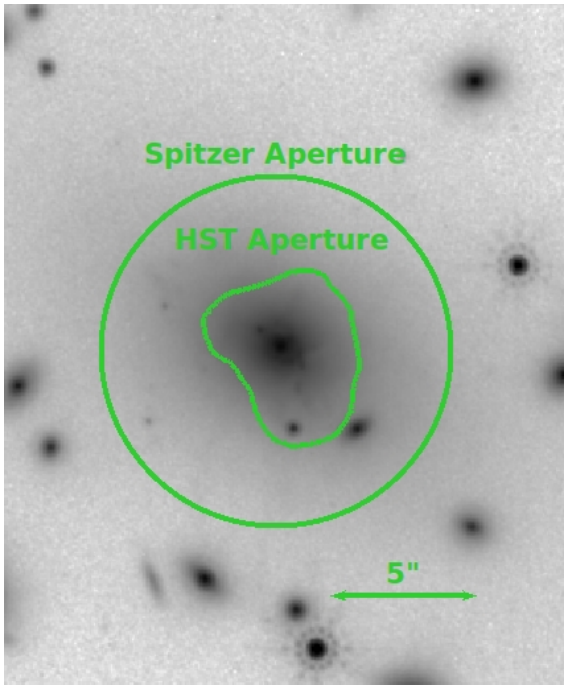

Figure 3.1 The UV-bright *Hubble* aperture and *Spitzer* photometric aperture for RXJ1532.9+3021 are shown on logarithmically scaled F160W band photometry of the cluster. The *Spitzer* aperture encompasses the *Hubble* aperture, and includes flux from the old stellar population in the BCG as well as contaminating light from nearby early-type satellite galaxies that needs to be modeled and subtracted to estimate the mid-IR flux within the *Hubble* aperture.

these lines to the *Spitzer* mid-IR photometry.

We extracted *Herschel* PACS and SPIRE photometry from archival data using the `HIPE` software package. Since *Herschel* bands are dominated by dust re-emission of UV flux, we assumed that all of the *Herschel* flux in each BCG comes from the star forming features. We measured photometry in circular apertures large enough to cover the PSF of each *Herschel* filter. Aperture radii were chosen to be 8", 12" , 18" , 24" , and 36" for the 100 μm, 160 μm, 250 μm, 350 μm, and 500 μm filters respectively. To obtain fluxes we took the mean of pairs of cross scans, while we estimated uncertainties using the difference between scans. For each *Herschel* band, we found typical uncertainties on the order of $\lesssim 2\%$ for the PACS filters and $\sim 10\%$ for the SPIRE filters. Since the BCGs occupy crowded fields, we measured crowded source backgrounds in annuli centered on the BCG with inner radii of 16", 24", 36", 48", 72" for the respective PACS and SPIRE filters and outer radii of 180".

3.3.1.1 Photometric Errors

Error budgets for the fluxes in our SEDs include uncertainty from counting statistics, systematic uncertainties from weight maps (produced as output from Drizzling in the case of the *Hubble* data and provided by the level 2 data pipeline in the case of the *Herschel* PACS and SPIRE data), and the absolute calibration uncertainty for each instrument. In the case of the *Spitzer* IRAC

data, the total counting and formal systematic uncertainties are available in the CLASH/*Spitzer* catalogs from the fluxes and `MOPEX` weight maps (see Section 3.2.2). Calculating uncertainties for the mid-IR fluxes obtained using `Spitzer` IRAC photometry required propagating the additional uncertainty involved in estimating and subtracting the excess old stellar light component from the mid-IR photometry.

Source confusion noise is an important component of the error budget for SPIRE detections (Nguyen et al., 2010). We incorporate confusion noise terms of 5.8 μJy, 6.3 μJy, and 6.8 μJy from Nguyen et al. (2010) into our estimates of the uncertainty on SPIRE 250 μm, 350 μm, and 500 μm fluxes respectively. In bands where we do not detect significant flux from the BCG, we use the confusion and instrument noise estimates computed in Nguyen et al. (2010) to estimate 3σ upper limits.

For *HST* ACS and WFC3 data, we included a 5% total absolute and relative calibration uncertainty in our error budget. For the ACS and WFC3/IR filters, the absolute calibration is the dominant term in the overall error budget. Since several of the early CLASH WFC3/UVIS observations were affected by non-uniform flat-fielding at large (hundreds to thousands of pixels) scales, we calculated the scatter in identical apertures placed in empty patches of sky for each UV observation. This extra uncertainty component in the WFC3/UVIS error budget is in most cases similar to the absolute calibration uncertainty, al-

though for several filters with only faintly detected BCG UV emission it is the main source of uncertainty.

We adopted an additional 3% uncertainty for the *Spitzer* IRAC fluxes, and 10% uncertainty for *Herschel* PACS and SPIRE fluxes. The 3% figure accounts for the absolute flux calibration uncertainty in *Spitzer* (Reach et al., 2005). For *Herschel*, we incorporate the absolute calibration uncertainty ($\sim 5\%$), the relative calibration uncertainty ($\sim 2\%$), and allow for an additional factor of ~ 2 applied to the systematic uncertainty to account for the fact that we are measuring the fluxes of marginally extended sources and that our method of estimating the uncertainty in the *Herschel* images may underestimate the uncertainty (Griffin et al., 2013; Balog et al., 2014).

For most of the BCGs, the error budget for the *Hubble* photometry is dominated by the absolute calibration uncertainty, the *Spitzer* error budget is dominated by the uncertainty from modeling and subtracting the old stellar excess, the *Herschel* PACS uncertainties are dominated either by counting statistics or the calibration, and the *Herschel* SPIRE uncertainties are dominated by the calibration uncertainty or the confusion noise.

3.3.2 SED Fitting

We fit SEDs for the CLASH BCGs using the Bayesian fitting code `iSEDfit` (Moustakas et al., 2013). In order to take full advantage of the CLASH UV-FIR

observations, we incorporated modifications to `iSEDfit` to account for emission from dust. The `iSEDfit` package fits SEDs by first generating a grid of parameters that describe models of dust–attenuated stellar emission by a composite stellar population. Grids are produced by randomly sampling a bounded section of parameter space. The sampling is weighted with either a uniform prior or a logarithmic scale prior. With these parameters, `iSEDfit` constructs a grid of model spectra given a choice of synthetic stellar population (SSP), initial mass function (IMF), and dust attenuation model. The package then computes synthetic photometry by convolving these model spectra with the filter responses of the CLASH SEDs, and uses this grid of synthetic SEDs to sample the posterior probability distribution that the model stellar population and dust parameters produce the observed SED.

The `iSEDfit` package uses a Bayesian Monte Carlo approach to estimate probability distributions for model parameters. For each BCG, we constructed a model grid consisting of 20000 models. The likelihood and mass scaling $\mathcal{A}$ of each model given the observed SED was calculated by minimizing χ^2 for each model,

$$\chi^2 = \sum_{i=1}^{N} \frac{(F_i - \mathcal{A}M_i)^2}{\sigma_i^2}, \tag{3.1}$$

where F_i and σ_i are the SED fluxes and uncertainties, and M_i are the model fluxes. The minimum χ^2 and $\mathcal{A}$ are found by solving for $\partial\chi^2/\partial\mathcal{A} = 0$. We obtained a posterior probability distribution for the models using a weighted

random sampling of the model grid, where model weights were determined by the likelihoods. Posterior probability distributions for individual physical parameters were obtained by taking the distribution of parameters of the sampled models. For the SFR, the posterior consists of the distribution of the instantaneous normalized SFR determined by the parameterized star formation history, multiplied by $\mathcal{A}$. For a detailed discussion of `iSEDfit`, see Moustakas et al. (2013).

We model the star formation history of each BCG with an exponentially decaying curve (the early-type population) and a super-imposed exponentially decaying burst at recent times. The initial exponentially decaying curve is parameterized by the age of the BCG t and the decay rate of the curve τ, while the exponentially decaying burst is parameterized by the duration of the starburst Δt_b, the decay rate of the burst, and the mass of the burst relative to the old stellar population (see Figure 3.2). The bounds on parameter space for the entire model and assumptions we made for the BCG stellar populations are given in Table 3.2.

We modified the SED–fitting routine to incorporate dust emission models from Draine & Li (2007) into the parameter grid and synthetic spectra used in `iSEDfit`. The dust parameter space was sampled using bounds and priors given in Table 3.2. For each synthetic spectrum, the total luminosity of the dust spectrum was normalized by the difference between the un-attenuated

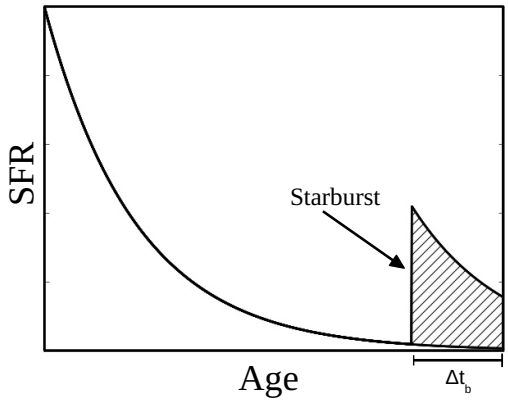

Figure 3.2 A schematic of the double-exponential star formation history adopted in this paper. The solid line shows the SFR as a function of time. The horizontal line under the lower-right part of the x-axis depicts the starburst duration Δt_b, which is the amount of time since the onset of the BCG starburst. The area under the curve is equal to the total mass of stars formed by the BCG, and the portion of the area highlighted with hatching is the contribution of the starburst to the BCG stellar mass.

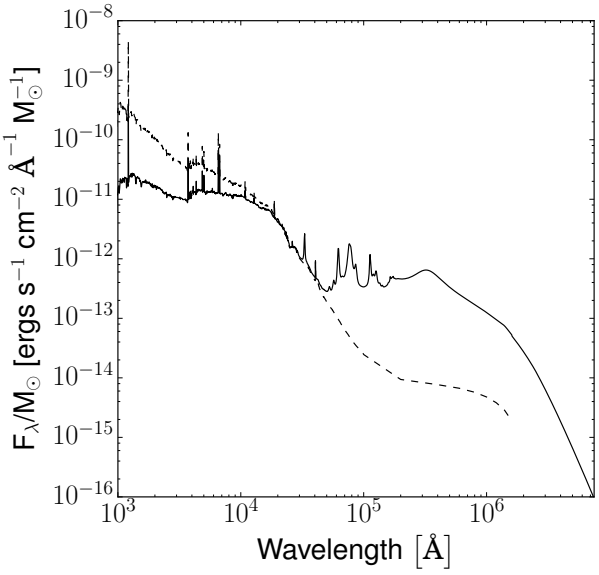

Figure 3.3 An example synthetic spectrum produced by our modified version of `iSEDfit`. The dashed line shows the model stellar emission spectrum in the absence of dust. The solid line shows the model spectrum after the stellar emission has been absorbed by dust obeying a modified Calzetti et al. (2000) attenuation law and re-emitted in the far-IR.

and attenuated stellar spectrum. Figure 3.3 shows an example of the synthetic attenuated stellar plus dust spectrum, and the Appendix shows best-fit synthetic spectrum for each BCG.

With our modified version of `iSEDfit`, we were able to test multiple stellar population and dust attenuation models in order to examine the dependence of our results on the choice of SSP, IMF, and attenuation law. We adopt a Bruzual & Charlot (2003) SSP, the Salpeter (1955) IMF defined over the interval 0.1-100 $M_\odot$, and the Calzetti et al. (2000) attenuation law. We chose

to adopt a Salpeter (1955) IMF in order to produce SFRs consistent with the SFRs estimated in our previous paper using the Kennicutt (1998) relationship. In order to examine the effect of an $A_{\rm V}$-dependent attenuation curve, we also performed fits using a modified Calzetti attenuation law, where we multiplied the Calzetti curve with an attenuation-dependent slope that matches the attenuation dependence of the curves published in Witt & Gordon (2000). To test if our results have any dependence on our choice to adopt a Calzetti attenuation law, we also ran `iSEDfit` assuming clumpy SMC-like dust in a shell geometry. We found our results to be largely consistent with results using the regular Calzetti curve, as well as the attenuation-dependent version of the Calzetti curve. This is because, in the typical CLASH BCG, the attenuation is $A_{\rm V} \lesssim 1.0$, where overall attenuation dependence on the shape of the curve has a only a modest effect. As a further test of the model dependence of our results, we performed SED fits assuming a Chabrier (2003) IMF. Altering the IMF shifts the SFRs downwards by 0.25 dex, but otherwise does not significantly alter the stellar and dust parameters we seek to measure (Δt_b, $\rm M_{\it d}$, $\rm A_V$).

3.3.3 Cooling and Freefall Time Profiles

We calculated radial profiles of the cooling time, defined to be the ratio of the thermal energy density to the rate of radiative energy density loss for an optically thin plasma undergoing Bremsstrahlung emission, for each cluster

Table 3.2 SED Fitting Parameters

Stellar Population Model			
Synthetic Stellar Population	Bruzual & Charlot (2003)		
Initial Mass Function	Salpeter (1955)		
Attenuation Law	Calzetti et al. (2000)		
Dust Emission	Draine & Li (2007)		
Model Parameter Space Constraints	*Minimum Value*	*Maximum Value*	*Sampling Interval*
Old Stellar Population			
Age, t	6 Gyr	z^a_{Age}	Linear
Decay Rate, τ	$0.05t$	$0.2t$	Linear
Metallicity	$3 \times 10^{-2} Z_\odot$	$1.5 Z_\odot$	Linear
Burst Population			
Burst Duration, Δt_b	10^{-2} Gyr	5.0 Gyr	Logarithmic[b]
Burst Decay Percentage	0.01	0.99	Linear
Relative Burst Mass, FBURST[c]	0.0016	6.4	Logarithmic
Dust Parameters			
Attenuation A_V	0	2	Linear
PAH Abundance Index q_{PAH}	0.10	4.58	Linear[d]
γ^e	0.0	1.0	Linear
U^e_{min}	0.10	25.0	Logarithmic
U^e_{max}	10^3	10^7	Logarithmic

[a] Z_{Age} is the age of the universe at redshift the BCG redshift Z.
[b] Burst parameters were sampled logarithmically, since their qualitative effect on the model SED of the galaxy occurs on order-of-magnitude scales. The exception to this is the burst decay percentage, which is one minus the amplitude of current star formation activity relative to the amplitude of the burst Δt_b yr ago.
[c] Mass of stars created by the starburst at t relative to the mass of stars created by the exponentially decaying old stellar population at t. The burst mass percentage is calculated by FBURST/(1+FBURST).
[d] Draine & Li (2007) model parameters sampling intervals were chosen based on the model parameter distributions of the template spectra.
[e] The Draine & Li (2007) treats dust in a galaxy as consisting of two components. The first component consists of a fraction γ of the dust is exposed to a power law distribution of starlight intensity, ranging from U_{min} to U_{max}, while the second component consists of the remainder of the dust, and is only exposed to a starlight intensity U_{min}. U is defined to be the intensity of starlight relative to the local radiation field, and U_{min} and U_{max} are bounds on the distribution of U.

using

$$t_{cool}(r) = \frac{3}{2}\frac{n(r)\,k_B T(r)}{n_e(r)\,n_H(r)\,\Lambda[T(r), Z(r)]} = \frac{6.9}{2}\frac{k_B T(r)}{n_e(r)\,\Lambda[T(r), Z(r)]}, \tag{3.2}$$

where k_B is the Boltzmann constant, $n(r)$ is the total number density profile of the plasma, $n_H(r)$ is the H number density, $n_e(r)$ is the electron number density, $T(r)$ is the temperature profile, $Z(r)$ the metallicity profile, and $\Lambda(T, Z)$ is the cooling function. We obtained values of the cooling function for specific temperatures and metallicities by interpolating the cooling function values in Sutherland & Dopita (1993), and assumed $n \approx 2.3 n_H$ (Cavagnolo et al., 2009). The ICM density, temperature, and metallicity profiles used in this study are available in Donahue et al. (2014). We used the non-parametric Joint Analysis of Cluster Observations (JACO) profiles (see Mahdavi et al. (2007) and Mahdavi et al. (2013) for a description of the JACO algorithm), which are reported in concentric shells spaced so that each annulus contains at least 1500 X-ray counts.

We measured t_{cool} at specific radii by interpolating on $n_e(r)$, $T(r)$, and $Z(r)$ at the desired radius and solving Equation 3.2. In order to determine the uncertainty on t_{cool} we produced an ensemble of 1000 n_e, T, and Z profiles, where the values in each profile were obtained by drawing from normal distributions defined by the observed values and uncertainties in each profile. By calculat-

ing the distribution of t_{cool} given the interpolated values of n_e, T, and Z for the ensemble of profiles, we sampled the probability distribution of t_{cool} and thus estimated uncertainties. We constrained the ensemble of metallicity profiles to only allow values of Z in the range $0.15 - 1.5Z_{\odot}$, since ICM metallicities are typically $0.3Z_{\odot}$ and tend to be $\gtrsim 0.6 - 0.8Z_{\odot}$ in the centers of cool core clusters (De Grandi et al., 2004).

We calculated freefall times by assuming cluster masses obey an NFW profile (Navarro et al., 1997). NFW mass concentration parameters and values of M_{200} were obtained from Merten et al. (2015a). We computed the enclosed mass for each cluster as a function of radius,

$$M_{enc}\left(r\right) = 4\pi\rho_0 r_s^3 \left[\ln\left(\frac{r_s + r}{r_s}\right) - \frac{r}{r_s + r}\right], \tag{3.3}$$

where ρ_0 and r_s are NFW scale factors determined by the mass and concentration parameter of the galaxy cluster, as well as the critical density at the cluster redshift. We then calculated freefall time profiles,

$$t_{ff}\left(r\right) = \sqrt{\frac{2r^3}{GM_{enc}\left(r\right)}}. \tag{3.4}$$

We estimated the contribution of BCG stellar mass to the free-fall time using the Cooke et al. (2016) stellar mass estimates of CLASH BCGs. We did not estimate BCG stellar masses with our SED fits since our photometry does

not cover the entire extent of the BCG. Stellar mass density profiles were estimated from the stellar mass of each BCG assuming a Hernquist (1990) profile and the Shen et al. (2003) mass-size relationship (Ruszkowski & Springel, 2009; Laporte et al., 2013). The inclusion of stellar mass in our estimates of $M_{enc}\,(r)$ does not significantly affect the freefall time profiles at radii $\gtrsim 25$ kpc (or similarly $\gtrsim 0.025R_{500}$), which is not surprising given that BCG stellar mass dominates the cluster density profile only within the central ~ 10 kpc of a cluster (Newman et al., 2013; Monna et al., 2017; Caminha et al., 2017). Still, we include the BCG stellar mass in our estimation of the free-fall time profiles and find that the BCG stellar masses alter the free fall times by $\lesssim 4\%$ at ~ 10 kpc and $\lesssim 1\%$ at ~ 20 kpc.

Comparing the characteristics of BCG starbursts to ICM thermodynamic parameters requires choosing a radius in the ICM profile at which to measure these parameters. We measure ICM parameters at $0.025R_{500}$ (~ 25 kpc in most cases), which is the smallest fraction of R_{500} that does not require extrapolation of the X-ray profiles for the 11 CLASH clusters studied. We chose this radius since we expect feedback effects to be strongest near the centers of cool cores, and negligible outside the core. At radii outside the cool core the thermodynamical state of the ICM is only weakly tied to feedback and cooling, and therefore should be weakly related to the BCG (Cowie et al., 1983; Hu et al., 1985).

We also base our expectation of the radial dependence between the properties of the ICM and feedback on BCG simulations in Li et al. (2015). At large radii ($\gtrsim 100$ kpc), the variation in t_{cool}/t_{ff} with time in the simulation (and with the level of star formation and AGN-driven feedback) is weak, so a relationship between SFR and cluster dynamical state would be difficult to detect (see their Figure 9). On the other hand, t_{cool}/t_{ff} varies wildly at small radii ($\lesssim 10$ kpc), so in this case too, relationships involving t_{cool}/t_{ff} and other parameters related to cooling and feedback in the cluster would be difficult to interpret (although the variation in simulations may be due to the idealized AGN entering periods of complete quiescence as the fuel supply reaches zero). However, since $0.025R_{500}$ is greater than 10 kpc for all the CLASH clusters, even if this effect is physically realistic we would not expect to observe it.

3.4 Results

Table 3.3 lists our estimates for the best-fit SFR, the duration of the exponentially decaying starburst Δt_b, and dust mass M_d for each active BCG, expressed as the mean of the marginalized posterior probability distribution with uncertainties given as the 68.3% confidence interval. We also list the best-fit intrinsic optical attenuation, $A_{\rm V}$. The SFRs in the CLASH BCGs span the range from ~ 0.5 M$_\odot$ yr^{-1} to ~ 250 M$_\odot$ yr^{-1}. The BCGs have dust masses

ranging from 10^7 $M_\odot$ in the case of RXJ2129.7+0005 to 10^9 $M_\odot$ in the case of MACS1931.8-2653. Our multiband photometry and the corresponding best fit SEDs for each star forming CLASH BCG are shown in the appendix of this chapter in Figure 3.16.

Burst durations (Δt_b) range from $\lesssim 100$ Myr to several Gyr with very large uncertainties for any given galaxy. Estimating the posterior probability distribution of Δt_b is more complicated than estimating the distribution of the SFR or M_d, owing to the strong dependence of Δt_b on FBURST, the ratio of the stellar mass of the burst population to the stellar mass of the old population in the apertures we use. We find the mean Spearman correlation coefficient between Δt_b and FBURST is $R_S = 0.72$ (see Figure 3.13 in the Appendix).

Since the uncertainties on Δt_b are large and the probability distribution of Δt_b is highly correlated with FBURST, we can increase the precision of our Δt_b estimates by imposing physically motivated constraints on FBURST. We do this by using literature estimates of the fraction of stellar mass contributed to BCGs by star formation at a redshift < 1 as the range of plausible burst mass percentages (referring back to Table 3.2, the percentage of stellar mass due to the starburst in our models is FBURST/(1 + FBURST)). This range is on the order of $1\% - 10\%$ (e.g. McIntosh et al., 2008; Inagaki et al., 2015; Cooke et al., in prep.). By restricting the burst mass percentage (and therefore FBURST) to a single order of magnitude, we reduce the uncertainty in our estimates of Δt_b

by slightly more than a factor of 1.5, and can provide estimates of the best-fit Δt_b in some cases where we otherwise report lower limits.

Restricting FBURST for each SED is slightly complicated by the fact that we measure our SEDs in apertures that do not cover the entire surface area of the BCG. While the range of burst mass percentages we cite above correspond to $M_{\rm burst}/M_{\rm BCG}$, the stellar mass contributed by the starburst over the stellar mass of the BCG, the burst mass percentage in our SED models is $M_{\rm burst}/M_{\rm aperture}$, the stellar mass contributed by the starburst over the stellar mass in the aperture. However,

$$\frac{M_{\rm burst}}{M_{\rm aperture}} = \left(\frac{M_{\rm burst}}{M_{\rm BCG}}\right) \times \left(\frac{L_{F160,\rm BCG}}{L_{F160,\rm aperture}}\right), \tag{3.5}$$

where we assume that the F160W near-IR luminosity, L_{F160}, is a reasonable proxy for stellar mass. We measured $L_{F160,\rm BCG}/L_{F160,\rm aperture}$ using the 2D image model of the BCG from the isophotal fitting procedure described in § 2.3.2 in Lauer et al. (2014). The 2D image models are free of contamination by light from surrounding galaxies. By multiplying the $1\%-10\%$ burst mass percentage range by $L_{F160,\rm BCG}/L_{F160,\rm aperture}$ for each BCG, we were able to find appropriate ranges of $M_{\rm burst}/M_{\rm aperture}$, and therefore FBURST, for each SED. For example, $L_{F160,\rm BCG}/L_{F160,\rm aperture}$ is $\sim 2.5-2.7$ in the case of RXJ1532.9+3021, implying that $2.5\% \lesssim M_{\rm burst}/M_{\rm aperture} \lesssim 25\%$. This implies a range of FBURST of 0.025-0.4. Since MACS1931.8-2635 does not have a 2D image model available, we used the same range for FBURST, but otherwise calculated the restricted range

of FBURST for each BCG individually.

The best fit values for Δt_b assuming restricted ranges of FBURST are reported in Table 3.3. By restricting the range of FBURST to values that correspond to modest contributions to the BCG stellar mass from recent star formation, we produce a more precise set of Δt_b results compared to fits with no restrictions on FBURST. We adopt these values in the rest of our analysis.

The trends we report below between quantities measured with SED fits are not caused by correlations in the posterior probability distributions of individual fits. The posterior probability distributions of SFR, Δt_b, and M_d for individual BCGs are either uncorrelated or only weakly correlated. We report Spearman correlation coefficients in Table 3.3 and two-dimensional posterior probability distributions in Figure 3.12 in the Appendix. Across the sample of CLASH BCGs, the posterior probability distributions of SFR and M_d are the most correlated, but only with a mean Spearman correlation coefficient of 0.19, while M_d and Δt_b are the least correlated, with a mean Spearman correlation coefficient of 0.01.

Our modified version of `iSEDfit` produces fits with a mean χ^2_ν of 0.93, and a range between $\chi^2_\nu = 0.57$ and $\chi^2_\nu = 1.63$. The χ^2_ν statistic for the best fitting model in the grid for each BCG is listed in Table 3.4. Table 3.4 lists χ^2_ν values we obtain for each dust attenuation law we try using, coupled with a Salpeter (1955) IMF, and the values we obtain using a Calzetti et al. (2000) attenuation

law coupled with a Chabrier (2003) IMF. The choice of the adopted attenuation law and IMF can affect the quality of the fits to each individual SED but does not affect the average χ^2_ν for the full sample nor does it affect our qualitative conclusions. When the Calzetti et al. (2000) attenuation law is replaced by Witt & Gordon (2000) clumpy SMC attenuation, the mean χ^2_ν increases by 16% to 1.08; when we use a modified Calzetti et al. (2000) law instead the mean is 1.10.

The best-fit stellar and dust parameters are similarly minimally affected by choice of attenuation law. Adopting a Chabrier (2003) IMF systematically shifts the SFRs ~ 0.25 dex downwards but does not otherwise significantly alter the probability distributions or correlations between parameters, and does not strongly affect values of χ^2_ν. The fits using the Chabrier IMF have a mean χ^2_ν of 0.98, and any offsets in SED fit parameters are comparable to, or smaller than, our reported uncertainties. We report the parameters obtained for each model used in the appendix, but in our analyses of the results we only discuss the SED fits obtained using the Calzetti et al. (2000) law and Salpeter (1955) IMF, unless otherwise noted.

3.4.1 The Starburst - ICM Connection

For BCGs with detectable star-formation activity, we find a tight correlation between the BCG SFR and the ratio t_{cool}/t_{ff} measured at $0.025R_{500}$. The trend

Table 3.3 BCG Stellar and Dust Parameters

BCG	$\log_{10}$ SFR ($M_\odot$ yr^{-1})	$\log_{10}\Delta t_b$ (Gyr)	$\log_{10}\Delta t_b$ restr. FBURST[b] (Gyr)	$\log_{10} M_d$ ($M_\odot$)	A_V (mag)	R_S[a] SFR$\times\Delta t_b$	R_S SFR$\times M_d$	R_S $M_d\times\Delta t_b$
Abell 383	$0.18^{+0.24}_{-0.25}$	> -0.49[d]	$0.19^{+0.35}_{-0.34}$	$7.47^{+0.84}_{-0.87}$	$0.48^{+0.22}_{-0.24}$	-0.16	0.36	-0.03
MACS0329.7-0211	$1.6^{+0.18}_{-0.2}$	> -0.73	$0.01^{+0.37}_{-0.40}$	$8.4^{+0.71}_{-0.73}$	$0.56^{+0.18}_{-0.19}$	-0.06	0.07	0.07
MACS0429.6-0253	$1.53^{+0.23}_{-0.24}$	> -0.36	$0.09^{+0.36}_{-0.37}$	$8.49^{+0.7}_{-0.68}$	$0.75^{+0.23}_{-0.24}$	0.03	0.20	0.07
MACS1115.9+0219	$0.85^{+0.29}_{-0.28}$	> -0.40	$0.19^{+0.35}_{-0.36}$	$7.6^{+0.85}_{-0.81}$	$0.44^{+0.3}_{-0.3}$	-0.03	0.44	-0.01
MACS1423.8+2404	$1.41^{+0.18}_{-0.18}$	> -0.65	> -0.03	$8.47^{+0.69}_{-0.72}$	$0.42^{+0.18}_{-0.18}$	-0.11	0.25	0.02
MACS1720.3+3536	$0.19^{+0.27}_{-0.26}$	> -0.34	> -0.01	$7.6^{+0.67}_{-0.71}$	$0.6^{+0.26}_{-0.26}$	-0.10	0.10	-0.0
MACS1931.8-2653	$2.42^{+0.22}_{-0.18}$	$-0.97^{+0.53}_{-0.56}$	$-1.01^{+0.34}_{-0.35}$	$8.88^{+0.39}_{-0.4}$	$0.87^{+0.21}_{-0.21}$	-0.52	-0.23	0.19
MS2137-2353	$0.25^{+0.29}_{-0.29}$	> -0.43	> 0.08	$7.41^{+0.86}_{-0.87}$	$0.43^{+0.31}_{-0.31}$	-0.23	0.47	-0.21
RXJ1347.5-1145	$1.07^{+0.23}_{-0.23}$	> -0.39	$0.13^{+0.36}_{-0.35}$	$7.76^{+0.96}_{-0.9}$	$0.31^{+0.22}_{-0.23}$	0.03	0.47	-0.10
RXJ1532.9+3021	$1.99^{+0.2}_{-0.19}$	$-0.29^{+0.54}_{-0.59}$	$-0.39^{+0.38}_{-0.41}$	$8.77^{+0.47}_{-0.51}$	$0.9^{+0.19}_{-0.19}$	-0.40	-0.16	0.11
RXJ2129.7+0005	$-0.5^{+0.22}_{-0.23}$	$0.29^{+0.28}_{-0.31}$	> 0.25	$6.81^{+0.87}_{-0.71}$	$0.28^{+0.14}_{-0.17}$	-0.19	0.12	0.01

[a] Spearman correlation coefficients for the sample of pairs of parameters obtained by sampling the posterior probability distribution of models. The Spearman correlation coefficient measures the rank correlation of two datasets, and is between -1 (a perfect negative correlation) and 1 (a perfect positive correlation).
[b] Results obtained for Δt_b when the fractional burst strength, FBURST, is restricted to the range [0.025, 0.4] and the SED fit is re-run.
[c] Uncertainties denote the 1σ credible intervals for each value.
[d] For $\log_{10}\Delta t_b$ posterior probability histograms that peak near the upper bound of the parameter space (5 Gyr), we report the 1σ confidence interval as a lower limit on $\log_{10}\Delta t_b$.

Table 3.4 Best Fit χ^2 Values

BCG	Calzetti χ^2_ν	Modified Calzetti χ^2_ν	Witt Clumpy SMC χ^2_ν	Chabrier IMF χ^2_ν
Abell 383	0.99	1.33	1.54	1.41
MACS0329.7−0211	0.57	0.76	0.60	0.64
MACS0429.6−0253	1.53	1.53	2.25	1.39
MACS1115.9+0219	0.59	0.53	0.46	0.52
MACS1423.8+2404	0.80	1.44	1.24	0.80
MACS1720.3+3536	1.41	1.48	1.02	1.31
MACS1931.8−2653	0.66	1.39	1.22	1.17
MS2137−2353	0.64	0.70	0.68	0.67
RXJ1347.5−1145	0.72	0.72	0.66	0.78
RXJ1532.9+3021	1.63	1.51	1.28	1.40
RXJ2129.7+0005	0.70	0.73	0.79	0.73

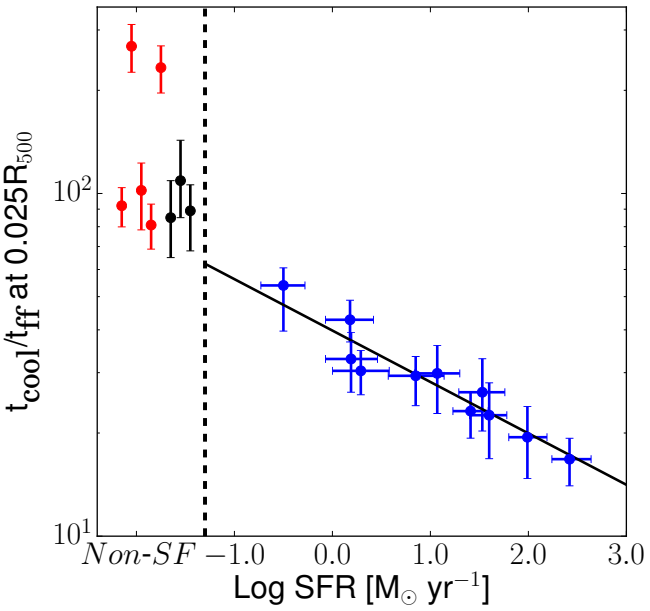

Figure 3.4 The t_{cool}/t_{ff} ratio is shown as a function of Log_{10} SFR. Values of the ratio t_{cool}/t_{ff} were measured at a radius of $0.025R_{500}$ for each cluster. The blue data points are the measured values from the active BCG sample. The solid black line depicts the best-fit straight line to the data in log-log space. Values of t_{cool}/t_{ff} at $0.025R_{500}$ for CLASH clusters with non-starforming BCGs are shown to the left of the vertical dashed line. The black points show clusters where t_{cool}/t_{ff} values were obtained using X-ray profiles from Donahue et al. (2014), while the red points were obtained using temperature and density profiles from Cavagnolo et al. (2009) and assuming a metallicity of 0.3 $Z_\odot$. Uncertainties for the SFR is taken to be the 68.3% confidence interval for the marginal posterior probability distribution, which for a Gaussian distribution is equal to the 1σ uncertainty. For t_{cool}/t_{ff}, the 1σ uncertainties are shown.

and the data are shown in Figure 3.4. The best fit line between these two parameters is

$$\log_{10} \frac{t_{cool}}{t_{ff}} = (1.6 \pm 0.4) - (0.15 \pm 0.03) \log_{10} \frac{\mathrm{SFR}}{\mathrm{M_\odot\ yr^{-1}}}, \tag{3.6}$$

and is shown as the black curve in Figure 3.4. The data are fit by this trend with no detectable intrinsic scatter ($\sigma_i < 0.15$ dex at 3σ). We estimated the best fit lines and intrinsic scatters using the least squares method in Hogg et al. (2010) for fitting data with uncertainties in two dimensions and intrinsic scatter. The data have a Spearman correlation coefficient $R_S = -0.98$ and a Pearson correlation coefficient $R = -0.95$.

We estimated both the strength of the relationship we observe, and the strength of the claim that the relationship has little intrinsic scatter. We first investigated the possibility that there is no relationship between SFR and t_{cool}/t_{ff}, by calculating the marginal probability distribution of the slope using Equation 35 of Hogg et al. (2010), and find that the slope of the relationship is less than 0 at 99.993% confidence.

We then examined the possibility that a relationship obeying the trend in Equation 3.6 but with a large intrinsic scatter produced the results we observe. We created an ensemble with 10^4 synthetic datasets, consisting of 11 SFR values randomly sampled in logarithmic units from 0.1 $\mathrm{M_\odot\ yr^{-1}}$ to 1000 $\mathrm{M_\odot\ yr^{-1}}$,

and calculated the corresponding predicted values of $\log_{10} t_{cool}/t_{ff}$. Assuming a given intrinsic scatter, σ_i, we generated an offset from the trend line for each of the 11 points by sampling a normal distribution of standard deviation σ_i to obtain the amplitude of the offset and determined a direction of the offset by sampling a uniform distribution between 0 and 2π. We added an additional offset for each point in the x-direction and in the y-direction by sampling normal distributions with standard deviations equal to the mean uncertainty of the observed SFRs and the observed t_{cool}/t_{ff} values, respectively. The probability that data more tightly correlated than our dataset ($\|R\| = 0.95$) would be produced given σ_i was calculated for the ensemble of datasets. Since we used log-normally distributed variables to generate our synthetic data, we used the Pearson coefficient R to measure the strength of the correlation. We repeated this procedure for σ_i ranging from 0.0 to 0.6, and found that for $\sigma_i \gtrsim 0.22$ dex, the probability of drawing a dataset with a trend tighter than the one we observe is $< 0.3\%$. The results of the above correlation test are presented in Figure 3.5.

The ratio t_{cool}/t_{ff} is thought to be a proxy for the thermal instability of ICM gas – when the gas can cool quickly relative to the time it takes for it to infall, it can more readily become thermally unstable and collapse (Gaspari et al., 2012; Li & Bryan, 2014). Assuming ICM instability increases with decreasing t_{cool}/t_{ff}, our results suggest that BCG SFRs will increase with the thermal

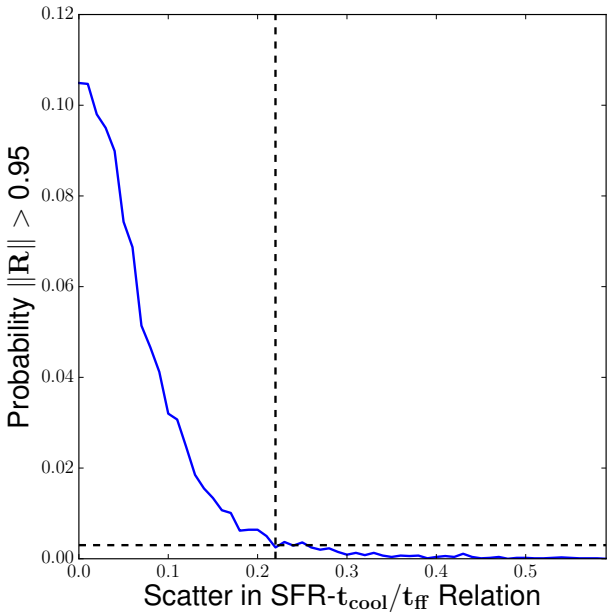

Figure 3.5 The probability of a synthetic dataset of SFR and t_{cool}/t_{ff} observations with an underlying relationship corresponding to the best-fit relationship measured for CLASH active BCGs and measured uncertainties comparable to the CLASH data set having a Pearson correlation $\|R\| > 0.95$ is shown as a function of intrinsic scatter. The horizontal dashed line denotes where the probability falls below 0.3% (corresponding to a 3σ outlier for a Gaussian process). The vertical dashed line denotes an intrinsic scatter of 0.22 dex, which is approximately where the probability curve dips below 0.3%.

instability of the surrounding ICM.

The relationship between the star formation duration Δt_b and cooling time at $0.025R_{500}$, $t_{\rm cool}$, is shown in Figure 3.6. The relationship between these two parameters is difficult to quantify owing to the large uncertainties on Δt_b. In order to estimate the strength of this correlation, we calculated the Spearman coefficients both including and excluding MACS1931.8-2653. In performing these computations, we also need to address the fact that some of the Δt_b values are only lower limits even with a restricted FBURST prior. If we use the lower limit values to compute the Δt_b ranking, then Δt_b and t_{cool} are strongly correlated, with a Spearman coefficient of 0.86 including MACS1931.8-2653, and a coefficient of 0.81 excluding it. If we assume that the lower limits in Δt_b are tied for the highest rank, then the Spearman coefficient including MACS1931.8-2653 is 0.57, implying a weak correlation ($p < 0.065$), while if MACS1931.8-2653 is excluded, the data are not significantly correlated ($R_S = 0.427$, $p < 0.22$). In the limit of the worst possible Δt_b ranking for the lower limit data (e.g., the data point with the highest ranked t_{cool} amongst the 'lower limit' points has the lowest relative Δt_b rank), the two datasets are not correlated ($R_S = 0.433$, $p < 0.18$ with MACS1931.8-2653, $R_S = 0.24$, $p < 0.50$ without). Therefore, cooling times and burst durations are likely weakly positively correlated (although this observation may be driven by MACS1931.8-2653), and Δt_b and $t_{\rm cool}$ become comparable in amplitude when Δt_b reaches Gyr timescales.

All the BCGs either lie to the left of the line where $\Delta t_b = t_{\rm cool}$ or are consistent with lying to the left of this line. This is the region where starbursts occur on timescales shorter than the timescale for the ICM to cool. In clusters where Δt_b and t_{cool} fall to the left of this line, star formation has been ongoing for a shorter duration than the time it would take for the ICM at $0.025R_{500}$ to radiatively cool. Therefore, assuming t_{cool} profiles typically increase monotonically with radius, if the cold gas reservoir fueling star formation is the result of the ICM radiatively cooling, then the body of low-cooling time gas inside $0.025R_{500}$ that was present at the onset of star formation will be depleted. Alternatively, in clusters where Δt_b and t_{cool} fall to the right of this line, either higher cooling time gas will have radiatively cooled and replenished the gas inside $0.025R_{500}$ in order to continue forming the cold gas fueling star formation, or radiative cooling has been arrested and t_{cool} is locally static.

3.4.2 Star Formation and Dust Parameters

We find that both the dust mass and burst duration of CLASH BCGs are correlated with their SFRs. The relationship between Δt_b and SFR is shown in Figure 3.7. Large SFRs are consistent with star formation episodes that have recently begun, and as the bursts persist to $\sim$ Gyr timescales, the SFRs diminish by several orders of magnitude.

Figure 3.8 shows the relationship between M_d and SFR. In order to be con-

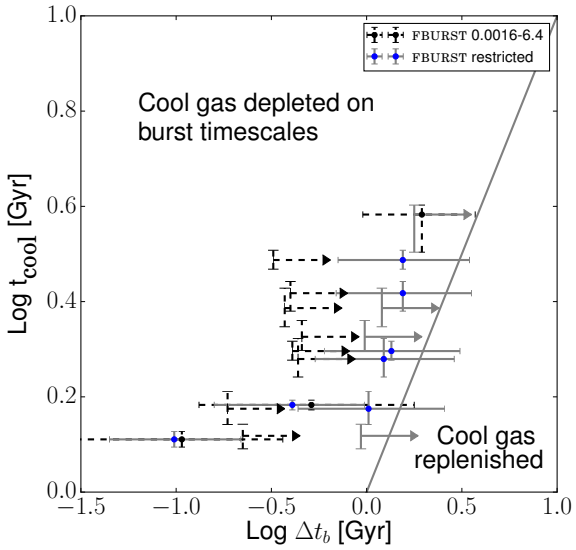

Figure 3.6 $\text{Log}_{10}\ \Delta\ \text{t}_b$ vs. $\text{Log}_{10}\ \text{t}_{\text{cool}}$ is shown. Cooling times were measured at a radius of $0.025R_{500}$ in each cluster. The solid grey line shows where $\Delta\ \text{t}_b = \text{t}_{\text{cool}}$. Blue points with grey errorbars show values of Δt_b obtained when limiting the range of FBURST according to the procedure discussed in § 4. For reference, black points with dashed black errorbars show Δt_b measured assuming $0.0016 < \text{FBURST} < 6.4$. For points in the region to the left of the line, labelled 'cool gas depleted on burst timescales', the cooling time of gas at $0.025R_{500}$ exceeds the duration of the starburst. For points in the region to the right of the line, labelled 'cool gas replenished', the duration of the starburst exceeds the cooling time of the gas at $0.025R_{500}$. Uncertainties for both parameters are defined analogous to Figure 3.4 .

sistent with studies of SFR and M_d conducted by da Cunha et al. (2010) and Hjorth et al. (2014), when comparing these two quantities we analyze SFRs and dust masses obtained with a Chabrier (2003) IMF. We continue to use Salpeter (1955) when discussing results in the rest of our paper.

Dust masses and SFRs are correlated, with a best-fit trendline of

$$\log_{10}\frac{M_d}{\mathrm{M}_\odot} = \left(7.1^{+0.4}_{-0.3}\right) + \left(0.97^{+0.34}_{0.24}\right)\log_{10}\frac{\mathrm{SFR}}{\mathrm{M}_\odot\ \mathrm{yr}^{-1}} \tag{3.7}$$

with an intrinsic scatter of < 0.83 dex (3σ limit). The analysis of da Cunha et al. (2010) derived dust masses and SFRs for field galaxies using a UV-IR SED fitting technique that was similar to ours. We overlay their best-fit trendline, which has a best-fit slope of 1.11 ± 0.01 and intercept of 7.1 ± 0.01 in Figure 3.8. In order to constrain the behavior of the trend at the large SFR end, we include the dust mass and SFR of the Phoenix Cluster BCG (e.g. McDonald et al., 2013). We adopt the Mittal et al. (2017) estimate of 454-494 $\mathrm{M}_\odot$ yr^{-1} for the Phoenix SFR and fit the far-IR SED of Phoenix to estimate M_d. This extended dataset shows a flattening slope at the high-SFR end of the relationship. When we overlay a trend drawn from Hjorth et al. (2014) that takes into account the evolution of star formation and dust for starbursting galaxies with large ($\gtrsim$ 1000 $\mathrm{M}_\odot$ yr^{-1}) SFRs, we find excellent correspondence to our data across the range of SFRs studied. While our confidence that we observe a change in the

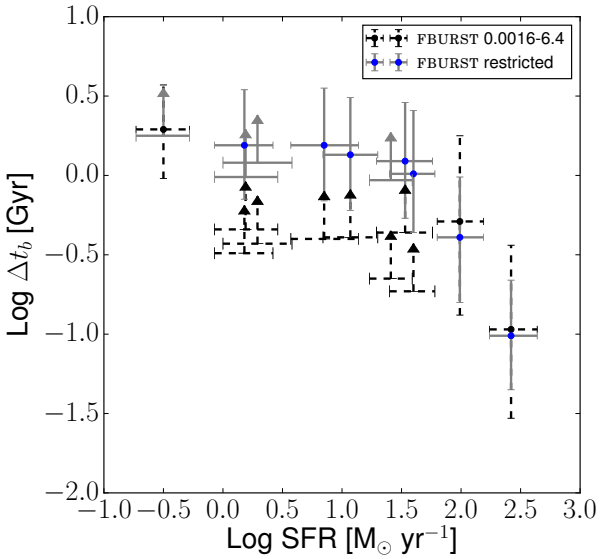

Figure 3.7 Log_{10} SFR vs. Log_{10} Δt_b is shown. Blue points with grey errorbars show values of Δt_b obtained when limiting the range of FBURST according to the procedure discussed in § 4. For reference, black points with dashed black errorbars show Δt_b measured assuming $0.0016 <$ FBURST < 6.4. Uncertainties for both parameters are taken to be the 68.3% confidence interval for their respective marginal posterior probability distributions.

SFR-M_d trend at the high SFR-end is limited by the size of our sample, our results are fully consistent with starforming BCGs producing dust reservoirs like starbursts in the field.

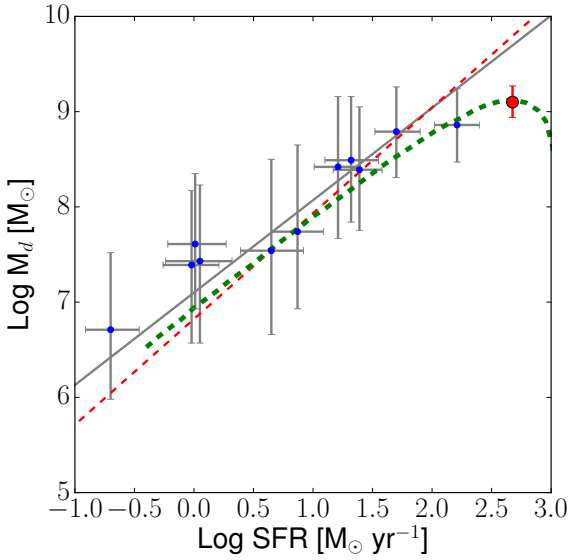

Figure 3.8 Log_{10} SFR vs. Log_{10} M_d is shown. The solid grey line depicts the best fit trend line for these parameters for the CLASH active BCG sample. The dashed red line shows the SFR-M_d relationship of da Cunha et al. (2010), which was obtained using SDSS field galaxies. The dashed green line shows the Hjorth et al. (2014) relationship. The red data point is the BCG of the Phoenix cluster. Uncertainties for both parameters are taken to be the 68.3% confidence interval.

3.4.3 Testing Impact of AGN Emission on SED Results on MACS1931.8-2653

We wish to understand the possible impact of AGN emission on our SED fitting results. Therefore, we analyzed the impact of AGN emission on the SED fit to MACS1931.8-2653, since this BCG shows the strongest evidence for AGN emission. If the AGN component has little impact on the SED fit to MACS1931.8-2653, we do not believe there will be substantial AGN contamination of our fits to the other starbursting BCGs in CLASH, which host weaker or quiescent AGN. The X-ray point source in this BCG is well-fit by an AGN power spectrum with a 2-10 keV luminosity of $5.32^{+0.40}_{-0.37} \times 10^{43}$ ergs s^{-1} cm^{-2} (Hlavacek-Larrondo et al., 2013a). Moreover, the IR template-fitting results of Santos et al. (2016) imply a substantial AGN contribution may exist in the case of MACS1931.8-2653, so it is important to investigate the effect of adding an AGN component to the model used to fit the UV-IR SED of this X-ray loud BCG.

As Santos et al. (2016) postulate a potentially large AGN contribution to the UV-IR SED of MACS1931.8-2653, we ran a separate SED fitting analysis for this BCG wherein we include the IR AGN model of Siebenmorgen et al. (2015). We allowed `iSEDfit` to sample the full range of parameters that describe the Siebenmorgen et al. (2015) AGN emission model library, which for

our purposes are nuisance parameters. The contribution of the AGN to the total UV-IR luminosity of the galaxy was allowed to range between $0.001\times$ and $10\times$ the stellar contribution.

We find that the effect of AGN emission in MACS1931.8-2653 is marginal. The best fit χ^2 degrades slightly, to 1.09, most likely owing to the addition of AGN model nuisance parameters. After incorporating AGN emission, we find the $\log_{10}$ SFR = 2.36 ± 0.19 $M_\odot$ yr^{-1}, $\log_{10}$ Δt_b = $-0.69^{+0.46}_{-0.80}$ Gyr, and that $\log_{10}$ M_d = $8.86^{+0.34}_{-0.38}$ $M_\odot$. Compared to our AGN-free model, we find the SFR changes by $\sim 0.3\sigma$, Δt_b by $\sim 0.5\sigma$, and M_d by $\sim 0.05\sigma$. This is not surprising, since the AGN contribution to the UV-FIR luminosity relative to the stellar contribution is $\log_{10}$ f_{AGN} = -1.65 ± 0.87.

One possible explanation for the discrepancy between these findings and the results published in Santos et al. (2016) for MACS1931.8-2653 is our decision not to incorporate WISE photometry in our SED fitting. WISE W3 and W4 filters cover the region of the MIR spectrum (~ 10 μm) sensitive to the contribution of AGN flux. Since for our purposes, the AGN flux is a contaminant, it does not make sense to include these filters in our SED. The difference may also be explained, in part, by the fitting technique– the theoretical modelling we employ to fit the data allows us greater flexibility to fit the data than the empirical templates used in Santos et al. (2016).

3.5 Discussion

CLASH galaxy clusters provide a data-rich sample for the study of feedback in the environments of BCGs. Just over 50% of the CLASH X-ray selected clusters host BCGs that exhibit signs of vigorous feedback and their relatively low redshifts allow us to study their properties in detail. We find a strong observational relationship between BCG star formation and the ratio t_{cool}/t_{ff}, which is a proxy for thermal instability in the ICM. As we will discuss below, this relationship appears to strongly support the AGN-regulated cooling mechanism in the condensation and precipitation model advocated in Voit et al. (2015) and Voit et al. (2017). However, several of the implications of our findings have not been anticipated by models of cooling and feedback in the ICM, and raise interesting questions about the dynamics of condensation and heating in the BCG and its environs.

3.5.1 t_{cool}/t_{ff} As A Proxy For Thermal Instability and ICM Condensation

Models of AGN-driven condensation and precipitation that involve t_{cool}/t_{ff} as a proxy for thermal instability in the ICM provide a natural foundation for interpreting our observed correlation between between t_{cool}/t_{ff} and the SFR. If t_{cool}/t_{ff} is related to the rate of molecular gas production around an active BCG,

it should be correlated with the SFR. Specifically, recent simulations show that t_{cool}/t_{ff} determines the critical overdensity at which ICM density perturbations can condense (Singh & Sharma, 2015). We hypothesize this critical overdensity, in turn, determines the mass deposition efficiency ϵ_{MD}, defined to be the mass fraction in a region of the ICM that cools into molecular gas. Assuming that density perturbations of the ICM follow a log-normal distribution in the core of the cluster, ϵ_{MD} at a radius r ought to be

$$\begin{aligned} \epsilon_{MD} &= \int_{\delta_c\left(\frac{t_{cool}}{t_{ff}}\right)}^{\infty} \frac{1}{\sqrt{2\pi}\sigma\rho} e^{-\frac{(\ln\rho)^2}{2\sigma^2}} d\rho \\ &= \frac{1}{2} Erfc\left(\frac{\ln \delta_c\left(\frac{t_{cool}}{t_{ff}}\right)}{\sqrt{2}\sigma}\right), \end{aligned} \tag{3.8}$$

where $\delta_c\left(\frac{t_{cool}}{t_{ff}}\right)$ is the critical overdensity for ICM condensation as a function of t_{cool}/t_{ff} and σ is the width of the ICM density perturbation distribution. The observed relation between SFR and t_{cool}/t_{ff} would therefore imply that SFR scales with ϵ_{MD}.

We can use the t_{cool}/t_{ff}-SFR relationship to infer properties of the relationship between t_{cool}/t_{ff} and ϵ_{MD}, and therefore constrain models of feedback-regulated cooling. As a first-order approximation, we assume that a condition close to equilibrium exists between cooling and star-formation for most of the duration of an episode of feedback-regulated cooling, so that SFR $\sim \dot{M}_{g,real}$, where $\dot{M}_{g,real}$ is the actual ICM cooling rate. By measuring $\dot{M}_g \equiv M_g/t_{cool}$ within

$0.025R_{500}$ with the X-ray parameter profiles used in this paper, we find that

$$\log_{10}\epsilon_{MD} \sim \log_{10}\mathrm{SFR} - \log_{10}\dot{M}_g = \frac{t_{cool}/t_{ff} - 10}{-17.1^{+1.9}_{-2.3}}, \tag{3.9}$$

where for the purposes of this simple model we have set $\log_{10}\epsilon_{MD} = 0.0$ when $t_{cool}/t_{ff} = 10.0$, which is a 'critical' value for mechanical feedback-triggered condensation (Voit & Donahue, 2015). In a relatively uniform sample of clusters like CLASH, where core gas masses occupy a narrow range ($\sim$0.4-1.4$\times10^{13}$ $M_\odot$), $\dot{M}_g$ does plays a relatively minor role in Equation 3.9, resulting in a tight relationship between SFR and t_{cool}/t_{ff}. While it is important to bear in mind that we have made a simple estimate of ϵ_{MD} which may not be the actual mass deposition efficiency, our analysis demonstrates how the relationship between t_{cool}/t_{ff} and star formation may be used to constrain the processes governing the cooling and condensation of gas in the ICM.

In Fogarty et al. (2015), we attempted to estimate the cooling rate of the ICM by measuring $\dot{M}_g$ for gas that was at a radius < 35 kpc or for gas that had an average t_{cool}/t_{ff} ratio below 70 [5]. We found that while reddening-corrected UV photometric SFRs scale with $\dot{M}_g$ in both cases, star formation appears to be increasingly 'inefficient' as the SFR decreases. The lowest SFRs we observed

[5]The cooling times quoted in Fogarty et al. (2015) were taken from the ACCEPT website (http://www.pa.msu.edu/astro/MC2/accept/). ACCEPT website cooling times are incorrect and need to be multiplied by a factor of 6.9/2. Values of t_{cool} were calculated using ACCEPT profiles and assuming fixed metallicity.

were $\sim 0.1 - 1\%$ of $\dot{M}_g$, while at the other extreme the two quantities were comparable. Such a trend would be expected if, as Equation 3.9 indicates, the ϵ_{MD} scales with the SFR.

3.5.1.1 The Role of t_{ff} in the SFR-t_{cool}/t_{ff} relationship

Recent work examining the critical condition for the onset of BCG activity in a cool core cluster suggests that this activity is driven by t_{cool}, not t_{cool}/t_{ff} (Hogan et al., 2017). These results may imply that we ought to observe a relationship between SFR-t_{cool}, without any significant contribution from t_{ff}. An SFR-t_{cool} relationship may be observed if the dominant driver of condensation is the AGN jet propelling low cooling time gas from lower to higher altitudes, where it can condense. Since the cooling time of the uplifted gas determines the radius where the gas becomes thermally unstable, it also determines how much work must be done by the jet to lift the gas to a radius where condensation can occur. Therefore, if the uplift of plasma is driving condensation, we expect to see a SFR-mass condensation efficiency relationship in the form of a SFR-t_{cool} relationship. Such a relationship would appear similar to an SFR-t_{cool}/t_{ff} relationship in a sample such as CLASH with a narrow range of cluster masses, since all of the clusters in CLASH have similar free-fall times in their cores.

We thus investigated the possibility that the underlying relationship we

observe in Figure 5 is primarily between SFR and t_{cool}. The range of t_{ff} at $0.025R_{500}$ in CLASH clusters with star-forming BCGs is smaller than the range of t_{cool} – while t_{ff} varies by a factor of $\sim$ 1.5 across the sample, t_{cool} varies by a factor of $\sim$ 3. Hence, the effect of t_{ff} on the relationship with SFR is modest, and our ability to distinguish between an underlying SFR-t_{cool}/t_{ff} relationship vs. a SFR-t_{cool} relationship is limited. Several lines of reasoning provide evidence for a non-negligible contribution from t_{ff}, although we cannot rule out the interpretation that the underlying relationship we observe is solely between SFR and t_{cool}.

SFR and t_{cool} are correlated as shown in Figure 3.9, with a Spearman correlation coefficient of -0.90 (and a Pearson coefficient of -0.90). We calculate an intrinsic scatter between the two quantities of $0.05^{+0.03}_{-0.01}$ dex (< 0.18 dex at 3σ). The Spearman correlation coefficient in the SFR-t_{cool}/t_{ff} and SFR-t_{cool} relationships as a function of sampling radius are presented in Figure 3.10. We do not find a substantial difference between t_{cool} and t_{cool}/t_{ff} in terms of how tightly these quantities relate to the SFR. However, the distinction between t_{cool} in the star-forming and non-starforming CLASH clusters is less clear than the distinction between t_{cool}/t_{ff} in these two populations, and t_{cool} for two clusters with non-starforming BCGs is comparable to t_{cool} in the clusters with BCGs exhibiting $0.1 - 1$ $M_\odot$ yr^{-1} of star formation (see Figure 3.9).

The situation becomes clearer when we examine the relationship between

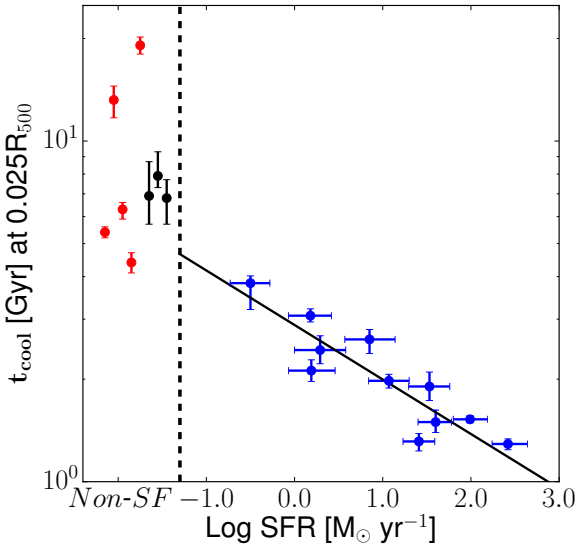

Figure 3.9 Log_{10} t_{cool} as a function of Log_{10} SFR is shown, with color-coding and uncertainties analogous to those given in Figure 3.4. Values of the ratio t_{cool} were measured at a radius of $0.025R_{500}$ for each cluster. Values of t_{cool} at $0.025R_{500}$ for CLASH clusters with non-starforming BCGs are shown to the left of the vertical dashed line.

t_{cool}, t_{ff}, and the residuals in the fits to the CLASH SFR-t_{cool}/t_{ff} and SFR-t_{cool} datasets. In Figure 3.11, we show t_{ff} vs. the residuals when we fit a log-log relationship to the SFR-t_{cool} dataset at a radius of $0.025R_{500}$ and at $0.075R_{500}$. We also show t_{ff} vs. the residuals of SFR-t_{cool}/t_{ff} at $0.025R_{500}$ and t_{cool} vs. the residuals of SFR-t_{cool}/t_{ff} at $0.025R_{500}$. We find that at $0.025R_{500}$, $t_{ff}/\langle t_{ff}\rangle$, where $\langle t_{ff}\rangle$ is the mean t_{ff} for the sample, is correlated with the residuals in the fit to the SFR-t_{cool} dataset, $\frac{t_{cool}}{Predicted\, t_{cool}}$, where $Predicted\, t_{cool}$ is t_{cool} predicted by the SFR-t_{cool} relationship for a given SFR. These two quantities are consistent with $\frac{t_{cool}}{Predicted\, t_{cool}} = t_{ff}/\langle t_{ff}\rangle$, implying that dividing t_{cool} by t_{ff} will offset the residuals in the SFR-t_{cool} relationship. The relationship between t_{ff} and $\frac{t_{cool}}{Predicted\, t_{cool}}$ at $0.025R_{500}$ has a positive slope with $\sim 98\%$ confidence. The plot in Figure 3.11 does not have obvious outliers, so the scatter reduction seen at $0.025R_{500}$ by dividing t_{cool} by t_{ff} is not attributable to reducing the residuals in an extreme outlier. There is also no evidence that t_{ff} or t_{cool} are correlated with the residuals in the other three plots we examined.

3.5.2 BCG Activity and Low Cooling Time Gas

We find a relationship between Δt_b and t_{cool} that shows a possible positive correlation between these two quantities with Δt_b approaching t_{cool} at Gyr timescales. Since Δt_b is potentially correlated with the SFR, and individual measurement uncertainties are relatively large ($\sim$0.3 – 0.4 dex) compared to

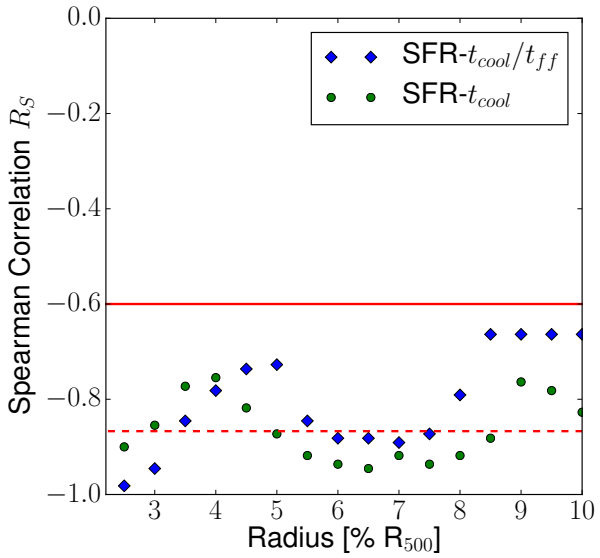

Figure 3.10 The Spearman correlation coefficient for Log_{10} SFR and Log_{10} t_{cool}/t_{ff} is shown as a function of the radius used to measure t_{cool}/t_{ff}. Correlations are measured at 5 kpc intervals, and are plotted as the blue diamonds. The solid red line denotes where the one-tailed P-value = 0.05, points below it have $P < 0.05$. Points below the dashed red line have $P < 0.0025$.

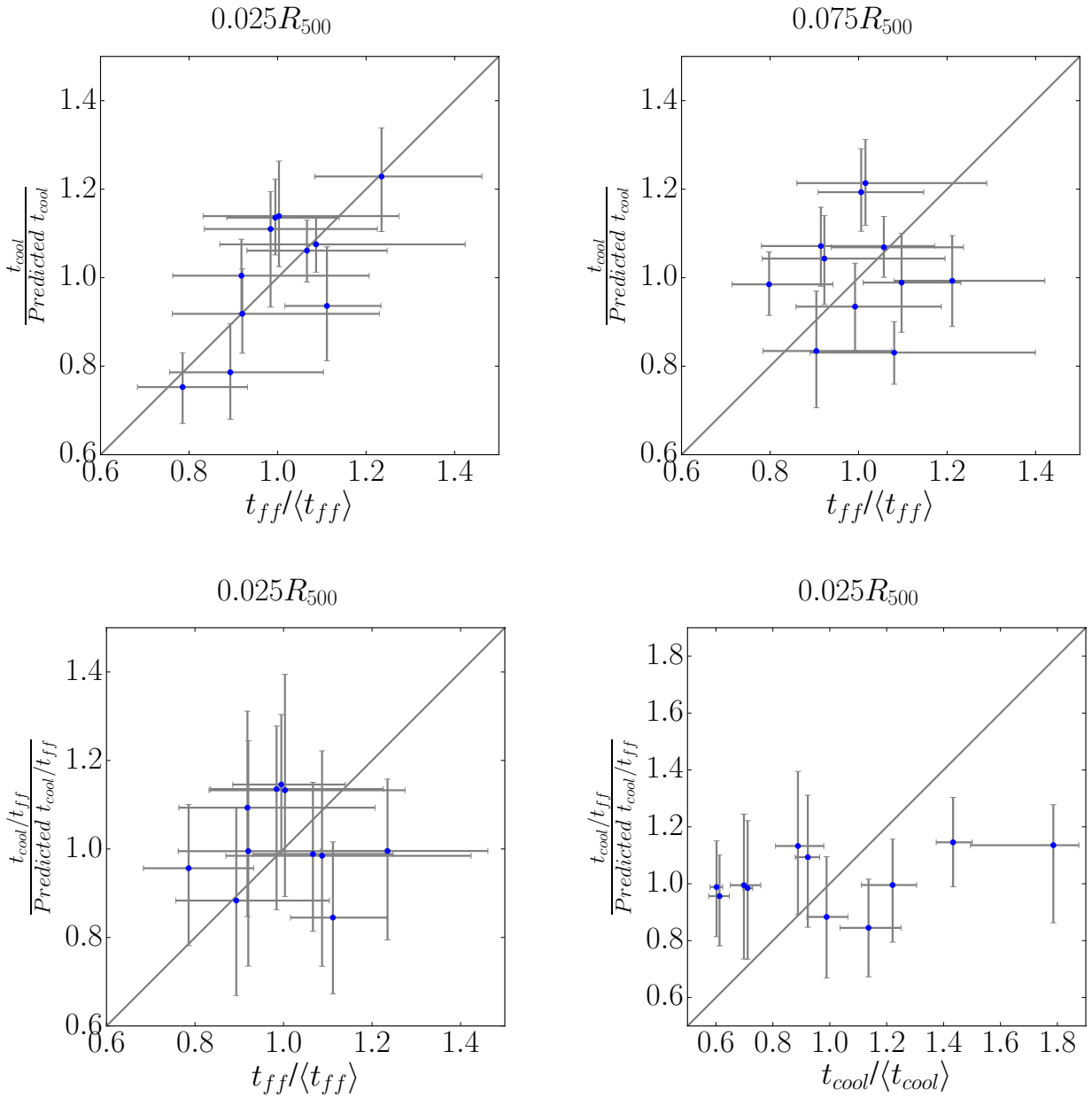

Figure 3.11 Plots showing best fit residuals vs t_{ff} and t_{cool}. The top row shows t_{ff} vs. the residuals for t_{cool}-SFR at $0.025R_{500}$ and $0.075R_{500}$. The bottom row shows t_{ff} vs. the residuals for t_{cool}/t_{ff}-SFR and t_{cool} vs. the residuals for t_{cool}/t_{ff}-SFR, both at $0.025R_{500}$. The x-axis values are normalized by the mean values of these quantities for the CLASH star forming sample. In each case, the grey line denotes where the plotted quantities are equal.

the range of Δt_b values measured in the sample (1.5 dex), the observed relationship has limited power to constrain models of cluster-scale feedback evolution. However, our measurements of the starburst durations have implications for understanding how AGN-regulated feedback progresses over time.

Four of the 11 BCG starburst durations are reported as lower limits. These BCGs may be undergoing continuous star formation. However, given the association between longer Δt_b and lower SFR, and shorter Δt_b and higher SFR, we suspect that star formation in these BCGs is slowly decaying. Alternatively, BCGs undergoing feedback may initially exhibit large starbursts before settling down to a relatively steady state with anywhere between $\sim$ 1-10 $M_\odot$ yr^{-1} of star formation. Star formation may also 'flicker' on timescales that are short relative to the values of Δt_b we measure.

Along with recent spectroscopic observations in the far-UV, the long burst durations we observe suggest that star formation and the thermodynamical state of the ICM in the cool-core is temporally decoupled from the gas condensation rate fueling AGN feedback, which may feature irregular spikes and dips over time. Recent observations of RXJ1532.9+3021 with Cosmic Origins Spectrograph (COS) (Green et al., 2012) reveal that star formation in this BCG exceeds the upper limit on gas cooling measured by N V and O VI by a factor of $\sim$10, suggesting the initial build up of molecular gas in this system has run its course (Donahue et al., 2016). Meanwhile similar spectroscopy in Abell

1795 and the Phoenix cluster reveal that gas cooling outstrips the SFR (McDonald et al., 2014a, 2015). Delayed consumption of molecular gas may allow the star formation history of BCGs to 'smooth over' these intermittent spikes. Slowly decaying BCG starbursts may also trace a transition from an initial mode of rapid condensation (with $\sim$100-1000 $M_{\odot}$ yr^{-1} of gas condensing) to a long-duration mode of more modest condensation (with $\sim$1-10 $M_{\odot}$ yr^{-1} of condensation). If star formation lags behind cooling in making this transition, the resulting observables would be consistent both with our results and the offset between SFRs and cooling rates seen in Molendi et al. (2016) and Donahue et al. (2016).

A positive correlation between Δt_b and t_{cool} and the existence of long-lived (> 1 Gyr) starbursts are consistent with the mass condensation efficiency interpretation of the t_{cool}/t_{ff}-SFR scaling relationship discussed in Section 3.5.1. Assuming that the duration of the BCG starburst is a proxy for the duration of AGN feedback, then longer periods of star formation in a BCG imply more energy injection into the surrounding ICM, which in turn raises the cooling time of the surrounding ICM. This in turn diminishes the rate at which molecular gas condenses, and gradually shuts off both the starburst and feedback. The duration Δt_b and t_{cool} ought to converge in the limit of a long starburst, although feedback mechanisms could run out of fuel and shut down before the two quantities converge depending on how inefficiently mass condenses out of

the ICM. Alternatively, a quasi-steady state may be reached with effectively continuous star formation in the BCG coupled with ICM plasma with t_{cool} of a few Gyr being replenished by hotter gas at about the same rate it condenses. In this case, star formation and feedback may decay very slowly, or not at all. Our results do not rule this latter scenario out, leaving the following possible options: (1) BCG activity is cyclical, (2) BCG activity approaches a slowly decaying quasi-steady state, or (3) BCG activity is cyclical but the duty cycle is comparable to the age of the cool core of the cluster.

Finally, it has been noted that there are few examples of BCGs with post-starburst spectra in most BCG samples (Liu et al., 2012a; Loubser et al., 2016). Indeed, none of the SOAR or SDSS spectra of CLASH BCGs in Fogarty et al. (2015) show post–starburst features. The lack of post-starburst BCGs is consistent with our estimates of $\sim$ Gyr duration episodes of star formation. Wild et al. (2009) notes that for a galaxy with an exponentially decaying starburst to feature a post-starburst spectrum, the burst's decay timescale would have to be $\lesssim 0.1$ Gyr and the burst would have to account for at least 5-10$\%$ of the galaxy's stellar mass. Given the nature of long-duration star formation in our observations and models of feedback-regulated cooling, we would not expect to see a substantial population of post-starburst BCGs.

3.5.3 Characteristics of Large Starbursts in BCGs

Large BCG starbursts (with SFRs $\gtrsim 100$ $M_\odot$ yr^{-1}) may differ from their more modest counterparts in several ways. Firstly, the SFRs and dust masses in the CLASH BCGs are consistent with using Hjorth et al. (2014) to describe the relationship between BCG star formation and dust mass. Specifically, MACS1931.8-2653 and the Phoenix cluster match the flattening slope and eventual turnover in the Hjorth et al. (2014) relation closely, raising the possibility that these BCGs harbor starbursts similar to the starbursts in the submillimeter-detected population of galaxies studied by Hjorth et al. (2014). The Hjorth et al. sample extends the study of dust and star formation conducted in da Cunha et al. (2010) to cover starbursts to galaxies forming stars at $\gtrsim 1000$ $M_\odot$ yr^{-1}. Since the largest BCG starbursts in the CLASH sample also began forming stars more recently we hypothesize that, like these massive field galaxy starbursts, BCGs with large star formation rates are either forming or building up their dust reservoirs.

Secondly, both MACS1931.8-2653 and RXJ1532.9 +3021 boast prodigious SFRs and distinctive X-ray cavities. Furthermore, MACS1931.8-2653 exhibits an X-ray loud AGN, a feature which is not obvious in the other CLASH clusters. These features are noteworthy because the starbursts in RXJ1532.9+3021 and MACS1931.8-2653 are the youngest in our sample at $\log_{10} \Delta t_b = -0.39^{+0.38}_{-0.41}$ and $-1.01^{+0.35}_{-0.34}$ Gyr, respectively. Our findings suggest that stronger X-ray fea-

tures may be associated with younger, larger BCG starbursts, such as the extreme example of BCG star formation present in the Phoenix Cluster (McDonald et al., 2012, 2013, 2014b).

3.6 Conclusions

We use multi-wavelength observations from *HST, Spitzer* and *Herschel* to derive SFRs, starburst durations and dust masses from fitting the SEDs of the 11 CLASH BCGs with extended UV and nebular line emission features. The SFRs and dust masses span nearly three orders of magnitude, with SFRs ranging from $\sim$0.3 to $\sim$ 250 $M_{\odot}$ yr^{-1}, and dust masses ranging from $\sim 10^6$ to $\sim 10^9$ $M_{\odot}$. BCG starbursts are $\lesssim$ 100 Myr to several Gyr old.

We find compelling evidence for a direct link between the thermodynamic state of the ICM and BCG star formation. Specifically, we observe a tight SFR-t_{cool}/t_{ff} relationship and a relationship with an intrinsic scatter $\sigma_i < 0.15$ dex and a slope of -0.15 ± 0.03. These results strongly suggest that thermally unstable ICM plasma with a low cooling time is the source of material that forms the reservoir of cool gas fueling star formation in the CLASH BCGs and that BCG star formation and feedback either exhausts the supply of this material on Gyr timescales or settles into a state with relatively modest ($\sim 1 - 10$ $M_{\odot}$ yr^{-1}) continuous star formation.

Even if the trend we observe between SFR and t_{cool}/t_{ff} is due to an underlying trend between SFR and t_{cool} we would still find the AGN-driven condensation and precipitation model to provide a compelling explanation. However, since we find a $\sim 2\sigma$ detection of a correlation between t_{ff} and the residuals from the best-fit line SFR-t_{cool} relationship, we suspect that t_{ff} plays a role in the physics governing the relationship between SFR and the ICM. With larger datasets spanning a larger range of t_{ff} that include both measurements of t_{cool} and t_{ff}, it will be possible to constrain the role of t_{ff} in cluster core dynamics with greater confidence.

While our results are not a direct observation of feedback-induced condensation, the condensation model provides predictions that are consistent with our observations and provides a framework for understanding why the star formation rate in BCGs would scale with t_{cool}/t_{ff}. If t_{cool}/t_{ff} scales with the critical density for ICM perturbation collapse, t_{cool}/t_{ff} measures the efficiency of condensation, and our findings can be interpreted as a relationship between SFR and the condensation efficiency of the ICM.

Our study also raises several questions about the life-cycle of cooling and feedback. We present evidence that star formation episodes in BCGs with larger SFRs are younger relative to BCGs with more modest SFRs, suggesting that BCG starbursts decay over time. We also present evidence that BCG star formation can persist over $\gtrsim$ Gyr timescales. However, it is not clear whether

the starbursts in BCGs are cyclical, or slowly decaying single events that may eventually settle into a low level of persistent star formation. It is also possible we are observing the superposition of several shorter-lived events.

The dust and star formation in BCGs is consistent with the SFR-M_d relationship described in Hjorth et al. (2014). This consistency holds even when we include the SFR and dust mass measured for the Phoenix cluster BCG, which forms stars at a rate of ~ 500 $M_\odot$ yr^{-1}. Our results lead us to hypothesize that, while uncommon in BCGs, large starbursts like those in MACS1931.8-2635 and the Phoenix cluster may have properties in common with young, violent starbursts in field galaxies.

Our work shows a direct link between the amount of star formation occurring in a BCG and the thermodynamical state of the surrounding ICM. The quality of the data we used in combination with the sample selected allowed us to study specifically the interaction between BCG and the ICM in a uniformly-selected sample of cool-core clusters. These clusters and their BCGs have properties that are consistent with a process of cooling and feedback and the results presented herein bring us closer to a complete understanding of feedback in galaxy clusters. A clear extension of this study would be to examine how the BCG-ICM relationships evolve with redshift and cluster mass by analyzing additional deep, multi-wavelength galaxy cluster surveys.

Acknowledgments

We acknowledge insightful discussions with Mark Voit and Anton Koekemoer that helped enhance our interpretation of the observations. We thank Michael McDonald for providing the infrared SED of the Phoenix Cluster BCG. We also thank the anonymous referee for insightful comments that significantly improved the quality of this paper. This research is supported, in part, by NASA grants HSTGO-12065.01-A and HSTGO-13367. The CLASH Multi-Cycle Treasury Program is based on observations made with the NASA/ESA *Hubble Space Telescope* and which is operated by the Space Telescope Science Institute. This work is also based, in part, on observations made with the *Spitzer Space Telescope* and the *Herschel Space Observatory*. The *Spitzer Space Telescope* is operated by the Jet Propulsion Laboratory, California Institute of Technology under a contract with NASA. *Herschel* is an ESA space observatory with science instruments provided by European-led Principal Investigator consortia and with important participation from NASA.

3.7 Appendix

In this appendix, we explore the impact of the choice of stellar initial mass function and of the dust models. The attenuation law can significantly affect both the shape of the UV-through-optical of our synthetic SEDs and the nor-

malization of the dust emission component of the SEDs. Hence, understanding if there are significant changes to the derived stellar population properties is essential in assessing the robustness of our work. We also examine the posterior probability distributions for SFR, Δt_b and M_d obtained with `iSEDfit`.

We specifically investigate the sensitivity of our results when we adopt a modified Calzetti et al. (2000) law (Table 3.6) or a Witt & Gordon (2000) clumpy SMC-like dust in a shell geometry (Table 3.7). Tables of SED fitting results analogous to Table 3.3 are presented assuming a modified Calzetti attenuation law (Table 3.6) and clumpy SMC-like attenuation (Table 3.7). The values of SFR, Δt_b and M_d we report vary little between both attenuation models and the attenuation model assumed in the main paper. The largest difference is in Δt_b between the Witt & Gordon (2000) model and either model based on the Calzetti et al. (2000) law– burst durations fit assuming the former dust law are systematically 0.1-0.3 dex shorter. However, the differences between these sets of results are statistically insignificant, and do not qualitatively affect the interpretation of our data.

Adopting a Chabrier (2003) IMF results in a systematic shift downward in the inferred SFRs, consistent with the Chabrier (2003) IMF being about 0.25 dex lighter than the Salpeter (1955) IMF. However, like variations caused by assuming different dust attenuation models, these shifts are not statistically significant, and do not qualitatively change the trends between stellar

and ICM parameters we observe. The systematic shift in SFR is due to the fact that the mass-to-light ratio changes when changing from a Salpeter (1955) to a Chabrier (2003).

The marginal probability distributions for parameters of interest to our study (SFR, Δt_b and M_d) are depicted in Figure 3.12, and are seen to have a well-defined mode for each distribution, although there is evidence for bi-modality in some of the distributions. We show an example of marginal posteriors SFR, Δt_b, M_d, A_V, burst decay percentage, galaxy age, τ, and metallicity for Abell 383, in order to demonstrate which parameters are and are not well constrained by our fits. For five of the BCGs, the marginal distributions for Δt_b are cut off by the age of the Universe at the redshift of the galaxy cluster. In 3.14, we show the marginal posterior distributions for Δt_b when the SED fit parameter FBURST is constrained to the range [0.025, 0.4]

In summary, reasonable variations in the assumed attenuation law or in the assumed IMF do not significantly change any of the key results or conclusions in this study.

Table 3.5 BCG Stellar and Dust Parameters assuming a Chabrier IMF and Calzetti attenuation law

BCG	$\log_{10}$ SFR ($M_\odot$ yr^{-1})	$\log_{10} \Delta t_b$ (Gyr)	$\log_{10} M_d$ ($M_\odot$)	A_V (mag)	R_S[a] SFR$\times\Delta t_b$	R_S SFR$\times M_d$	R_S $M_d \times \Delta t_b$
Abell 383	$-0.02^{+0.23}_{-0.24}$	> -0.47	$7.39^{+0.78}_{-0.82}$	$0.48^{+0.22}_{-0.24}$	-0.11	0.30	0.04
MACS0329.7-0211	$1.39^{+0.19}_{-0.22}$	> -0.68	$8.39^{+0.66}_{-0.64}$	$0.53^{+0.18}_{-0.19}$	0.07	0.01	-0.07
MACS0429.6-0253	$1.32^{+0.23}_{-0.22}$	> -0.73	$8.49^{+0.67}_{-0.65}$	$0.74^{+0.24}_{-0.22}$	0.10	0.17	0.09
MACS1115.9+0219	$0.65^{+0.27}_{-0.26}$	> -0.75	$7.54^{+0.96}_{-0.88}$	$0.43^{+0.29}_{-0.29}$	-0.08	0.45	-0.04
MACS1423.8+2404	$1.21^{+0.19}_{-0.2}$	> -0.71	$8.42^{+0.74}_{-0.75}$	$0.41^{+0.17}_{-0.18}$	-0.10	0.18	0.04
MACS1720.3+3536	$0.01^{+0.26}_{-0.23}$	$0.13^{+0.4}_{-0.41}$	$7.61^{+0.74}_{-0.68}$	$0.62^{+0.26}_{-0.26}$	-0.19	0.17	-0.0
MACS1931.8-2653	$2.21^{+0.19}_{-0.19}$	$-0.93^{+0.49}_{-0.51}$	$8.86^{+0.38}_{-0.39}$	$0.88^{+0.19}_{-0.21}$	-0.43	-0.27	0.11
MS2137-2353	$0.05^{+0.27}_{-0.29}$	$0.15^{+0.4}_{-0.44}$	$7.43^{+0.8}_{-0.86}$	$0.44^{+0.32}_{-0.3}$	-0.27	0.36	-0.15
RXJ1347.5-1145	$0.87^{+0.22}_{-0.22}$	> -0.66	$7.74^{+0.91}_{-0.81}$	$0.31^{+0.23}_{-0.22}$	-0.11	0.45	0.04
RXJ1532.9+3021	$1.8^{+0.2}_{-0.18}$	$-0.2^{+0.51}_{-0.55}$	$8.79^{+0.47}_{-0.48}$	$0.91^{+0.21}_{-0.21}$	-0.34	-0.10	0.07
RXJ2129.7+0005	$-0.7^{+0.24}_{-0.21}$	> -0.01	$6.71^{+0.81}_{-0.73}$	$0.28^{+0.14}_{-0.14}$	-0.30	0.27	-0.19

[a] Spearman correlation coefficients for the sample of pairs of parameters obtained by sampling the posterior probability distribution of models.
[b] For $\log_{10} \Delta t_b$ posterior probability histograms that peak near the upper bound of the parameter space, we report the 1σ confidence interval as a lower limit on $\log_{10} \Delta t_b$.

Table 3.6 BCG Stellar and Dust Parameters assuming a modified Calzetti attenuation law

BCG	$\log_{10}$ SFR ($M_\odot$ yr^{-1})	$\log_{10}\ \Delta t_b$ (Gyr)	$\log_{10}\ M_d$ ($M_\odot$)	A_V (mag)	R_S[a] SFR$\times\Delta t_b$	R_S SFR$\times\ M_d$	R_S $M_d\times\Delta t_b$
Abell 383	$0.18^{+0.24}_{-0.26}$	>-0.54[b]	$7.41^{+0.83}_{-0.78}$	$0.47^{+0.25}_{-0.26}$	-0.13	0.35	0.05
MACS0329.7-0211	$1.6^{+0.19}_{-0.21}$	>-0.31	$8.39^{+0.72}_{-0.69}$	$0.53^{+0.19}_{-0.18}$	-0.11	0.08	0.04
MACS0429.6-0253	$1.54^{+0.24}_{-0.25}$	>-0.80	$8.5^{+0.75}_{-0.75}$	$0.76^{+0.24}_{-0.24}$	0.02	0.26	-0.01
MACS1115.9+0219	$0.85^{+0.28}_{-0.28}$	>-0.38	$7.61^{+0.87}_{-0.82}$	$0.43^{+0.28}_{-0.28}$	-0.0	0.42	0.03
MACS1423.8+2404	$1.4^{+0.21}_{-0.23}$	>-0.76	$8.37^{+0.77}_{-0.78}$	$0.42^{+0.19}_{-0.2}$	0.02	0.21	-0.02
MACS1720.3+3536	$0.19^{+0.24}_{-0.24}$	>-0.37	$7.64^{+0.68}_{-0.74}$	$0.59^{+0.23}_{-0.24}$	-0.17	0.27	-0.04
MACS1931.8-2653	$2.41^{+0.21}_{-0.19}$	$-0.95^{+0.52}_{-0.58}$	$8.89^{+0.37}_{-0.37}$	$0.85^{+0.2}_{-0.2}$	-0.53	-0.25	0.15
MS2137-2353	$0.27^{+0.3}_{-0.27}$	$0.14^{+0.44}_{-0.52}$	$7.43^{+0.75}_{-0.78}$	$0.44^{+0.33}_{-0.34}$	-0.21	0.36	0.0
RXJ1347.5-1145	$1.07^{+0.23}_{-0.21}$	$-0.11^{+0.59}_{-0.61}$	$7.71^{+0.92}_{-0.87}$	$0.31^{+0.23}_{-0.22}$	0.05	0.37	0.09
RXJ1532.9+3021	$1.99^{+0.2}_{-0.19}$	$-0.26^{+0.57}_{-0.55}$	$8.77^{+0.51}_{-0.49}$	$0.88^{+0.2}_{-0.19}$	-0.43	-0.12	0.03
RXJ2129.7+0005	$-0.53^{+0.24}_{-0.24}$	>0.06	$6.65^{+0.83}_{-0.73}$	$0.26^{+0.18}_{-0.17}$	-0.14	0.04	0.18

[a] Spearman correlation coefficients for the sample of pairs of parameters obtained by sampling the posterior probability distribution of models.
[b] For $\log_{10}\ \Delta t_b$ posterior probability histograms that peak near the upper bound of the parameter space, we report the 1σ confidence interval as a lower limit on $\log_{10}\ \Delta t_b$.

Table 3.7 BCG Stellar and Dust Parameters assuming Witt clumpy SMC-like dust in a shell geometry

BCG	$\log_{10}$ SFR ($M_\odot$ yr^{-1})	$\log_{10}\ \Delta t_b$ (Gyr)	$\log_{10}\ M_d$ ($M_\odot$)	A_V (mag)	R_S[a] SFR$\times\Delta t_b$	R_S SFR$\times\ M_d$	R_S $M_d \times \Delta t_b$
Abell 383	$0.36^{+0.25}_{-0.24}$	> -0.39	$7.6^{+0.75}_{-0.78}$	$0.9^{+0.61}_{-0.56}$	-0.23	0.27	-0.06
MACS0329.7-0211	$1.61^{+0.19}_{-0.19}$	$-0.31^{+0.74}_{-0.83}$	$8.41^{+0.7}_{-0.69}$	$0.58^{+0.39}_{-0.42}$	-0.19	-0.08	-0.01
MACS0429.6-0253	$1.57^{+0.21}_{-0.2}$	> -1.24[b]	$8.54^{+0.65}_{-0.64}$	$1.05^{+0.56}_{-0.57}$	-0.10	0.17	0.01
MACS1115.9+0219	$0.98^{+0.26}_{-0.26}$	> -1.06	$7.84^{+0.82}_{-0.81}$	$0.67^{+0.57}_{-0.52}$	-0.15	0.27	-0.04
MACS1423.8+2404	$1.51^{+0.19}_{-0.19}$	$-0.27^{+0.72}_{-0.77}$	$8.49^{+0.73}_{-0.75}$	$0.56^{+0.4}_{-0.42}$	-0.15	0.05	-0.01
MACS1720.3+3536	$0.43^{+0.26}_{-0.26}$	$-0.1^{+0.57}_{-0.62}$	$7.66^{+0.7}_{-0.71}$	$1.12^{+0.6}_{-0.62}$	-0.19	0.11	-0.01
MACS1931.8-2653	$2.36^{+0.18}_{-0.18}$	$-1.12^{+0.54}_{-0.56}$	$8.88^{+0.37}_{-0.37}$	$1.09^{+0.51}_{-0.52}$	-0.33	-0.23	0.03
MS2137-2353	$0.55^{+0.31}_{-0.31}$	$-0.07^{+0.58}_{-0.61}$	$7.66^{+0.79}_{-0.82}$	$1.01^{+0.68}_{-0.68}$	-0.21	0.31	-0.08
RXJ1347.5-1145	$1.21^{+0.19}_{-0.21}$	$-0.26^{+0.68}_{-0.76}$	$8.08^{+0.78}_{-0.78}$	$0.43^{+0.32}_{-0.33}$	-0.09	0.23	-0.04
RXJ1532.9+3021	$1.98^{+0.18}_{-0.18}$	$-0.49^{+0.67}_{-0.81}$	$8.79^{+0.5}_{-0.5}$	$1.18^{+0.46}_{-0.5}$	-0.36	-0.13	0.04
RXJ2129.7+0005	$-0.24^{+0.27}_{-0.24}$	> -0.32	$6.82^{+0.75}_{-0.71}$	$0.83^{+0.67}_{-0.62}$	-0.31	0.07	0.04

[a] Spearman correlation coefficients for the sample of pairs of parameters obtained by sampling the posterior probability distribution of models.
[b] For $\log_{10}\ \Delta t_b$ posterior probability histograms that peak near the upper bound of the parameter space, we report the 1σ confidence interval as a lower limit on $\log_{10}\ \Delta t_b$.

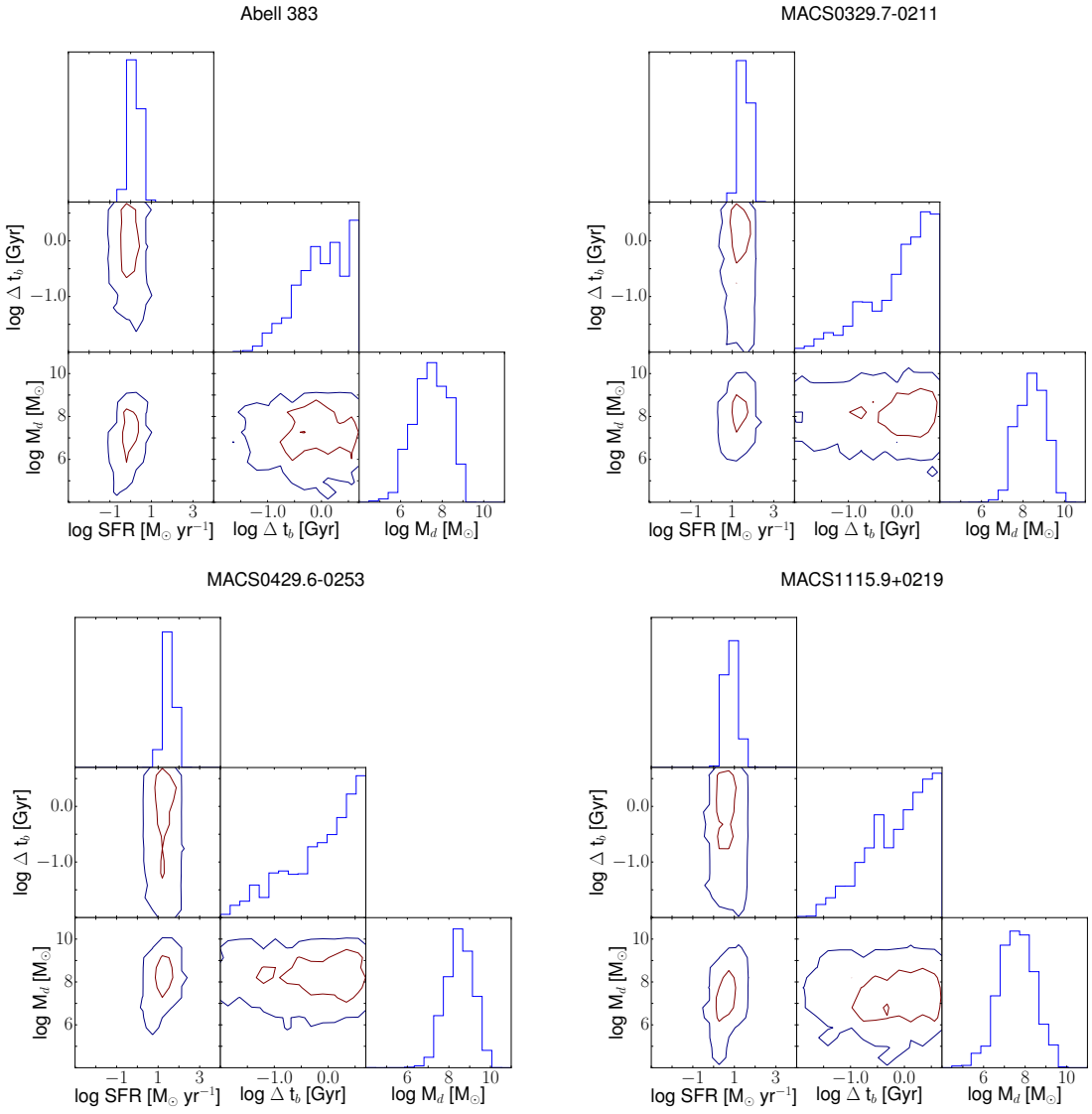

Figure 3.12 Marginal posterior probability distributions for the SFR, burst duration Δt_b, and dust mass M_d are shown for each BCG. Marginal distributions for individual parameters are obtained from the distribution of each parameter for the model SEDs sampled using `iSEDfit`, and are depicted by the histograms in the diagonal sub-plots of each figure. Two-dimensional slices of the posterior probability distribution (for SFR$\times\Delta t_b$, SFR$\times M_d$, and $M_d \times \Delta t_b$), are obtained from the distribution of pairs of parameters for each model SED, and are depicted by the contours drawn on the two-dimensional histograms in the off-diagonal sub-plots. The contours represent the 68.3% and 99.7% credible intervals, which correspond to the 1σ and 3σ contours for Gaussian distributions.

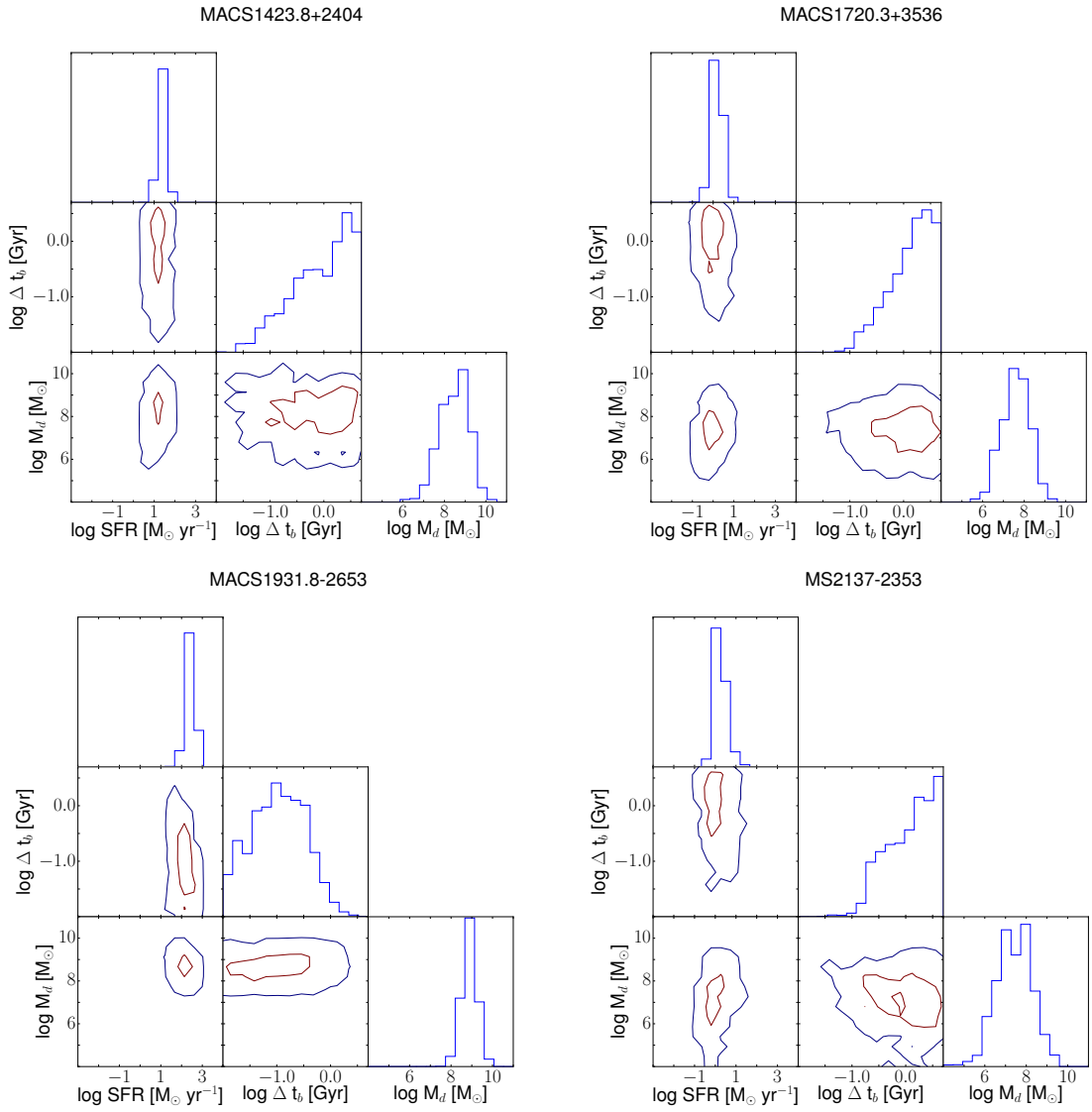

Figure 3.12 *Continued*

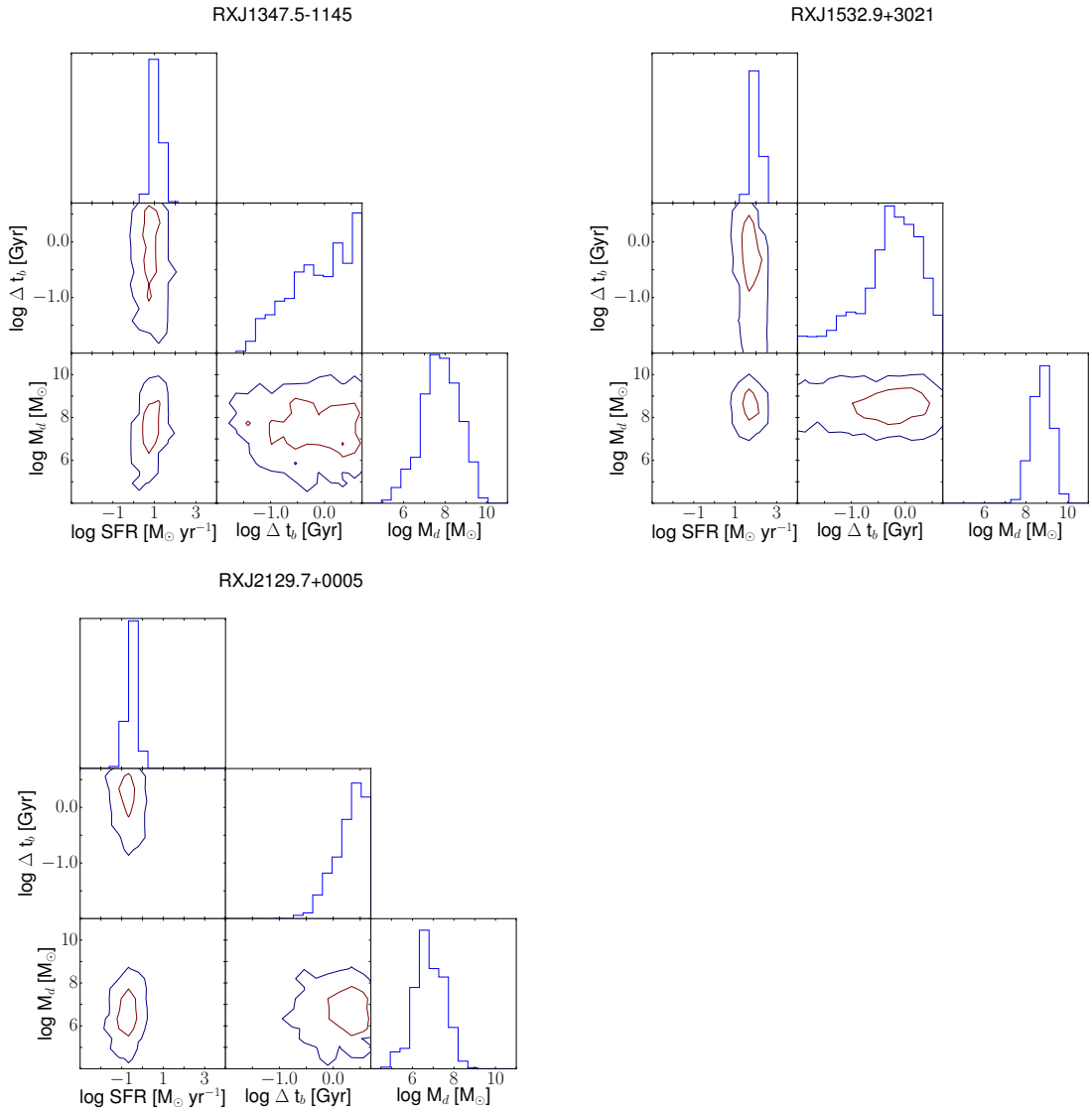

Figure 3.12 *Continued*

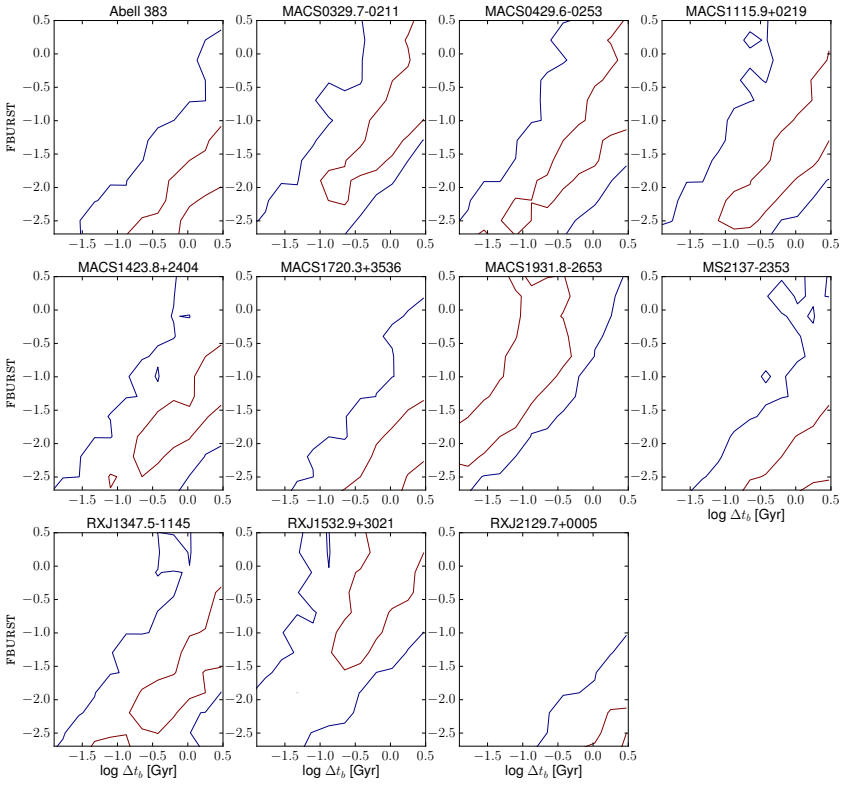

Figure 3.13 Marginal posterior probability distributions are shown for the burst duration, Δt_b, in log Gyr, and FBURST, also in log units.

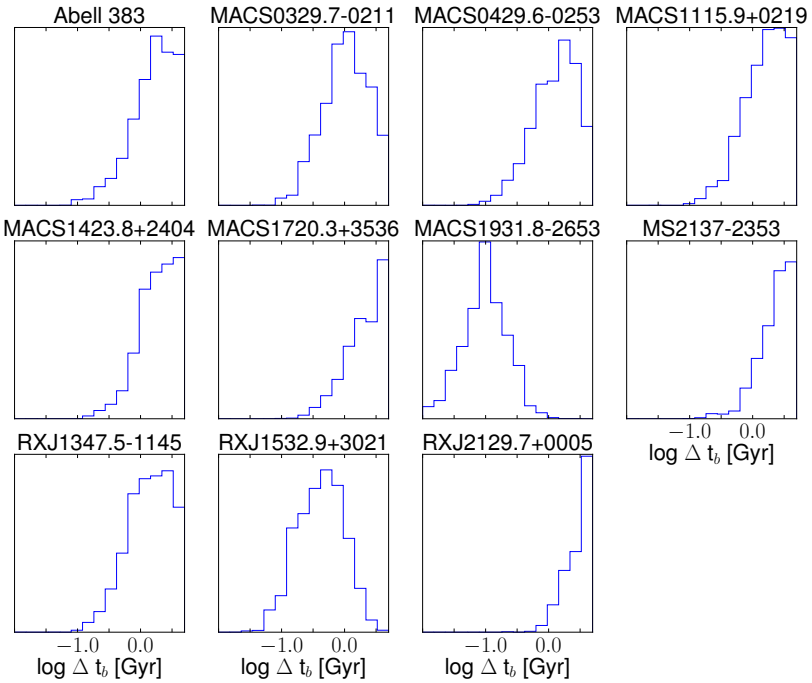

Figure 3.14 Marginal posterior probability distributions are shown for the burst duration, Δt_b, in log Gyr, when FBURST is restricted as described in Section 3.4. Results were obtained by generating a new model grid for each BCG with the new prior on FBURST and re-fitting the data.

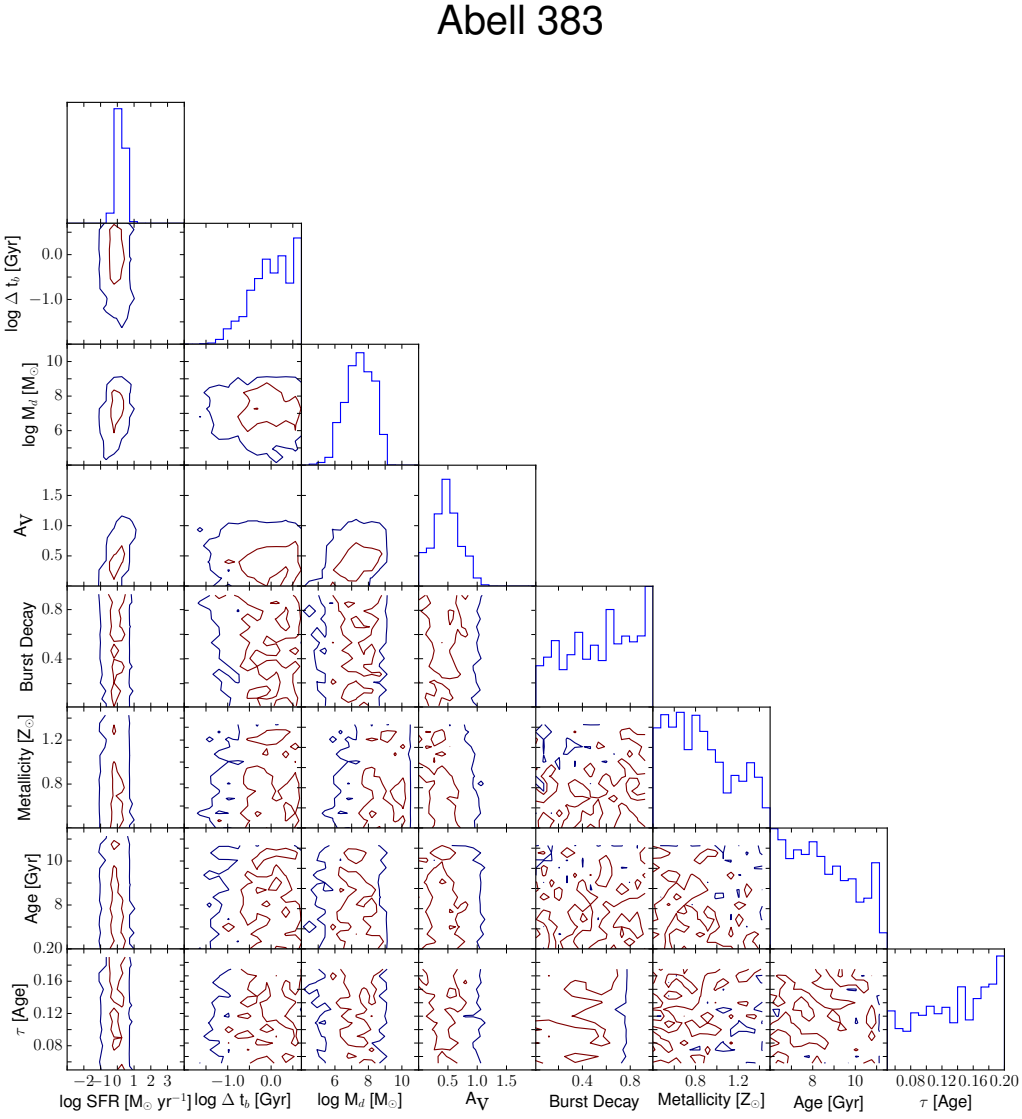

Figure 3.15 Marginal posterior probability distributions for the SFR, burst duration Δt_b, and dust mass M_d, dust attenuation A_V, burst decay percentage, metallicity, galaxy age, and τ shown for Abell 383. Plots are analogous to the marginal distributions presented in Figure 3.12.

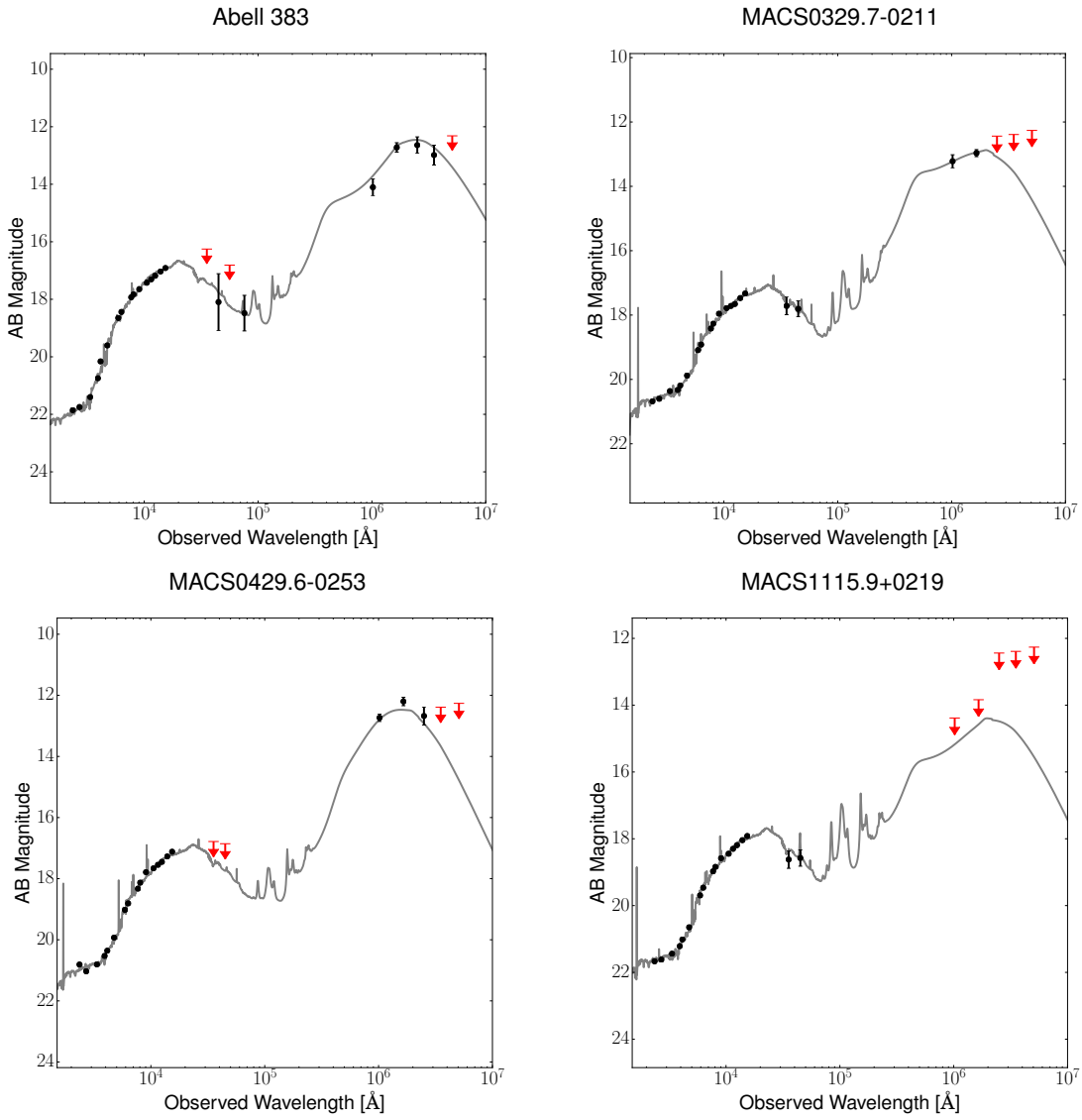

Figure 3.16 Best fit SEDs for each CLASH star forming BCG. SED photometry data points with 1σ error bars are shown as black points or as 3σ upper limits denoted by red arrows. Grey lines depict the 'best fit' synthetic spectra, where 'best fit' is defined to be the synthetic spectrum producing the smallest reduced χ^2 in the `iSEDfit` Monte Carlo grid.

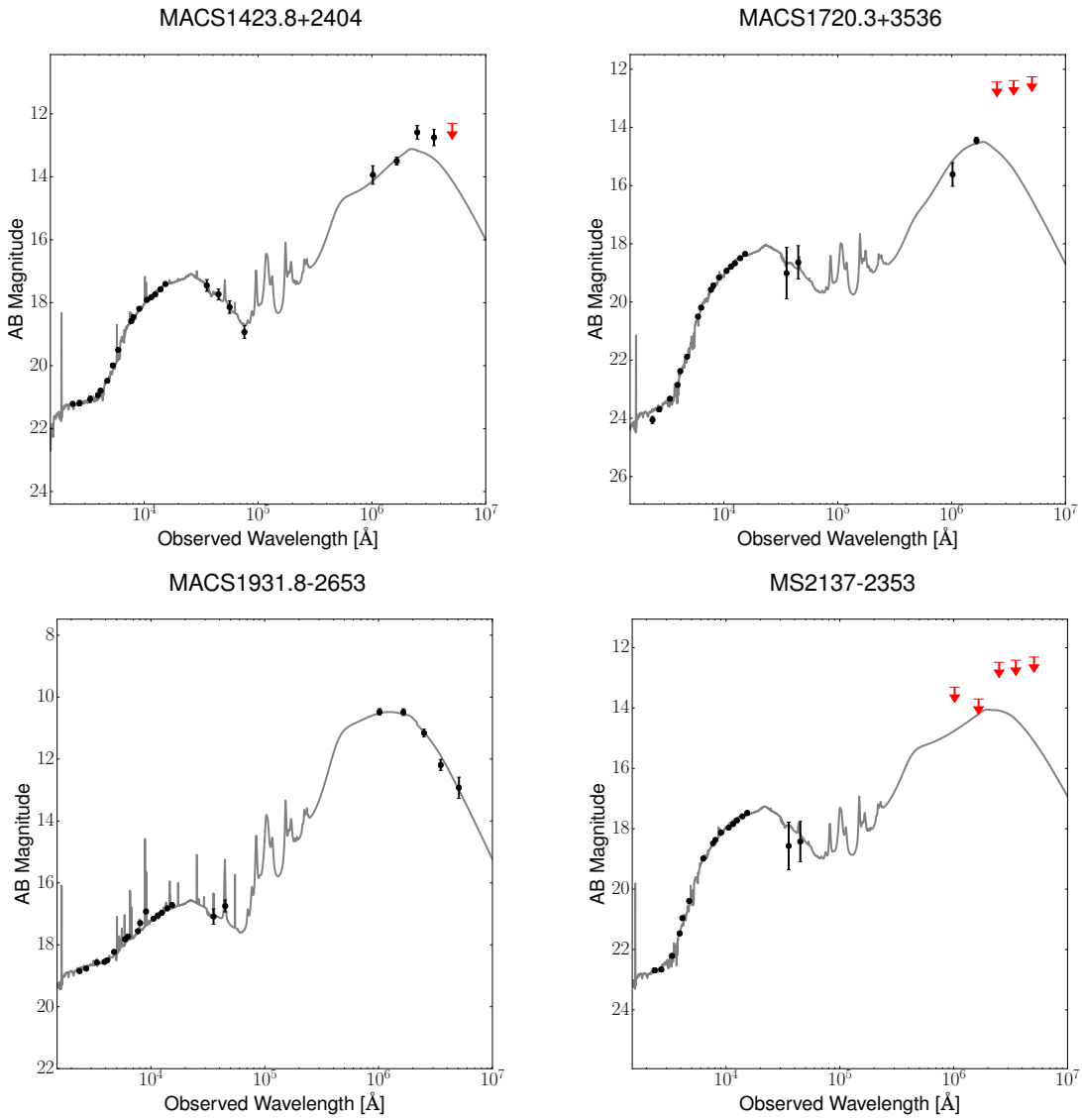

Figure 3.16 *Continued*

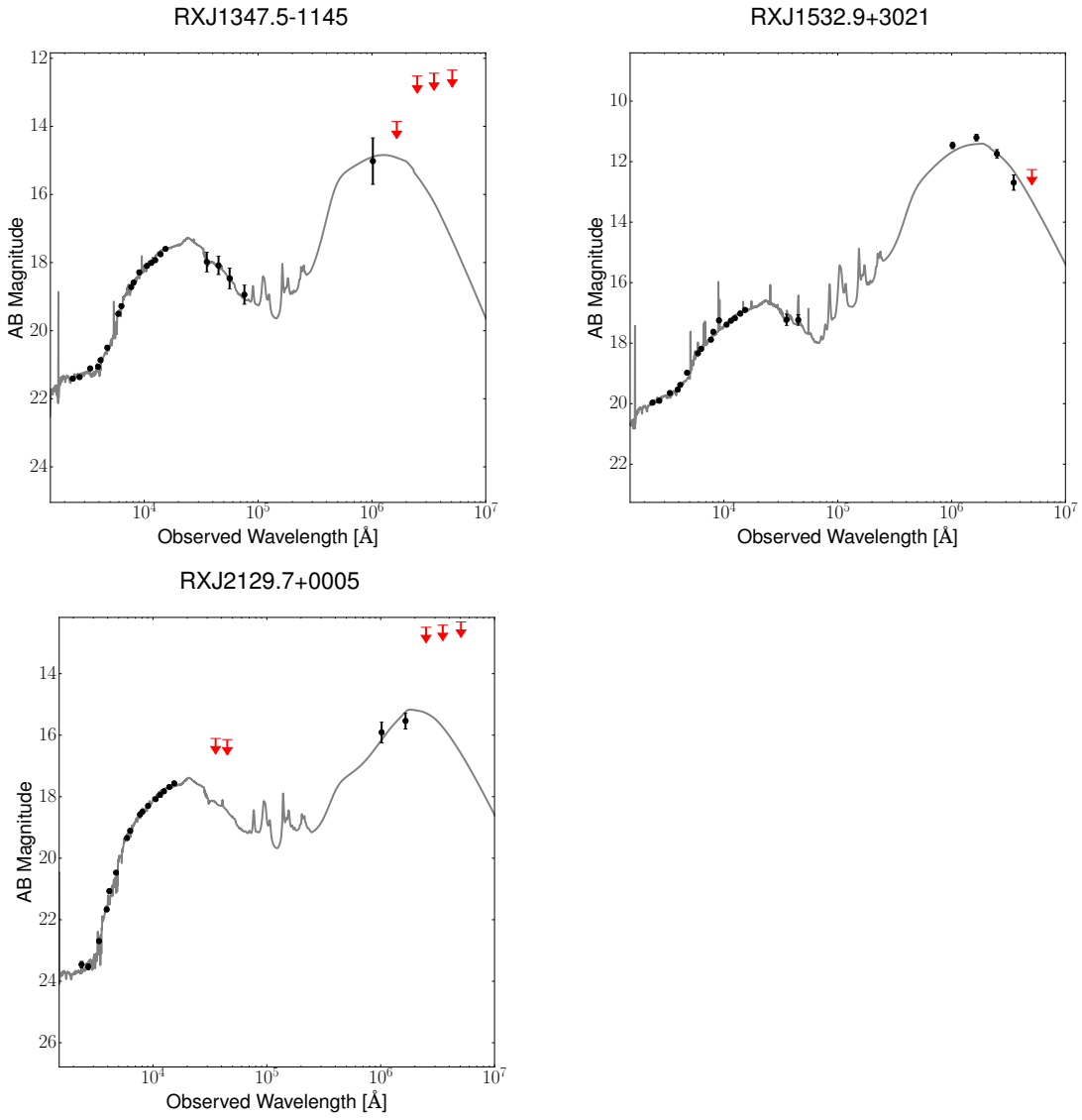

Figure 3.16 *Continued*

Chapter 4

3.4μm M/L Ratio and Stellar Mass Evolution of BCGs in COSMOS from $z < 1.0$

Abstract

We investigate the evolution of star formation rate, stellar mass, and M/L$_{3.4\mu m}$ ratio of high mass ($> 10^{11} M_{\odot}$) Brightest Cluster Galaxies (BCGs) in the COSMOS survey from $z < 1$ to determine the growth rate of BCG stellar mass over time from intermediate to low redshift. We estimate stellar mass and star formation rates through SED fitting of archival *GALEX*, *CFHT*, *Subaru*, *Vista*, *Spitzer*, and *Herschel* photometric data available in the COSMOS2015 catalog. A modified version of `iSEDfit` is used to fit both quiescent and star forming population models and examine the role of dust model selection. We find that BCGs grow in stellar mass at a rate of $\sim$1%/Gyr through $in-situ$ star formation since z $\sim$ 1. Additionally, we find an evolution of BCG baryonic mass-to-light ratio ($M/L_{3.4\mu m}$) with redshift consistent with passive evolution. We use this to build upon Wen et al. (2013)'s $\nu L_{3.4\mu m} - M_{Stellar}$ relation for use in approximating the stellar mass of high mass ($> 10^{11} M_{\odot}$) BCGs out to z $\sim$ 1. We finally compare results from the literature using SZ versus X-ray selected samples, and conclude that the diversity of results in the literature may

be affected cluster environment or by X-ray vs. SZ selection criteria.

4.1 Introduction

Dominating the luminosity and stellar mass of the cores of galaxy clusters, and influencing their evolution, are Brightest Cluster Galaxies (BCGs). These massive ellipticals occupy a narrow distribution of position-velocity space in relation to the clusters in which they formed (Lauer et al., 2014), indicating a relaxed state within the parent cluster. However, they do not represent the same population of ellipticals (Von Der Linden et al., 2007b) as other ellipticals in the cluster or the field. One unique characteristic of BCGs is their extended light profiles (e.g. Oemler, 1976; Graham et al., 1996), indicating a rich merger history (e.g Bernardi et al., 2007; Liu et al., 2008). Additionally, BCGs exhibit larger sizes and luminosities than predicted from cluster luminosity functions (e.g. Loh & Strauss, 2006; Shen et al., 2014).

Recent observations of star-forming BCGs has led to a revision of their formation scenario in the past decade. The initial model derived from theoretical predictions (e.g. Merritt, 1984) and observations (e.g. Stott et al., 2010, 2011) postulates a BCG formation mechanism in which the original gas and stellar content of a BCG formed in the initial matter density peaks (Treu et al., 2005). The rest of its constituent stars form via in–situ processes rapidly be-

fore $z = 1.5$, which evolve passively to the present day. This is contrasted by semi-analytical models in which BCGs grew in stellar mass by a factor of three from $z = 1$ to the present day (De Lucia & Blaizot, 2007). The newest models exhibit a factor of two growth over the same redshift range (e.g. Shankar et al., 2015), in which BCG stellar mass is accumulated through many minor mergers (e.g. Naab et al., 2009; Edwards & Patton, 2012), which has led to greater agreement between observations and models (Lin et al., 2013; Lidman et al., 2012). Whether this merger-driven era dominates mass growth is still under investigation, as minor mergers are not 100% efficient in the delivery of their gas supply or stars (Liu et al., 2009), and major mergers still occur rarely at low redshift (Burke & Collins, 2013; Liu et al., 2015).

Determining an accurate BCG growth model has been difficult, as the literature has found a diverse range of stellar mass growth rates using a diverse range of selection methods and stellar population models. For example, Tonini et al. (2012)'s semi-analytical BCG growth, using Maraston (2005) stellar population models, is effectively complete by $z \sim 0.4$. Bai et al. (2014)'s BCG sample, which are selected from RCS1 (Gladders & Yee, 2005) and a flux-limited X-ray sample (Mullis et al., 2003), exhibit 50% growth between $0.1 < z < 0.5$. Meanwhile, Inagaki et al. (2015) selects their sample using the $Planck$ Sunyaev-Zeldovich Source Catalog, finding up to 14% growth between $0.2 < z < 0.4$. Bellstedt et al. (2016)'s study of 98 clusters in the RELICS survey finds 9% growth

from $0.25 < z < 0.60$. Finally, Oliva-Altamirano et al. (2014)'s study of SDSS BCGs finds no buildup of stellar mass from $0.09 < z < 0.27$. This is contrasted by McIntosh et al. (2008) in which cluster centers of BCGs from the SDSS Group Catalog are gaining 2-9% of their stellar mass from $0.01 < z < 0.12$. Selection effects between optical and x-ray samples may play a role (Burke et al., 2000), different observed wavelengths, or assumptions such as selection of IMF or evolution model may each play a part in the disparity in results.

In this paper, we seek to address the inconsistency in mass growth findings through the use of a customized SED fitting code based on `iSEDfit` and comparisons to low-mass clusters identified in the Cosmic Energy Survey (COSMOS) (Scoville et al., 2007). COSMOS is a multi-wavelength survey which observed a 2 sq. deg. field centered at RA(J2000) = 10:00:28.600, DEC(J2000) = +02:12:21.00 from the X-ray to the radio, with publicly available multi-wavelength data available in the COSMOS2015 catalog. By modeling BCG SEDs using far-UV (FUV) to far-infrared (FIR) observations, we can better constrain the old and young stellar populations in a self consistent manner that considers stellar populations obscured by infrared emitting dust. By estimating specific star formation rates (sSFR) and star formation episode age in BCGs over a wide redshift range, we better constrain when mass assembly takes place and whether or not star formation episodes in different clusters share a common ending epoch.

In §4.2 we discuss target selection criteria and sample completeness. We review the archival data used in the SED fitting procedure in §4.3 and discuss the data reduction and SED fitting software in §4.4. We discuss the results in §4.6. Finally, we summarize our results and future prospects in §4.7. We use the lambda cold dark matter (ΛCDM) standard cosmological parameters of H_0 = 70 Mpc^{-1} km s^{-1}, Ω_M = 0.3, and Ω_{vac} = 0.7.

4.2 Sample Selection

In order to build our sample from a common field and selection method, we select BCGs from clusters in the COSMOS X-ray group and cluster catalog (George et al., 2011; Finoguenov et al., 2007) between $0 < z < 1$, with greater than thirty confirmed cluster members (to limit the sample to clusters), and a most massive group galaxy stellar mass of $>10^{11}$ M$_\odot$. This yields an initial sample of 40 BCGs with no selection for star formation rate (SFR) activity. Their parent clusters span the range of log(m$_{200c}$/M$_\odot$) $\sim$13.1-14.2, as determined by the cluster X-ray luminosity (Finoguenov et al., 2007).

COSMOS groups and clusters were originally detected by identifying extended sources on the scale of 32"; and 64" using the wavelet analysis of Vikhlinin et al. (1998); in the Chandra and 1.4 Ms XMM-Newton observations of the COSMOS field. Once identified, George et al. (2011) ran a red-sequence find-

ing algorithm to identify an optical counterpart within a projected distance of 500 kpc of the X-ray center. A galaxy is included as a member galaxy using a Bayesian analysis of galaxy properties such as location with respect to cluster or group center, redshift error, and relative number of field and cluster or group galaxies (See §4 of George et al., 2011). Our sample requires no completion correction as the COSMOS X-ray group catalog is complete down to $M_* \geqslant 10^{10.4}$ $M_\odot$ at z = 1 (George et al., 2011). Stellar mass estimates used in the COSMOS X-ray group catalog are estimated via SED fitting of galaxies with 3σ detections in the K_s band, using Bruzual & Charlot (2003) stellar population models with a Chabrier (2003) IMF. Two targets, COSMOS CLJ100028.3+024103 and COSMOS CL J095824.0+024916, had updated photometric redshifts above z =1 in the the more recent COSMOS2015 catalog (Laigle et al., 2016) and were excluded from the final sample, resulting in a total of 38 BCGs.

4.3 Archival Data

To characterize each BCG from the FUV-FIR, we use archival multi-wavelength observations of the COSMOS field (Scoville et al., 2007). A short review of each observation set is below, for further details of the data reduction in COSMOS2015, see Laigle et al. (2016). The following photometry has been corrected for photometric and systematic offsets as detailed in Eq. 9 in Laigle

et al. (2016). For observations from *GALEX* FUV-*Spitzer* IRAC4, we also correct for Milky Way foreground extinction using a galactic reddening of R_v = 3.1 (Morrissey et al., 2007) and $E(B-V)$ values from the Schlegel et al. (1998) dust maps.

For our SED fitting, we use errors which include the observational error reported in the COSMOS2015 catalog as well as the absolute calibration uncertainty unique to each telescope. For GALEX NUV and FLUX flux errors, we include a 10% uncertainty [1]. Subaru photometric calibration is accurate to within 0.02 magnitudes (Taniguchi et al., 2015), therefore we include a systematic error of 2%. For CFHT u*, we err on the side of caution and use the 5% error from worst quality data of the original CFHT observations of the COSMOS field (Capak et al., 2007). According to the Vista/VIRCAM User Manual[2], Vista photometry is accurate to within 3-5% and so we include a 5% error in addition to the observational error for data from Vista/VIRCAM filters. *Spitzer* absolute flux calibration is considered accurate to within 3% Van Dyk et al. (2013), and we add an additional 3% to our final *Spitzer* IRAC errors. Most *Herschel* data used here are upper limits defined by the sensitivity of the original Herschel survey of the COSMOS fields. For the handful of Herschel detections in our sample, we adopt the 10% systematic uncertainty term used in Fogarty et al. (2017).

[1] https://asd.gsfc.nasa.gov/archive/galex/FAQ/counts_background.html
[2] Doc. No. VIS-MAN-ESO-06000-0002

4.3.1 GALEX Observations

To constrain the degree of unobscured star formation, we retrieve the *Galaxy Evolution Explorer* (*GALEX*; Martin et al., 2005) archival far-UV (FUV) and near-UV (NUV) band PSF-fit photometric magnitudes (For details see Zamojski et al., 2007). *GALEX* observes a 1.2 degree circular field of view through a 50 cm diameter Richey–Chretien telescope. To measure FUV and NUV magnitudes, Zamojski et al. (2007) use a PSF-fitting routine using u^* band observations as a prior to minimize blending effects due to GALEX's FWHM of 5".

4.3.2 Canada–France–Hawaii Telescope (CFHT)

We use COSMOS2015 archival CFHT/MegaPrime (Aune et al., 2003; Boulade et al., 2003) u^* magnitudes to constrain the blue and NUV res-frame emission. The COSMOS field was observed in queue mode with a consistent PSF (with a FWHM of 0.9") across all observations, to a depth of $m_{u^*} \sim 26.4$ and seeing of 0.9". For further details, see Capak et al. (2007).

Additionally, we use K_s magnitudes from CFHT/WIRCam (Puget et al., 2004) taken during the COSMOS-WIRCam Near-Infrared Imaging Survey (McCracken et al., 2010), down to a 3σ detection limit of m_{K_s}=23.4 and FWHM of 1.1" or less. The K_s filter has PSF FHWM of ~ 1.02" (Laigle et al., 2016).

4.3.3 Subaru

To constrain the optical continuum of each BCG, we retrieve Subaru/Suprime-Cam optical magnitudes from the COSMOS2015 catalog in 5 broad filters (B,V,R,$i+$,$z+$ $+$) and 11 medium filters (IA427, IA464, IA484, IA505, IA527, IA574, IA624, IA679, IA738, IA767, and IA827). The Subaru observations with the worst resolution are from the IA464 filter with a PSF FWHM of 1.89", which is still sufficient to resolve the BCGs from their parent clusters for our sample. All observations reach a 3σ depth of $m_{AB} \sim 25.2$ or deeper. For further details, see Taniguchi et al. (2007, 2015).

4.3.4 Vista

Near-infrared (NIR) observations are an important constraint for the old stellar population which dominates the emission and stellar mass of BCGs. We retrieve Y, J, and H-band archival Vista (Dalton et al., 2006; Emerson et al., 2006) observations taken with VIRCAM (Sutherland et al., 2015) during the UltraVISTA-DR2 survey (McCracken et al., 2012). For UltraVISTA, the COSMOS field was observed with Y, J, and H filters down to limiting magnitude m_{AB} of 25.3, 24.9, and 24.6 respectively with a median FWHM of 0.6".

4.3.5 Spitzer Observations

Additional observations of the old stellar population are available through near-infrared observations taken by the *Spitzer Space Telescope* (*Spitzer*; Werner et al., 2004). We include archival data from *Spitzer*'s Infrared Array Camera (IRAC)'s 3.6, 4.5, 5.7, and 7.9 μm channels (For more information, see Fazio et al., 2004). IRAC observes 5.2 arcmin x 5.2 armin fields with PSF widths 1.6 arcsec, 1.6 arcsec, 1.8 arcsec, and 1.9 arsec for bands IRAC1 to IRAC4 respectively. IRAC magnitudes in COSMOS2015 are measured from observations taken as part of SPLASH (Steinhardt et al., 2014) and S-COSMOS surveys (Sanders et al., 2007) to a 3σ depth of m_{AB} of 25.5, 25.5, 23.0, and 22.9 for IRAC1-4 respectively. We also include archival Multiband Imaging Photometer (MIPS, Rieke et al., 2004) 24μm fluxes originally observed and reduced in (Le Floc'h et al., 2009) to a 5σ depth of 71 μJy.

4.3.6 Herschel Observations

The far-infrared is an important regime that is sensitive to the re-radiated energy from dust surrounding optically bright, but obscured, star forming regions. We use *Herschel Space Observatory* (*Herschel*; Pilbratt et al., 2010) Photoconductor Array Camera and Spectrometer (PACS) Oliver et al. (2012) in the green (100 μm) and red (160 μm) bands as well as the Spectral and Photomet-

ric Imaging Receiver (SPIRE) 250 μm and 350 μm bands. 500 μm observations, which in Chapter 3 provided very little constraining power in massive CLASH clusters with known starbursts, were not used in SEDs for the COSMOS sample. While the large beam size at 250 & 350 μm (18.1, 24.9" respectively) guarantees blending, all targets at 350μm and all but one target (COSMOSCLJ100035.2+020346) at 250μm have S/N < 3 and are treated as upper limits. PACS observations were taken as part of the PACS Evolutionary Probe (PEP: Lutz et al., 2011) to a 3σ depth of 5 and 10.2 mJy for 100 and 160 μm bands respectively. SPIRE observations originate from the Herschel Multi-tiered Extragalactic Survey (HerMES: Oliver et al., 2012) and reach a 3σ depth of 8.1 and 10.7 mJy respectively.

4.4 Methods

4.4.1 SED Construction

SEDs were composed of photometry taken from *GALEX*, *SDSS*, *Subaru*, *Vista*, *Spitzer*, and *Herschel* archival magnitudes in the COSMOS2015 public catalog, so as to maximize coverage of UV-through-IR flux.

Out of an initial sample of 40 BCGs, 2 were excluded for updated photometric redshifts currently beyond z = 1. In the remaining sample of 38 BCGs; 27

have *GALEX* NUV and/or FUV detections, 37 have full *Spitzer*/IRAC detections with the 38th (COSMOS CLJ100056.0+022834) detected in only IRAC1-3 , 4 are detected in MIPS 24 μm , and 4 with *Herschel* PACS or SPIRE. Therefore, every BCG in the final catalog has rest-frame U-band through NIR coverage, with limiting magnitudes out to 350 μm.

4.4.2 SED Fitting

SEDs were fit using a modified version of `iSEDfit` (Moustakas et al., 2013). `iSEDfit` is a Bayesian SED fitting tool that uses a grid of synthetic SEDs generated using a set of input priors to estimate the posterior probability distribution of parameters of the stellar population emitting an observed SED. We used the modified version of this tool described in Fogarty et al. (2017) in order to take into account both the stellar and dust emission observed in the near-UV through IR SEDs of our sample.

A detailed description of `iSEDfit` is available in Appendix A of Moustakas et al. (2013). `iSEDfit` takes a synthetic stellar population (SSP), initial mass function (IMF), and dust attenuation law, and creates a grid of synthetic SEDs that randomly sample the parameter space of metallicity, A_V , emission line ratios, and the parameters governing the star formation history (SFH). For each BCG, we assume a Salpeter (1955) IMF. We tested two SFH parameterizations, a one component model and a two component model. The one component model

consists of an exponentially decaying SFH with a decay constant between 0.6 and 60 Gyr sampled logarithmically. The two component model consists of an exponentially decaying SFH with a decay constant between 0.3 and 1.5 Gyr, and for half of the models in our grid we incorporated an exponentially decaying starburst at present time. For either model, the age of the BCG was allowed to vary between 6 and 9 Gyr if the BCG is at $z \leq 0.45$, or between 4 and 6 Gyr if the BCG is at $z > 0.45$. This enables us to fit SEDs of both quiescent (nominally 'red and dead') and star-forming BCGs, and to make a statistical determination for the presence of a star formation episode. Our choices of stellar population model and parameter space are given in Table 4.1.

The relative likelihood that each model SED is the observed SED is determined by calculating $e^{-\chi^2}$, where χ^2 is the reduced chi square value for the model compared to the data. By randomly sampling the model grid, weighted by the relative likelihood, `iSEDfit` recovers the posterior probability distribution of the model SEDs, and therefore the probability distribution of the physical stellar parameters we hope to infer from the fit.

Dust emission is incorporated into the synthetic SED grid, allowing us to take advantage of the mid- and far-IR data available from *Spitzer*, and *Herschel*. SED fits incorporating observations of the IR dust emission are always preferable to those that do not since they reduce the degeneracy between A_V and the SFR in fits to dusty star-forming systems. Following the prescription

Table 4.1 SED Fitting Parameters

Stellar Population Model			
Synthetic Stellar Population	Bruzual & Charlot (2003)		
Initial Mass Function	Salpeter (1955)		
Attenuation Law	Calzetti et al. (2000)		
Dust Emission	Draine & Li (2007)		
Model Parameter Space Constraints			
Parameter Name	*Minimum Value*	*Maximum Value*	*Sampling Interval*
One Component SFH			
Age, t	4 Gyr (6 Gyr)	6 Gyr (9 Gyr)	Linear
Decay Timescale, τ	0.6 Gyr	60.0 Gyr	Logarithmic
Two Component SFH			
Age, t	4 Gyr (6 Gyr)	6 Gyr (9 Gyr)	Linear
Decay Timescale, τ	0.3 Gyr	1.5 Gyr	Linear
Burst Age, t_b	10^{-2} Gyr	5.0 Gyr	Logarithmic[a]
Burst Decay Percentage	0.01	0.99	Linear
Burst Mass Percentage	0.0015	0.85	Logarithmic
Metallicity	$3 \times 10^{-2} Z_{\odot}$	$1.5 Z_{\odot}$	Linear
Dust Parameters			
Attenuation A_V	0	2	Linear
PAH Abundance Index q_{PAH}	0.10	4.58	Linear[b]
γ^c	0.0	1.0	Linear
U^c_{min}	0.10	25.0	Logarithmic
U^c_{max}	10^3	10^7	Logarithmic

[a] Burst parameters were sampled logarithmically, since their qualitative effect on the model SED of the galaxy occurs on order-of-magnitude scales. The exception to this is the burst decay percentage, which is one minus the amplitude of current star formation activity relative to the amplitude of the burst t_b yr ago.
[b] Draine & Li (2007) model parameters sampling intervals were chosen based on the model parameter distributions of the template spectra.
[c] The Draine & Li (2007) treats dust in a galaxy as consisting of two components. The first component consists of a fraction γ of the dust is exposed to a power law distrubition of starlight intensity, ranging from U_{min} to U_{maxs}, while the second component consists of the remainder of the dust, and is only exposed to a starlight intensity U_{min}. The quantities U_{min} and U_{max} are unitless measures of intensity relative to the ambient local radiation field.

in Fogarty et al. (2017), we used the dust emission templates in Draine & Li (2007). The choice dust model parameter space is given in Table 4.1. The dust emission component of each synthetic SED was normalized such that the total energy re-emitted by the dust equals the total energy absorbed via attenuation of the synthetic stellar spectrum.

Our choice of dust model is the Calzetti et al. (2000) attenuation law for dusty starburst galaxies. As BCGs are generally dust poor, any given choice of dust model will only effect the results of our BCG fits where the target contains prominent dust components, and likely an affiliated star formation episode. To explore the impact of our choice of dust model, we also perform an identical set of SED fits using model grids derived using a modified version of the Calzetti law, which takes into account a mild dependence of the attenuation curve on A_V, as well as attenuation from SMC-like dust with a "shell-like" geometry described in Witt & Gordon (2000). Model grids consisting of 10^4 models were constructed for each BCG. The SFH of approximately half of the models in each grid include a recent burst of star formation activity, and half consist solely of an exponentially decaying model. Stellar, dust, and SFH parameters were randomly sampled at either linear or logarithmic intervals, as indicated in Table 4.1. The age of each BCG was assumed to be the cosmic age at the redshift of the BCG.

4.5 Results

4.5.1 BCG Redshift Evolution

From an initial sample of 40 BCGs we are left with 33 after cutting SED fits with a best-fit $\chi^2 \geq 10$. To explore the evolution of BCG SFRs and sSFRs for this sample of BCGs, we present the SFRs and redshifts in Figure 4.1, and sSFRs and redshifts in Figure 4.2. We use the median of the posterior probability distribution to define the best-fit SFR and sSFR for BCGs in this sample. Unlike Chapter 3, the posteriors for these quantities are not unimodal for the two-component SFH, making the mean obtained for the two-component fit difficult to interpret. Furthermore, for BCGs with SEDs that may be fit by a range of star-formation activities, the posterior may have a low-SFR tail.

Unless otherwise specified, we report results obtained with the single-component SFH parameterization throughout. We demonstrate SFR is independent of redshift, within our errors, and can place limits on the evolution of the sSFR. We also defined four redshifts bins, $0.15 \leq z < 0.35$, $0.35 < z \leq 0.5$, $0.5 < z \leq 0.65$ and $0.65 < z$, and calculated the two weighted mean SFRs and sSFRs for each bin. These are reported in the figures with red crosses, depicting the widths of the bins and of the 1σ credible intervals for the SFRs and sSFRs.

Redshift binned results are reported in Table 4.2. SFR does not change significantly in any of the four redshift bins across our sample. Across all redshift

Table 4.2. Redshift Binned SFR and sSFR

Parameter	$0.15 \leq z < 0.35$	$0.35 \leq z < 0.5$	$0.5 \leq z < 0.65$	$0.65 \leq z$
$\log_{10}$ SFR *(One-Component SFH)* [$M_\odot$ yr^{-1}]	$-0.8^{+0.3}_{-0.4}$	$-0.7^{+0.4}_{-0.6}$	$0.1^{+0.3}_{-0.3}$	$-0.1^{+0.4}_{-0.5}$
$\log_{10}$ SFR *(Two-Component SFH)*	$-1.0^{+0.4}_{-0.9}$	$-0.9^{+0.6}_{-1.3}$	$-0.1^{+0.5}_{-1.0}$	$-0.5^{+0.6}_{-1.5}$
$\log_{10}$ sSFR *(One-Component SFH)* [yr^{-1}]	$-12.4^{+0.3}_{-0.4}$	$-12.3^{+0.4}_{-0.6}$	$-11.4^{+0.3}_{-0.3}$	$-11.8^{+0.4}_{-0.5}$
$\log_{10}$ sSFR *(Two-Component SFH)*	$-12.7^{+0.5}_{-0.9}$	$-12.6^{+0.6}_{-1.3}$	$-11.6^{+0.4}_{-1.0}$	$-12.2^{+0.6}_{-1.55}$

bins, we find a typical BCG SFR of $\sim$0.1–1 $M_\odot$ yr^{-1}. The SFR trends are similar whether we consider the one-component or two-component SFH, although SFRs and sSFRs are marginally higher when measured using a one-component SFH.

The mean sSFR is roughly constant for our sample, for all four redshift bins. In Figure 4.2 we find that, regardless of redshift, the typical sSFR for a BCG in our sample is $10^{-11.9}$ yr^{-1}. Since the catalog we use probes masses uniformly across the range of redshifts we study, our results in Figure 4.1 suggest some evolution in the weighted mean sSFR may occur at $z \sim 0.6$, which would be consistent with McDonald et al. (2016). However, an upward evolution would not be consistent with our highest redshift bin, which has a similar mean sSFR to the bins below $z = 0.5$. We find that across our redshift range, the sample we study probes the mass range 11.2 $M_\odot$ - 12.5 $M_\odot$ relatively uniformly, as seen in Figure 4.3.

Finally, we examined the redshift evolution of the BCG mass-to-light ratio. These results are presented in Figure 4.4. Studies such as Fraser-McKelvie et al. (2014) and Wen et al. (2013) use the M_*–$WISE$ W1 luminosity relation-

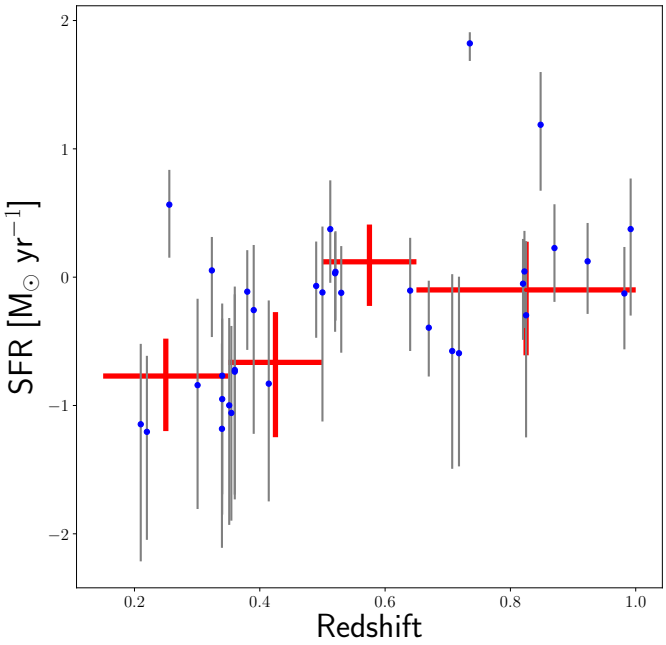

Figure 4.1 Best fit SFRs, defined to be the median of the marginal posterior probability distribution of the SFR versus redshift for all BCGs in the sample. The error bars for SFR denote the 68.3% credible intervals, corresponding to 1σ uncertainties for approximately Gaussian probability distributions. The red crosses show the χ^2 weighted mean SFRs in each of four redshift bins. The horizontal bars depict the width of each bin in redshift, and the vertical bar depicts the 1σ credible interval for the mean.

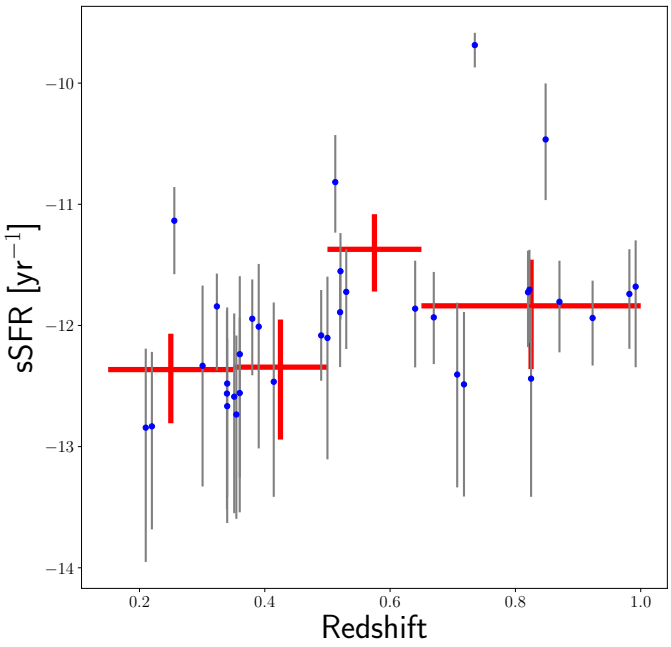

Figure 4.2 Best fit sSFR versus redshift for all BCGs. The definition of the best fit, color scheme and redshift bins are the same as those in Figure 4.1.

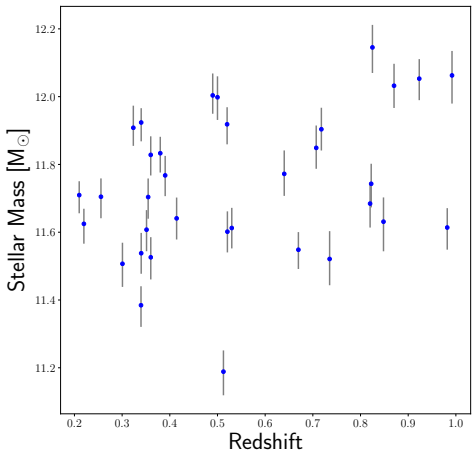

Figure 4.3 Best fit total masses versus redshift for all BCGs. The definitions of best fit is the same as in Figure 4.1.

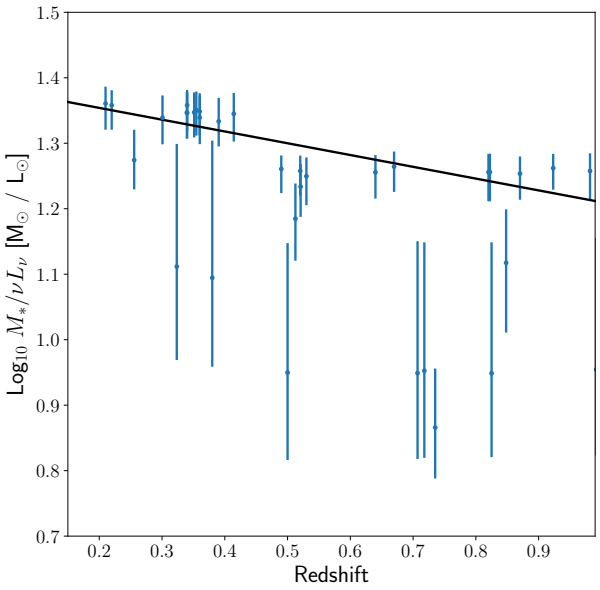

Figure 4.4 $M_*/\nu L_{3.4\mu m}$ values are plotted against redshift to depict the effect of passive evolution on the BCG sample, in which the population ages and becomes redder over time. Luminosities are K-corrected and corrected for distance modulus. The solid line is a linear fit to the data using Hogg et al. (2010).

ship to estimate stellar masses of BCGs at $z < 0.1$ and $z <$ 0.35 respectively. However, further estimation of BCG stellar masses at higher redshifts will require estimates of the evolution of $M_*/L_{3.4\mu m}$ with redshift. Therefore, we computed $WISE$ W1 rest frame luminosities by estimating the best-fit model W1 photometry in `iSEDfit`. This band observes the population of old stars which compose the majority of the BCG's stellar mass, in addition to being less sensitive to recent star formation and dust than other bands. A linear model is fit to the $M_*/L_{3.4\mu m}$ ratio versus redshift using the least-squares method in Hogg et al. (2010). The resulting redshift-sensitive conversion between νL_ν(3.4μm) and M_* is detailed in Equation 4.1:

$$log_{10}\left(\frac{M_{Stellar}(M_\odot)}{\nu L(3.4\mu m)_\nu(L_\odot)}\right) = 1.39\ (+0.02, -0.01) \\ -0.18\ (+0.02, -0.05) \times z. \tag{4.1}$$

We find the negative slope is < -0.08 with 3σ significance.

Our wide range of redshifts enables us to probe the evolution of the stellar $M_*/L_{3.4\mu m}$ ratio, and derive a redshift dependent relationship between the two quantities. We measure $M_*/L_{3.4\mu m}$ for high stellar mass ($> 10^{11} M_\odot$) BCGs from redshifts between z $\sim$ 0.2 and z $\sim$ 1.0. Across this range of redshift space, there are no obvious outliers, and the $M_*/L_{3.4\mu m}$ ratio changes by a factor of $\sim$ 1.7.

Wen et al. (2013) find $M_*/\nu L_{3.4\mu m}$ ratios of $\sim$1.5-2 for some massive early-type galaxies with $M_* > 11.5 M_\odot$, consistent with an extrapolation to low red-

shift from Eq. 4.1 (Fig. 4.4). The nearest contaminant in the NIR which could effect our result is the 3.3 PAH emission feature, which will not be detected since the rest-frame W1 central wavelengths span 1.8 – 2.5 μm across the redshifts observed in our sample.

4.6 Discussion

4.6.1 Comparison Between Literature and Our Work

Our typical sSFR values are $< 10^{-11.0}\ yr^{-1}$ across all redshift bins, indicative of a doubling time of $> 10^{11}$ yr, and thus a stellar growth rate due to star formation of $\sim 1\%$ Gyr^{-1}.

This is an order of magnitude less growth than McDonald et al. (2016), which diverges further from our results at higher redshift as merger-driven stellar mass growth drives higher star formation rates. Using detections from the SPT, McDonald et al. (2016)'s sample probes the highest Y_{SZ}-clusters (Y_{SZ} is the spatially integrated Compton Y-parameter from the SZ effect) in the southern hemisphere, and consists of clusters with approximately $10\times$ more massive than the COSMOS clusters. We believe the discrepancy in stellar mass growth rate is due to their mass selection requiring a more agressive merger-driven

mass growth in their past in order to reach their observed masses, an aggressive growth rate not required by our lower mass sample.

Our results are closest to McIntosh et al. (2008)'s 1.4-6.4%/Gyr growth rate and consistent with Oliva-Altamirano et al. (2014)'s lack of significant change at lower redshift ($0.09 < z < 0.27$). However, our results show an order of magnitude less growth than Bai et al. (2014) and Inagaki et al. (2015), which used red sequence and X-ray luminosity selected BCGs. Inagaki et al. (2015) fit Sunyaev-Zel'dovich (SZ)-effect selected BCGs using only SDSS $ugriz$ magnitudes via `kcorrect` and `NewHyperZ`, using Bruzual & Charlot (2003) stellar population models and a Chabrier IMF. Out result is consistent with their lower limit of 2%, but not their upper limit of 14%. They also noted that `NewHyperZ` yielded higher masses than their `kcorrect` models and that their selection of early type galaxy models may have influenced the result. Bai et al. (2014) used the GALFIT luminosity of their targets combined with the M/L ratio given by the Maraston et al. (2009) luminous red galaxy models. This difference in stellar and M/L ratio assumptions may be contributors to our different results.

This work's mean sSFR is higher than Cooke et al. 2016's mean sSFR of 9.42 $\times 10^{-12}\, yr^{-1}$ which investigated the Sloan Giant Arcs Survey (SGAS) and Cluster Lensing and Supernova Survey with Hubble (CLASH) samples. This is expected, as their estimators only measured obscured rates while our inclusion

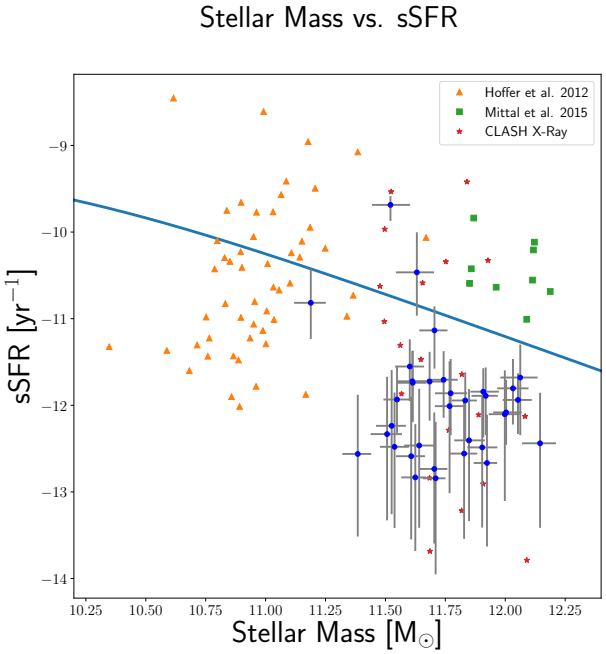

Figure 4.5 sSFR vs. stellar mass for COSMOS BCGs, with Hoffer et al. (2012), Mittal et al. (2015), and CLASH X-ray selected clusters shown for comparison. The blue line represents the star-forming main sequence as found by Lee et al. (2015) at the mean redshift of all BCGs plotted.

of more infrared upper limits are capable of constraining and approximating the star formation obscured by dust as well as the un-obscured component.

4.6.1.1 Differences in Behavior Between Literature Samples

We use available archival data from three other X-ray selected BCG studies in order to provide a larger sample to test whether BCG star formation is typical of other massive galaxies; the ACCEPT survey (Cavagnolo et al., 2009), the BCGs studied by Mittal et al. (2015), and the Cluster Lensing and

Supernova Survey with Hubble (CLASH; Postman et al., 2012). Of these samples, the CLASH BCGs occupy a mass and redshift range most like the present sample, having masses above $10^{11} M_{\odot}$ and a redshift range of $0.2 < z < 0.7$. However, the CLASH survey selected massive ($kT > 5$ keV), morphologically symmetrical (ellipticity ≤ 0.3) clusters, and so contains more massive clusters than COSMOS and a large fraction $> 50\%$ of cool cores Postman et al. (2012). Meanwhile, the ACCEPT clusters overlap with our masses. Explicitly limiting our sample to high mass BCGs was done in order to minimize the risk of misidentifying BCGs, and by doing so, we are able to examine the impact of BCG and halo mass on star formation.

The ACCEPT survey selected 239 X-ray clusters in the temperature range $T_x \sim 1 - 20$ keV and the bolometric luminosity range $L_{bol} \sim 10^{42-46}$ erg s^{-1}, spanning redshifts $0.05 - 0.89$ (Cavagnolo et al., 2009). Star formation rates and stellar masses of ACCEPT cluster BCGs were measured in Hoffer et al. (2012). We include sSFR values for BCGs with SFRs detected using 70 μm *Herschel* observations.

The CLASH survey (Postman et al., 2012) selected twenty massive clusters from X-ray observed dynamically relaxed systems. Sixteen clusters are from the massive, relaxed, X-ray observed sample of Allen et al. (2008). Five more strongly lensing clusters with Einstein radii > 35"; are also included. Fogarty et al. (2015) and Donahue et al. (2015) independently investigate the star

formation characteristics of the CLASH sample. CLASH BCGs are expected to select a higher star-forming BCG sample than optically or SZ selected samples. The high X-ray luminosity of these clusters originates from cooling ICM gas, which should fall down the cluster gravitational potential and condense into the cluster BCG, fueling star formation. Optically selected BCG samples have no such dependence, while the effect of cool cores is much less pronounced on SZ selected cluster samples than X-ray selected cluster samples, since X-ray luminosity is $\propto n^2$, while $Y_{sz} \propto n$, where n is the ICM density and Y_{SZ} is the intengrated Compton-Y parameter. Recent results suggest that cool-core clusters may occur about twice as frequently in X-ray selected samples compared to SZ-selected ones (Rossetti et al., 2017).

As seen in Fig. 4.5, overall the comparison sample is consistent with the star-forming main sequence at this redshift (Noeske et al., 2007; Lee et al., 2015) COSMOS and CLASH BCGs exhibit some of the lowest SFRs of the four compared samples; however, and the COSMOS BCGs are systematically more quiescent than would be predicted with the star-forming main sequence. COSMOS targets were initially detected by identifying red sequence galaxies in extended X-ray sources observed by XMM-Newton or Chandra. The COSMOS X-ray selection criteria for these targets require that their log(L_X) > 41.3 (erg s^{-1}), while CLASH X-ray detection required a relaxed system with $kT_x > 5$ keV.

Intriguingly, the tendency of COSMOS BCGs towards quiescence may be a function of the cluster environment. Figure 4.6 displays sSFR vs. cluster M_{500} for the COSMOS, ACCEPT, and CLASH samples, as well as the SZ-selected sample in McDonald et al. (2016). Cluster masses were estimated for COSMOS and ACCEPT by converting X-ray luminosities to M_{500} using the scaling relation in Pratt et al. (2009). Masses for CLASH were estimated through a combination of strong and weak lensing (Merten et al., 2015b).

These results suggest BCG evolution may be affected by cluster mass, although it is possible that different effects might dominate at different redshifts. First, we consider the COSMOS and SPT samples. The COSMOS sample is both significantly more quiescent and lower mass than the SPT sample. The majority of the high-sSFR BCGs in the SPT sample occur at high redshift– while the sSFR characteristics of the COSMOS sample are still systematically lower at low redshift ($\log_{10]}$ sSFR ~ -12.4 yr^{-1} as opposed to -11.7--11.2 yr^{-1}), the sSFR of the SPT sample grows by ~ 1 dex across $0.25 \lesssim z \lesssim 1.0$. Meanwhile, the sSFR of the COSMOS sample grows by ~ 0.5 dex, and the evidence of growth is of marginal statistical significance. McDonald et al. (2016) cite merger driven star-formation in young cluster environments at high redshift as driving the evolution of star formation in their sample. If this evolution is merger driven, then in the high redshift bins, the BCGs of more massive clusters will have undergone more mergers that may drive star formation. As a

result, a high-cluster mass sample like the SPT sample would have BCGs with higher sSFRs than a low-cluster mass sample like COSMOS at high redshifts.

The CLASH and ACCEPT samples, meanwhile, occupy the full range of cluster masses and BCG sSFRs bracketed by the COSMOS and SPT samples. These X-ray selected samples are lower redshift ($\langle z \rangle = 0.39$ for CLASH and 0.14 for the ACCEPT clusters used in this paper, as opposed to 0.75 for the SPT sample), and therefore we expect star formation to be induced by cooling. Taken togethe, they show that the BCG sSFR dependence on mass is much less pronounced in X-ray selected clusters and low- to moderate- redshifts. While the ACCEPT BCGs show a trend between sSFR and M_{500}, we suspect the bolometric luminosity-derived masses in ACCEPT may be biased by cool cores, and so higher masses are actually reflective of brighter cores.

One major caveat has been our assumption that the most massive BCGs in our sample are representative of the massive BCGs investigated in previous studies. When comparing results from discrete redshift bins with a large separation (e.g. $z < 0.1$ and $z > 0.4$), BCGs undergoing cluster and major mergers may be undergoing enhanced star forming activity triggered by compression of gas during the merger. To verify our sample does not include spurious merging systems, we use the COSMOS field ACS/F814W mosaic (Koekemoer et al., 2007; Massey et al., 2010) to visually inspect each target for signs of merging activity. Finding no cases of morphologically disturbed BCGs, disturbed close

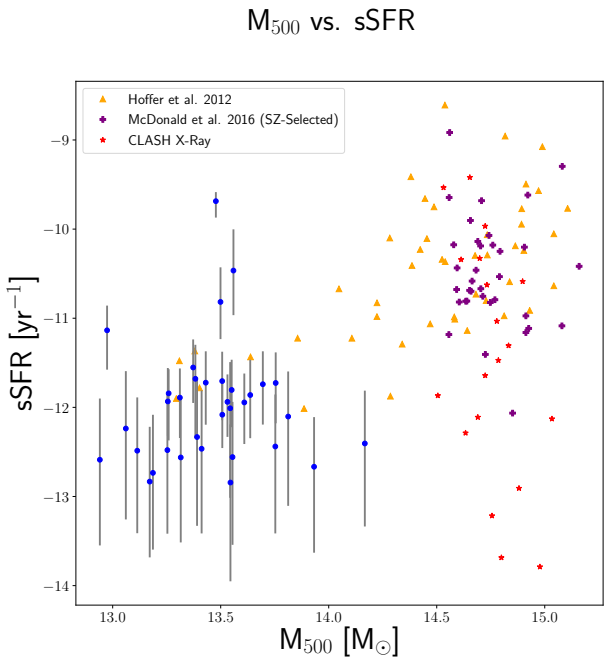

Figure 4.6 sSFR vs. cluster M_{500}. Blue points correspond to BCGs in the COSMOS sample, purple points to BCGs in the McDonald et al. (2016) SPT SZ-selected clusters, yellow points to BCGs with 70 μm detections in the ACCEPT catalog, and red points to BCGs in the CLASH X-ray selected sample.

companions, or tidal tails, we are confident we are not including mid-merger BCGs.

4.6.2 Evolution of $M/L_{3.4\mu m}$ With Redshift

Previous studies at low redshift (e.g. Wen et al., 2013; Fraser-McKelvie et al., 2014) found a correlation between stellar mass and W1 luminosity density at $z < 0.1$. This correlation will evolve with redshift as the W1 band observations include emission from a younger, and brighter, stellar population. Therefore, we measured the evolution of the $M_*/L_{3.4\mu m}$ ratio across a redshift

range between 0.2 - 1.0 using our COSMOS dataset. Our estimated $M_*/L_{3.4\mu m}$ ratio at $z = 0$, $10^{1.38}$, is consistent with the high-mass end of the $M_*/L_{3.4\mu m}$ relationship in Wen et al. (2013). For a $10^{12} M_\odot$ galaxy, Wen et al. (2013) predict a ratio of $10^{1.29}$. Since the masses used in their results were estimated from colors calibrated assuming a Chabrier (2003) IMF, it matches our results given the $\sim$ 0.2 dex offset between the Chabrier (2003) and Salpeter (1955) IMFs.

The slope in our relationship is consistent with the passive evolution of a stellar population becoming redder over time, following a Bruzual & Charlot (2003) evolutionary track from $\sim$ 3 to $\sim$ 10 Gyr old. Our measurement of the $M_*/L_{3.4\mu m}$ ratio is consistent with the body of results supporting dry-merger driven stellar mass growth in BCGs (e.g De Lucia & Blaizot, 2007; Whiley et al., 2008; Vulcani et al., 2016). In particular, our results imply that the addition of new mass to a BCG does not change its mass-to-light ratio, so the stellar population of new mass must be similar to the existing population in the galaxy. Since observations indicate that BCG masses grow by a factor of $\sim$ 2 between z = 0.9 and 0.2, stars from early-type stellar populations must accrete onto the BCGs without triggering star formation (Lidman et al., 2012, 2013; Rodriguez-Gomez et al., 2017). Our findings also align with observations of the evolution of the M_*/L_B ratio out to $z = 0.5$, which also imply passive BCG evolution (van der Marel & van Dokkum, 2007).

4.7 Conclusions

To address the current discrepancies in stellar mass growth for intermediate redshift BCGs, we have fit the SEDs of 38 high mass ($M_{Stellar} > 10^{11} M_{\odot}$) BCGs below $z < 1$ in the COSMOS survey. By retrieving archival data from the FUV to FIR, we have modeled the stellar populations of 33 BCGs (out of a total of 38 fit) and estimated SFR and M_* across 4 redshift bins ($0.15 < z < 0.35$, $0.35 < z < 0.5$, $0.5 < z < 0.65$ and $0.65 < z$). From these estimations we conclude that:

- BCG SFR and sSFR have reached a steady state by $z \sim 1$ in low-mass clusters, which continues to the present-day universe, in contrast to high-mass clusters.

- An evolution of the baryonic $M/L_{3.4\mu m}$ ratio with redshift is observed and fit. This redshift dependent correlation provides an extension of the correlation found by Wen et al. (2013), previously limited to $z < 0.1$.

- Sample selection criteria play a role in stellar mass evolution studies, and we find a possible effect of cluster mass or X-ray vs. SZ selection criterion.

While BCGs exhibit the passive behavior expected, further efforts to understand the history of BCGs require a larger, homogeneously observed and selected census of massive BCGs at high redshift. As it is not clear how many

effects give rise to the diverse results in the field, the differences in BCG stellar mass and SFR characterization practices should be investigated further in order better understand how such different stellar mass growth rates are determined.

Acknowledgments

Based on the COSMOS2015 catalog reduced and compiled by Clotilde Laigle using data taken as part of the COSMOS Collaboration. Based on observations made with the NASA Galaxy Evolution Explorer. GALEX is operated for NASA by the California Institute of Technology under NASA contract NAS5-98034. Based on observations made with the NASA/ESA Hubble Space Telescope, obtained from the Data Archive at the Space Telescope Science Institute, which is operated by the Association of Universities for Research in Astronomy, Inc., under NASA contract NAS 5-26555. Based on observations obtained with Vista/VIRCAM. Based on observations obtained with MegaPrime/MegaCam, a joint project of CFHT and CEA/DAPNIA, at the Canada-France-Hawaii Telescope (CFHT) which is operated by the National Research Council (NRC) of Canada, the Institut National des Sciences de l'Univers of the Centre National de la Recherche Scientifique of France, and the University of Hawaii. Based [in part] on data collected at Subaru Telescope, which is operated by

the National Astronomical Observatory of Japan. Based on observations obtained with WIRCam, a joint project of CFHT, Taiwan, Korea, Canada, France, and the Canada-France-Hawaii Telescope (CFHT) which is operated by the National Research Council (NRC) of Canada, the Institut National des Sciences de l'Univers of the Centre National de la Recherche Scientifique of France, and the University of Hawaii. This work is based [in part] on observations made with the Spitzer Space Telescope, which is operated by the Jet Propulsion Laboratory, California Institute of Technology under a contract with NASA. Herschel is an ESA space observatory with science instruments provided by European-led Principal Investigator consortia and with important participation from NASA. HCSS / HSpot / HIPE is a joint development (are joint developments) by the Herschel Science Ground Segment Consortium, consisting of ESA, the NASA Herschel Science Center, and the HIFI, PACS and SPIRE consortia.

4.8 Appendix

Table 4.3. BCG Best-Fit Parameters

BCG	Redshift	χ^2	SFR[a] $\log_{10}(M_\odot\ yr^{-1})$	sSFR[a] yr^{-1}
COSMOSCLJ100056.8+021225	0.3601000011	1.34	$-0.72^{+0.65}_{-1.01}$	$-12.24^{+0.64}_{-1.02}$
COSMOSCLJ100051.5+021648	0.8482000232	3.09	$1.19^{+0.41}_{-0.51}$	$-10.47^{+0.46}_{-0.5}$
COSMOSCLJ100013.9+022249	0.3400000036	2.47	$-0.95^{+0.63}_{-0.9}$	$-12.48^{+0.63}_{-0.94}$
COSMOSCLJ095907.2+022358	0.3512000144	2.34	$-1.0^{+0.68}_{-0.93}$	$-12.59^{+0.69}_{-0.96}$
COSMOSCLJ100027.4+022123	0.2197999954	4.37	$-1.21^{+0.59}_{-0.84}$	$-12.83^{+0.61}_{-0.85}$
COSMOSCLJ095847.9+022410	0.3546000123	3.51	$-1.06^{+0.68}_{-0.84}$	$-12.74^{+0.65}_{-0.86}$
COSMOSCLJ095945.1+023622	0.3395999968	2.63	$-1.18^{+0.66}_{-0.93}$	$-12.56^{+0.68}_{-0.95}$
COSMOSCLJ100135.3+024617	0.8201000094	1.71	$-0.05^{+0.35}_{-0.44}$	$-11.73^{+0.34}_{-0.45}$
COSMOSCLJ100111.9+014037	0.5124999881	0.87	$0.37^{+0.38}_{-0.42}$	$-10.82^{+0.39}_{-0.42}$
COSMOSCLJ095924.4+014623	0.1099999994	11.79	–	–
COSMOSCLJ100049.6+014923	0.5299999714	1.85	$-0.12^{+0.36}_{-0.47}$	$-11.72^{+0.35}_{-0.47}$
COSMOSCLJ100139.3+015051	0.9818999767	0.29	$-0.13^{+0.36}_{-0.44}$	$-11.74^{+0.37}_{-0.45}$
COSMOSCLJ095805.4+015256	0.5207999945	1.47	$0.04^{+0.32}_{-0.38}$	$-11.55^{+0.31}_{-0.4}$
COSMOSCLJ100217.7+015601	0.3007000089	7.5	$-0.84^{+0.67}_{-0.97}$	$-12.33^{+0.66}_{-1.0}$
COSMOSCLJ100128.6+015958	0.8223999739	1.38	$0.04^{+0.32}_{-0.44}$	$-11.71^{+0.33}_{-0.44}$
COSMOSCLJ100035.2+020346	0.7351999879	9.84	$1.82^{+0.09}_{-0.14}$	$-9.69^{+0.1}_{-0.18}$
COSMOSCLJ100200.6+020405	0.4142999947	2.14	$-0.83^{+0.65}_{-0.92}$	$-12.46^{+0.65}_{-0.95}$
COSMOSCLJ095940.6+023603	0.2556000054	4.95	$0.57^{+0.27}_{-0.41}$	$-11.14^{+0.28}_{-0.44}$
COSMOSCLJ095957.1+023506	0.6697000265	0.71	$-0.39^{+0.37}_{-0.38}$	$-11.93^{+0.37}_{-0.39}$
COSMOSCLJ100141.0+015904	0.301699996	12.76	–	–
COSMOSCLJ100139.2+022435	0.3903000057	2.71	$-0.26^{+0.51}_{-0.96}$	$-12.01^{+0.52}_{-1.0}$
COSMOSCLJ100201.2+021330	0.8249999881	2.84	$-0.3^{+0.58}_{-0.95}$	$-12.44^{+0.58}_{-0.98}$
COSMOSCLJ100005.7+021211	0.9232000113	1.42	$0.12^{+0.3}_{-0.41}$	$-11.94^{+0.31}_{-0.39}$
COSMOSCLJ095833.6+022056	0.9919000268	2.59	$0.37^{+0.39}_{-0.67}$	$-11.68^{+0.38}_{-0.67}$
COSMOSCLJ100021.8+022328	0.2099999934	9.37	$-1.15^{+0.63}_{-1.07}$	$-12.84^{+0.65}_{-1.11}$
COSMOSCLJ095931.8+022654	0.3600000143	2.99	$-0.74^{+0.6}_{-0.96}$	$-12.56^{+0.62}_{-0.98}$
COSMOSCLJ100016.0+023850	0.7070999742	1.88	$-0.58^{+0.6}_{-0.92}$	$-12.41^{+0.59}_{-0.93}$
COSMOSCLJ095941.6+023129	0.7178999782	1.25	$-0.59^{+0.6}_{-0.88}$	$-12.49^{+0.6}_{-0.93}$
COSMOSCLJ100056.0+022834	0.3799999952	5.31	$-0.11^{+0.32}_{-0.45}$	$-11.94^{+0.32}_{-0.47}$
COSMOSCLJ100013.0+023519	0.6399999857	2.65	$-0.1^{+0.41}_{-0.47}$	$-11.86^{+0.4}_{-0.48}$
COSMOSCLJ100028.3+024103[b]	1.2903000116	–	–	–
COSMOSCLJ095901.5+024740	0.4900000095	4.04	$-0.07^{+0.35}_{-0.4}$	$-12.08^{+0.37}_{-0.37}$
COSMOSCLJ095824.0+024916[b]	1.2108000517	–	–	–
COSMOSCLJ100020.7+023153	0.8702999949	2.27	$0.23^{+0.34}_{-0.42}$	$-11.8^{+0.34}_{-0.42}$
COSMOSCLJ100027.0+023321	0.5	5.65	$-0.12^{+0.51}_{-1.01}$	$-12.1^{+0.51}_{-1.0}$
COSMOSCLJ100031.5+015108	0.5202000141	3.74	$0.03^{+0.32}_{-0.46}$	$-11.89^{+0.33}_{-0.45}$
COSMOSCLJ100045.6+013926	0.2099999934	12.81	–	–
COSMOSCLJ095951.4+014049	0.3802999854	15.45	–	–
COSMOSCLJ100043.2+014607	0.3400000036	7.44	$-0.77^{+0.56}_{-0.92}$	$-12.67^{+0.56}_{-0.96}$
COSMOSCLJ100147.3+020314	0.3235000074	7.58	$0.05^{+0.26}_{-0.52}$	$-11.84^{+0.27}_{-0.53}$

Note. — [a] Uncertainties denote the 1σ credible intervals for each value based on `iSEDfit`. [b] Excluded from the sample owing to ambiguous estimated redshifts.

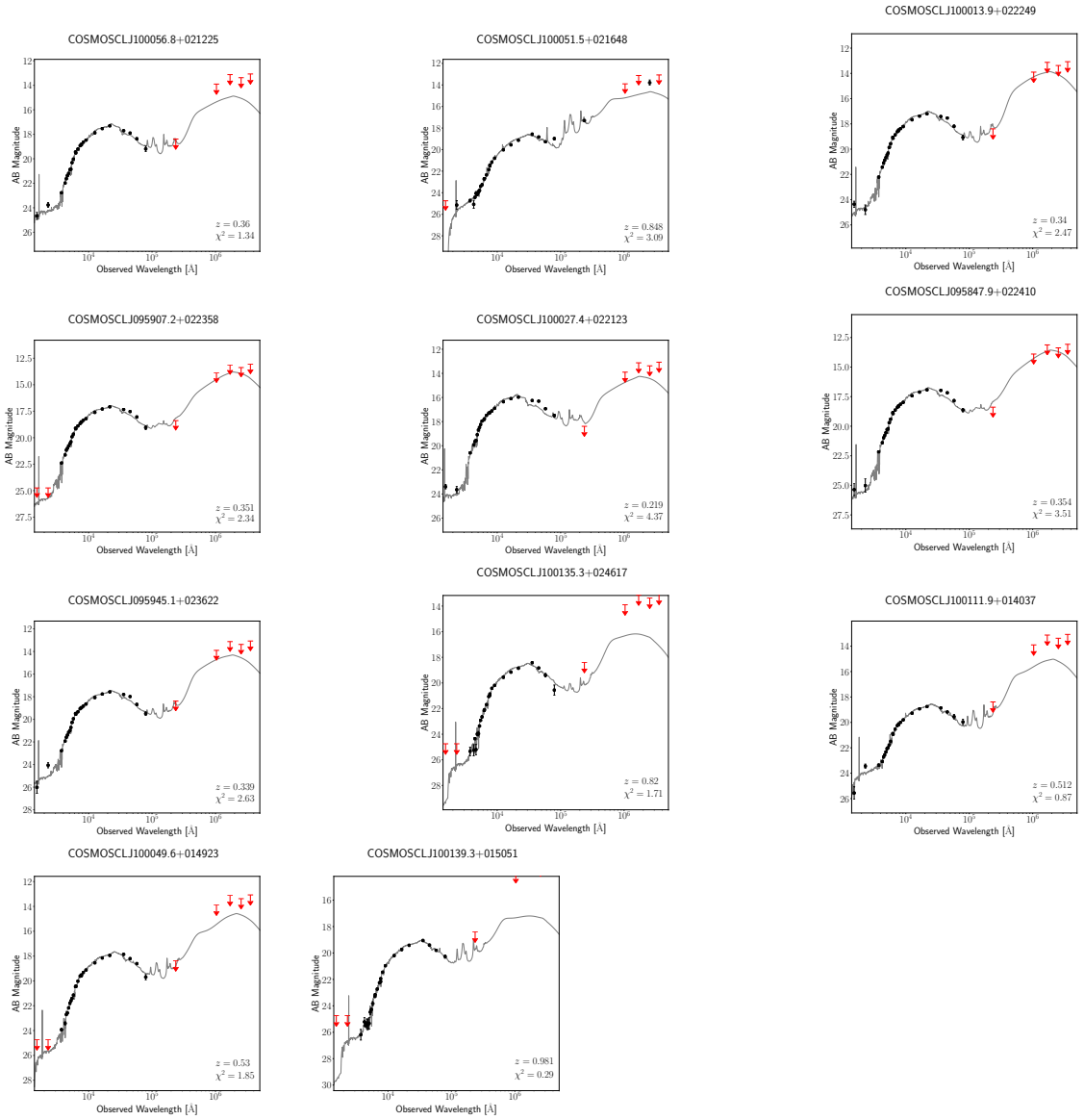

Figure 4.7 Best-fit models for the COSMOS BCGs. COSMOS SEDs are plotted in each figure as black points (for detections) and red arrows (for 3σ upper limits). Error bars depicted on the SEDs are 1σ error bars. The gray line in each plot depicts the best-fit spectrum, corresponding to the model producing the smallest reduced χ^2 in the `iSEDfit` Monte Carlo grid.

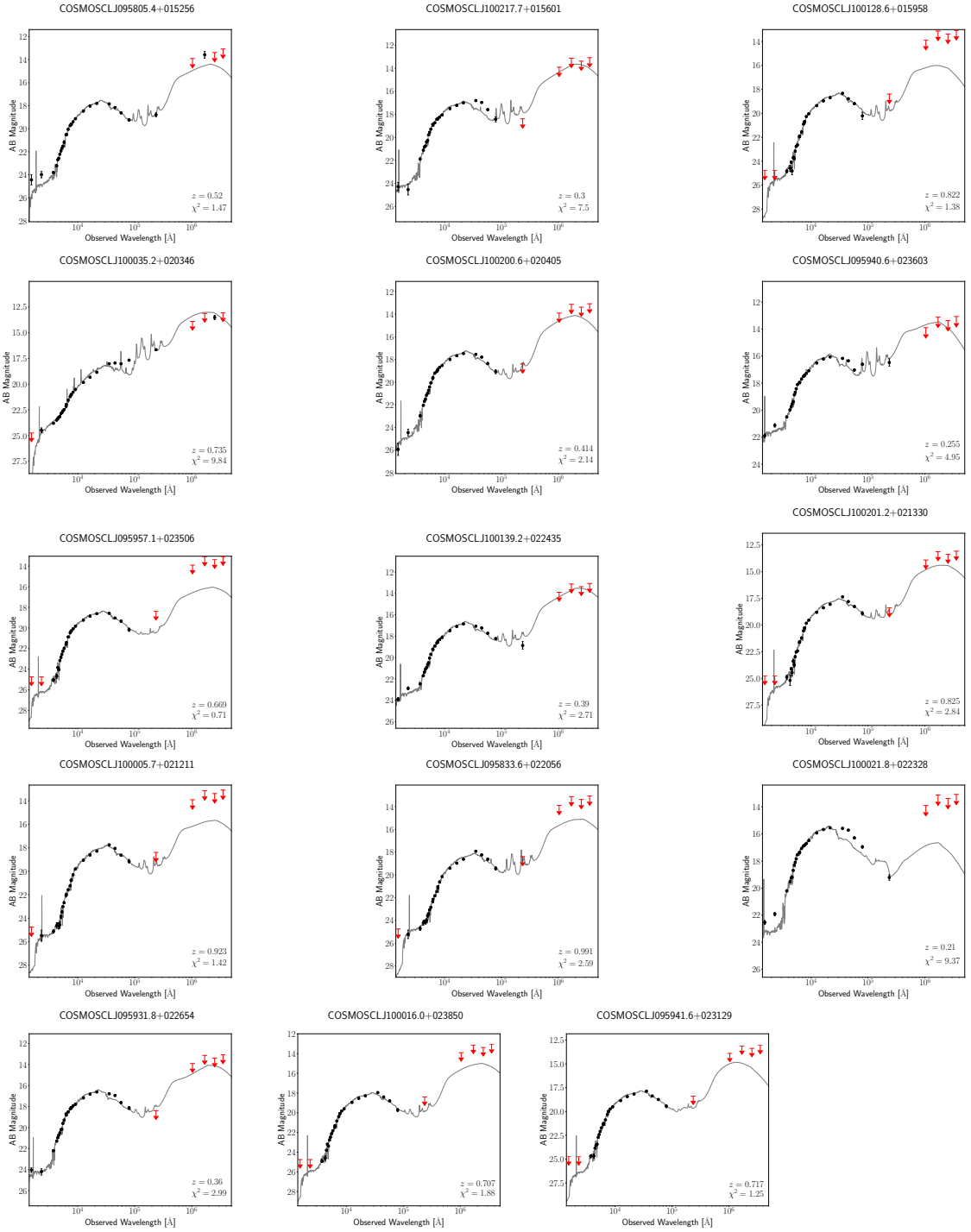

Figure 4.7 *Continued*

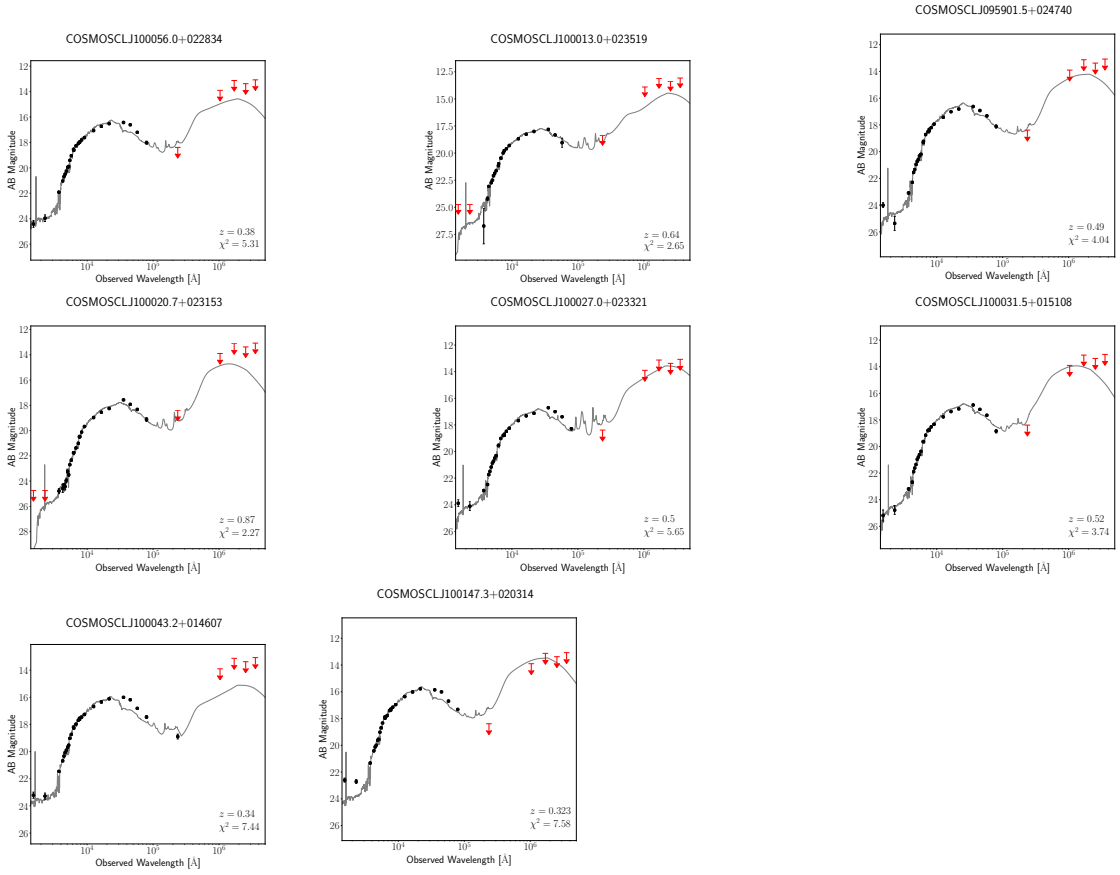

Figure 4.7 *Continued*

Chapter 5

Concluding Remarks

In this thesis, I primarily used SED fitting techniques to estimate the properties of BCG stellar populations to provide a new observational perspective on how BCGs are regulated by cluster environments. The datasets produced by multi-wavelength, multi-observatory surveys such as CLASH and COSMOS are ideal for exploiting this technique, allowing one to measure SFRs, stellar and dust masses, and provide constraints on the ages of stellar populations. While CLASH represented an ideal dataset for the analysis I performed in Chapters 2 and 3, I hope to augment the results presented here with additional overlapping UV-IR and X-ray datasets.

In particular, the relationship between SFR and t_{cool}/t_{ff} in Chapter 3 provides a new constraint on cluster-scale feedback models that I hope may be explored further. Considering that providing strong evidence of the role of t_{ff}

in condensation one way or another will constrain what 'modes' of AGN feedback are present in cool-core clusters, it will be worthwhile to replicate the results Chapter 3 with larger samples, such as SDSS Stripe 82 clusters observed with *Chandra* (LaMassa et al., 2016), the SPT cluster sample (McDonald et al., 2016), or a successor to ACCEPT.

The results of Chapter 3 also pose something of a mystery, since taken together with UV and X-ray observations of cooling they demonstrate a temporal disconnect between condensation, precipitation, and feedback. BCG star formation often does not accompany UV emission lines indicative of cooling, and while there is often evidence of radio-mode AGN, AGN-related X-ray point source emission is rarely detected. Do star formation and the cooling time of the ICM represent time-average proxies for feedback-regulated condensation? Does condensation occur stochastically, or possibly cyclically? Further study of far-UV and soft X-ray cooling lines may shed light on these questions.

Recently, we have proposed ALMA observations to observe both the molecular gas and dust in core of MACS1931.8-2635, which hosts an extreme starburst producing stars at a rate of ~ 250 $M_\odot$ yr^{-1}. Our observations will constrain the origin and distribution of dust in this system, which is a component of the multiphase medium that has yet to be fully accounted for. We have been awarded Cycle 5 time for to address this question, and have recently obtained Cycle 4 data as well. Unfortunately, the Cycle 4 data is still being processed

as of this writing, and so could not be included in this thesis. The *Chandra* image of MACS1931.8-2635 also reveals a bow shock in the cluster core, and our Cycle 4 data will determine whether condensation occurs at the site of this shock.

Finally, this thesis has examined the condensation of the ICM and its imprints on the stellar population of BCGs. A natural extension of this effort is to examine precipitation and accretion of this material onto AGN. Studying precipitation and accretion entails the sorts of small inner working angle imaging achievable with radio interferometers and high contrast imaging. I have been fortunate to have the opportunity to work on a wide range of projects during my graduate school career, including both the observational work I presented in the body of my thesis and the instrument design work I present in the appendix. Eventually I expect to achieve synthesis between these two domains, as high-contrast imaging pushes the limits not only of directly observing extrasolar systems, but also of the inner reaches of bright AGN and quasars.

Appendix A

Polynomial Apodizers for Centrally Obscured Vortex Coronagraphs

Abstract

Several coronagraph designs have been proposed over the last two decades to directly image exoplanets. Among these designs, vector vortex coronagraphs provide theoretically perfect starlight cancellation along with small inner working angles when deployed on telescopes with unobstructed pupils. However, current and planned space missions and ground-based extremely large telescopes present complex pupil geometries, including large central obscurations caused by secondary mirrors, that prevent vortex coronagraphs from rejecting on-axis sources entirely. Recent solutions combining the vortex phase mask with a ring-apodized pupil have been proposed to circumvent this issue, but provide a limited throughput for vortex charges > 2. We present pupil plane apodizations for charge 2, 4, and 6 vector vortex coronagraphs that compensate for pupil geometries with circularly symmetric central obstructions caused by on-axis secondary mirrors. These apodizations are derived analytically and allow vortex coronagraphs to retain theoretically perfect nulling in the presence of obstructed pupils. For a charge 4 vortex, we design polynomial apodiza-

tion functions assuming a greyscale apodizing filter that represent a substantial gain in throughput over the ring-apodized vortex coronagraph design, while for a charge 6 vortex, we design polynomial apodized vortex coronagraphs that have $\gtrsim 70\%$ total energy throughput for the entire range of central obscuration sizes studied. We propose methods for optimizing apodizations produced with either greyscale apodizing filters or shaped mirrors. We conclude by demonstrating how this design may be combined with apodizations numerically optimized for struts and primary mirror segment gaps to design terrestrial exoplanet imagers for complex pupils.

planets and satellites: detection - instrumentation: adaptive optics - instrumentation: high angular resolution - techniques: high angular resolution - telescopes

A.1 Introduction

Upcoming and proposed space and large ground-based telescope designs offer the sensitivity and resolution necessary to begin probing sub-Jovian and, in the case of space missions, terrestrial exoplanets with high contrast direct imaging (Kasper et al., 2010; Hinkley et al., 2011; Bolcar et al., 2015; Dalcanton et al., 2015). Recently, protoplanetary discs and massive, young exoplanets have been directly imaged using coronagraphs to suppress starlight to the level where these orbiting bodies can be observed (Marois et al., 2008; Kalas et al., 2008; Lagrange et al., 2009; Marois et al., 2010; Andrews et al., 2011; Carson et al., 2013; Kuzuhara et al., 2013; Rameau et al., 2013; Oppenheimer et al.,

2013; Mancini et al., 2015; Macintosh et al., 2015; Wagner et al., 2015; Pueyo et al., 2015). However, observing fainter objects, such as Earth-like exoplanets, with future observatories poses a challenge for coronagraph designs, which will need to be adapted to the obstructed pupil geometries of telescopes with on-axis secondary mirrors and segmented primary mirrors(Pueyo & Norman, 2013; Soummer et al., 2011; Guyon et al., 2014).

Several strategies are being developed to design coronagraphs for telescopes with obstructed pupils. Using one approach, the original Lyot coronagraph design can be modified by altering the shape of the Lyot stop to block artifacts introduced by the pupil geometry (Sivaramakrishnan et al., 2001; Sivaramakrishnan & Yaitskova, 2005). Other approaches involve a combination of modifications to the pupil and focal plane geometries of the coronagraph, both to improve coronagraphic performance for unobstructed pupils and to compensate for complicated pupils. For example, the apodized pupil Lyot coronagraph (APLC) modifies the Lyot coronagraph by introducing a pupil apodizing mask in order to improve starlight suppression for broadband light with an obstructed pupil (Soummer, 2005; N'Diaye et al., 2015).

Furthermore, the occulting spot in the Lyot coronagraph can be replaced by more complicated focal plane masks that involve a combination of phase shifting and apodization, such as the hybrid Lyot coronagraph (Kuchner & Traub, 2002; Moody & Trauger, 2007; Moody et al., 2008; Trauger et al., 2012; Trauger

et al., 2016).

Phase Induced Amplitude Apodization (PIAA) of the pupil plane with fixed shaped mirrors, combined with a system of apodizers and inverse-optics, has also been widely explored as a method for overcoming arbitrary pupil shapes (Guyon, 2003; Traub & Vanderbei, 2003; Guyon et al., 2005; Cady, 2012). Fixed mirror apodization has also been combined with some of the complex coronagraph designs described above, such as the PIAA complex mask coronagraph (PIAACMC), which combines PIAA with a complex focal plane mask (Guyon et al., 2014). These recent instrument designs depart considerably from the coronagraph proposed in Lyot (1939), and represent substantial progress towards achieving terrestrial exoplanet direct imaging capability.

Coronagraphs using a vector vortex phase mask in the focal plane potentially provide substantial gains over other designs in terms of starlight suppression while maintaining high instrumental throughput for sources at close separations from a target star (Foo et al., 2005; Mawet et al., 2005). In principle, the vector vortex coronagraph provides full cancellation of on-axis starlight in the absence of pupil obstructions with little suppression of nearby off-axis sources (Mawet et al., 2011a). Vector vortex coronagraphs also permit small inner working angles (IWAs) (in some cases as small as $\sim 1\lambda/D$), enabling observations of planets with relatively tight orbits (Mawet et al., 2009, 2011b). In addition to entirely rejecting the light from a target star, these masks can

be made theoretically achromatic by using subwavelength gratings to create phase shifts in the focal plane (Mawet et al., 2005, 2007). However, vector vortex coronagraphs only provide ideal starlight suppression with clear circular pupils, and are particularly impacted by the central obscuration imposed by a secondary mirror, which is the largest cause of pupil-geometry induced stellar flux residual in the coronagraphic image. (Mawet et al., 2011a, 2013; Fogarty et al., 2014).

Recent work has made progress adapting the vector vortex coronagraph to on-axis telescopes. Mawet et al. (2013) proposed an analytical solution to the problem of the central obscuration by apodizing the pupil of the vector vortex coronagraph with a filter consisting of semi-transmissive, hard edged annuli or 'rings'. The ring apodized vortex coronagraph (RAVC) solves the issue of suppression loss due to the central obscuration. Unfortunately, the throughput of the RAVC decreases rapidly as the radius of the central obscuration increases, so we seek alternatives to the RAVC for high-contrast imaging applications with on-axis telescopes.

In this paper we present a new method to compensate for the central obscuration of an on-axis telescope with a vortex coronagraph. Our results are a generalization of the RAVC, obtained by extending the formalism of previous work presented in Fogarty et al. (2014) to derive novel solutions. Our previous work used linear programming to find apodization functions composed of basis

APPENDIX A. POLYNOMIAL APODIZERS FOR CENTRALLY OBSCURED VORTEX CORONAGRAPHS

Bessel functions that resolve the issue of limited throughput in the RAVC while providing 10^{-10} starlight suppression in monochromatic light. We adopt the linear programming formalism used in that paper to optimize pupil apodizations composed of piecewise polynomials. Using this new basis, we are able to use this approach to find throughput-maximizing pupil plane apodizations for vector vortex coronagraphs that produce theoretically perfect cancellation of on-axis starlight.

Taking advantage of the the large number of possible solutions available that null the Lyot plane electric field, we can create apodizations for the PAVC that are either discontinuous or smooth. We present PAVCs with topological charges 2, 4, and 6 that are optimized to maximize transmission if the pupil apodization is produced by an apodizing filter. We also present examples of apodization functions that may be produced by pairs of shaped mirrors, using a similar technique to PIAA, and that minimize the curvature of these mirrors.

The polynomial apodized vortex coronagraph (PAVC) designs we describe in this paper have several desirable properties that make them a good candidate for delivering extremely high contrast imaging on large, on-axis telescopes. Like the RAVC, PAVC designs are inherently broadband and offer an exact solution to the problem posed by centrally obscured pupils. However, since the RAVC 'ring' apodization functions are a special case of PAVC apodizations, we are able to significantly improve throughput performance. We find that

the throughput of a PAVC increases as the topological charge (the topological charge of the vortex is described in § 2.1) of the vortex increases, and that throughput falls as a function of secondary mirror radius more gradually than the RAVC for charges > 2. As a result, the PAVC is a viable option for designing a high-throughput vortex coronagraph on a telescope with a large central obscuration, particularly if the topological charge of the vector vortex is > 2. By combining the PAVC with techniques to mitigate diffraction due to the discontinuities imposed on the pupil by secondary struts and primary mirror gaps, we can design intruments that deliver both high throughput and on-axis starlight suppression on telescopes with complex apertures.

A.2 The Analytical Vortex Operator and Optimal Mask Algorithm

A.2.1 The Vector Vortex

A vortex phase mask is an azimuthal phase ramp that replaces the occulting Lyot spot in the focal plane of a coronagraph. It causes the phase of an electric field propagating through it to undergo a rotation $e^{ic\theta}$, where θ is the angular coordinate in the coordinate system whose origin is the center of the phase mask and c is the topological charge of the phase mask. The topological

charge (hereafter referred to as 'charge') determines the number of 'rotations' the phase of the electric field undergoes per rotation around the center of the mask (see Figure 2 in Mawet et al. (2011c)). A vortex phase mask in the focal plane of a coronagraph suppresses on-axis starlight by shifting it out of the radius of the original pupil in the subsequent Lyot plane. Vortices always carry even-numbered charges, since odd-numbered charges do not suppress on-axis starlight in un-obscured pupils (Mawet et al., 2005).

The charge of a vortex coronagraph affects both its IWA and how stable the instrument must be kept to prevent on-axis starlight from 'leaking' into the final image. In particular, charge 2 vortex coronagraphs permit small, $\sim 1\lambda/D$ IWAs, at the expense of sensitivity to low-order aberrations and finite stellar angular size (Mawet et al., 2009, 2011b). Charge 2 vortex coronagraphs are suitable for instruments designed to achieve contrasts of $\sim 10^{-6}$; however, the sensitivity of the charge 2 vortex phase mask to low-order aberrations prevents it from being useful for obtaining larger contrasts (Mawet et al., 2010). Vortex coronagraphs with charges higher than 2, which offer lower sensitivity to low-order aberration at the expense of larger IWAs, are typically considered more likely candidates for terrestrial exoplanet characterizing instruments (Jenkins, 2008; Mawet et al., 2010).

The same property that allows a vortex phase mask in the focal plane to reject on-axis starlight from an unobscured pupil is what causes the vortex

coronagraph to lose starlight suppression in the presence of a central obscuration (Mawet et al., 2011a, 2013; Fogarty et al., 2014). Namely, multiplying the Airy pattern of a uniform aperture in the focal plane by $e^{ic\theta}$ causes the light through that aperture to disperse into a ring with an inner radius corresponding to the outer radius of the aperture when it propagates into the Lyot plane. The amplitude of this ring peaks at the aperture radius, and falls off as the radius increases. However, a central obscuration in the pupil serves to subtract a uniform disc from the center of the pupil, essentially creating two concentric Airy patterns in the focal plane. Therefore, the vortex coronagraph disperses some of the on-axis starlight into a ring around the central obscuration in the Lyot plane, putting it back into the aperture of the pupil. Depending on the the size of the central obscuration, the residual starlight in the aperture limits the contrast achievable by the vortex coronagraph to $10^{-2} - 10^{-1}$ if left uncorrected (Mawet et al., 2011a).

Table A.1 Summary of Important Variables for Deriving the Apodized Vortex Formalism

Summary of Variables

Description	Variable
Pupil/Lyot Plane Coordinates	(r, θ)
Focal Plane Coordinates	(k, θ)
Vortex Topological Charge	c
Secondary Mirror Radius	R_S
Primary Mirror Radius	R_P
Inner Lyot Stop Radius	R_I
Vortex Operator for a vortex of charge c	V_c

A.2.2 Apodized Vortex Formalism

We intend to solve the problem posed by telescope pupils with central obscurations by apodizing the entrance pupil of the vortex coronagraph. The coronagraphic setup we use is shown in Figure A.1 and consists of three stages, which are labelled in the figure as Stages A, B, and C. Light from a directly on-axis source enters a pupil of radius R_P, which is obscured by a secondary mirror of radius R_S. At stage A, the pupil is apodized, which in Figure A.1 is accomplished by using a greyscale apodizing filter. At stage B, the light passes through the vortex mask in the focal plane, before arriving the inner Lyot stop at stage C, which blocks flux within a radius R_I in the Lyot plane. The final coronagraphic image is formed by focusing the beam in the Lyot plane onto a detector placed downstream of the coronagraph. Throughout this paper, we will use the polar coordinates (r, θ) when discussing the pupil and Lyot planes (stages A and C), and coordinates (k, θ) when discussing the focal plane (stage B) and final image (see Table A.1 for an overview of the important variables used in this discussion).

We define the "vortex operator" to be the operator mapping the electric field at the coronagraph entrance pupil to the electric field in the Lyot plane for the PAVC setup depicted in Figure A.1. We will show that when the pupil plane is apodized by a polynomial apodization function ($A(r) = c_0 + c_1 r + c_2 r^2 + ...$ at Stage A in Figure A.1), the vortex operator may be solved analytically. Us-

ing this analytical solution, we can constrain the coefficients of the polynomial apodization function to find optimal PAVCs that have no on-axis source flux in the Lyot plane using linear programming.

We proceed to derive the vortex operator for a PAVC with a vortex of charge c and a pupil apodization function $A(r)$, which we label $V_c[A(r)]$. Since the pupil radius in Figure A.1 is R_P and the radius of the central obscuration is R_S, the field in the pupil due to an on-axis point source of unit flux is

$$P(r) = \Pi_{0,R_P}(r) - \Pi_{0,R_S}(r), \tag{A.1}$$

where $\Pi_{a,b}(x)$ is the unit boxcar function with lower bound a and upper bound b. Since the pupil is apodized by $A(r)$, the electric field at stage A, F_A, is

$$F_A(r) = A(r)\,P(r). \tag{A.2}$$

At stage B, the beam undergoes a Fourier transformation, and is acted on by a vortex phase mask of charge c in the focal plane. F_A is an axisymmetric function, so the Fourier Transform of F_A is equivalent to the zeroth order Hankel Transform, H_0. The field at stage B just before the vortex phase mask is therefore

$$F_B(k) = H_0[F_A(r)]. \tag{A.3}$$

APPENDIX A. POLYNOMIAL APODIZERS FOR CENTRALLY OBSCURED VORTEX CORONAGRAPHS

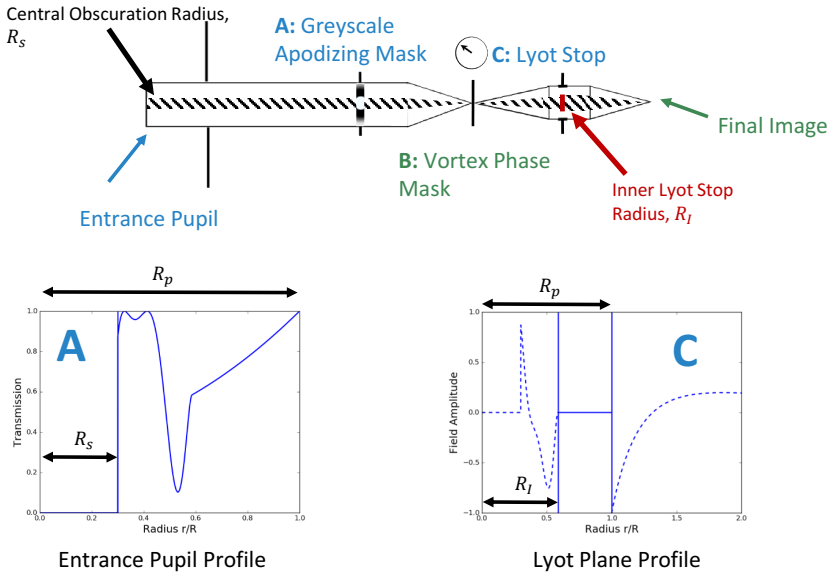

Figure A.1 An overview of the coronagraphic setup discussed in this paper. The coronagraph consists of three stages: (A) the apodizing mask, (B) the vortex phase mask, and (C) the inner Lyot stop. When the beam hits stages A and C, it is in the pupil plane, and at stage B it is in the focal plane. The diagonal hatching indicates the region of the beam that is blocked by the secondary mirror and by the inner Lyot stop. In this figure, blue text refers to parts of the beam in the pupil plane, while green text refers to parts of the beam in the focal plane, including the final image point spread function (PSF). The bottom left inset shows an example of the apodized transmission of flux from an on-axis source through stage A, with an apodization function optimized for a charge 4 vortex and a central obscuration that is 30% the radius of the pupil. The bottom right inset shows the field at stage C- the dashed lines show where the field is either outside the radius of the pupil R_P or is blocked by the inner Lyot stop with radius R_I.

APPENDIX A. POLYNOMIAL APODIZERS FOR CENTRALLY OBSCURED VORTEX CORONAGRAPHS

After the beam passes through the vortex phase mask, the electric field is

$$\boldsymbol{F_{B2}\left(k,\theta\right)=F_{B}\left(k\right)e^{ic\theta}}. \tag{A.4}$$

The beam is transformed back to the pupil plane (referred to in this case as the Lyot plane) at stage C. Just before the Lyot stop, the field at stage C is $F_C\left(r\right)=H_c^{-1}\left[F_B\left(k\right)\right]$, where H_c^{-1} is the inverse Hankel transform of order c. This can be obtained by re-arranging the inverse Fourier transform:

$$\begin{aligned} F_C\left(r\right) &= \frac{1}{2\pi}\int F_B\left(k\right)e^{ic\theta}e^{i\sin kr\theta}kdkd\theta_k \\ &= \int_0^\infty F_B\left(k\right)\left(\frac{1}{2\pi}\int_{-\pi}^{\pi}e^{-i(c\tau-kr\sin\tau)}d\tau\right)kdk \\ &= \int_0^\infty F_B\left(k\right)J_c\left(kr\right)kdk \\ &= \mathbf{H_c^{-1}}\left[\mathbf{F_B}\left(\mathbf{k}\right)\right], \end{aligned} \tag{A.5}$$

where J_c is the Bessel function of order c and where we have dropped the final phase term. Putting equations A.2 through A.5 together, we get the expression for the vortex operator: $V_c\left[A\left(r\right)\right]=H_c^{-1}\left[H_0\left[A\left(r\right)P\left(r\right)\right]\right]$. Expanding this out, we

get,

$$\begin{aligned} V_c\left[A\left(r\right)\right] = \int_0^\infty \Bigg(\int_0^\infty A\left(r'\right) \left(\Pi_{0,R_P}\left(r'\right) - \right. \\ \left. \Pi_{0,R_S}\left(r'\right)\ \right) J_0\left(kr'\right) r' dr' \Bigg) J_c\left(kr\right) k dk \\ = \int_0^\infty \left(\int_{R_S}^{R_P} A\left(r'\right) J_0\left(kr'\right) r' dr' \right) J_c\left(kr\right) k dk. \end{aligned} \tag{A.6}$$

When the apodization function $A\left(r\right)$ is of the form r^n (where n is an integer), equation A.6 takes on a simple form for even charges c. For $c = 2$, we get,

$$V_2\left[r^n\right] = \begin{cases} 0, & \text{if } r < R_S \\ \frac{-n}{n+2} r^n + \frac{2}{n+2} R_S^{n+2} \frac{1}{r^2}, & \text{if } R_S \leq r \leq R_P \\ \frac{-2}{n+2}\left(R_S^{n+2} - R_P^{n+2}\right) \frac{1}{r^2}, & \text{if } r > R_P, \end{cases} \tag{A.7}$$

for $c = 4$,

$$V_4\left[r^n\right] = \begin{cases} 0, & \text{if } r < R_S \\ \frac{(n-2)nr^n}{(n+2)(n+4)} - \frac{4R_S^{n+2}}{n+2} \frac{1}{r^2} & \text{if } R_S \leq r \leq R_P \\ + \frac{12R_S^{n+4}}{n+4} \frac{1}{r^4} & \\ - \frac{4\left(R_S^{n+2} - R_P^{n+2}\right)}{n+2} \frac{1}{r^2} + & \text{if } r > R_P \\ \frac{12\left(R_S^{n+4} - R_P^{n+4}\right)}{n+4} \frac{1}{r^4} & \end{cases} \tag{A.8}$$

and for $c = 6$,

$$V_6\left[r^n\right] = \begin{cases} 0, & \text{if } r < R_S \\ \frac{-n(n-2)(n-4)}{(n+2)(n+4)(n+6)} r^n + \frac{6R_S^{n+2}}{n+2}\frac{1}{r^2} & \text{if } R_S \leq r \leq R_P \\ -\frac{48R_S^{n+4}}{n+4}\frac{1}{r^4} + \frac{60R_S^{n+6}}{n+6}\frac{1}{r^6} & \\ \frac{6\left(R_S^{n+2} - R_P^{n+2}\right)}{n+2}\frac{1}{r^2} & \text{if } r > R_P \\ -\frac{48\left(R_S^{n+4} - R_P^{n+4}\right)}{n+4}\frac{1}{r^4} & \\ +\frac{60\left(R_S^{n+6} - R_P^{n+6}\right)}{n+6}\frac{1}{r^6} & \end{cases} \tag{A.9}$$

For larger even charges, similar expressions of increasing length may be calculated. We show $V_c\left[r^n\right]$ for $c = 2, 4, 6$ and $n = 0, 1, 2, 3$ in Figure A.2. Equations A.7-A.9 show that the vortex operator $V_c\left[A\left(r\right)\right]$ can be solved in closed form for any apodization function $A\left(r\right)$ that is in piecewise polynomial form (i.e. that can be decomposed into terms r^n that are non-zero over some range of radii). We also note that analytical solutions to equation A.6 for non-axisymmetric pupil geometries exist and are presented in Appendix A.

A.2.3 Optimal Mask Algorithm

By taking advantage of the simple expressions for $V_c\left[r^n\right]$ in Equations A.7-A.9, we can set up a linear program to find optimal apodizing masks that

APPENDIX A. POLYNOMIAL APODIZERS FOR CENTRALLY OBSCURED VORTEX CORONAGRAPHS

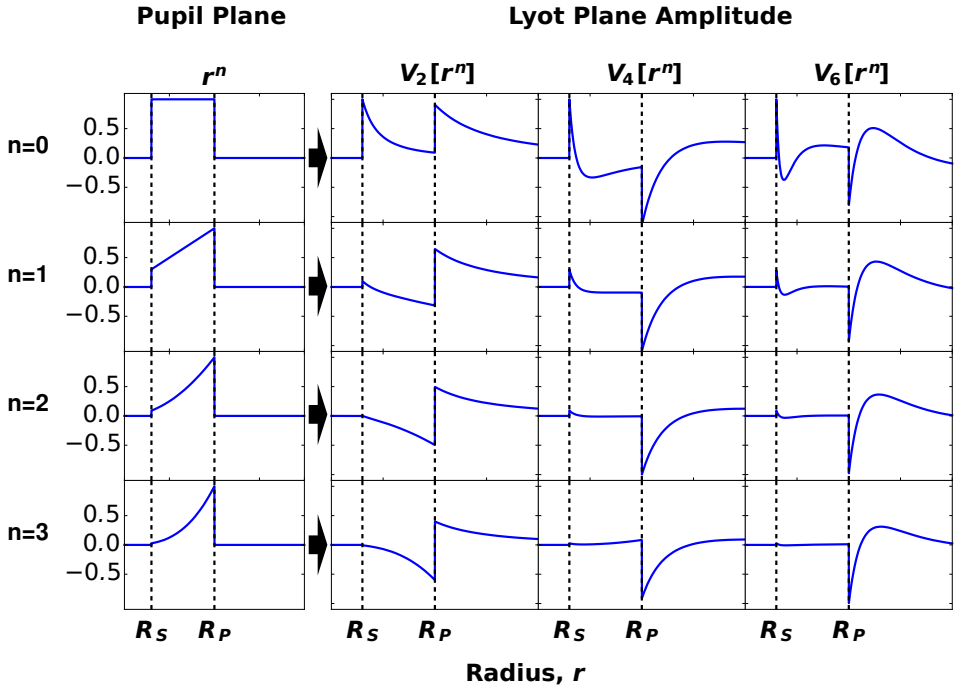

Figure A.2 The vortex operator for a charge 2, 4, and 6 PAVC acting on r^n for $n = 0, 1, 2, 3$. The left hand column shows the electric field amplitude in the pupil as a function of radius, apodized by (from top to bottom) $A(r) = 1$, r, r^2, or r^3. The plots in the 3x4 grid to the right depict the electric field amplitude in the Lyot plane as a function of radius after the pupil geometries in the left column are acted on by the vortex operator. The column depicts the the results of V_2 acting on r^n for each value of n, the second column the results for V_4, and the third column for V_6. Solid blue lines depict electric field amplitude. The black dashed lines depict the positions of R_S and R_P in each plot.

null an on-axis point source observed with an obstructed pupil. We search for apodizations of the form:

$$A(r) = \begin{cases} \sum_{n=0}^{N} a_n r^n, & \text{if } R_S < r \leq R_I. \\ \sum_{n=0}^{N} a_n r^n + b_n r^n, & \text{if } R_I < r \leq R_P, \end{cases} \tag{A.10}$$

where $R_I \geq R_S$ and where N is the order of the piecewise polynomial we wish to use to describe $A(r)$.

Using the closed-form solutions we found for $V_c[r^n]$, we can find linear constraints on the coefficients a_n and b_n of the apodization function such that in the Lyot plane (Stage C in Figure A.1), the electric field is exactly zero at radii greater than R_I and less than R_P. Since the inner Lyot stop at Stage C covers the region $r < R_I$, an apodization function that is a solution to this linear program produces perfect cancellation of the on-axis starlight.

The apodization function in Equation A.10 consists of two sets of components– 'a_n' components which are non-zero between R_S and R_P and zero elsewhere, and 'b_n' components which are non-zero between R_I and R_P and zero elsewhere. The b_n components can be thought of as seeing a central obscuration of radius R_I instead of R_S. Therefore, when these components are acted on by the vortex operator in Equations A.7, A.8, or A.9, R_S is replaced by R_I. Defining $A(r)$ this way ensures that when we sum up the terms of $A(r)$ propagated into the Lyot plane, there exists a solution with zero electric field at $R_I < r \leq R_P$.

APPENDIX A. POLYNOMIAL APODIZERS FOR CENTRALLY OBSCURED VORTEX CORONAGRAPHS

For the case of a charge 2 vortex, the constraints that allow $V_2\left[A\left(r\right)\right]=0$ in $R_I<r\leq R_P$ are:

$$\sum_{n=0}^{N}\left(\frac{2R_S^{n+2}}{n+2}a_n+\frac{2R_I^{n+2}}{n+2}b_n\right)=0, \tag{A.11a}$$

$$a_n+b_n=0, \text{if } n>0. \tag{A.11b}$$

For a charge 4 vortex, the constraints are

$$\sum_{n=0}^{N}\left(-\frac{4R_S^{n+2}}{n+2}a_n-\frac{4R_I^{n+2}}{n+2}b_n\right)=0, \tag{A.12a}$$

$$\sum_{n=0}^{N}\left(\frac{12R_S^{n+4}}{n+4}a_n-\frac{12R_I^{n+4}}{n+4}b_n\right)=0, \tag{A.12b}$$

$$a_n+b_n=0, \text{if } n\neq(0,2). \tag{A.12c}$$

For a charge 6 vortex, they are

$$\sum_{n=0}^{N}\left(\frac{6R_S^{n+2}}{n+2}a_n+\frac{6R_I^{n+2}}{n+2}b_n\right)=0, \tag{A.13a}$$

$$\sum_{n=0}^{N}\left(-\frac{48R_S^{n+4}}{n+4}a_n-\frac{48R_I^{n+4}}{n+4}b_n\right)=0, \tag{A.13b}$$

$$\sum_{n=0}^{N}\left(\frac{60R_S^{n+6}}{n+6}a_n+\frac{60R_I^{n+6}}{n+6}b_n\right)=0, \tag{A.13c}$$

$$a_n+b_n=0, \text{if } n\neq(0,2,4). \tag{A.13d}$$

It is also necessary that the solution correspond to a physically real apodizing

mask, which is guaranteed by the additional constraint

$$0 \leq A(r) \leq 1. \tag{A.14}$$

If we wish to produce $A(r)$ using a classical apodizing mask, the constraints in either Equations A.11, A.12, or A.13, and in Equation A.14 are sufficient. However, if we wish to produce $A(r)$ using shaped mirrors, we also desire mask shapes that are smooth. We can constrain mask shapes to be continuous, using

$$\sum_{n=0}^{N} b_n R_I^n = 0, \tag{A.15}$$

and smooth, using

$$\sum_{n=0}^{N} n b_n R_I^{n-1} = 0. \tag{A.16}$$

It is interesting to note that since we are free to add degrees of freedom to the problem by increasing the order N of the piecewise polynomial describing $A(r)$, we can continue to add linear constraints while ensuring that the problem remains solvable. For example, we can ensure that the mask solution be C^k smooth for any order k.

Having specified the constraints on $A(r)$, it remains choose a figure-of-merit (FOM) in order to calculate an optimal apodization function. The choice of FOM depends on both instrument performance goals and how the apodization

APPENDIX A. POLYNOMIAL APODIZERS FOR CENTRALLY OBSCURED VORTEX CORONAGRAPHS

Table A.2 Definitions of Throughput

Definitions of Throughput for Coronagraphic Instruments used in §3-5.

Name	Definition
Total Energy Throughput	The integrated energy in the Lyot plane of a PAVC that is transmitted through the pupil and Lyot stop. For a classically apodized PAVC, this quantity can be calculated by $$T.E. = \frac{2\pi \int_{R_I}^{R_P} A^2(r)\, r dr}{\pi (R_P^2 - R_S^2)}. \quad \text{(A.17)}$$
Total Energy Off-Axis Throughput	The total energy of an off-axis source in the Lyot plane. For a classicaly apodized PAVC, this quantity can be calculated by $$T.E.(r) = \frac{\int_{R_I}^{R_P} \int_0^{2\pi} \left(V_c \left[A(r) F(r,\theta)\right]\right)^2 d\theta r dr}{\pi (R_P^2 - R_S^2)}, \quad \text{(A.18)}$$ where $F(r,\theta)$ is the off-axis source flux in the telescope pupil.
Encircled Energy Throuhput	The integral of the energy contained in an aperture of diameter 0.7λ/D centered on the off-axis source position in the image plane of the PAVC. If (K_x, K_y) is the position of the off-axis source in coordinates centered on the on-axis star, then the encircled energy throughput is $$E.E.(K_r) = \frac{\int_{(k_x-K_x)^2+(k_y-K_y)^2 \leq (0.35\lambda/D)^2} I^2(k_x,k_y)\, dk_x dk_y}{\pi (R_P^2 - R_S^2)}, \quad \text{(A.19)}$$ where $K_r \equiv \sqrt{K_x^2 + K_y^2}$ and $I(k_x,k_y)$ is the amplitude in the image plane. This quantity approximates the relative signal strength that would be obtained for an off-axis source when performing aperture photometry on the source position in the image plane.

function is produced. One of the key features of the PAVC is that it can be optimized according to different combinations of FOM and constraints.

APPENDIX A. POLYNOMIAL APODIZERS FOR CENTRALLY OBSCURED VORTEX CORONAGRAPHS

For a PAVC with $A(r)$ produced with a classical apodizing filter, the FOM ought to maximize filter transmission, while the smoothness and continuity constraints can be neglected. Meanwhile, for a PAVC with shaped mirrors, a FOM must be selected that minimizes mirror curvature. In the following sections, we motivate the FOMs for PAVCs produced with either apodizing filters or with shaped mirrors, and demonstrate the results we obtain for a range of central obscuration sizes.

***

To summarize, the linear program that needs to be solved to find a perfectly nulling apodizing pupil mask is defined by:

- A figure of merit (FOM) which depends on the desired properties of the coronagraph,

and by the set of constraints that ensure:

- Lyot plane nulling (equations A.11, A.12, or A.13)
- Feasibility (equation A.14)
- Continuity (equation A.15) (optionally)
- Smoothness (equation A.16) (optionally).

A.3 The Apodizing Filter PAVC

A.3.1 Figure of Merit Selection

The apodization function for a PAVC incorporating an apodizing mask/filter at Stage A in Figure A.1 ought to be optimized to permit as much flux through the filter as possible. Therefore, the linear FOM we use is the transmission through the mask,

$$T = \int_{R_I}^{R_P} A(r)\, r dr. \tag{A.20}$$

To calculate the FOM, we only integrate T between R_I and R_P since light inside R_I is blocked by the inner Lyot stop.

For a charge 2 PAVC, maximizing T is equivalent to maximizing total energy throughput (defined as the integrated energy in the Lyot plane that is transmitted through the pupil apodizing filter and inner Lyot stop; see Table A.2 for an overview of how 'throughput' is defined and used throughout this paper), since given the constraints in Equation A.11, only the a_0 and b_0 terms in $A(r)$ do not sum to zero in the region $R_I < r < R_P$. We emphasize that T is not the same quantity as total energy throughput, which is a non-linear function of the apodization. T in this case is

$$\boldsymbol{T = \frac{a_0 + b_0}{2}\left(R_P^2 - R_I^2\right),} \tag{A.21}$$

while the total energy throughput is

$$\boldsymbol{T.E.} = \frac{\left(\boldsymbol{a_0} + \boldsymbol{b_0}\right)^2}{\boldsymbol{2}} \left(\boldsymbol{R_P^2} - \boldsymbol{R_I^2}\right), \tag{A.22}$$

so subject to the constraint that $a_0 + b_0 \geq 0$, it can clearly be seen that finding the solution to the linear program that maximizes $a_0 + b_0$ will optimize both T and total energy throughput.

This is not the case for higher charges, so strictly speaking optimizing T will not allow us to find the maximum total energy throughput attainable with a classically apodized $c > 2$ PAVC. To find the maximum total energy throughput achievable by a charge 4 or higher PAVC for a given R_S, one would have to use a non-linear optimizer rather than the linear programming routine we use here. For this reason, maximizing transmission instead of throughput is a commonly used method to linearize problems involving optimizing apodized coronagraph designs (Vanderbei et al., 2003; Carlotti et al., 2012; N'Diaye et al., 2015). Therefore, we use T as the FOM for charge 4 and 6 PAVCs, while bearing in mind that we may overlook solutions to Equations A.12 and A.13 that produce higher total energy throughputs than we report.

A.3.2 Total Energy Throughput Performance

In order to explore the PAVC parameter space, we generated optimal smooth

APPENDIX A. POLYNOMIAL APODIZERS FOR CENTRALLY OBSCURED VORTEX CORONAGRAPHS

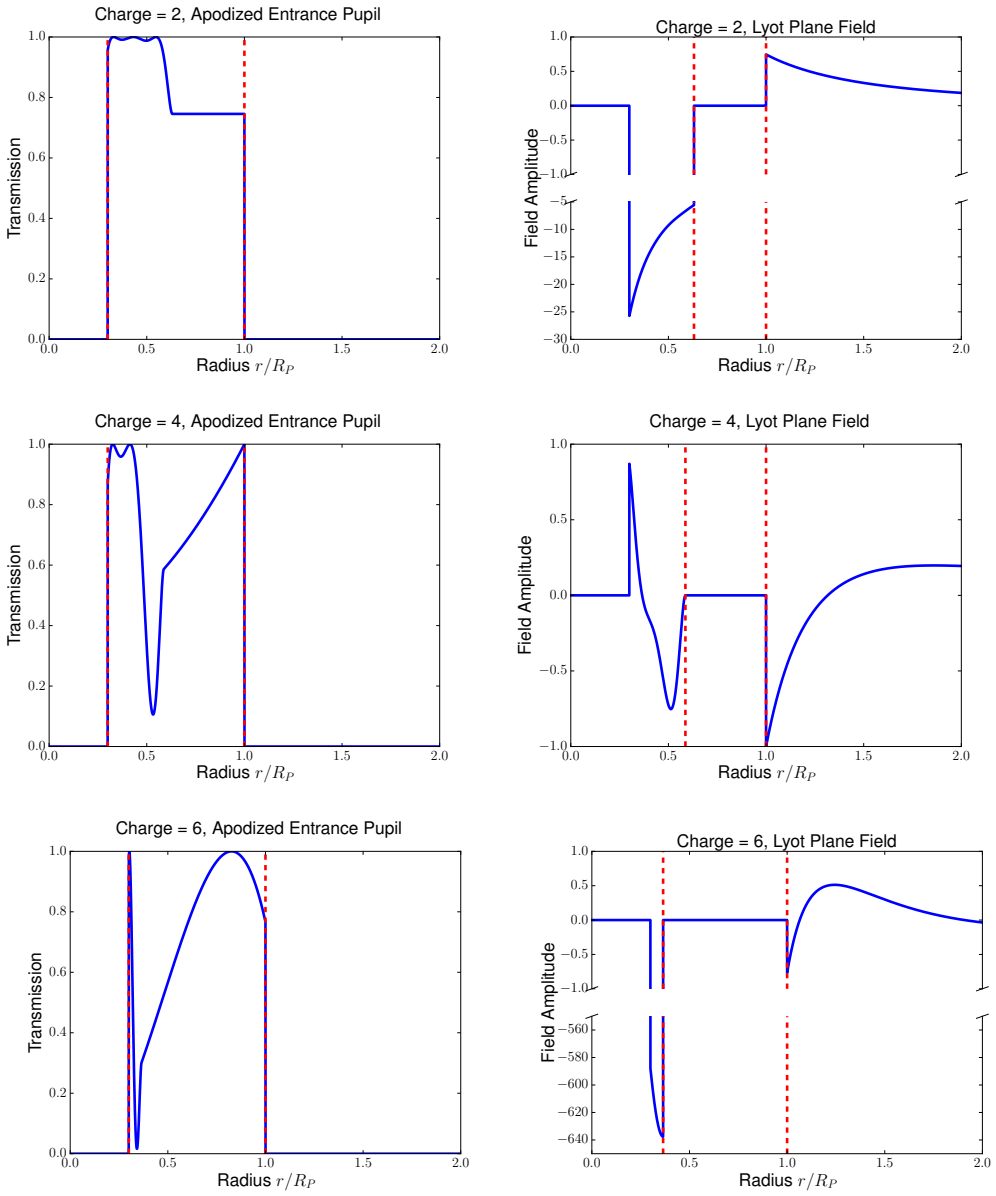

Figure A.3 *Top Row:* The left-hand plot depicts the optimal smooth apodizing mask geometry for a coronagraph designed with a charge 2 vortex for a telescope with $R_S = 0.3R_P$. Dashed red lines depict the secondary and primary mirror radii. The right-hand panel depicts the Lyot field going out to a radius of twice the radius of the pupil. Dashed red lines depict the inner Lyot stop and pupil radii. *Middle Row:* The same set of plots are shown as in the above row, this time for a coronagraph designed with a charge 4 vortex. *Bottom Row:* The same set of plots are shown as in the above two rows, but for a charge 6 vortex.

apodizing masks for charge 2, 4, and 6 vortices described by various orders of polynomial for different sized central obscurations. We also generated masks with non-continuous apodization functions, where we did not impose the constraints in Equations A.15 and A.16. Profiles of smooth apodizing masks with apodization functions described by polynomials of order 20 are shown in Figure A.3 for charge 2 through 6 PAVCs designed for a central obscuration with $R_S = 0.3R_P$.

The optimal total energy throughput achieved by our linear programming algorithm as a function of secondary mirror radius is shown in Figure A.4. For each R_S we chose the value of R_I that maximizes T. We find that the non-continuous apodizations have the highest total energy throughput for each charge, and that smooth apodizations approach the throughput of the non-continuous apodization for a given charge as the order of the smooth piecewise polynomial increases.

Since $A(r)$ need not be continuous for a classically apodized PAVC, the optimal apodization function for charge 2 PAVC is the same as for the charge 2 RAVC. Therefore, the ideal classically apodized charge 2 vortex coronagraph is the RAVC. This is not surprising, since the Lyot plane nulling constraint for a charge 2 PAVC (Equation A.11) constrains the portion of the apodization function where $r > R_I$ to be flat. For higher charges, we find apodization functions with substantially higher total energy throughputs than the RAVC

apodizations presented in Mawet et al. (2013). In fact, for a given central obscuration size, we find that the total energy throughput of the PAVC increases as the charge increases. This improvement stems from the fact that for higher charges, the apodization function at $r > R_I$ can be expressed by progressively higher orders of polynomial.

The increasing complexity of $A(r)$ at $r > R_I$ with increasing charge in turn explains why total energy throughput vs. R_S for the charge 6 PAVC is not perfectly monotonic– maximizing T may start to noticeably underestimate total energy throughput through the apodizing mask. While $T = \int_{R_I}^{R_P} [a_0 + b_0 + (a_2 + b_2) r^2 + (a_4 + b_4) r^4] \, r dr$, the total energy throughput is $T.E. = \int_{R_I}^{R_P} [a_0 + b_0 + (a_2 + b_2) r^2 + (a_4 + b_4) r^4]^2 \, r dr$, which has an integrand with higher-ordered terms and three additional cross terms. Meanwhile, optimizing T for a charge 4 vortex provides a better approximation for optimizing throughput, since there are fewer terms in both the integrands for T and $T.E.$, and fewer cross terms in the integrand for throughput. For both the charge 4 and 6 PAVC, the theoretically optimal total energy throughput is slightly higher than what we report. However, for the purposes of demonstrating the characteristics of the PAVC, the approximate optimal total energy throughput curves we obtain by optimizing T suffice.

Total energy throughput as a function of both R_S and R_I is shown in Figure A.5. We find that the total energy throughput as a function of either radius

increases with charge. For the charge 2 PAVC, the optimal value of R_I increases monotonically with R_S, while the dependence of the optimal value of R_I on R_S is more complicated for the charge 4 and 6 cases. Indeed, the throughput surface for the charge 6 coronagraph exhibits a saddle point at around $R_S/R_P = 0.3$ and $R_I/R_P = 0.4$, owing to the competing effects of throughput loss due to increased Lyot stop size and gain in the apodizing mask transmission. Like the result that PAVC total energy throughput improves as charge increases, the behavior of the charge 4 and 6 throughput surfaces results from the increasing number of available degrees of freedom at $r > R_I$ as the charge increases. This is true whether or not the PAVC apodization is constrained to be smooth. As shown in Figure A.5, forcing the apodization to be smooth affects the performance of the PAVC, but throughputs for both smooth and discontinuous apodizations are similar and depend on R_S and R_I in nearly the same way.

A.3.3 Off-Axis Source Performance

Total and encircled energy throughputs for an off-axis source (see Table A.2) as a function of the source's angular separation from the on-axis star are shown in Figure A.6. We present curves depicting throughput vs. angular separation for charge 2, 4, and 6 PAVCs, and for $R_S = 0.1R_P$ and $R_S = 0.3R_P$. By plotting the encircled energy throughout, we provide an estimate of the actual flux an observer would measure when performing aperture photometry on the final

APPENDIX A. POLYNOMIAL APODIZERS FOR CENTRALLY OBSCURED VORTEX CORONAGRAPHS

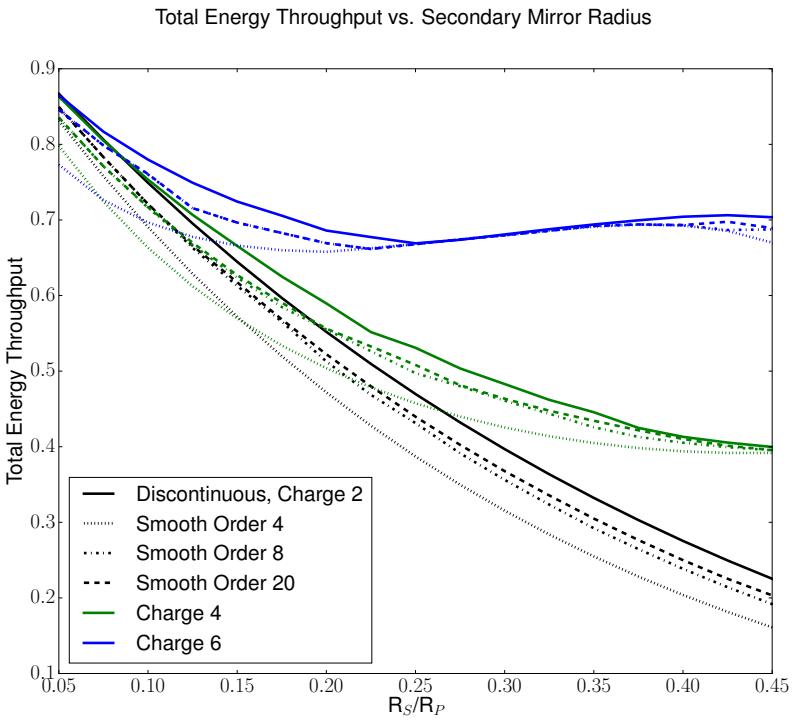

Figure A.4 Total energy throughput of charge 2, 4, and 6 apodized vortex coronagraphs are shown as a function of the secondary mirror radius relative to the primary mirror radius, where an apodizing filter is used. Solid curves are for apodizations that are not required to be smooth, while dotted, dash-dotted, and dashed lines are for smooth apodizations described by polynomials of order 4, 8, and 20. The black curves are for a $c = 2$ coronagraph, and the black solid line corresponds to the ring-apodized vortex coronagraph. The green curves are for a $c = 4$ coronagraph, and the blue curves are for a $c = 6$ coronagraph.

APPENDIX A. POLYNOMIAL APODIZERS FOR CENTRALLY OBSCURED VORTEX CORONAGRAPHS

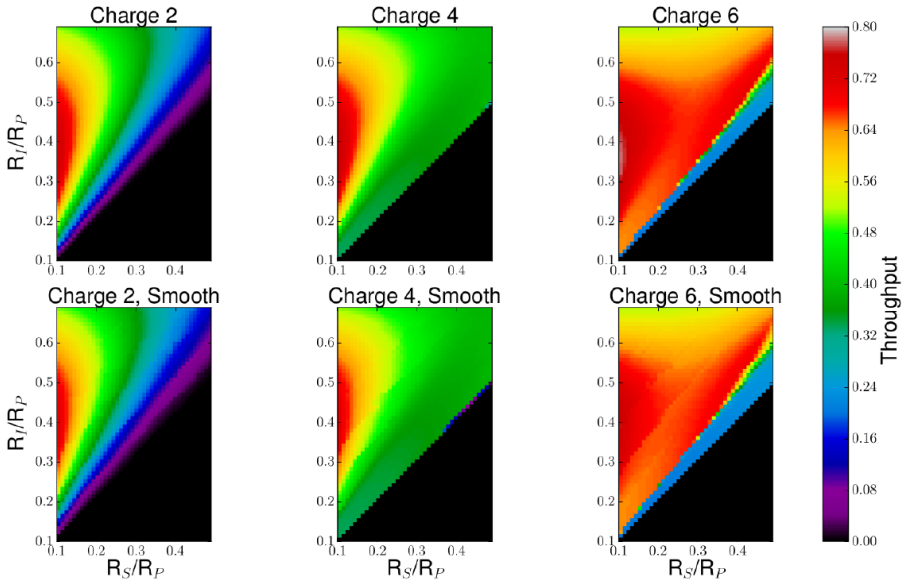

Figure A.5 *Top Row:* Total energy throughputs of apodizing masks optimized to maximize transmission for combinations of inner Lyot stop radius R_I and secondary mirror radius R_S for charge 2, 4, and 6 vortex phase masks. Results are shown for discontinuous apodizations. R_I and R_S are shown in units relative to the primary mirror radius, R_P. Throughput for coronagraph designs where $R_S > R_I$ are 0. *Bottom Row:* Results for smooth apodizations described by order-20 polynomials.

coronagraphic image (Ruane et al., 2016). Plotting the total energy throughput as well indicates the total amount of flux from the off-axis source present in the final coronagraphic image.

In the charge 2 and 4 plots, the encircled energy throughput curve of the corresponding charge RAVC is shown for reference. The smooth charge 2 PAVC underperforms the charge 2 RAVC in terms of throughput, since the ideal charge 2 apodized vortex coronagraph is the RAVC. However, the situation is the reverse for the charge 4 PAVC, especially when $R_S = 0.3R_P$. In that case the smooth PAVC outperforms the off-axis throughput of the RAVC by a factor of 3. We do not show RAVC curves on our charge 6 plots, since in Mawet et al. (2013), charge > 4 RAVCs were not discussed due to low total energy throughput performance.

While going from an $0.1R_P$ central obscuration to an $0.3R_P$ central obscuration reduces the encircled energy throughput for an off-axis source by a little more than half for the charge 4 PAVC (from $\sim 50\%$ to $\sim 22\%$), for the charge 6 PAVC the maximum off-axis throughput is essentially unchanged (changing from $\sim 52\%$ to $\sim 50\%$). However, when going from a central obscuration of $0.1R_P$ to $0.3R_P$, the angular separation at which the encircled energy throughput reaches 20% increases from ~ 3.5 λ/D to ~ 4.25 λ/D for the charge 6 PAVC. By comparsion, the charge 4 PAVC with a central obscuration of $0.1R_P$ obtains a 20% encircled energy throughput at an angular separation of ~ 2.0 λ/D.

The charge 6 PAVC addresses the issue of throughput performance for coronagraphs designed for telescopes with large secondary mirrors. The charge 4 PAVC, meanwhile, represents a trade-off between sensitivity to central obscuration size and inner working angle.

Either the charge 4 or charge 6 PAVC may provide the optimal basis for designing an instrument for an on-axis telescope. Depending on the secondary mirror size, as well as the relative importance of overall throughput performance and the minimum angular separation for an observable off-axis source, one version of the PAVC may be preferable over the other. The charge 2 RAVC may be preferable on ground-based telescopes with relatively small secondary mirrors when sensitivity to low-order aberrations is not a priority but a small IWA is.

A.4 The Shaped Mirror PAVC

We now show how the PAVC can be implemented with shaped mirrors. In essence, we are combining the vortex coronagraph with PIAA shaped mirror apodization, except that the shapes of the mirrors and apodizations we use differ significantly from those in Guyon et al. (2014). We modify the PAVC setup slightly, replacing the apodizing filter in Figure A.1 with a pair of shaped mirrors, as shown in Figure A.7. In some cases it may be advantageous to reshape the pupil with mirrors, instead of apodizing with a filter, since there is no loss of

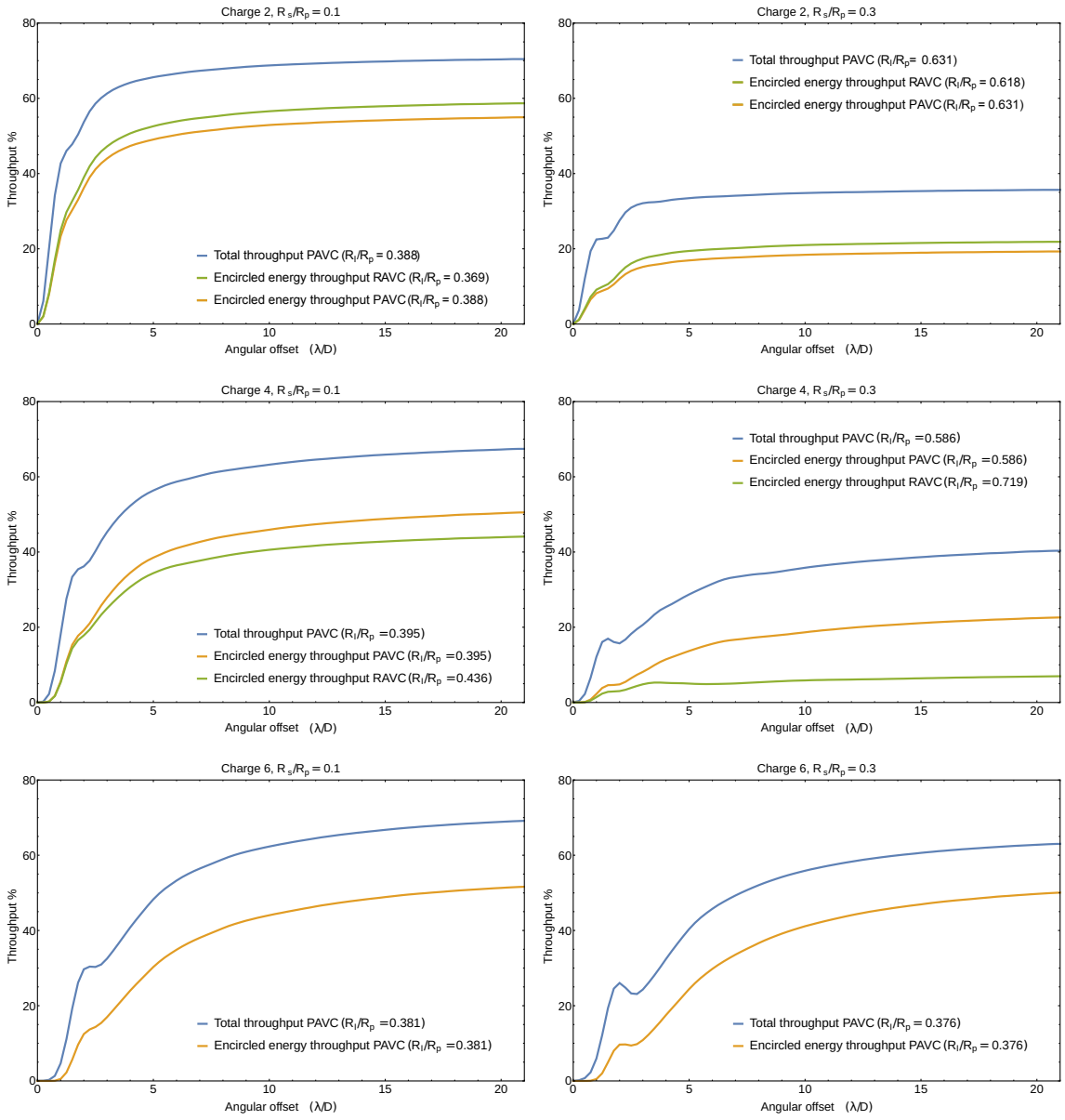

Figure A.6 *First Row:* Off-axis throughputs for optimal coronagraph designs with a charge 2 vortex. The left-hand panel shows the throughput of an off-axis source, such as a planet, as a function of distance from the on-axis star in units of λ/D for a coronagraph designed for a telescope with $R_S = 0.1R_P$ The blue line is the total throughput, and the yellow line is the encircled energy throughput. For comparison, the green line shows the encircled energy throughput of the charge 2 RAVC for the same secondary mirror radius. The right-hand panel show the same set of curves, this time for a coronagraph designed for a telescope with $R_S = 0.3R_P$. *Middle Row:* Same as above for a charge 4 vortex. *Bottom Row:* For a charge 6 vortex.

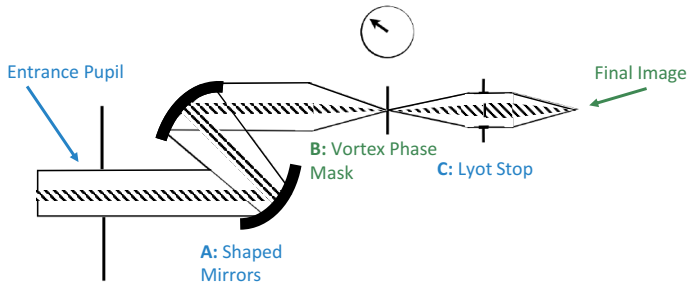

Figure A.7 The coronagraph design from Figure A.1 modified to replace the pupil plane apodizer with a pair of shaped mirrors. The shaped mirrors remap the on-axis flux to has the pupil geometry necessary to null the Lyot field. As in Figure A.1, parts of the beam labeled in blue are in the pupil plane and those in green are in the focal plane.

flux due to transmission through the filter, and total energy throughput is limited by the size of the Lyot stop. We first calculate the mirror shapes needed for PAVC apodization and describe the tradeoff between the total energy throughput and mirror curvature. Then, we find mirror shapes that produce apodizations for a charge 4 and charge 6 PAVC.

A.4.1 Mirror Apodizations for the PAVC

We obtain expressions to describe the circularly symmetric mirror shapes we use to construct an apodizing shaped pupil following the derivation given in Vanderbei & Traub (2005) (V05), with some modifications. A pair of mirrors is used to produce a desired apodization function– the first mirror 'spreads out' the incoming point source flux, and the second mirror re-collimates the beam. We describe the shape of the first mirror with coordinates (ρ, θ) and mirror

height (relative to a flat mirror) $h(\rho,\theta)$. The second mirror is in the pupil plane, so its coordinates are $(\boldsymbol{r},\boldsymbol{\theta})$ and its height is $\tilde{h}(r,\theta)$. We drop the θ dependence throughout, since the mirror shapes and apodization functions we wish to solve for are circularly symmetric, and note that the more general expressions may be found in V05.

To solve for the mirror heights, we use Equations 24, 29[1] and 34 in V05, which, dropping the θ dependence and other constants, are

$$\partial_r \tilde{h} = \rho(r) - r, \tag{A.23}$$

$$h(\rho) = \tilde{h}(r) + \frac{1}{2}(r-\rho)^2, \tag{A.24}$$

and

$$\frac{d}{dr}\rho(r)^2 = 2CA^2(r)\,r. \tag{A.25}$$

The extra coefficient $\boldsymbol{C}$ in Equation A.25 normalizes the apodization function, so that energy is conserved across the two mirrors, such that

$$2\pi C\int_0^{R_P} A^2(r)\,r dr = 2\pi R_P^2. \tag{A.26}$$

In order to solve Equation A.25, we set $A(r)=1$ for $r < R_S - \epsilon$, and use spline

[1]There is a sign error in equation 29 of V05, which reads $H(\rho,\theta) = \tilde{H}(r,\theta) - \frac{P_0}{2} - \frac{(r-\rho)^2+2(r-\rho)\delta\cos(\theta)+\delta^2}{2P_0}$, but ought to read $H(\rho,\theta) = \tilde{H}(r,\theta) - \frac{P_0}{2} + \frac{(r-\rho)^2+2(r-\rho)\delta\cos(\theta)+\delta^2}{2P_0}$. Note that V05 uses coordinates (r,θ), $(\tilde{r},\theta)$ instead of (ρ,θ), (r,θ); we express their equation 29 in the coordinates we use in this paper for clarity.

interpolation to smoothly connect $A(R_s)$ and $A(R_S - \epsilon)$, where ϵ is an arbitrary small separation. We note that it can be shown from the expression for $\rho(r)$ that the equation for the derivative of the second mirror is equivalent to the second-order Monge-Ampère equation for the second mirror shape presented in Pueyo et al. (2011) and Pueyo & Norman (2013).

We wish the optimize $A(r)$ to maximize the shaped mirrors' radii of curvature. Mirror shapes with sharper curvatures are both more difficult to manufacture and increase the magnitude of diffraction effects introduced by the optics, so we want to use the smoothest mirror shapes possible (Pluzhnik et al., 2006). We focus on the shape of the first mirror, which we empirically observe has the sharpest curvatures. The radius of curvature (reciprocal of the curvature, K) for this mirror is

$$\frac{1}{K} = \frac{\left(1 + (\partial_\rho h)^2\right)^{3/2}}{\left|\partial_\rho^2 h\right|}. \tag{A.27}$$

Finding $\partial_\rho h$ and $\partial_\rho^2 h$ is difficult using the setup described in V05, so we solve for the setup in reverse, where an initial pupil with electric field amplitude $A(r)$ is reshaped by a series of mirrors to an outgoing beam of uniform amplitude. In this setup, $h(r)$ is the height of the second mirror, and the desired apodization function is $A^{-1}(r)$. Making these adjustments to Equations A.23 and A.24, we

find that

$$\frac{1}{K} = \frac{A^2\left(1 + \left(\frac{2}{A} - r\right)^2\right)^{3/2}}{2\partial_r A}. \tag{A.28}$$

To maximize the radius of curvature across the mirror shape, it follows that we want to maximize A and minimize $\partial_r A$. However, as seen in Figure A.8, the minimum value of $A(r)$ depends on R_I, which in turn limits the total energy throughput. For a desired level of throughput, then, we can optimize for curvature by adopting $\partial_r A$ as the FOM to minimize.

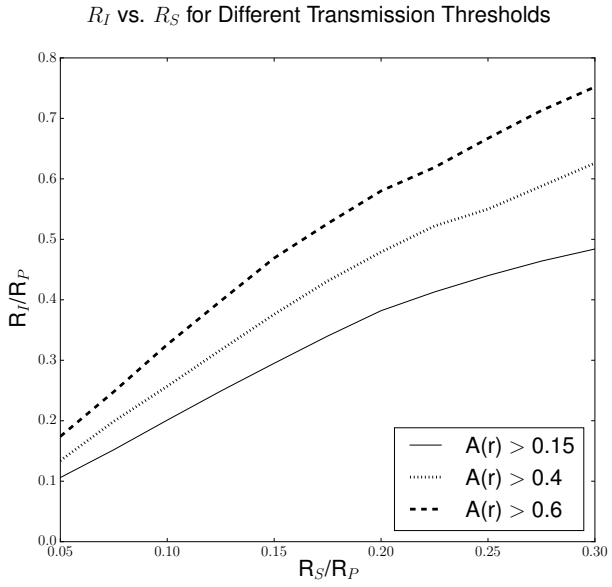

Figure A.8 Minimum inner Lyot stop radii allowing for minimum values of $A(r)$ of 0.15 (solid lines), 0.4 (dotted), and 0.6 (dashed) are shown as a function of secondary mirror radius. For simplicity of the figure, only curves for charge 4 are shown.

A.4.2 Mirror Apodized PAVC Performance

Mirror shapes for the charge 4 PAVC are shown in Figure A.9 for $R_S = 0.1R_P$ and $R_S = 0.3R_P$. Mirrors for the charge 6 PAVC are shown in Figure A.10. Since mirror shapes are normalized to conserve energy, the total energy throughput is:

$$T.E. = \frac{\pi\left(R_P^2 - R_I^2\right)}{\pi\left(R_P^2 - R_S^2\right)}. \tag{A.29}$$

For the charge 4 PAVCs in Figure A.9, the total energy throughput is 88% for $R_s = 0.1R_P$ and 68% for $R_S = 0.3R_P$. For the charge 6 PAVCs total energy throughput is 86% and 88%, respectively.

The off-axis throughput curves for shaped-mirror PAVCs are shown in Figure A.11. Total energy throughputs are shown as blue curves, and demonstrate a gain in throughput over the use of a greyscale apodizer for each combination of charge and secondary mirror radius we examined. Encircled energy throughputs are denoted by yellow curves. For each shaped-mirror PAVC, except for the charge 4 PAVC with secondary mirror radius $R_S/R_P = 0.1$, the mirror shapes we calculate severely distort the off-axis point spread function (PSF) and result in a narrow range of angular separations from the on-axis star where even a modest encircled energy throughput can be obtained. Therefore, we propose using inverse mirrors placed after the Lyot stop in Stage C in Figure A.7, similar to the inverse optics proposed for PIAA mirrors (Guyon et al., 2005, 2014). Our

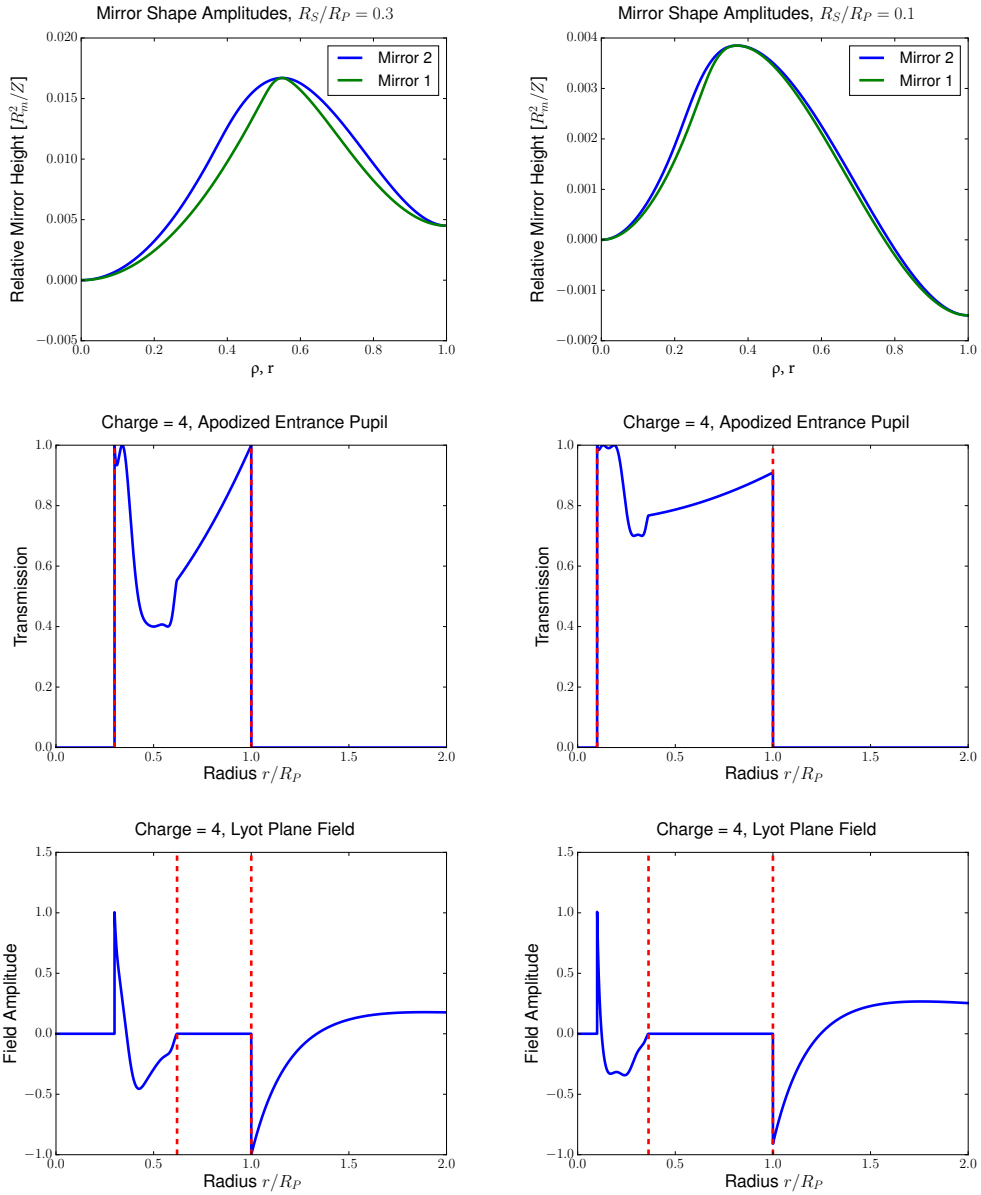

Figure A.9 Mirror shape pairs are presented for a charge 4 PAVC for $R_S = 0.3R_P$ (left) and $R_S = 0.1R_P$ (right). Mirror shapes are on the top row, and the overall height displacement of the shapes is relative to the sizes and separation of the mirrors. Physical mirror heights depend on the radii of the shaped mirrors R_m and the separation Z between the two and go as R_m^2/Z, and translating the relative heights to a physical mirror shape involves multiplying by this factor (Traub & Vanderbei, 2003; Pueyo et al., 2011; Pueyo & Norman, 2013). The apodizations produced by these pairs are shown in the second row, with dashed red lines denoting the radii of the central obscuration and the pupil. The nulled field in the Lyot plane (before the inner Lyot stop) is shown in the third row, with dashed red lines denoting the inner Lyot stop and pupil radii.

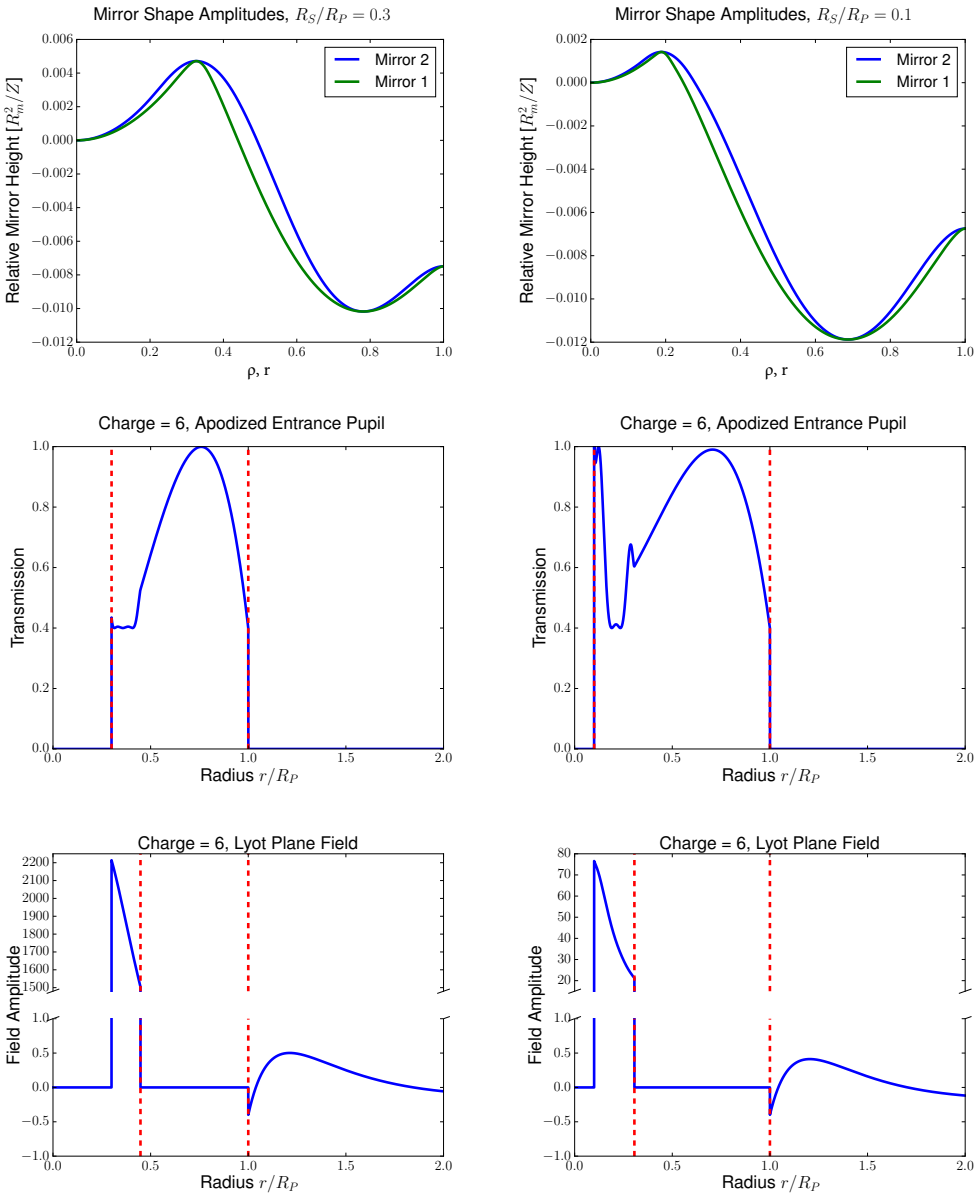

Figure A.10 The same as Figure A.9, except for a charge 6 PAVC for $R_S = 0.3R_P$ and $R_S = 0.1R_P$.

estimate of the encircled energy throughput after the off-axis PSF is restored by inverse optics is shown by the green curve for each coronagraph design in Figure A.11.

We estimated restored off-axis PSFs by propagating the off-axis point source flux through the coronagraphic setup without a pair of shaped mirrors to reshape the pupil, and with the total energy normalized by the total energy in the final image plane of the apodized coronagraph. The restored encircled energy throughputs we present are therefore upper limits on what may be achieved with inverse optics. If we treat the encircled energy throughput of an off-axis source as the best estimate for the 'usable' photometric flux, then using shaped mirrors with inverse optics represents an improvement over greyscale filters for the charge 4 PAVC by a factor of 2 and the charge 6 PAVC by about 50%.

A.5 Application To Future Telescopes

Moving forward, the PAVC formalism can be used in the design of instruments for arbitrary telescope pupils. In combination with techniques for minimizing the impact of pupil features imposed by secondary mirror support struts and primary mirror segmentation gaps, the PAVC enables vortex coronagraphs to be used with the complicated pupils of future space and ground based large-aperture on-axis telescopes. Eventually, it will be necessary to extend the PAVC formalism to address the sensitivity of obstructed vortex coronagraphs

APPENDIX A. POLYNOMIAL APODIZERS FOR CENTRALLY OBSCURED VORTEX CORONAGRAPHS

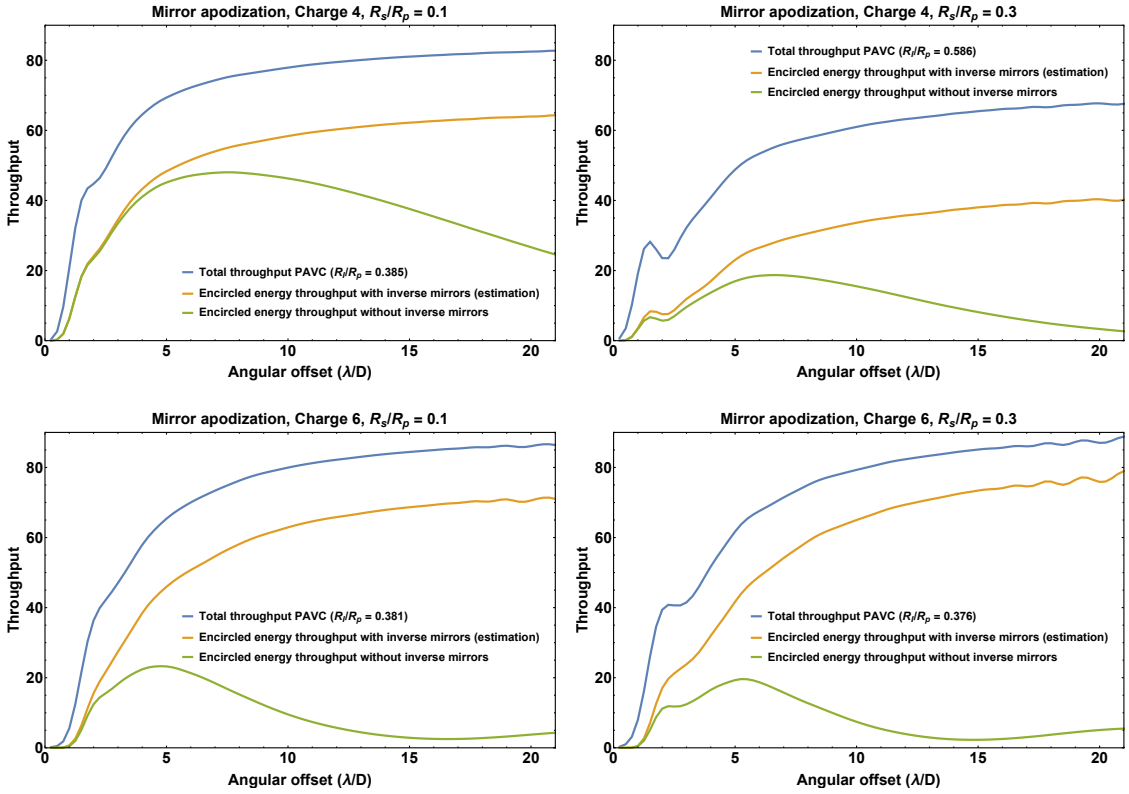

Figure A.11 *Top Row:* Off-axis throughputs for optimal coronagraph designs with a charge 4 PAVC, where apodizations were obtained with shaped mirrors. The left-hand panel shows the throughput of an off-axis source, as a function of distance from the on-axis star in units of λ/D for a coronagraph designed for a telescope with $R_S = 0.1R_P$. The blue line is the total throughput, and the yellow line is the encircled energy throughput. The green line depicts the approximate encircled energy throughput obtained when the off-axis PSF is restored by inverse mirrors placed after the Lyot plane. The right-hand panel show the same set of curves, this time for a coronagraph designed for a telescope with $R_S = 0.3R_P$. *Bottom Row:* The same set of plots as the top two rows, but for a coronagraph designed with a charge 6 vortex.

to low-order aberrations, and to define and optimize figures of merit that are best suited to real-world on-axis telescopes. However, by effectively solving posed by central obscurations, the PAVC provides the basis for designing vortex coronagraphs for on-axis telescopes.

Recently, numerical algorithms have been put forward to calculate either apodizing mask or shaped mirror geometries that mitigate the impact of struts and primary mirror gaps (so-called 'spiders') on vortex coronagraph starlight suppression (Ruane et al., 2016; Mazoyer et al., 2015, 2016). By using a PAVC apodizer to correct the central obscuration, we are able to provide a first order correction for the vortex coronagraph on a pupil obstructed by both a secondary mirror and spiders. Higher order corrections to the PSF can then be obtained using either e.g. Ruane et al. (2016) or Mazoyer et al. (2016) to create a dark hole with $\sim 10^{-10}$ contrast while minimizing losses to throughput.

Figure A.12 depicts an example of how a such a combined approach works on a pupil with a central obscuration of radius $R_S/R_P = 0.17$ and spiders. The pupil shown in Figure A.12 is a realistic aperture for future space telescope missions taken from the Segmented Coronagraph Design and Analysis (SCDA) program.[2] Using a charge 6 PAVC with an inner Lyot stop of radius $R_I = 0.414R_P$, we correct for the central obscuration. In the absence of spiders, the PAVC alone provides an encircled energy throughput of 44%. With the ad-

[2]https://exoplanets.nasa.gov/system/internal_resources/details/original/211_SCDAApertureDocument050416.pdf

dition of spiders, the PAVC alone has a contrast ratio of only 10^{-6} assuming broadband light with a 30% bandwidth.

When we combine the apodizing filter for the PAVC with mirror shapes obtained using the ACAD-OSM (Active Correction of Aperture Discontinuities-Optimized Stroke Minimization) algorithm described in Mazoyer et al. (2016), we obtain the PSF shown in the upper right portion of Figure A.12. ACAD-OSM builds on the deformable mirror-based Active Correction of Aperture Discontinuities (ACAD) algorithm presented in Pueyo & Norman (2013).

The shaped mirror corrections provide a PSF with a dark hole between 1.5 and 15 λ/D with a contrast of 10^{-10} in 30% bandwidth light. Encircled energy throughput of an off-axis point source as a function of angular separation from the star is shown in Figure A.13. The additional correction to the pupil geometry provided by the shaped mirrors reduces encircled energy throughput by only a few percent, and the encircled energy throughput in the dark hole exceeds 20% at 4.5 λ/D. At the outer edge of the dark hole, where throughput is highest, this rises to $\sim 41\%$.

The example coronagraph design discussed here provides proof of concept for combining the PAVC with algorithms that compensate for the effects of struts and segments on telescope pupils. It may be optimized substantially depending on demands imposed on the coronagraph by the initial pupil geometry. In particular, throughput of the spider correction depends heavily on the

inner Lyot stop radius used, and it may be possible to determine an ideal inner Lyot stop radius for a combination of polynomial apodizing filter and spider-correcting apodization. Furthermore, polynomial apodizing geometries that correct for the central obscuration may also be optimized to result in a pupil geometry that requires less correction with numerical techniques.

Application of the PAVC to real-world obstructed pupils with spiders will likely require us to optimize the throughput of a combined PAVC + spider correcting apodization design. As discussed in § 4, we calculated PAVC apodizations by maximizing transmission through the apodizing filter, which is a linear quantity that approximates throughput. However, the actual quantity that determines the relative flux from an exoplanet or other off-axis source that the observer will be able to detect is best approximated by the encircled energy throughput shown in Figures A.6, A.11, and A.13. Since the encircled energy throughput is a function of angular separation, the optimal FOM will depend on performance goals for effective inner working angle as well as overall throughput. For example, the optimal FOM for a given coronagraph may be the encircled energy throughput at 3 λ/D. Such a FOM will require us to adopt a non-linear algorithm for optimizing the pupil apodization. Fortunately, since PAVC designs have a large number of degrees of freedom compared to the constraints needed to ensure ideal starlight suppression, they are well-suited to addressing complex optimization problems.

APPENDIX A. POLYNOMIAL APODIZERS FOR CENTRALLY OBSCURED VORTEX CORONAGRAPHS

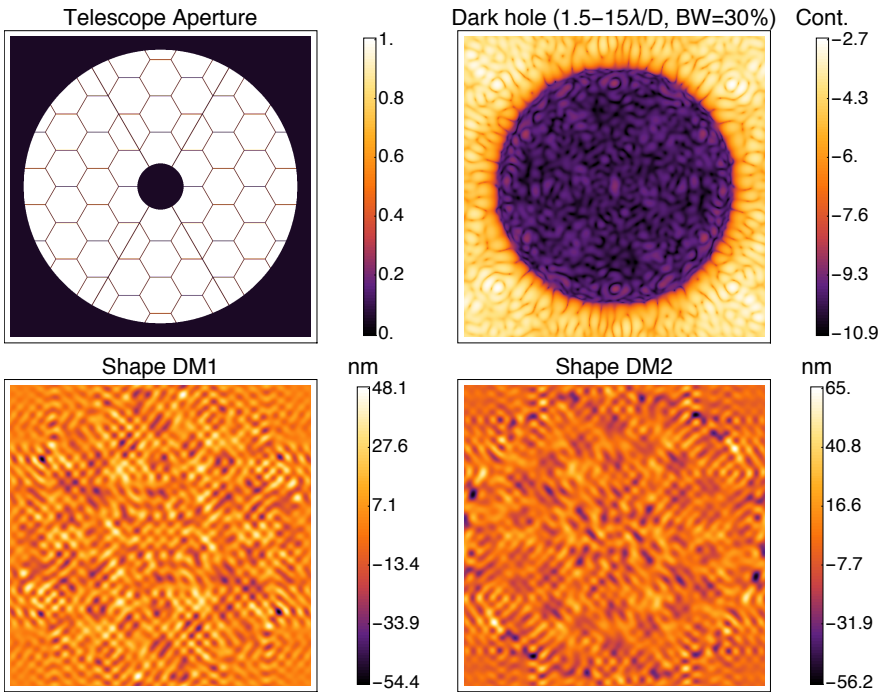

Figure A.12 An example deformable mirror (DM) solution that creates a dark hole PSF for a centrally obstructed aperture in conjunction with a polynomial apodizing mask. The pupil, featuring a secondary mirror obscuration with $R_S/R_P = 0.17$ and segment gaps is shown in the upper left. The lower left and lower right show the mirror shapes that provide the higher-order correction for segment gaps using ACAD-OSM (Mazoyer et al., 2016) and, in conjunction with an apodizing mask, produce the PSF in the upper right. The PSF features a dark hole with a contrast of approximately 10^{-10} in the region $1.5 - 15$ λ/D.

APPENDIX A. POLYNOMIAL APODIZERS FOR CENTRALLY OBSCURED VORTEX CORONAGRAPHS

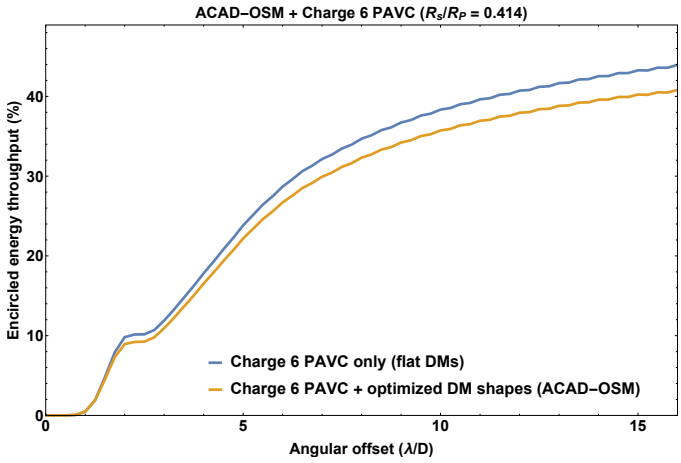

Figure A.13 Encircled energy throughput vs. offset for a polynomial apodized + ACAD-OSM vortex coronagraph design. The blue curve shows the throughput obtained in the absence of deformations on the deformable mirrors (DMs), while the purple curve shows the throughput obtained when both a polynomial apodizer and shaped mirrors are used to correct the central obscuration and segment gaps.

Our derivation of analytical expressions for $V_c\left[A\left(r\right)\right]$ also raises the possibility of creating PAVC designs that are highly robust to low-order aberrations. Currently, we are working on extending our technique for deriving PAVC apodizations to analytically describe impacts of low-order aberrations on PAVC designs, and to optimize the PAVC to minimize sensitivity to these effects. With an unobstructed circular aperture, the sensitivity of a vortex coronagraph to small angular offsets of the on-axis source caused by low-order aberrations goes approximately as s^c, where s is angular separation of the offset between the telescope pointing and aberrant flux from the on-axis source (typically $\ll 1$ λ/D) and c is the charge of the vortex (Jenkins, 2008; Mawet et al., 2010). Therefore, as the charge of a vortex coronagraphs increases, the corona-

graph becomes more robust to low-order aberrations. However, in the presence of a central obscuration, vortex coronagraphs are less robust to these aberrations for a given charge, and the flux 'leak' caused by small angular offsets rises more steeply than s^c. Since the PAVC allows for high-throughput coronagraphs be constructed for on-axis telescopes with charge 4 and 6 vortices, addressing this issue of robustness will allow the PAVC to take advantage of the stability of these charges relative to the charge 2 vortex, as well as their relative insensitivity to finite stellar angular size.

A.6 Conclusion

The analytical prescription we derived for the PAVC overcomes a fundamental hurdle associated with the vortex coronagraph– the loss of starlight suppression due to the obscuration created by the secondary mirrors of on-axis telescopes. With the apodizing pupil masks in this paper, we are able to restore the theoretically total and achromatic starlight suppression of the vortex coronagraph while maintaining off-axis throughput. When produced with a classically apodizing mask, the apodization functions we derive offer throughputs that are competitive with or substantially higher than other high-contrast coronagraph designs (e.g. Mawet et al., 2013; N'Diaye et al., 2015; Guyon et al., 2014) for centrally obscured pupils, especially with a charge 6 vortex. When

produced with shaped mirrors, PAVC throughput can be improved even further, albeit at the cost of a more complicated instrument design.

The classically apodized PAVC has a total energy throughput of ∼75%, 75%, and 80% for charges 2-6 respectively with a central obscuration with $R_S = 0.1R_P$, and ∼ 35%, 45%, and 70% with a central obscuration with $R_S = 0.3R_P$. Predictably, total energy throughput decreases as the radius of the central obscuration increases. However, the apodizations produced with our PAVC formalism perform better for all definitions of throughput discussed in this paper as the vector vortex charge increases, particularly with large central obscurations. For a central obscuration of $R_S = 0.3R_P$, the encircled energy throughput is $\sim 22\%$ for the charge 4 PAVC, dropping from $\sim 50\%$ when $R_S = 0.1R_P$. For the charge 6 PAVC, total energy throughput is $\sim 50\%$ when $R_S = 0.3R_P$, and only slightly higher for smaller central obscurations.

Using shaped mirror pairs to apodize the PAVC allows us to further improve throughput, but requires a more complicated design. We found mirror shapes for charge 4 and 6 PAVCs. For the case of the charge 4 PAVC, we obtained a total energy throughput of 88% with $R_S = 0.1R_P$ and 68% with $R_S = 0.3R_P$. For the charge 6 PAVC, these figures are 86% and 88%, respectively. Since the shaped mirrors induce considerable distortion to the off-axis PSF, in order to obtained reasonable encircled energy throughputs for off-axis sources, it is necessary to add inverse optics to the PAVC downstream of the Lyot plane. With

inverse optics, designing the PAVC with shaped mirrors instead of an apodizing filter could improve the encircled energy throughput of the charge 4 PAVC by as much as a factor of 2, and the charge 6 PAVC by 50%. While the PAVCs we present use mirror shapes that require inverse-mirror optics to obtain useful off-axis PSFs, our algorithm can also be used to find the trade-off between throughput and curvature that may allow us to overcome the limitation imposed by off-axis PSF distortion by the shaped mirrors.

Our results overcome the challenge posed to vortex coronagraphs by large central obscurations. We describe a formalism for finding pupil apodizations that restore ideal starlight suppression while preserving high throughputs for off-axis sources for vortex coronagraphs with charges > 2. As mentioned in Ruane et al. (2016), synergy exists between apodized vortex coronagraph designs that compensate for central obscurations and designs that compensate for pupil obstructions introduced by struts and primary mirror gaps. We provide an example of implementing a synergistic PAVC + numerical design by combining the PAVC with ACAD-OSM pupil shaping (Mazoyer et al., 2016). Apodized vortex coronagraphs such as this example are promising candidates for high-contrast instruments designed for on-axis telescopes with complicated pupils. Our results greatly expand the flexibility of vortex coronagraph designs, and represent a step forward towards implementing vortex coronagraphs capable of directly imaging Earth-sized exoplanets.

APPENDIX A. POLYNOMIAL APODIZERS FOR CENTRALLY OBSCURED VORTEX CORONAGRAPHS

Acknowledgments

We acknowledge discussions with Garreth Ruane and Dimitri Mawet that helped enhance our discussion on combining the PAVC with numerical apodization techniques to design coronagraphs for telescopes with pupils that feature both central obscurations and 'spiders.' This material is partially based upon work carried out under subcontract 1496556 with the Jet Propulsion Laboratory funded by NASA and administered by the California Institute of Technology.

A.7 Vortex Operator for Analytical Pupil Shapes

While the central obscuration imposed by the secondary mirror is the largest feature in the pupil geometry of an on-axis telescope design, on axis designs will also feature a number of spiders. In the following, we demonstrate how the prescription we present in Section 2 for circularly symmetric pupils may be extended to describe the propagation of non-circularly symmetric components of a telescope pupil.

The vortex operator we have described in this paper may be extended for any aperture geometry that can be described by a Zernike polynomial expan-

sion. Such a description allows us to analytically propogate the effects of both the secondary mirror of an on-axis telescope and the pupil 'spiders' which result from discontinuities in the primary mirror and the support structure for the secondary mirror.

We consider a pupil geometry which can be expanded into terms $r^{n_p}e^{im_p\theta}$, in the region $R_S \leq r \leq R_P$, and an apodizing mask which can be expanded into terms $r^{n_m}e^{im_m\theta}$. The apodized pupil geometry therefore consists of terms

$$r^n e^{im\theta} = \left(r^{n_p}e^{im_p\theta}\right)\left(r^{n_m}e^{im_m\theta}\right). \tag{A.30}$$

The electric field at the Lyot plane for a $c = 4$ coronagraph for one of these terms is analytic so long as $n + m$ is even, unless $n \geq 0$ and $n + m = -4$ or $n + m = -2$. For a given term

$$f_{n,m}(r,\theta) = \begin{cases} 0, & \text{if } r < R_i. \\ r^n e^{im\theta}, & \text{if } R_i \leq r \leq R_P \end{cases} \tag{A.31}$$

the electric field in the Lyot plane at $R_i \leq r \leq R_P$ is

$$V_4\left[f_{n,m,p}(r,\theta)\right] = e^{i(m+4)}\left[C_0(n,m)\,r^n + C_1(n,m)\,r^{-m-2} + C_2(n,m)\,r^{-m-4}\right] \tag{A.32}$$

where

$$C_0(n,m) = \frac{(n-m)(n-m-2)}{(n+m+4)(n+m+2)}, \tag{A.33}$$

$$C_1(n,m) = \frac{-2(m+1)(m+2)}{m+n+2} \begin{cases} R_i^{m+n+2}, & \text{if } m \geq -1 \\ R_P^{m+n+2}, & \text{if } m < -1, \end{cases} \tag{A.34}$$

and

$$C_2(n,m) = \frac{2(m+2)(m+3)}{m+n+4} \begin{cases} R_i^{m+n+4}, & \text{if } m \geq -1 \\ R_P^{m+n+4}, & \text{if } m < -1. \end{cases} \tag{A.35}$$

Bibliography

Abell, G. O. 1958, Astrophys. J. Supp., 3, 211

Alam, S., Albareti, F. D., Allende Prieto, C., et al. 2015, ArXiv e-prints, arXiv:1501.00963

Allen, S. W., Rapetti, D. A., Schmidt, R. W., et al. 2008, MNRAS, 383, 879

Andrews, S. M., Wilner, D. J., Espaillat, C., et al. 2011, Astrophys. J, 732, 42

Aune, S., Boulade, O., Charlot, X., et al. 2003, in Society of Photo-Optical Instrumentation Engineers (SPIE) Conference Series, Vol. 4841, Instrument Design and Performance for Optical/Infrared Ground-based Telescopes, ed. M. Iye & A. F. M. Moorwood, 513–524

Bahcall, N. A. 1999, in Formation of Structure in the Universe, ed. A. Dekel & J. P. Ostriker, 135

Bai, L., Yee, H. K. C., Yan, R., et al. 2014, Astrophys. J, 789, 134

Baldwin, J. A., Phillips, M. M., & Terlevich, R. 1981, PASP, 93, 5

BIBLIOGRAPHY

Balog, Z., Müller, T., Nielbock, M., et al. 2014, Experimental Astronomy, 37, 129

Begelman, M. C., & Fabian, A. C. 1990, MNRAS, 244, 26P

Bellstedt, S., Lidman, C., Muzzin, A., et al. 2016, MNRAS, 460, 2862

Bernardi, M., Hyde, J. B., Sheth, R. K., Miller, C. J., & Nichol, R. C. 2007, Astron. J., 133, 1741

Bertin, E., & Arnouts, S. 1996, A&AS, 117, 393

Bildfell, C., Hoekstra, H., Babul, A., & Mahdavi, A. 2008, MNRAS, 389, 1637

Binney, J., & Tremaine, S. 2008, Galactic Dynamics: Second Edition (Princeton University Press)

Blanton, M. R., & Moustakas, J. 2009, ARA&A, 47, 159

Bolcar, M. R., Balasubramanian, K., Clampin, M., et al. 2015, in Society of Photo-Optical Instrumentation Engineers (SPIE) Conference Series, Vol. 9602, Optics for EUV, X-Ray, and Gamma-Ray Astronomy VII, 960209

Boulade, O., Charlot, X., Abbon, P., et al. 2003, in Society of Photo-Optical Instrumentation Engineers (SPIE) Conference Series, Vol. 4841, Instrument Design and Performance for Optical/Infrared Ground-based Telescopes, ed. M. Iye & A. F. M. Moorwood, 72–81

BIBLIOGRAPHY

Brinchmann, J., Charlot, S., White, S. D. M., et al. 2004, MNRAS, 351, 1151

Brown, T. M. 2004, Ap&SS, 291, 215

Bruzual, G., & Charlot, S. 2003, MNRAS, 344, 1000

Buote, D. A., & Tsai, J. C. 1996, Astrophys. J, 458, 27

Burke, C., & Collins, C. A. 2013, MNRAS, 434, 2856

Burke, C., Hilton, M., & Collins, C. 2015, MNRAS, 449, 2353

Burke, D. J., Collins, C. A., & Mann, R. G. 2000, Astrophys. J Lett., 532, L105

Cady, E. 2012, Astrophys. J. Supp., 201, 25

Calzetti, D., Armus, L., Bohlin, R. C., et al. 2000, Astrophys. J, 533, 682

Caminha, G. B., Grillo, C., Rosati, P., et al. 2017, A&A, 600, A90

Capak, P., Aussel, H., Ajiki, M., et al. 2007, Astrophys. J. Supp., 172, 99

Carlotti, A., Kasdin, N. J., Vanderbei, R. J., & Delorme, J.-R. 2012, in Society of Photo-Optical Instrumentation Engineers (SPIE) Conference Series, Vol. 8442, Space Telescopes and Instrumentation 2012: Optical, Infrared, and Millimeter Wave, 844254

Carson, J., Thalmann, C., Janson, M., et al. 2013, Astrophys. J Lett., 763, L32

BIBLIOGRAPHY

Cavagnolo, K. W., Donahue, M., Voit, G. M., & Sun, M. 2008, Astrophys. J Lett., 683, L107

—. 2009, Astrophys. J. Supp., 182, 12

Chabrier, G. 2003, PASP, 115, 763

Charlot, S., & Longhetti, M. 2001, MNRAS, 323, 887

Conselice, C. J., Gallagher, III, J. S., & Wyse, R. F. G. 2001, Astron. J., 122, 2281

Cooke, K., Fogarty, K., & et al. in prep.

Cooke, K. C., O'Dea, C. P., Baum, S. A., et al. 2016, ArXiv e-prints, arXiv:1610.05310

Cowie, L. L., Hu, E. M., Jenkins, E. B., & York, D. G. 1983, Astrophys. J, 272, 29

Crawford, C. S., Allen, S. W., Ebeling, H., Edge, A. C., & Fabian, A. C. 1999, MNRAS, 306, 857

da Cunha, E., Eminian, C., Charlot, S., & Blaizot, J. 2010, MNRAS, 403, 1894

Dalcanton, J., Seager, S., Aigrain, S., et al. 2015, ArXiv e-prints, arXiv:1507.04779

BIBLIOGRAPHY

Dalton, G. B., Caldwell, M., Ward, A. K., et al. 2006, in Society of Photo-Optical Instrumentation Engineers (SPIE) Conference Series, Vol. 6269, Society of Photo-Optical Instrumentation Engineers (SPIE) Conference Series, 62690X

De Grandi, S., Ettori, S., Longhetti, M., & Molendi, S. 2004, A&A, 419, 7

De Lucia, G., & Blaizot, J. 2007, MNRAS, 375, 2

De Lucia, G., & Blaizot, J. 2007, MNRAS, 375, 2

Donahue, M., Connor, T., Voit, G. M., & Postman, M. 2016, ArXiv e-prints, arXiv:1612.08297

Donahue, M., de Messières, G. E., O'Connell, R. W., et al. 2011, Astrophys. J, 732, 40

Donahue, M., & Voit, G. M. 1991, Astrophys. J, 381, 361

Donahue, M., Bruch, S., Wang, E., et al. 2010, Astrophys. J, 715, 881

Donahue, M., Voit, G. M., Mahdavi, A., et al. 2014, Astrophys. J, 794, 136

Donahue, M., Connor, T., Fogarty, K., et al. 2015, Astrophys. J, 805, 177

Draine, B. T., & Li, A. 2007, Astrophys. J, 657, 810

Edge, A. C., Wilman, R. J., Johnstone, R. M., et al. 2002, MNRAS, 337, 49

Edwards, L. O. V., Hudson, M. J., Balogh, M. L., & Smith, R. J. 2007, MNRAS, 379, 100

BIBLIOGRAPHY

Edwards, L. O. V., & Patton, D. R. 2012, MNRAS, 425, 287

Ehlert, S., Allen, S. W., von der Linden, A., et al. 2011, MNRAS, 411, 1641

Emerson, J., McPherson, A., & Sutherland, W. 2006, The Messenger, 126, 41

Fabian, A. C. 1994, ARA&A, 32, 277

—. 2012, ARA&A, 50, 455

Fabian, A. C., Zarneck, J. C., Culhane, J. L., et al. 1974, Astrophys. J Lett., 189, L59

Fazio, G. G., Hora, J. L., Allen, L. E., et al. 2004, Astrophys. J. Supp., 154, 10

Ferguson, H. C., & Davidsen, A. F. 1993, Astrophys. J, 408, 92

Ferland, G. J., Fabian, A. C., Hatch, N. A., et al. 2009, MNRAS, 392, 1475

Finoguenov, A., Guzzo, L., Hasinger, G., et al. 2007, Astrophys. J. Supp., 172, 182

Fitzpatrick, E. L., & Massa, D. 1986, Astrophys. J, 307, 286

Fogarty, K., Postman, M., Connor, T., Donahue, M., & Moustakas, J. 2015, Astrophys. J, 813, 117

Fogarty, K., Postman, M., Larson, R., Donahue, M., & Moustakas, J. 2017, ArXiv e-prints, arXiv:1701.05903

BIBLIOGRAPHY

Fogarty, K., Pueyo, L., & Mawet, D. 2014, in Society of Photo-Optical Instrumentation Engineers (SPIE) Conference Series, Vol. 9143, Space Telescopes and Instrumentation 2014: Optical, Infrared, and Millimeter Wave, 914326

Foo, G., Palacios, D. M., & Swartzlander, Jr., G. A. 2005, Optics Letters, 30, 3308

Fraser-McKelvie, A., Brown, M. J. I., & Pimbblet, K. A. 2014, MNRAS, 444, L63

Gaspari, M., Brighenti, F., & Temi, P. 2015, A&A, 579, A62

Gaspari, M., Ruszkowski, M., & Oh, S. P. 2013, MNRAS, 432, 3401

Gaspari, M., Ruszkowski, M., & Sharma, P. 2012, Astrophys. J, 746, 94

Gaspari, M., Temi, P., & Brighenti, F. 2016, ArXiv e-prints, arXiv:1608.08216

—. 2017, MNRAS, 466, 677

George, M. R., Leauthaud, A., Bundy, K., et al. 2011, Astrophys. J, 742, 125

Gladders, M. D., & Yee, H. K. C. 2005, Astrophys. J. Supp., 157, 1

Gonzalez, A. H., Sivanandam, S., Zabludoff, A. I., & Zaritsky, D. 2013, Astrophys. J, 778, 14

Graham, A., Lauer, T. R., Colless, M., & Postman, M. 1996, Astrophys. J, 465, 534

BIBLIOGRAPHY

Green, J. C., Froning, C. S., Osterman, S., et al. 2012, Astrophys. J, 744, 60

Griffin, M. J., North, C. E., Schulz, B., et al. 2013, MNRAS, 434, 992

Guyon, O. 2003, A&A, 404, 379

Guyon, O., Hinz, P. M., Cady, E., Belikov, R., & Martinache, F. 2014, Astrophys. J, 780, 171

Guyon, O., Pluzhnik, E. A., Galicher, R., et al. 2005, Astrophys. J, 622, 744

Heckman, T. M. 1981, Astrophys. J Lett., 250, L59

Heckman, T. M., Baum, S. A., van Breugel, W. J. M., & McCarthy, P. 1989, Astrophys. J, 338, 48

Hernquist, L. 1990, Astrophys. J, 356, 359

Hicks, A. K., Mushotzky, R., & Donahue, M. 2010, Astrophys. J, 719, 1844

Hinkley, S., Oppenheimer, B. R., Zimmerman, N., et al. 2011, PASP, 123, 74

Hjorth, J., Gall, C., & Michałowski, M. J. 2014, Astrophys. J Lett., 782, L23

Hlavacek-Larrondo, J., Fabian, A. C., Edge, A. C., et al. 2013a, MNRAS, 431, 1638

Hlavacek-Larrondo, J., Allen, S. W., Taylor, G. B., et al. 2013b, Astrophys. J, 777, 163

BIBLIOGRAPHY

Hoffer, A. S., Donahue, M., Hicks, A., & Barthelemy, R. S. 2012, Astrophys. J. Supp., 199, 23

Hogan, M. T., McNamara, B. R., Pulido, F., et al. 2017, ArXiv e-prints, arXiv:1704.00011

Hogg, D. W., Bovy, J., & Lang, D. 2010, ArXiv e-prints, arXiv:1008.4686

Hu, E. M., Cowie, L. L., & Wang, Z. 1985, Astrophys. J. Supp., 59, 447

Hudson, D. S., Mittal, R., Reiprich, T. H., et al. 2010, A&A, 513, A37

Inagaki, T., Lin, Y.-T., Huang, H.-J., Hsieh, B.-C., & Sugiyama, N. 2015, MNRAS, 446, 1107

Jee, M. J., Hughes, J. P., Menanteau, F., et al. 2014, Astrophys. J, 785, 20

Jenkins, C. 2008, MNRAS, 384, 515

Johnstone, R. M., Fabian, A. C., & Nulsen, P. E. J. 1987, MNRAS, 224, 75

Jones, C., & Forman, W. 1992, in NATO Advanced Science Institutes (ASI) Series C, Vol. 366, NATO Advanced Science Institutes (ASI) Series C, ed. A. C. Fabian, 49

Jones, C., & Forman, W. 1999, Astrophys. J, 511, 65

Kaastra, J. S., Paerels, F. B. S., Durret, F., Schindler, S., & Richter, P. 2008, Space Sci. Rev., 134, 155

BIBLIOGRAPHY

Kalas, P., Graham, J. R., Chiang, E., et al. 2008, Science, 322, 1345

Kasper, M., Beuzit, J.-L., Verinaud, C., et al. 2010, EPICS: direct imaging of exoplanets with the E-ELT, doi:10.1117/12.856850

Kauffmann, G., Heckman, T. M., White, S. D. M., et al. 2003a, MNRAS, 341, 33

Kauffmann, G., Heckman, T. M., Tremonti, C., et al. 2003b, MNRAS, 346, 1055

Kennicutt, Jr., R. C. 1992, Astrophys. J, 388, 310

—. 1998, ARA&A, 36, 189

Kewley, L. J., & Dopita, M. A. 2002, Astrophys. J. Supp., 142, 35

Kewley, L. J., Dopita, M. A., Sutherland, R. S., Heisler, C. A., & Trevena, J. 2001, Astrophys. J, 556, 121

Kewley, L. J., Geller, M. J., & Jansen, R. A. 2004, Astron. J., 127, 2002

Kirk, B., Hilton, M., Cress, C., et al. 2015, MNRAS, 449, 4010

Koekemoer, A. M., Aussel, H., Calzetti, D., et al. 2007, Astrophys. J. Supp., 172, 196

Koekemoer, A. M., Faber, S. M., Ferguson, H. C., et al. 2011, Astrophys. J. Supp., 197, 36

Kroupa, P. 2001, MNRAS, 322, 231

BIBLIOGRAPHY

Kuchner, M. J., & Traub, W. A. 2002, Astrophys. J, 570, 900

Kuzuhara, M., Tamura, M., Kudo, T., et al. 2013, Astrophys. J, 774, 11

Lagrange, A.-M., Gratadour, D., Chauvin, G., et al. 2009, A&A, 493, L21

Laigle, C., McCracken, H. J., Ilbert, O., et al. 2016, Astrophys. J. Supp., 224, 24

Lamareille, F. 2010, A&A, 509, A53

Lamareille, F., Mouhcine, M., Contini, T., Lewis, I., & Maddox, S. 2004, MNRAS, 350, 396

LaMassa, S. M., Urry, C. M., Cappelluti, N., et al. 2016, Astrophys. J, 817, 172

Laporte, C. F. P., White, S. D. M., Naab, T., & Gao, L. 2013, MNRAS, 435, 901

Lauer, T. R., Postman, M., Strauss, M. A., Graves, G. J., & Chisari, N. E. 2014, Astrophys. J, 797, 82

Lauer, T. R., Gebhardt, K., Faber, S. M., et al. 2007, Astrophys. J, 664, 226

Le Floc'h, E., Aussel, H., Ilbert, O., et al. 2009, Astrophys. J, 703, 222

Lee, N., Sanders, D. B., Casey, C. M., et al. 2015, Astrophys. J, 801, 80

Leitherer, C. 2005, in American Institute of Physics Conference Series, Vol. 783, The Evolution of Starbursts, ed. S. Hüttmeister, E. Manthey, D. Bomans, & K. Weis, 280–295

BIBLIOGRAPHY

Lewis, A. D., Stocke, J. T., & Buote, D. A. 2002, Astrophys. J Lett., 573, L13

Li, Y., & Bryan, G. L. 2014, Astrophys. J, 789, 153

Li, Y., Bryan, G. L., Ruszkowski, M., et al. 2015, ArXiv e-prints, arXiv:1503.02660

Lidman, C., Suherli, J., Muzzin, A., et al. 2012, MNRAS, 427, 550

Lidman, C., Iacobuta, G., Bauer, A. E., et al. 2013, MNRAS, 433, 825

Lin, Y.-T., Brodwin, M., Gonzalez, A. H., et al. 2013, Astrophys. J, 771, 61

Lin, Y.-T., Mohr, J. J., & Stanford, S. A. 2003, Astrophys. J, 591, 749

Liu, F., Wen, Z., Han, J., & Meng, X. 2012a, Science China Physics, Mechanics, and Astronomy, 55, 354

Liu, F. S., Lei, F. J., Meng, X. M., & Jiang, D. F. 2015, MNRAS, 447, 1491

Liu, F. S., Mao, S., Deng, Z. G., Xia, X. Y., & Wen, Z. L. 2009, MNRAS, 396, 2003

Liu, F. S., Mao, S., Deng, Z. G., Xia, X. Y., & Wen, Z. L. 2009, MNRAS, 396, 2003

Liu, F. S., Mao, S., & Meng, X. M. 2012b, MNRAS, 423, 422

Liu, F. S., Xia, X. Y., Mao, S., Wu, H., & Deng, Z. G. 2008, MNRAS, 385, 23

BIBLIOGRAPHY

Loh, Y.-S., & Strauss, M. A. 2006, MNRAS, 366, 373

Loubser, S. I., Babul, A., Hoekstra, H., et al. 2016, MNRAS, 456, 1565

Loubser, S. I., & Soechting, I. K. 2013, MNRAS, 431, 2933

Lutz, D., Poglitsch, A., Altieri, B., et al. 2011, A&A, 532, A90

Lynds, R. 1970, Astrophys. J Lett., 159, doi:10.1086/180500

Lyot, B. 1939, MNRAS, 99, 580

Macintosh, B., Graham, J. R., Barman, T., et al. 2015, Science, 350, 64

Mahdavi, A., Hoekstra, H., Babul, A., et al. 2013, Astrophys. J, 767, 116

—. 2007, Astrophys. J, 664, 162

Mancini, L., Hartman, J. D., Penev, K., et al. 2015, A&A, 580, A63

Maraston, C. 2005, MNRAS, 362, 799

Maraston, C., Strömbäck, G., Thomas, D., Wake, D. A., & Nichol, R. C. 2009, MNRAS, 394, L107

Markevitch, M., Govoni, F., Brunetti, G., & Jerius, D. 2005, Astrophys. J, 627, 733

Marois, C., Macintosh, B., Barman, T., et al. 2008, Science, 322, 1348

BIBLIOGRAPHY

Marois, C., Zuckerman, B., Konopacky, Q. M., Macintosh, B., & Barman, T. 2010, Nature, 468, 1080

Martin, D. C., Fanson, J., Schiminovich, D., et al. 2005, Astrophys. J Lett., 619, L1

Massey, R., Stoughton, C., Leauthaud, A., et al. 2010, MNRAS, 401, 371

Mawet, D., Pueyo, L., Carlotti, A., et al. 2013, Astrophys. J. Supp., 209, 7

Mawet, D., Pueyo, L., Moody, D., Krist, J., & Serabyn, E. 2010, in Society of Photo-Optical Instrumentation Engineers (SPIE) Conference Series, Vol. 7739, Society of Photo-Optical Instrumentation Engineers (SPIE) Conference Series

Mawet, D., Riaud, P., Absil, O., & Surdej, J. 2005, Astrophys. J, 633, 1191

Mawet, D., Riaud, P., Hanot, C., et al. 2007, in Society of Photo-Optical Instrumentation Engineers (SPIE) Conference Series, Vol. 6693, Society of Photo-Optical Instrumentation Engineers (SPIE) Conference Series

Mawet, D., Serabyn, E., Wallace, J. K., & Pueyo, L. 2011a, Optics Letters, 36, 1506

Mawet, D., Trauger, J. T., Serabyn, E., et al. 2009, in Society of Photo-Optical Instrumentation Engineers (SPIE) Conference Series, Vol. 7440, Society of Photo-Optical Instrumentation Engineers (SPIE) Conference Series

BIBLIOGRAPHY

Mawet, D., Serabyn, E., Moody, D., et al. 2011b, in Society of Photo-Optical Instrumentation Engineers (SPIE) Conference Series, Vol. 8151, Society of Photo-Optical Instrumentation Engineers (SPIE) Conference Series

Mawet, D., Murakami, N., Delacroix, C., et al. 2011c, in Society of Photo-Optical Instrumentation Engineers (SPIE) Conference Series, Vol. 8151, Techniques and Instrumentation for Detection of Exoplanets V, 815108

Mazoyer, J., Pueyo, L., N'Diaye, M., et al. 2016, in Society of Photo-Optical Instrumentation Engineers (SPIE) Conference Series, Vol. 9904, Society of Photo-Optical Instrumentation Engineers (SPIE) Conference Series, 99044T

Mazoyer, J., Pueyo, L., Norman, C., et al. 2015, in Society of Photo-Optical Instrumentation Engineers (SPIE) Conference Series, Vol. 9605, Techniques and Instrumentation for Detection of Exoplanets VII, 96050M

McCracken, H. J., Capak, P., Salvato, M., et al. 2010, Astrophys. J, 708, 202

McCracken, H. J., Milvang-Jensen, B., Dunlop, J., et al. 2012, A&A, 544, A156

McDonald, M., Benson, B., Veilleux, S., Bautz, M. W., & Reichardt, C. L. 2013, Astrophys. J Lett., 765, L37

McDonald, M., Roediger, J., Veilleux, S., & Ehlert, S. 2014a, Astrophys. J Lett., 791, L30

McDonald, M., & Veilleux, S. 2009, Astrophys. J Lett., 703, L172

BIBLIOGRAPHY

McDonald, M., Veilleux, S., Rupke, D. S. N., & Mushotzky, R. 2010, Astrophys. J, 721, 1262

McDonald, M., Veilleux, S., Rupke, D. S. N., Mushotzky, R., & Reynolds, C. 2011, Astrophys. J, 734, 95

McDonald, M., Bayliss, M., Benson, B. A., et al. 2012, Nature, 488, 349

McDonald, M., Swinbank, M., Edge, A. C., et al. 2014b, Astrophys. J, 784, 18

McDonald, M., McNamara, B. R., van Weeren, R. J., et al. 2015, Astrophys. J, 811, 111

McDonald, M., Stalder, B., Bayliss, M., et al. 2016, Astrophys. J, 817, 86

McIntosh, D. H., Guo, Y., Hertzberg, J., et al. 2008, MNRAS, 388, 1537

McNamara, B. R., & Nulsen, P. E. J. 2007, ARA&A, 45, 117

—. 2012, New Journal of Physics, 14, 055023

McNamara, B. R., & O'Connell, R. W. 1989, Astron. J., 98, 2018

McNamara, B. R., Russell, H. R., Nulsen, P. E. J., et al. 2016, Astrophys. J, 830, 79

—. 2014, Astrophys. J, 785, 44

Meece, G. R., Voit, G. M., & O'Shea, B. W. 2016, ArXiv e-prints, arXiv:1603.03674

BIBLIOGRAPHY

Merritt, D. 1984, Astrophys. J, 276, 26

Merten, J., Meneghetti, M., Postman, M., et al. 2015a, Astrophys. J, 806, 4

—. 2015b, Astrophys. J, 806, 4

Mittal, R., McDonald, M., Whelan, J. T., & Bruzual, G. 2017, MNRAS, 465, 3143

Mittal, R., Whelan, J. T., & Combes, F. 2015, MNRAS, 450, 2564

Molendi, S., Tozzi, P., Gaspari, M., et al. 2016, A&A, 595, A123

Monna, A., Seitz, S., Balestra, I., et al. 2017, MNRAS, 466, 4094

Moody, D. C., Gordon, B. L., & Trauger, J. T. 2008, in Society of Photo-Optical Instrumentation Engineers (SPIE) Conference Series, Vol. 7010, Space Telescopes and Instrumentation 2008: Optical, Infrared, and Millimeter, 70103P

Moody, D. C., & Trauger, J. T. 2007, in Society of Photo-Optical Instrumentation Engineers (SPIE) Conference Series, Vol. 6693, Techniques and Instrumentation for Detection of Exoplanets III, 66931I

Morgan, W. W., & Lesh, J. R. 1965, Astrophys. J, 142, 1364

Morrissey, P., Conrow, T., Barlow, T. A., et al. 2007, Astrophys. J. Supp., 173, 682

BIBLIOGRAPHY

Moustakas, J., Kennicutt, Jr., R. C., & Tremonti, C. A. 2006, Astrophys. J, 642, 775

Moustakas, J., Coil, A. L., Aird, J., et al. 2013, Astrophys. J, 767, 50

Mullis, C. R., McNamara, B. R., Quintana, H., et al. 2003, Astrophys. J, 594, 154

Naab, T., Johansson, P. H., & Ostriker, J. P. 2009, Astrophys. J, 699, L178

Navarro, J. F., Frenk, C. S., & White, S. D. M. 1997, Astrophys. J, 490, 493

N'Diaye, M., Pueyo, L., & Soummer, R. 2015, Astrophys. J, 799, 225

Netzer, H. 2013, The Physics and Evolution of Active Galactic Nuclei

Newman, A. B., Treu, T., Ellis, R. S., & Sand, D. J. 2013, Astrophys. J, 765, 25

Nguyen, H. T., Schulz, B., Levenson, L., et al. 2010, A&A, 518, L5

Noeske, K. G., Weiner, B. J., Faber, S. M., et al. 2007, Astrophys. J Lett., 660, L43

Nurgaliev, D., McDonald, M., Benson, B. A., et al. 2013, Astrophys. J, 779, 112

O'Dea, C. P., Baum, S. A., Mack, J., Koekemoer, A. M., & Laor, A. 2004, Astrophys. J, 612, 131

O'Dea, C. P., Baum, S. A., Privon, G., et al. 2008, Astrophys. J, 681, 1035

BIBLIOGRAPHY

O'Donnell, J. E. 1994, Astrophys. J, 422, 158

Oemler, Jr., A. 1976, Astrophys. J, 209, 693

Oliva-Altamirano, P., Brough, S., Lidman, C., et al. 2014, MNRAS, 440, 762

Oliver, S. J., Bock, J., Altieri, B., et al. 2012, MNRAS, 424, 1614

Olsson, E., Aalto, S., Thomasson, M., & Beswick, R. 2010, A&A, 513, A11

Oppenheimer, B. R., Baranec, C., Beichman, C., et al. 2013, Astrophys. J, 768, 24

Peebles, P. J. E. 1980, The large-scale structure of the universe

Peterson, J. R., & Fabian, A. C. 2006, Phys. Rep., 427, 1

Peterson, J. R., Kahn, S. M., Paerels, F. B. S., et al. 2003, Astrophys. J, 590, 207

Peterson, J. R., Paerels, F. B. S., Kaastra, J. S., et al. 2001, A&A, 365, L104

Pilbratt, G. L., Riedinger, J. R., Passvogel, T., et al. 2010, A&A, 518, L1

Pluzhnik, E. A., Guyon, O., Ridgway, S. T., et al. 2006, Astrophys. J, 644, 1246

Postman, M., Coe, D., Benítez, N., et al. 2012, Astrophys. J. Supp., 199, 25

Postman, M., Coe, D., Ben, N., et al. 2012, Astrophys. J. Supp., 1689, arXiv:1106.3328v3

Prasad, D., Sharma, P., & Babul, A. 2015, Astrophys. J, 811, 108

BIBLIOGRAPHY

Pratt, G. W., Croston, J. H., Arnaud, M., & Böhringer, H. 2009, A&A, 498, 361

Pueyo, L., Kasdin, N. J., Carlotti, A., & Vanderbei, R. 2011, Astrophys. J. Supp., 195, 25

Pueyo, L., & Norman, C. 2013, Astrophys. J, 769, 102

Pueyo, L., Soummer, R., Hoffmann, J., et al. 2015, Astrophys. J, 803, 31

Puget, P., Stadler, E., Doyon, R., et al. 2004, in Society of Photo-Optical Instrumentation Engineers (SPIE) Conference Series, Vol. 5492, Ground-based Instrumentation for Astronomy, ed. A. F. M. Moorwood & M. Iye, 978–987

Rafferty, D. A., McNamara, B. R., & Nulsen, P. E. J. 2008, Astrophys. J, 687, 899

Rafferty, D. A., McNamara, B. R., Nulsen, P. E. J., & Wise, M. W. 2006, Astrophys. J, 652, 216

Rameau, J., Chauvin, G., Lagrange, A.-M., et al. 2013, Astrophys. J Lett., 772, L15

Rawle, T. D., Edge, A. C., Egami, E., et al. 2012, Astrophys. J, 747, 29

Reach, W. T., Megeath, S. T., Cohen, M., et al. 2005, PASP, 117, 978

Rieke, G. H., Young, E. T., Engelbracht, C. W., et al. 2004, Astrophys. J. Supp., 154, 25

BIBLIOGRAPHY

Rodriguez-Gomez, V., Sales, L. V., Genel, S., et al. 2017, MNRAS, 467, 3083

Rosa-González, D., Terlevich, E., & Terlevich, R. 2002, MNRAS, 332, 283

Rossetti, M., Gastaldello, F., Eckert, D., et al. 2017, MNRAS, 468, 1917

Ruane, G., Jewell, J., Mawet, D., Pueyo, L., & Shaklan, S. 2016, ArXiv e-prints, arXiv:1607.06400

Russell, H. R., McNamara, B. R., Edge, A. C., et al. 2014, Astrophys. J, 784, 78

Russell, H. R., McDonald, M., McNamara, B. R., et al. 2016, ArXiv e-prints, arXiv:1611.00017

Ruszkowski, M., & Springel, V. 2009, Astrophys. J, 696, 1094

Rybicki, G. B., & Lightman, A. P. 1986, Radiative Processes in Astrophysics, 400

Salpeter, E. E. 1955, Astrophys. J, 121, 161

Sanders, D. B., Salvato, M., Aussel, H., et al. 2007, Astrophys. J. Supp., 172, 86

Sanderson, A. J. R., Ponman, T. J., Finoguenov, A., Lloyd-Davies, E. J., & Markevitch, M. 2003, MNRAS, 340, 989

Santos, J. S., Balestra, I., Tozzi, P., et al. 2016, MNRAS, 456, L99

Sarazin, C. L. 1988, X-ray emission from clusters of galaxies

BIBLIOGRAPHY

Schlegel, D. J., Finkbeiner, D. P., & Davis, M. 1998, Astrophys. J, 500, 525

Scoville, N., Aussel, H., Brusa, M., et al. 2007, Astrophys. J. Supp., 172, 1

Shankar, F., Buchan, S., Rettura, A., et al. 2015, Astrophys. J, 802, 73

Shen, S., Mo, H. J., White, S. D. M., et al. 2003, MNRAS, 343, 978

Shen, S., Yang, X., Mo, H., van den Bosch, F., & More, S. 2014, Astrophys. J, 782, 23

Shields, J. C. 1992, Astrophys. J Lett., 399, L27

Siebenmorgen, R., Heymann, F., & Efstathiou, A. 2015, A&A, 583, A120

Singh, A., & Sharma, P. 2015, MNRAS, 446, 1895

Sivaramakrishnan, A., Koresko, C. D., Makidon, R. B., Berkefeld, T., & Kuchner, M. J. 2001, Astrophys. J, 552, 397

Sivaramakrishnan, A., & Yaitskova, N. 2005, Astrophys. J Lett., 626, L65

Soummer, R. 2005, Astrophys. J Lett., 618, L161

Soummer, R., Sivaramakrishnan, A., Pueyo, L., Macintosh, B., & Oppenheimer, B. R. 2011, Astrophys. J, 729, 144

Sparks, W. B., Macchetto, F., & Golombek, D. 1989, Astrophys. J, 345, 153

Spitzer, L. 1962, Physics of Fully Ionized Gases

BIBLIOGRAPHY

Steinhardt, C. L., Speagle, J. S., Capak, P., et al. 2014, Astrophys. J Lett., 791, L25

Stott, J. P., Collins, C. A., Burke, C., Hamilton-Morris, V., & Smith, G. P. 2011, MNRAS, 414, 445

Stott, J. P., Collins, C. A., Sahlén, M., et al. 2010, Astrophys. J, 718, 23

Sutherland, R. S., & Dopita, M. A. 1993, Astrophys. J. Supp., 88, 253

Sutherland, W., Emerson, J., Dalton, G., et al. 2015, A&A, 575, A25

Taniguchi, Y., Scoville, N., Murayama, T., et al. 2007, Astrophys. J. Supp., 172, 9

Taniguchi, Y., Kajisawa, M., Kobayashi, M. A. R., et al. 2015, PASJ, 67, 104

Tonini, C., Bernyk, M., Croton, D., Maraston, C., & Thomas, D. 2012, Astrophys. J, 759, 43

Traub, W. A., & Vanderbei, R. J. 2003, Astrophys. J, 599, 695

Trauger, J., Moody, D., Gordon, B., Krist, J., & Mawet, D. 2012, in Society of Photo-Optical Instrumentation Engineers (SPIE) Conference Series, Vol. 8442, Space Telescopes and Instrumentation 2012: Optical, Infrared, and Millimeter Wave, 84424Q

BIBLIOGRAPHY

Trauger, J., Moody, D., Krist, J., & Gordon, B. 2016, Journal of Astronomical Telescopes, Instruments, and Systems, 2, 011013

Tremblay, G. R., O'Dea, C. P., Baum, S. A., et al. 2012, MNRAS, 424, 1042

—. 2015, ArXiv e-prints, arXiv:1505.03533

Tremblay, G. R., Oonk, J. B. R., Combes, F., et al. 2016, Nature, 534, 218

Tremonti, C. A., Heckman, T. M., Kauffmann, G., et al. 2004, Astrophys. J, 613, 898

Treu, T., Ellis, R. S., Liao, T. X., et al. 2005, Astrophys. J, 633, 174

van der Marel, R. P., & van Dokkum, P. G. 2007, Astrophys. J, 668, 756

Van Dyk, S., Werner, M., & N., S. 2013, http://irsa.ipac.caltech.edu/

van Weeren, R. J., Andrade-Santos, F., Dawson, W. A., et al. 2017, Nature Astronomy, 1, 0005

Vanderbei, R. J., Kasdin, N. J., Spergel, D. N., & Kuchner, M. 2003, in Society of Photo-Optical Instrumentation Engineers (SPIE) Conference Series, Vol. 5170, Techniques and Instrumentation for Detection of Exoplanets, ed. D. R. Coulter, 49–56

Vanderbei, R. J., & Traub, W. A. 2005, Astrophys. J, 626, 1079

BIBLIOGRAPHY

Veilleux, S. 2002, in Astronomical Society of the Pacific Conference Series, Vol. 284, IAU Colloq. 184: AGN Surveys, ed. R. F. Green, E. Y. Khachikian, & D. B. Sanders, 111

Véron-Cetty, M. P., & Véron, P. 2000, A&A Rev., 10, 81

Vikhlinin, A., Kravtsov, A., Forman, W., et al. 2006, Astrophys. J, 640, 691

Vikhlinin, A., McNamara, B. R., Forman, W., et al. 1998, Astrophys. J, 502, 558

Voit, G. M., & Donahue, M. 2015, Astrophys. J Lett., 799, L1

Voit, G. M., Donahue, M., Bryan, G. L., & McDonald, M. 2015, Nature, 519, 203

Voit, G. M., Meece, G., Li, Y., et al. 2017, ArXiv e-prints, arXiv:1607.02212

Von Der Linden, A., Best, P. N., Kauffmann, G., & White, S. D. M. 2007a, MNRAS, 379, 867

Von Der Linden, A., Best, P. N., Kauffmann, G., & White, S. D. M. 2007b, MNRAS, 379, 867

Vulcani, B., Marchesini, D., De Lucia, G., et al. 2016, Astrophys. J, 816, 86

Wagner, K., Apai, D., Kasper, M., & Robberto, M. 2015, Astrophys. J Lett., 813, L2

Webb, T., Noble, A., DeGroot, A., et al. 2015a, Astrophys. J, 809, 173

Webb, T. M. A., Muzzin, A., Noble, A., et al. 2015b, Astrophys. J, 814, 96

Wen, X.-Q., Wu, H., Zhu, Y.-N., et al. 2013, MNRAS, 433, 2946

Werner, M. W., Roellig, T. L., Low, F. J., et al. 2004, Astrophys. J. Supp., 154, 1

Werner, N., Oonk, J. B. R., Canning, R. E. A., et al. 2013, Astrophys. J, 767, 153

Werner, N., Oonk, J. B. R., Sun, M., et al. 2014, MNRAS, 439, 2291

Whiley, I. M., Aragón-Salamanca, A., De Lucia, G., et al. 2008, MNRAS, 387, 1253

Wild, V., Walcher, C. J., Johansson, P. H., et al. 2009, MNRAS, 395, 144

Witt, A. N., & Gordon, K. D. 2000, Astrophys. J, 528, 799

Yang, H.-Y. K., & Reynolds, C. S. 2016, Astrophys. J, 818, 181

Yi, S., Demarque, P., & Oemler, Jr., A. 1998, Astrophys. J, 492, 480

Yi, S. K. 2008, in Astronomical Society of the Pacific Conference Series, Vol. 392, Hot Subdwarf Stars and Related Objects, ed. U. Heber, C. S. Jeffery, & R. Napiwotzki, 3

Zamojski, M. A., Schiminovich, D., Rich, R. M., et al. 2007, Astrophys. J. Supp., 172, 468

Zwicky, F. 1938, PASP, 50, 218

Vita

A.8 Refereed Articles

List does not include articles currently in preparation.

1. **Kevin Fogarty**, Rebecca Larson, Marc Postman, et al. *The Relationship Between Brightest Cluster Galaxy Star Formation and the Intracluster Medium in CLASH*, *accepted, ApJ*

2. **Kevin Fogarty**, Laurent Pueyo, Johan Mazoyer, Mamadou NDiaye, *Polynomial Apodizers for Centrally Obscured Vortex Coronagraphs*, *accepted, AJ*

3. Reinout J. van Weeren, Felipe Andrade-Santos, William A. Dawson, Nathan Golovich, Dharam V. Lal, Hyesung Kang, Dongsu Ryu, Marcus Brggen, Georgiana A. Ogrean, William R. Forman, Christine Jones, Vinicius M. Placco, Rafael M. Santucci, David Wittman, M. James Jee, Ralph P. Kraft, David Sobral, Andra Stroe, **Kevin Fogarty**, *The Case for Electron Re-Acceleration at*

Galaxy Cluster Shocks, 2017, Nature Astronomy, 1, doi:10.1038/s41550-016-0005

4. **Kevin Fogarty**, Marc Postman, Thomas Connor, Megan Donahue, John Moustakas, *Star Formation Activity in CLASH Brightest Cluster Galaxies*, 2015, ApJ, 813, 117

5. Megan Donahue, Thomas Connor, **Kevin Fogarty**, Yuan Li, Mark G. Voit, Marc Postman, Anton Koekemoer, John Moustakas, Larry Bradley, Holland Ford, *Ultraviolet Morphology and Unobscured UV Star Formation Rates of CLASH Brightest Cluster Galaxies*, 2015, ApJ, 805, 177

6. Mathew Madhavacheril, Neelima Sehgal, Rupert Allison, Nick Battaglia, Richard J Bond, Erminia Calabrese, Jerod Caliguiri, Kevin Coughlin, Devin Chrichton, Rahul Datat, Mark J Devlin, Joanna Dunkley, Rolando Dunner, **Kevin Fogarty**, Emily Grace, Amir Hajian, Matthew Hasselfield, Colin J Hill, Matt Hilton, Adam D Hincks, Renee Hlozek, John P Hughes, Arthur Kosowsky, Thibaut Louis, Marius Lungu, Jeff McMahon, Kavilan Moodley, Charles Munson, Sigurd Naess, Federico Nati, Laura Newburgh, Michael D Niemack, Lyman A Page, Bruce Partridge, Benjamin Schmitt, Blake D Sherwin, Jon Seiver, David N Spergel, Suzanne T Staggs, Robert Thornton, Alexander Van Engelen, Jonathan T Ward, Edward J Wollack, Atacama Cosmology Telescope Collaboration, *Evidence of Lensing of the Cosmic Microwave Background by Dark Matter Halos*, 2015, PhRvL, 114, 151302

7. R.J. van Weeren, **K. Fogarty**, C. Jones, W.R. Forman, T.E. Clarke, M. Bruggen, R.P. Kraft, D.V. Lal, S.S. Murray, H.J.A Rottgering, *Complex Diffuse Radio Emission in the Merging Planck ESZ Cluster A3411*, 2013, ApJ, 769, 101

A.9 Proceedings

List does not include articles currently in preparation.

1. **Kevin Fogarty**, Laurent Pueyo, Dimitri Mawet, *Optimal apodizations for on-axis vector vortex coronagraphs*, 2014, SPIE, 9143, 914326

2. C. Jones, W. Forman, **K. Fogarty**, S. Murray, A. Vikhlinin, *X-ray properties and scaling relations for Planck ESZ Clusters*, 2013, AN, 334, 437